

# CMS Draft Analysis Note

*The content of this note is intended for CMS internal use and distribution only*

2016/01/07

Head Id: 314200

Archive Id: 316911M

Archive Date: 2015/12/10

Archive Tag: trunk

## Search for supersymmetry in the multijet and missing transverse momentum channel in pp collisions at 13 TeV

A. Borzou<sup>1</sup>, K. Call<sup>1</sup>, K. Hatakeyama<sup>1</sup>, H. Liu<sup>1</sup>, J. W. Gary<sup>2</sup>, A. Ghiasi<sup>2</sup>, P. Jandir<sup>2</sup>, F. Lacroix<sup>2</sup>, O. Long<sup>2</sup>, J. Bradmiller-Feld<sup>3</sup>, J. Richman<sup>3</sup>, M. Franco Sevilla<sup>3</sup>, A. Ovcharova<sup>3</sup>, W. T. Ford<sup>4</sup>, F. O. Jensen<sup>4</sup>, T. Mulholland<sup>4</sup>, K. Stenson<sup>4</sup>, V. D. Elvira<sup>5</sup>, J. Hirschauer<sup>5</sup>, S. Mrenna<sup>5</sup>, K. Pedro<sup>5</sup>, N. Tran<sup>5</sup>, A. Whitbeck<sup>5</sup>, S. Bein<sup>6</sup>, H. Prosper<sup>6</sup>, A. Dräger<sup>7</sup>, S. Kurz<sup>7</sup>, M. Niedziela<sup>7</sup>, C. Sander<sup>7</sup>, S. Sharma<sup>8</sup>, B. Mahakud<sup>9</sup>, G. Mohanty<sup>9</sup>, K. A. Ulmer<sup>10</sup>, and R. Patel<sup>10</sup>

<sup>1</sup> Baylor University

<sup>2</sup> University of California, Riverside

<sup>3</sup> University of California, Santa Barbara

<sup>4</sup> University of Colorado at Boulder

<sup>5</sup> Fermi National Accelerator Laboratory

<sup>6</sup> Florida State University

<sup>7</sup> University of Hamburg

<sup>8</sup> Indian Institute of Science Education and Research, Pune

<sup>9</sup> Tata Institute of Fundamental Research

<sup>10</sup> Texas A&M University

## Abstract

An inclusive search for supersymmetry in the all-hadronic channel, based on the  $H_T$ ,  $H_T^{\text{miss}}$ ,  $N_{\text{jet}}$ , and  $N_{\text{b-jet}}$  variables, is described. The analysis is an inclusive search targeting gluino pair production, with or without bottom-quark jets as gluino decay products. The analysis techniques, expected sources of systematic uncertainty, anticipated discovery potential, and expected sensitivity are discussed. The targeted SUSY production scenarios are described by the T1qqqq, T1bbbb, and T1tttt simplified models.

This box is only visible in draft mode. Please make sure the values below make sense.

PDFAuthor: The RA2/b team  
PDFTitle: Search for supersymmetry in the multijet and missing transverse momentum channel in pp collisions at 13 TeV  
PDFSubject: CMS  
PDFKeywords: CMS, physics, software, computing

Please also verify that the abstract does not use any user defined symbols

DRAFT

## 1 Contents

2	1	Introduction . . . . .	5
3	2	Triggers . . . . .	5
4	2.1	Search region trigger . . . . .	5
5	2.2	Control sample triggers . . . . .	7
6	3	Event samples . . . . .	8
7	3.1	Standard model MC samples . . . . .	8
8	3.2	Signal models . . . . .	10
9	4	Event selection . . . . .	10
10	5	Search variables and binning: $H_T$ , $H_T^{\text{miss}}$ , $N_{\text{jet}}$ , and $N_{\text{b-jet}}$ . . . . .	19
11	6	Estimation of top quark and W+jets backgrounds . . . . .	21
12	6.1	Classical Lost-lepton ( $e/\mu$ ) estimation method . . . . .	21
13	6.2	Hadronically decaying $\tau$ lepton background estimation . . . . .	37
14	6.3	Lepton and isolated-track efficiency validation . . . . .	45
15	7	Estimation of QCD multijet background . . . . .	60
16	7.1	QCD background from low $\Delta\phi_{\min}$ control sample . . . . .	60
17	8	Estimation of $Z \rightarrow \nu\bar{\nu}$ background . . . . .	67
18	8.1	$Z \rightarrow \nu\bar{\nu}$ measurement for $N_{\text{b-jet}} = 0$ . . . . .	68
19	8.2	Summary of $\gamma + \text{jets}$ prediction and systematic uncertainty . . . . .	74
20	8.3	$Z \rightarrow \nu\bar{\nu}$ measurement for $N_{\text{b-jet}} > 0$ . . . . .	77
21	8.4	$Z \rightarrow \nu\bar{\nu}$ background prediction . . . . .	81
22	9	Data/MC comparisons . . . . .	84
23	10	Signal Systematic Uncertainties . . . . .	88
24	11	Statistical treatment . . . . .	89
25	11.1	Implementation of background predictions . . . . .	89
26	11.2	Implementation of signal systematics . . . . .	91
27	11.3	Computation of signal significance and 95% C.L. exclusion Limits . . . . .	91
28	11.4	Fit validation . . . . .	92
29	12	Results . . . . .	92
30	13	Summary . . . . .	97
31	A	Supplemental information on the triggers . . . . .	109
32	B	Comparison of QCD samples . . . . .	111
33	C	Supplemental materials for lost-lepton background estimation . . . . .	112
34	C.1	Closure test with varied MC cross sections . . . . .	112
35	C.2	Closure test in QCD binning . . . . .	114
36	D	Supplemental materials for hadronically-decaying $\tau$ background estimation . . . . .	115
37	E	Other track veto efficiency validation studies . . . . .	116
38	E.1	Effect of the $m_T$ cut on track isolation efficiency . . . . .	116
39	F	Full Table of Event Yields . . . . .	118
40	G	Estimating ( $Z \rightarrow \nu\nu$ )+jets background with $\gamma+\text{jets}$ . . . . .	122
41	G.1	Datasets . . . . .	122
42	G.2	Photon reconstruction . . . . .	122
43	G.3	Photon reconstruction efficiencies and purity . . . . .	122

44	G.4	Efficiencies for photon method . . . . .	126
45	H	$Z \rightarrow \ell^+ \ell^-$ with $\ell = e, \mu$ . . . . .	129
46	H.1	Lepton acceptance . . . . .	129
47	H.2	Lepton selection efficiency . . . . .	129
48	H.3	$Z$ sample purity . . . . .	129
49	H.4	Extrapolation factors . . . . .	130
50	H.5	Combinatorial model for extrapolation from zero to $n$ b-jets . . . . .	132
51	I	MC plots and expected yields with $3 \text{ fb}^{-1}$ . . . . .	135
52	J	Toy tests of statistical model . . . . .	135
53	K	Additional information on pre-fit vs post-fit results . . . . .	137
54	L	Additional Background Techniques . . . . .	141
55	L.1	QCD background from Rebalance-and-Smear . . . . .	141
56	L.2	Extrapolating background estimates from medium to high $H_T^{\text{miss}}$ . . . . .	147
57	L.3	Details of the $H_T^{\text{miss}}$ extrapolation method . . . . .	158
58	M	Study of QCD bad jet categorization and $H_T^{\text{miss}}$ dependence . . . . .	162
59	N	Signal contamination in the QCD background evaluation . . . . .	164
60	O	Study of $N_{\text{b-jet}}$ dependence in the QCD background model . . . . .	166
61	P	Detailed results of QCD BG estimation from $\min \Delta\phi_{\text{min}}$ . . . . .	167
62	Q	Additional data-MC comparisons . . . . .	169
63	Q.1	Single-muon control region plots requested by the inclusive searches group	169

DRAFT

64 The following changes have been made relative to v12

- 65 • Updated to current MET filters.  
66 • Zinv restored updated plots for photon purity.  
67 • Zinv Updated Table 19 and Fig. 78 with small bug fix, MC stat errors in the J factor.

68 The following changes have been made relative to v11

- 69 • Updated description of the uncertainties in the lost-lepton section (6.1)

70 The following changes have been made relative to v10

- 71 • Updates in the lost-lepton section (6.1): small changes to description of systematic uncertainties. Split up isotrack veto efficiencies into electron, muon and pion.  
72 Added appendix, closure tests in QCD binning (inverted and non-inverted region).  
73 • Updates in the hadronic tau background section (6.2): dataset update to  $2.1 \text{ fb}^{-1}$ , as well as small changes to description of systematic uncertainties. Added appendix, closure tests in QCD binning (inverted and non-inverted region).  
74 • Section 7.1 (QCD BG): With the update to  $2.1 \text{ fb}^{-1}$  of data, it's no longer necessary  
75 to constrain the HT1 or highest  $N_{\text{jet}}$  BG model parameters in the likelihood fit. They  
76 are now determined from the data. Added Fig. 61, which shows the results of the  
77 likelihood fit for the BG model parameters.  
78 • Section 8 ( $Z \rightarrow \nu\bar{\nu}$ ) Some figures and tables updated to  $2.1 \text{ fb}^{-1}$ , mostly in Subsection  
79 8.1. The double ratio treatment is revised and updated.  
80

83 The following changes have been made relative to v6

- 84 • Section 8: Table 19 corrected purity uncertainties.  
85 • Revised Section 6.2 to take into account the following changes: (1) In the step of  
86 removing the muon momenta from jets, now the jet energy correction factor is taken  
87 into account. (2) The binning to parametrize the acceptance,  $m_T$  cut efficiency, correc-  
88 tions for muons from taus, and isolated track veto efficiency is made finer in order to  
89 improve the closure tests and the predictions. (3) Now the HLT\_Mu15\_IsoVVVL\_PFHT350\_v  
90 trigger is specifically used and the dataset is corrected for the trigger efficiency.

91 The following changes have been made relative to v5

- 92 • Revised Section 7.1 (QCD BG from  $\Delta\phi_{\min}$ ) to take into account the following changes:  
93    - The 4th highest  $p_T$  jet was added to the jets included in  $\Delta\phi_{\min}$ .  
94    - Updated all MC samples. Now using  $H_T$ -binned Madgraph QCD samples.  
95    - Results are presented for the  $1.3 \text{ fb}^{-1}$  data sample.  
96 • Completely updated lost-lepton section (Section 6.1)  
97 • Added content (appendix) to answer questions from readiness talk

98 The following changes have been made relative to v4

- 99 • 7.1 (QCD, low- $\Delta\phi_{\min}$ ) Changed "LH fit" to "likelihood fit", corrected caption of Ta-  
100 ble 14.  
101 • 7.2.2 (QCD, R+S) corrected inverted inequality in the last paragraph.  
102 • 6.4 (Lost-lepton validation) corrections to Eq. (18), Figs. 44 and 45. Added plots for  
103 e  $\mu$  reconstruction, isoalated track efficiecnies (e $\mu$ ) along with recalculated  $m_T$ . Also

parts of the text was updated to account for the added figures.

- Appendix G.5 and reference thereto in 8.2 (b-jet combinatorics) new plots showing gen b vs b-jet distributions.
- Fixed table in lost-lepton section.
- Significant revisions to Section L.2, where we have changed from using  $(1 - \cos(\Delta\theta_T))/2$  distributions to directly using  $H_T^{\text{miss}}/p_T(W)$  distributions.
- Updates in the lost-lepton section: added new realisation of the isotracks veto (3 independent efficiencies), updated all plots, added content to take account for the comments of markus and alex
- Updated in the hadronic-tau section (Section 6.2): the closure plots are updated using  $t\bar{t}$ ,  $W+\text{jets}$ , and single top MC samples. In addition, some discussions on the systematic uncertainties are added.
- Sect. 8, Zinv, especially 8.2, moved several plots and accompanying text from appendices F and G to main section 8. Extensively revised the 0b to Nb extrapolation procedure description to say that we now use MC scale factors, taking binomial and flat as bounds for systematics.
- Updated Lost-lepton: section on systematic uncertainties

The following changes have been made relative to v3

- The section on QCD BG estimation from a low  $\Delta\phi_{\min}$  control sample (Sec.7.1) has been almost completely rewritten. The primary variable has been changed from  $\Delta\hat{\phi}_{\min}$  to  $\Delta\phi_{\min}$ .
- The trigger section (Sec.2.1) was updated to the current menu.
- Updated the section on the classical lost lepton approach (Section 6.1). All plots have been updated. Binning of the efficiencies has been changed to the ones that are used at the moment and the isolated track veto is now also included. The total prediction of the lost lepton background has been added as a conclusion.
- The Zinv section now contains a relatively high-level overview of the hybrid method. Details of the separate  $Z \rightarrow \ell\ell$  and gamma+jets methods have been moved to appendices.
- Improved description of Rzgamma uncertainties. – still missing on additional plot from Jim
- Updated plots showing  $Z \rightarrow \ell^+ \ell^-$  kinematic shapes differences between 0 b-tag and  $\geq 1$  b-tag. Added extrapolation factor toy study.
- Added table of  $Z \rightarrow \nu\bar{\nu}$  uncertainties

---

## 138 1 Introduction

139 This note describes a search for supersymmetry (SUSY) in the all-hadronic final state. Many  
 140 models of physics beyond the standard model (SM) predict final states with jets and trans-  
 141 verse momentum imbalance  $\vec{p}_T^{\text{miss}}$ . The momentum imbalance arises from weakly interacting  
 142 new-physics particles that escape without detection. Amongst new-physics models, SUSY has  
 143 received much attention because it may predict the unification of the strong, weak, and elec-  
 144 tromagnetic forces, and may provide a dark matter candidate. In particular, “natural” SUSY  
 145 models minimize the fine tuning associated with the value of the Higgs boson mass and its  
 146 radiative corrections. In natural SUSY, the top squark, left-handed bottom squark, gluino, and  
 147 higgsino are required to be light, i.e., to have masses near the electroweak energy scale, making  
 148 them potentially accessible at the LHC.

149 Amongst possible SUSY processes, gluino pair production has the largest cross section, making  
 150 it a pertinent channel for early SUSY searches at the LHC Run 2. In the natural SUSY frame-  
 151 work, gluinos might decay to bottom-antibottom ( $b\bar{b}$ ) or top-antitop ( $t\bar{t}$ ) quark pairs, plus the  
 152 lightest supersymmetric particle (LSP). In R-parity conserving models, such as are considered  
 153 here, the LSP is stable and assumed to be weakly interacting, leading to potentially large  $\vec{p}_T^{\text{miss}}$ .  
 154 Supersymmetry events thus might be characterized by a large number of jets, the presence of  
 155 bottom-quark jets, and significant  $\vec{p}_T^{\text{miss}}$ . Because of the all-hadronic requirement, the events  
 156 are, in addition, expected to exhibit large values of  $H_T$ , where  $H_T$  is the scalar sum of the trans-  
 157 verse momentum values ( $p_T$ ) of the jets.

158 We present a general search for gluino pair production leading to final states with large  $\vec{p}_T^{\text{miss}}$ ,  
 159 large  $H_T$ , and large jet multiplicity. The data are examined in bins of  $N_{\text{jet}}$ ,  $N_{b\text{-jet}}$ ,  $H_T$ , and  $H_T^{\text{miss}}$ ,  
 160 where  $N_{\text{jet}}$  is the number of jets,  $N_{b\text{-jet}}$  is the number of jets tagged as arising from a bottom-  
 161 quark ( $b$  jet), and  $H_T^{\text{miss}}$  – which is used as the measure of  $\vec{p}_T^{\text{miss}}$  – is the magnitude of the vector  
 162 sum of the jet momenta. The search is performed in exclusive bins of the four observables.  
 163 Events with  $t\bar{t}$  production can be identified in a complementary way by examining events with  
 164 large values of  $N_{\text{jet}}$  in addition to events with  $b$  jets.

165 This study combines and extends search strategies developed for the analysis of the CMS Run 1  
 166 data, specifically the study of Ref. [1] (SUS-12-024), which examined data in bins of  $N_{b\text{-jet}}$  but  
 167 not  $N_{\text{jet}}$ , and proved sensitive to SUSY scenarios with gluino decay to a  $b\bar{b}$  pair and the LSP,  
 168 and the study of Ref. [2] (SUS-13-012), which examined data in bins of  $N_{\text{jet}}$  but not  $N_{b\text{-jet}}$ , and  
 169 proved sensitive to scenarios with gluino decay to a  $t\bar{t}$  pair and the LSP. The two approaches are  
 170 combined in a unified framework to yield a more comprehensive and inclusive study with  
 171 improved sensitivity.

## 172 2 Triggers

### 173 2.1 Search region trigger

174 Events in the search region, as well as the single-lepton and QCD control samples, are collected  
 175 by the triggers

- 176     • `HLT_PFHT350_PFMET100_NoiseCleaned_v*`
- 177     • `HLT_PFHT350_PFMET100_JetIDCleaned_v*`,

178 which are seeded at Level 1 by `L1_HTT175`. At the start of the data taking, only the first trigger  
 179 was included in the trigger menu, and it was later exchanged for the second trigger. At the  
 180 level of the analysis, the triggers are considered to be equivalent. These triggers require an

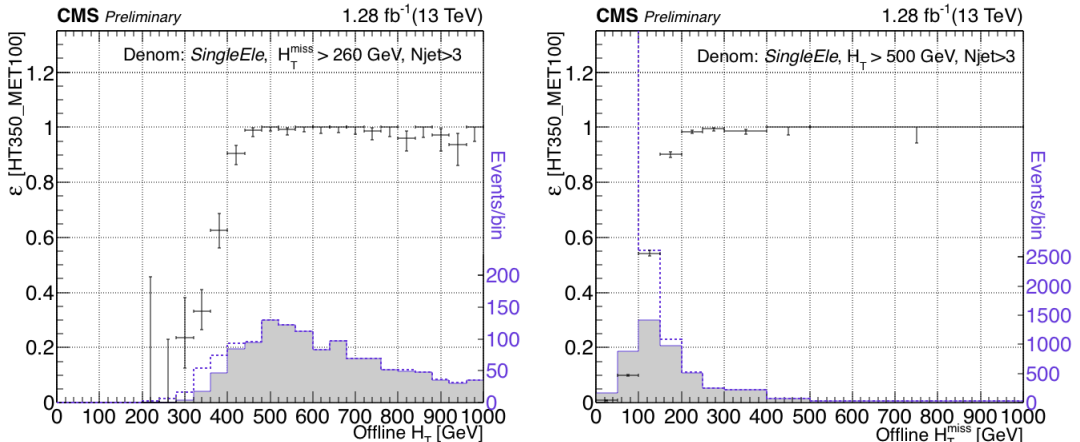


Figure 1: The trigger efficiency for `HLT_PFHT350_PFMET100*` as a function of the search variables. For the efficiency vs  $H_T$ , a threshold on the  $H_T^{\text{miss}}$  of 260 GeV is applied to ensure full efficiency of the  $E_T^{\text{miss}}$  component of the trigger. For the efficiency vs  $H_T^{\text{miss}}$ , the baseline selection of  $H_T > 500$  GeV is applied. The dashed (solid) blue lines show the distributions of the denominator (numerator) samples.

- 181 online calorimeter-based  $H_T > 280$  GeV and calorimeter-based  $E_T^{\text{miss}} > 70$  GeV.  
 182 The trigger efficiency is estimated as a function of the offline  $H_T$  and  $H_T^{\text{miss}}$ , which are defined  
 183 in Section 4, as follows. Events passing the nearly independent trigger  
 184 • `HLT_Ele27_eta2p1_WPLoose_Gsf_v*`  
 185 having  $N_{\text{jets}} > 3$  and a single reconstructed electron are taken as the base sample, and the  
 186 efficiency is taken as the fraction of base sample events that fire the primary trigger. Monte  
 187 Carlo studies (see Appendix A) show that this method, namely, the choice of reference trigger,  
 188 yields an unbiased estimate of the trigger efficiency in the 0-lepton region with  $H_T^{\text{miss}} > 150$  GeV  
 189 and  $H_T > 500$  GeV, which encompasses the baseline selection region.  
 190 Figure 1 shows the trigger efficiency vs the offline kinematic variables. The baseline selection  
 191 requires  $H_T > 500$  GeV and  $H_T^{\text{miss}} > 200$  GeV, and the efficiency is measured to be greater than  
 192 98% for events satisfying this selection. Because the  $H_T$  component of the efficiency is well  
 193 above the offline  $H_T$  plateau, but small inefficiencies are observed in the  $H_T^{\text{miss}}$  range between  
 194 200 and 400 GeV, we compute the efficiency in two bins of  $H_T^{\text{miss}}$ :  $200 \text{ GeV} < H_T^{\text{miss}} < 500 \text{ GeV}$   
 195 and  $H_T^{\text{miss}} > 500 \text{ GeV}$ , corresponding to the search regions. These efficiencies and the corre-  
 196 sponding uncertainties are listed in Table 1. The statistical uncertainty is based on the 68%CL  
 197 Clopper-Pearson interval. The systematic uncertainty is the residual difference between the  
 198 efficiency obtained from applying the described method to a sample of simulated  $t\bar{t}$  events and  
 199 the true efficiency derived from simulated signal events in the signal region.

Table 1: The estimated fraction of signal events with an  $H_T$  greater than 500 GeV and  $N_{\text{jets}} > 3$  that pass the `HLT_PFHT350_PFMET100*` trigger. Systematic uncertainties apply only to signal events.

$H_T^{\text{miss}}$ range (GeV)	efficiency	+/- (statistical)	+/- (systematic)
(200-500)	0.9887	0.0032/0.0043	0.0081/0.0130
(500-1000)	1.0000	0.0000/0.0156	0.0000/0.0001

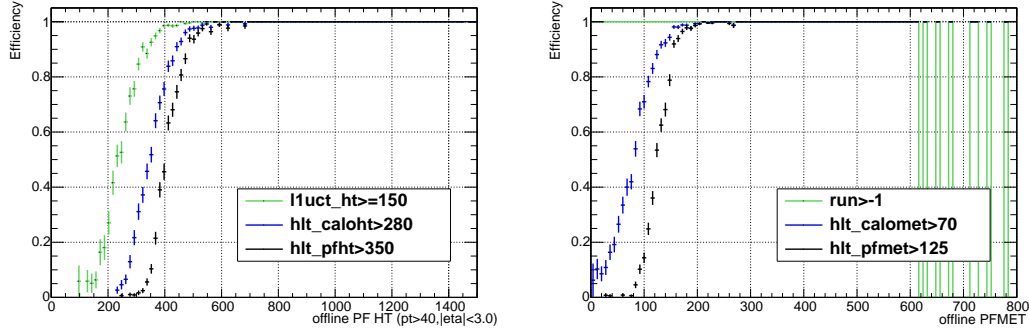


Figure 2: The trigger seed turn-on as a function of offline kinematic variables.

200 It is expected that the shape of the trigger efficiency as a function of the  $H_T^{\text{miss}}$  depends on  
 201 whether the  $H_T^{\text{miss}}$  arises from invisible particles in the events or from jet energy mis-measurements.  
 202 The latter is typically the case in high  $E_T^{\text{miss}}$  QCD events, sometimes called fake  $E_T^{\text{miss}}$  events.  
 203 For this reason, the trigger efficiency is measured separately in a QCD-enriched data control  
 204 sample and applied to simulated QCD events where appropriate. The fake  $H_T^{\text{miss}}$  trigger effi-  
 205 ciency is documented in Appendix A. Note that this fake  $E_T^{\text{miss}}$  trigger efficiency never directly  
 206 enters the analysis. It is used only to correct QCD MC in data-MC comparison plots.  
 207 The trigger seeds may need to be changed to the L1\_HTT200 when the LHC reaches higher in-  
 208 stantaneous luminosity. The HLT particle flow  $H_T$  threshold of 350 GeV was chosen with this in  
 209 mind, since the turn-on for lower thresholds would become limited by the L1\_HTT200 require-  
 210 ment, as can be seen in Fig. 2. The HLT particle flow  $E_T^{\text{miss}}$  threshold of 100 GeV was chosen  
 211 in order to keep the HLT rate at full instantaneous luminosity below around 40 Hz. The HLT  
 212 particle flow  $E_T^{\text{miss}}$  threshold was recently lowered from 120 to 100 GeV after improved pileup  
 213 subtraction was added to the HLT calorimeter reconstruction, which significantly reduced the  
 214 background rate for  $E_T^{\text{miss}}$ -based triggers.

## 215 2.2 Control sample triggers

216 For the hadronic  $\tau$  background determination we employ a  $\tau$  template method (Chapter 6.2)  
 217 that requires a control sample with a muon and a low amount of  $H_T^{\text{miss}}$ . We select these events  
 218 with the `HLT_Mu15_IsoVVVL_PFHT350_v*` trigger which requires a 15 GeV muon and  $H_T >$   
 219 350 GeV. The muon uses the standard ID at HLT, but the isolation requirement is calculated  
 220 with a reduced cone of  $R = 0.2$  to make more similar to the Mini isolation requirement applied  
 221 offline (see Sec. 4.2 in Ref. [3]).  
 222 Additionally, the  $Z \rightarrow \nu\bar{\nu}$  background estimation employs  $Z \rightarrow \ell^+\ell^-$  control samples se-  
 223 lected with the `HLT_Mu15_IsoVVVL_PFHT350_v*` trigger as well as with its electron counter-  
 224 part `HLT_Ele15_IsoVVVL_PFHT350_v*`.

Figure 3 shows the muon  $p_T$  and  $H_T$  turn-on curves for the muon trigger. Plateau efficiency is reached for lepton  $p_T > 20$  GeV and  $H_T > 475$  GeV for both the muon and electron triggers, with no significant dependence on the analysis variables  $H_T$ ,  $H_T^{\text{miss}}$ ,  $N_{\text{jet}}$ , and  $N_{\text{b-jet}}$ . We assign a 1-2% systematic uncertainty to account for residual dependence on these variables. The resulting single lepton efficiency estimated in  $2.1 \text{ fb}^{-1}$  of data using an orthogonal MET170 trigger

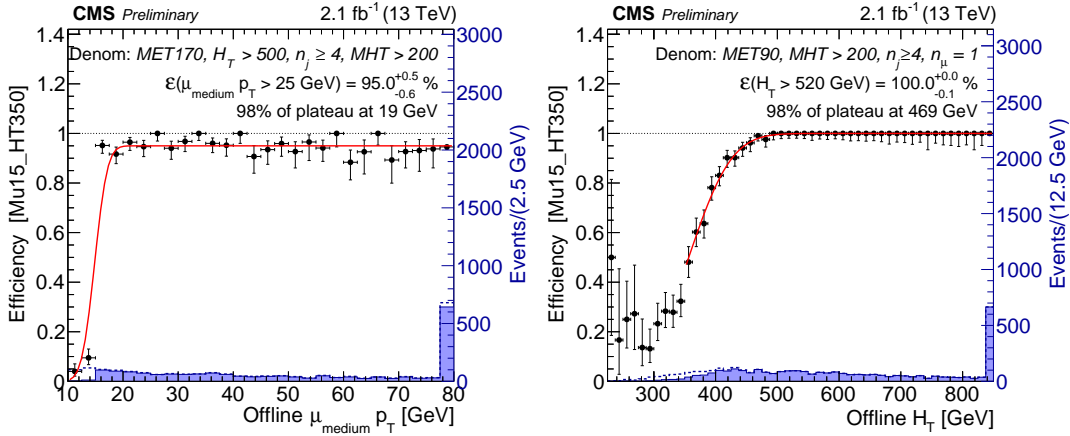


Figure 3: Turn-on curves for the  $H_T$  and muon  $p_T$  legs of the  $\mu + H_T$  triggers employed to select the leptonic control sample for the hadronic  $\tau$  background estimation.

is:

$$\epsilon_\mu = (95.1^{+0.5}_{-0.6} \pm 1.0)\% \quad (1)$$

$$\epsilon_e = (86.3^{+0.9}_{-0.9} \pm 2.0)\%. \quad (2)$$

225 These efficiencies include the effect from the prescaling of these triggers, which spent about  
226 0.5% of the time with a prescale of 10 at the beginning of LHC fills.

Given that these triggers require only one online lepton, the trigger efficiency for an offline selection with two leptons is higher. If we take the efficiency of reconstructing each lepton as independent of each other, the dilepton efficiency would increase as  $\epsilon_{2\ell} = \epsilon_\ell^2 + 2\epsilon_\ell(1 - \epsilon_\ell) = 98 - 100\%$ . We measure the dilepton trigger efficiency selecting events with  $H_T > 500$  GeV and two opposite-sign offline electrons with an invariant mass of  $70 < m_{\ell\ell} < 110$  GeV. The dilepton trigger efficiencies are thus

$$\epsilon_{\mu\mu} = (99.1^{+0.3}_{-0.5} \pm 0.5)\% \quad (3)$$

$$\epsilon_{ee} = (96.9^{+0.7}_{-0.8} \pm 1.0)\%. \quad (4)$$

227 We studied these efficiencies as a function of the analysis variables and saw no dependence  
228 on any of them. Figure 4 shows the trigger efficiency being flat as a function of the  $p_T$  of the  
229 dilepton system (the Z boson for the most part), even for very high  $p_T$ .

230 For the  $Z \rightarrow \nu\nu$  background estimation we also select a sample with one photon and a num-  
231 ber of jets (Chapter 8). This sample is triggered with `HLT_Photon90_CaloIdL_PFHT500_v*`,  
232 where the online  $H_T$  includes the  $p_T$  of the photon. Figure 5 shows the  $H_T$  and photon  $p_T$  turn-  
233 on curves for this trigger. Again, for  $H_T > 500$  GeV the efficiency is close to 100%. The photon  
234 plateau efficiency is  $96.4^{+0.2}_{-0.2}\%$ .

### 235 3 Event samples

#### 236 3.1 Standard model MC samples

237 Monte Carlo (MC) samples reconstructed with CMSSW release 7.4 (Spring15) are used through-  
238 out. The SM samples are listed in Tables 2-9. The cross sections listed correspond to next-to-  
239 leading-order (NLO) calculations unless otherwise noted. All samples except signal scans use

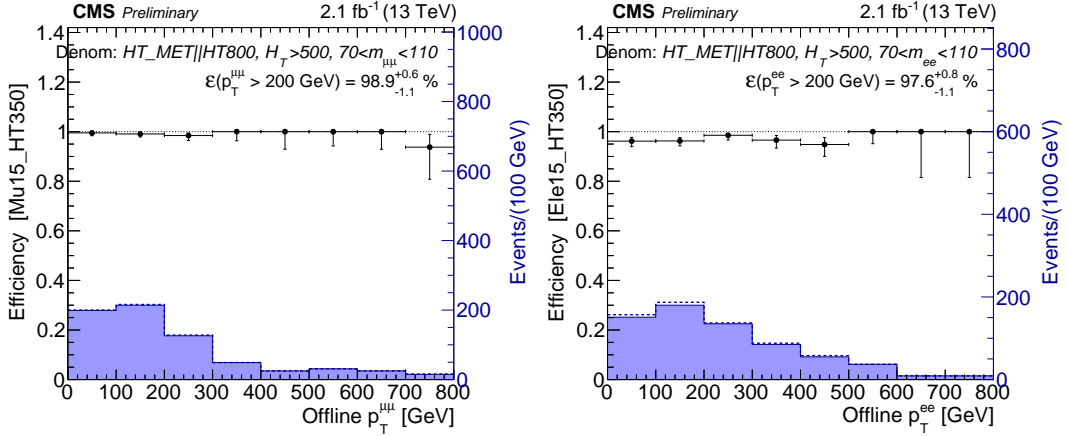


Figure 4: Trigger efficiency for an offline selection of two opposite-sign leptons as a function of the  $p_T$  of the dilepton system. No dependence of the efficiency on  $p_T^{\ell\ell}$  is found.

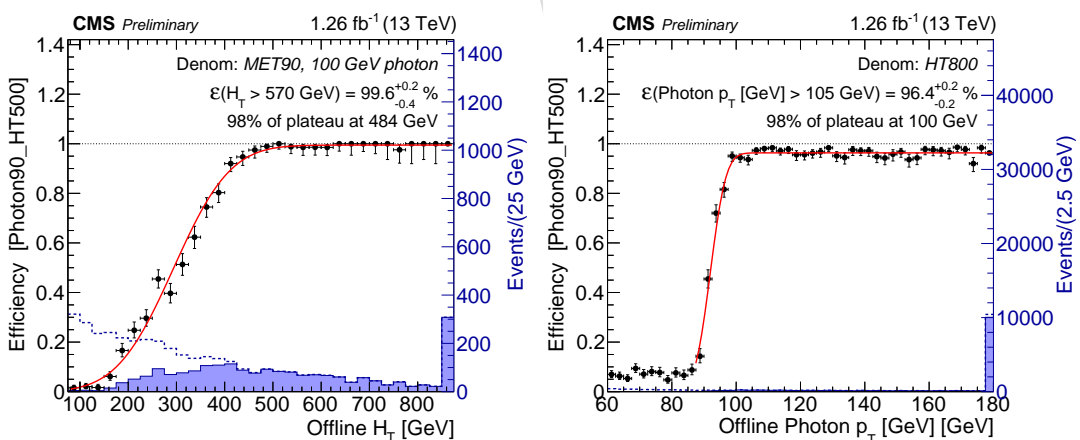


Figure 5: Turn-on curves for the  $H_T$  and photon  $p_T$  legs of the photon trigger.

the PU20bx25 pileup scenario, which simulates a pileup distribution with an average of 20 interactions per bunch crossing and a 25 ns interval between bunches.

Table 2: SM  $t\bar{t}$  MC samples used in the analysis. The cross sections are calculated to NNLO.

Dataset	$\sigma$ (pb)	$\int \mathcal{L} dt$ (fb $^{-1}$ )
TTJets.TuneCUETP8M1_13TeV-madgraphMLM-pythia8	816.0	13.90
TTJets_SingleLeptFromT.TuneCUETP8M1_13TeV-madgraphMLM-pythia8	179.3	324.6
TTJets_SingleLeptFromTbar.TuneCUETP8M1_13TeV-madgraphMLM-pythia8	179.3	335.7
TTJets.DiLept.TuneCUETP8M1_13TeV-madgraphMLM-pythia8	86.66	351.2
TTJets.HT-600to800.TuneCUETP8M1_13TeV-madgraphMLM-pythia8	2.615	1898
TTJets.HT-800to1200.TuneCUETP8M1_13TeV-madgraphMLM-pythia8	1.077	3198
TTJets.HT-1200to2500.TuneCUETP8M1_13TeV-madgraphMLM-pythia8	0.195	5063
TTJets.HT-2500toInf.TuneCUETP8M1_13TeV-madgraphMLM-pythia8	0.002	218575

Table 3: SM QCD MC samples used in the analysis. All cross sections are calculated to LO.

Dataset	$\sigma$ (pb)	$\int \mathcal{L} dt$ (fb $^{-1}$ )
QCD_HT200to300.TuneCUETP8M1_13TeV-madgraphMLM-pythia8	1735000	0.01
QCD_HT300to500.TuneCUETP8M1_13TeV-madgraphMLM-pythia8	366800	0.05
QCD_HT500to700.TuneCUETP8M1_13TeV-madgraphMLM-pythia8	29370	0.67
QCD_HT700to1000.TuneCUETP8M1_13TeV-madgraphMLM-pythia8	6524	2.30
QCD_HT1000to1500.TuneCUETP8M1_13TeV-madgraphMLM-pythia8	1064	4.67
QCD_HT1500to2000.TuneCUETP8M1_13TeV-madgraphMLM-pythia8	121.5	31.67
QCD_HT2000toInf.TuneCUETP8M1_13TeV-madgraphMLM-pythia8	25.42	77.17

Table 4: SM  $Z \rightarrow \nu\nu + \text{jets}$  MC samples used in the analysis. The cross sections are calculated to NNLO.

Dataset	$\sigma$ (pb)	$\int \mathcal{L} dt$ (fb $^{-1}$ )
ZJetsToNuNu.HT-100To200_13TeV-madgraph	345.0	14.92
ZJetsToNuNu.HT-200To400_13TeV-madgraph	96.38	52.22
ZJetsToNuNu.HT-400To600_13TeV-madgraph	13.46	75.34
ZJetsToNuNu.HT-600ToInf_13TeV-madgraph	5.170	196.5

### 3.2 Signal models

The signal models examined are the T1qqqq, T1bbbb, and T1tttt simplified model spectra (SMS) SUSY scenarios, illustrated in Fig. 6. Table 10 documents the event sets. The cross sections are calculated to NLO [4].

## 4 Event selection

For all plots and tables in this chapter, the MC samples are scaled to 10 fb $^{-1}$ . We reproduce all plots and tables with the MC samples scaled to 3 fb $^{-1}$  in Appendix I.

The search regions for the analysis require large  $H_T^{\text{miss}}$ , large  $H_T$ , a large number of jets  $N_{\text{jet}}$ , and no leptons. The analysis targets three signal models differing primarily in the number of jets and b-tagged jets produced in the gluino decay. Each of these models can be further divided into separate topologies with a different mass splitting between the gluino and LSP. To maximize sensitivity to this diverse collection of topologies, a loose baseline selection is initially applied in  $H_T^{\text{miss}}$ ,  $H_T$ , and  $N_{\text{jet}}$ . The resulting cutflow for the SM background events is given in Table 11. As indicated in Table 12, this baseline selection preserves about two-thirds of the non-compressed T1bbbb and T1qqqq events (which have no leptons), about one-third of the non-compressed T1tttt events (which may have leptons), and 10-20% of the compressed events.

Table 5: SM  $W \rightarrow \ell\nu + \text{jets}$  MC samples used in the analysis. The cross sections are calculated to NNLO.

Dataset	$\sigma$ (pb)	$\int \mathcal{L} dt$ (fb $^{-1}$ )
WJetsToLNu_HT-100To200_TuneCUETP8M1_13TeV-madgraphMLM-pythia8	1635	6.20
WJetsToLNu_HT-200To400_TuneCUETP8M1_13TeV-madgraphMLM-pythia8	437.0	11.97
WJetsToLNu_HT-400To600_TuneCUETP8M1_13TeV-madgraphMLM-pythia8	59.50	31.96
WJetsToLNu_HT-600ToInf_TuneCUETP8M1_13TeV-madgraphMLM-pythia8	22.80	45.44
WJetsToLNu_HT-600To800_TuneCUETP8M1_13TeV-madgraphMLM-pythia8	15.50	257.1
WJetsToLNu_HT-800To1200_TuneCUETP8M1_13TeV-madgraphMLM-pythia8	6.366	247.4
WJetsToLNu_HT-1200To2500_TuneCUETP8M1_13TeV-madgraphMLM-pythia8	1.614	158.4
WJetsToLNu_HT-2500ToInf_TuneCUETP8M1_13TeV-madgraphMLM-pythia8	0.037	6770

Table 6: SM single-top MC samples used in the analysis. The cross sections are calculated to NLO.

Dataset	$\sigma$ (pb)	$\int \mathcal{L} dt$ (fb $^{-1}$ )
ST_s-channel_4f_leptonDecays_13TeV-amcatnlo-pythia8_TuneCUETP8M1	3.340	183.6
ST_t-channel_antitop_4f_leptonDecays_13TeV-powheg-pythia8_TuneCUETP8M1	26.23	64.64
ST_t-channel_top_4f_leptonDecays_13TeV-powheg-pythia8_TuneCUETP8M1	44.07	74.88
ST_tW_antitop_5f_inclusiveDecays_13TeV-powheg-pythia8_TuneCUETP8M1	35.80	27.93
ST_tW_top_5f_inclusiveDecays_13TeV-powheg-pythia8_TuneCUETP8M1	35.80	27.81

Table 7: SM diboson and other rare process MC samples used in the analysis. The cross sections are calculated to NNLO.

Dataset	$\sigma$ (pb)	$\int \mathcal{L} dt$ (fb $^{-1}$ )
ttHJetTobb_M125_13TeV_amcatnloFXFX_madspin_pythia8	0.293	18269
TTZToLLNuNu_M-10_TuneCUETP8M1_13TeV-amcatnlo-pythia8	0.228	811.4
TTZToQQ_TuneCUETP8M1_13TeV-amcatnlo-pythia8	0.530	663.4
TTWJetsToLNu_TuneCUETP8M1_13TeV-amcatnloFXFX-madspin-pythia8	0.204	635.6
TTWJetsToQQ_TuneCUETP8M1_13TeV-amcatnloFXFX-madspin-pythia8	0.423	1018
ZH_HToBB_ZToNuNu_M125_13TeV_amcatnloFXFX_madspin_pythia8	0.100	12116
WH_HToBB_WToLNu_M125_13TeV_amcatnloFXFX_madspin_pythia8	0.260	4782
WWTo1L1Nu2Q_13TeV_amcatnloFXFX_madspin_pythia8	50.00	64.26
WWTo2L2Nu_13TeV-powheg	12.18	158.5
WZTo1L1Nu2Q_13TeV_amcatnloFXFX_madspin_pythia8	10.71	1339
WZTo1L3Nu_13TeV_amcatnloFXFX_madspin_pythia8	3.058	305.7
ZZTo2Q2Nu_13TeV_amcatnloFXFX_madspin_pythia8	4.040	5556
ZZTo2L2Q_13TeV_amcatnloFXFX_madspin_pythia8	3.220	3706
TTTT_TuneCUETP8M1_13TeV-amcatnlo-pythia8	0.009	57031
WWZ_TuneCUETP8M1_13TeV-amcatnlo-pythia8	0.165	1341
WZZ_TuneCUETP8M1_13TeV-amcatnlo-pythia8	0.056	3938
ZZZ_TuneCUETP8M1_13TeV-amcatnlo-pythia8	0.014	15297

Table 8: SM DY+jets MC samples used in the analysis. The cross sections are calculated to NNLO.

Dataset	$\sigma$ (pb)	$\int \mathcal{L} dt$ (fb $^{-1}$ )
DYJetsToLL_M-50_TuneCUETP8M1_13TeV-madgraphMLM-pythia8	6025	1.50
DYJetsToLL_M-50_HT-100to200_TuneCUETP8M1_13TeV-madgraphMLM-pythia8	171.5	15.31
DYJetsToLL_M-50_HT-200to400_TuneCUETP8M1_13TeV-madgraphMLM-pythia8	52.58	18.18
DYJetsToLL_M-50_HT-400to600_TuneCUETP8M1_13TeV-madgraphMLM-pythia8	6.761	155.0
DYJetsToLL_M-50_HT-600toInf_TuneCUETP8M1_13TeV-madgraphMLM-pythia8	2.718	363.5

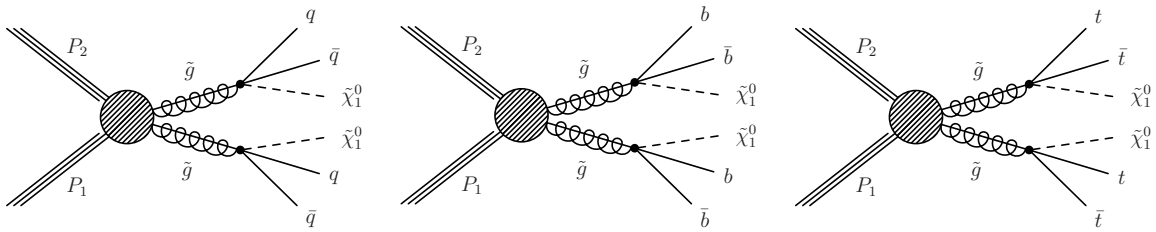


Figure 6: Event diagrams for the SUSY scenarios considered in this study: the (left) T1qqqq, (center) T1bbbb, and (right) T1tttt simplified model spectra scenarios, with  $\tilde{\chi}_1^0$  the lightest neutralino, taken to be a weakly interacting LSP.

258 The events satisfying this selection are then binned in  $H_T^{\text{miss}}$ ,  $H_T$ ,  $N_{\text{jet}}$ , and  $N_{\text{b-jet}}$ . Figures 7 and  
259 8 present  $N - 1$  plots of these variables after application of the baseline selection.

260 Jets used in this analysis are reconstructed from particle-flow (PF) candidates using the anti- $k_T$   
261 algorithm [5] with the size parameter 0.4. The PF algorithm is used to individually identify and  
262 reconstruct all particles produced in the collision (PF candidates); namely charged hadrons,  
263 photons, neutral hadrons, muons, and electrons [6]. Charged particles that emerge from ver-  
264 tices other than the primary vertex (the primary vertex is the reconstructed vertex with the  
265 largest sum of charged-track  $p_T^2$  values) are removed from the list of physics objects used for  
266 jet clustering. in order to reduce the impact of pileup collisions. No explicit subtraction of  
267 leptons from jet clustering is performed. The jet 4-momenta are corrected for residual pileup  
268 contributions, arising mainly from neutral particles, and for detector response effects using the  
269 standard level-1, 2, and 3 corrections [7, 8].

270 The following requirements define the baseline selection:

- 271 •  $N_{\text{jet}} \geq 4$ :

272 Since every pair of gluinos decays to four quarks, all events are required to contain  
273 at least four “good” jets, defined by

- 274 •  $p_T > 30 \text{ GeV}$ ,
- 275 •  $|\eta| < 2.4$ ,
- 276 • satisfying “loose” jet ID criteria for PF jets [9]:
  - 277 • neutral hadron fraction  $< 0.99$ ,
  - 278 • neutral EM fraction  $< 0.99$ ,
  - 279 • number of constituents  $> 1$ ,
  - 280 • charged hadron fraction  $> 0$ ,
  - 281 • charged multiplicity  $> 0$ ,
  - 282 • charged EM fraction  $< 0.99$

283 Jets that match isolated leptons, photons, and tracks (definitions are given  
284 below) within  $\Delta R = 0.04$  are not subject to these jet ID criteria, as these jet  
285 ID criteria may reject jets dominated by leptons or photons, whereas the  
286 intention of the jet ID requirements is only to remove anomalous jets that  
287 arise because of detector malfunctions or reconstruction failures.

288 A relatively low jet  $p_T$  threshold of 30 GeV is chosen to increase sensitivity to models  
289 with a small mass splitting between the gluino and LSP and thus with softer  $H_T^{\text{miss}}$   
290 and  $H_T$  spectra.

- 291 •  $H_T > 500 \text{ GeV}$ , where  $H_T = \sum_{\text{jets}} p_T$ . The jets must meet the criteria listed above.

- 292 •  $H_T^{\text{miss}} > 200 \text{ GeV}$ , where  $H_T^{\text{miss}} = \left| \sum_{\text{jets}} \vec{p}_T \right|$ . All jets included in this sum must satisfy  
 293  $p_T > 30 \text{ GeV}$ ,  $|\eta| < 5$ . The jets within tracker acceptance ( $-2.4 < \eta < 2.4$ ) must also  
 294 satisfy the “loose” jet ID listed above. The jets outside of tracker acceptance need  
 295 only satisfy

- 296 • For jets with  $3 < |\eta| < 5$ :
- 297 • neutral EM fraction  $< 0.90$ ,  
 298 • number of neutral particles  $> 10$
- 299 • Jets with  $2.4 < |\eta| < 3$ :
- 300 • neutral EM fraction  $< 0.99$ ,  
 301 • neutral hadron fraction  $< 0.99$ ,  
 302 • number of constituents  $> 1$

- 303 • Muon veto:

Muon candidates are selected using the POG-recommended “Medium Muon” selection [10] with the additional requirements:

$$\begin{aligned} d_{xy}(\mu, \text{PV}) &< 0.2 \text{ mm} \\ d_z(\mu, \text{PV}) &< 0.5 \text{ mm} \end{aligned} \quad (5)$$

Muon candidates are required to have  $p_T > 10 \text{ GeV}$  and  $|\eta| < 2.4$ . To distinguish between prompt muons and muons from b-hadron decays, muons are required to satisfy an isolation requirement,  $I_{\text{mini}} < 0.2$ , where  $I_{\text{mini}}$  is the mini-isolation variable described in Ref. [3]. Any event with a muon satisfying all of the above criteria is vetoed.

- 309 • Electron veto:

Electron candidates are selected using the POG-recommended “Cut Based VETO” selection [11]. Electron candidates are required to have  $p_T > 10 \text{ GeV}$  and  $|\eta| < 2.5$ . Electron candidates are required to satisfy an isolation requirement of  $I_{\text{mini}} < 0.1$ . Any event with an electron satisfying all of the above criteria is vetoed.

- 314 • Angular cut  $\Delta\phi(j_1, H_T^{\text{miss}}) > 0.5$ ,  $\Delta\phi(j_2, H_T^{\text{miss}}) > 0.5$ ,  $\Delta\phi(j_3, H_T^{\text{miss}}) > 0.3$ ,  $\Delta\phi(j_4, H_T^{\text{miss}}) > 0.3$ :

The majority of QCD multijet events in our high- $H_T^{\text{miss}}$  search region have jets with undermeasured momenta and thus a spurious momentum imbalance. A signature of such an event is a jet closely aligned in direction with the  $H_T^{\text{miss}}$  vector. To suppress this background, we reject all events in which the two highest- $p_T$  jets lie within 0.5 radians of the  $H_T^{\text{miss}}$  vector in the azimuthal coordinate:

$$\begin{aligned} \Delta\phi(j_1, H_T^{\text{miss}}) &> 0.5 \\ \Delta\phi(j_2, H_T^{\text{miss}}) &> 0.5 \end{aligned} \quad (6)$$

This requirement is relaxed for the third- and fourth-highest- $p_T$  jets:

$$\begin{aligned} \Delta\phi(j_3, H_T^{\text{miss}}) &> 0.3 \\ \Delta\phi(j_4, H_T^{\text{miss}}) &> 0.3 \end{aligned} \quad (7)$$

No such requirement is placed on other jets.

- 316 • Isolated track vetoes: Following the event selection described above, including the  
 317 muon and electron event vetoes, the dominant source of background for many of the  
 318

search regions is  $t\bar{t}$ , single-top, and  $W+jets$  events with one  $W \rightarrow \ell\nu$  decay. In about half these background events, the  $W$  boson decays to a  $\tau$  lepton and the  $\tau$  lepton decays hadronically, while in the other half, an electron or muon is not identified or does not satisfy the criteria for an isolated electron or muon candidate given above. To suppress these backgrounds, we reject events with one or more isolated charged track.

The requirements for the definition of an isolated track differ slightly depending on whether the track is identified as leptonic or hadronic by the PF algorithm. For leptonic tracks, we require:

- $p_T > 5 \text{ GeV}$ ,
- $I_{\text{tk}} < 0.2$ ,

where  $I_{\text{tk}}$  is the scalar  $p_T$  sum of other charged tracks within  $\Delta R \equiv \sqrt{(\Delta\phi)^2 + (\Delta\eta)^2} < 0.3$  of the primary track, divided by the  $p_T$  value of the primary track. For hadronic tracks, we apply slightly tighter requirements to reduce hadronic (non- $\tau$ ) signal loss:

- $p_T > 10 \text{ GeV}$ ,
- $I_{\text{tk}} < 0.1$ .

Since the isolation sum does not include neutral-particle candidates, the isolation distributions and efficiencies of leptonic tracks should be similar to those of pions from single-prong  $\tau$  decays. Thus we can validate the rate at which the hadronic track veto suppresses  $\tau \rightarrow \text{hadrons}$  events by measuring the leptonic track isolation efficiency in data via a tag-and-probe method.

To retain more signal and thus to improve the signal-to-background event discrimination, isolated tracks are considered only if they satisfy

$$m_T(\text{tk}, E_T^{\text{miss}}) = \sqrt{2p_T^{\text{tk}}E_T^{\text{miss}}(1 - \cos\Delta\phi)} < 100 \text{ GeV}, \quad (8)$$

where  $p_T^{\text{tk}}$  is the transverse momentum of the track and  $\Delta\phi$  is the azimuthal separation between the track and  $\vec{p}_T^{\text{miss}}$ . As illustrated in Fig. 9, a large fraction of the tracks from events with one-and-only-one source of  $E_T^{\text{miss}}$ , i.e., one  $W \rightarrow \ell\nu$  decay, satisfy this requirement. This  $m_T$  restriction improves the T1tttt event selection efficiency by up to 30% (depending on the search bin) while increasing the background by less than 10%.

To reduce the influence of tracks from extraneous  $pp$  interactions (pileup), isolated tracks are considered only if their nearest distance of approach along the beam axis to a reconstructed vertex is smaller for the primary event vertex than for any other vertex.

The false rejection rates of the track vetoes, that is, the fraction of events without a prompt electron, muon, or hadronically decaying  $\tau$  lepton rejected by a track veto, is 4% for the muon veto, 15% for the electron veto, and 22% for the isolated track veto.

A detailed study of the sources of these background events, both before and after the selection requirement on isolated tracks, is presented in Section 6.

#### 355 • Event cleaning:

We reject events with a jet that satisfies  $p_T > 30 \text{ GeV}$  and  $|\eta| < 5$  if the jet fails the loose jet ID criteria given above.

As the commissioning of early data progresses, we will also begin to apply event filters designed by various POGs to reject events with spurious  $E_T^{\text{miss}}$  signals.

- 360 • Tagging of b-jets:

361 Although not used for a selection criterion, the number of selected jets  $N_{\text{b-jet}}$  satisfying  
362 the CSV b-tagging algorithm at the medium working point (CSVM) is used as a  
363 discriminating variable.

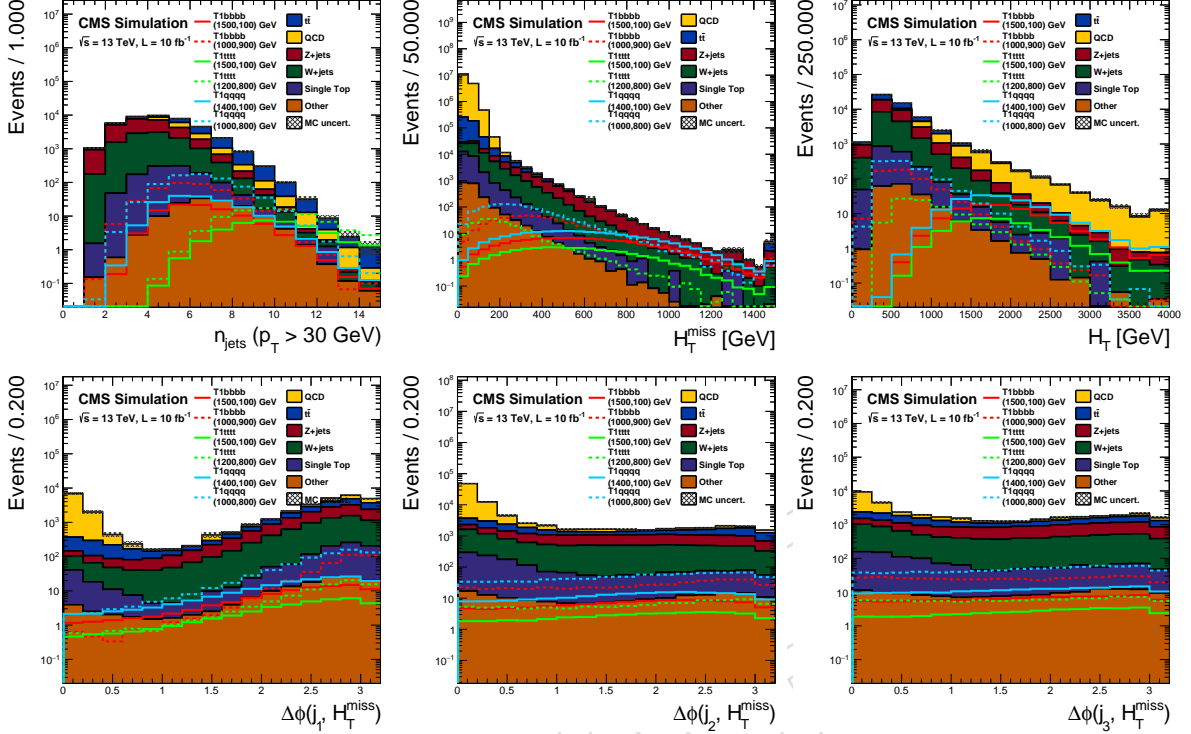


Figure 7:  $N - 1$  plots of  $N_{\text{jet}}$ ,  $H_T^{\text{miss}}$ ,  $H_T$ , and the  $\Delta\phi$  variables. The SM and signal MC samples are scaled to  $10 \text{ fb}^{-1}$ .

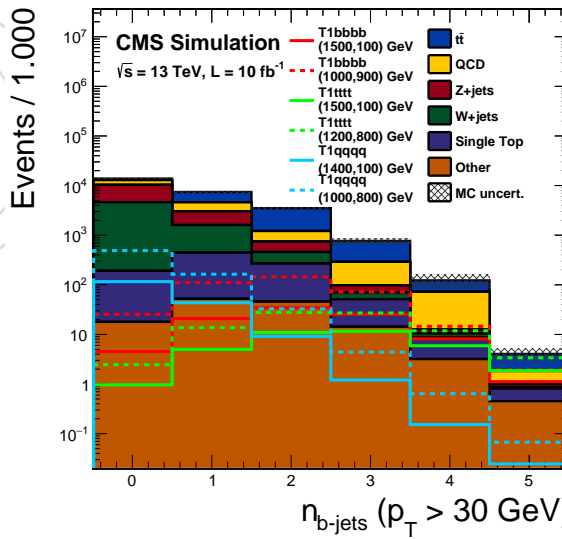


Figure 8: The number of b-tagged jets after the baseline selection. There is no minimum  $N_{\text{b-jet}}$  requirement in the baseline selection.

- 364 The relative importance of the background sources across the binned subspace ( $N_{\text{b-jet}}, N_{\text{jet}}$ ) can  
365 be seen in Fig. 10.

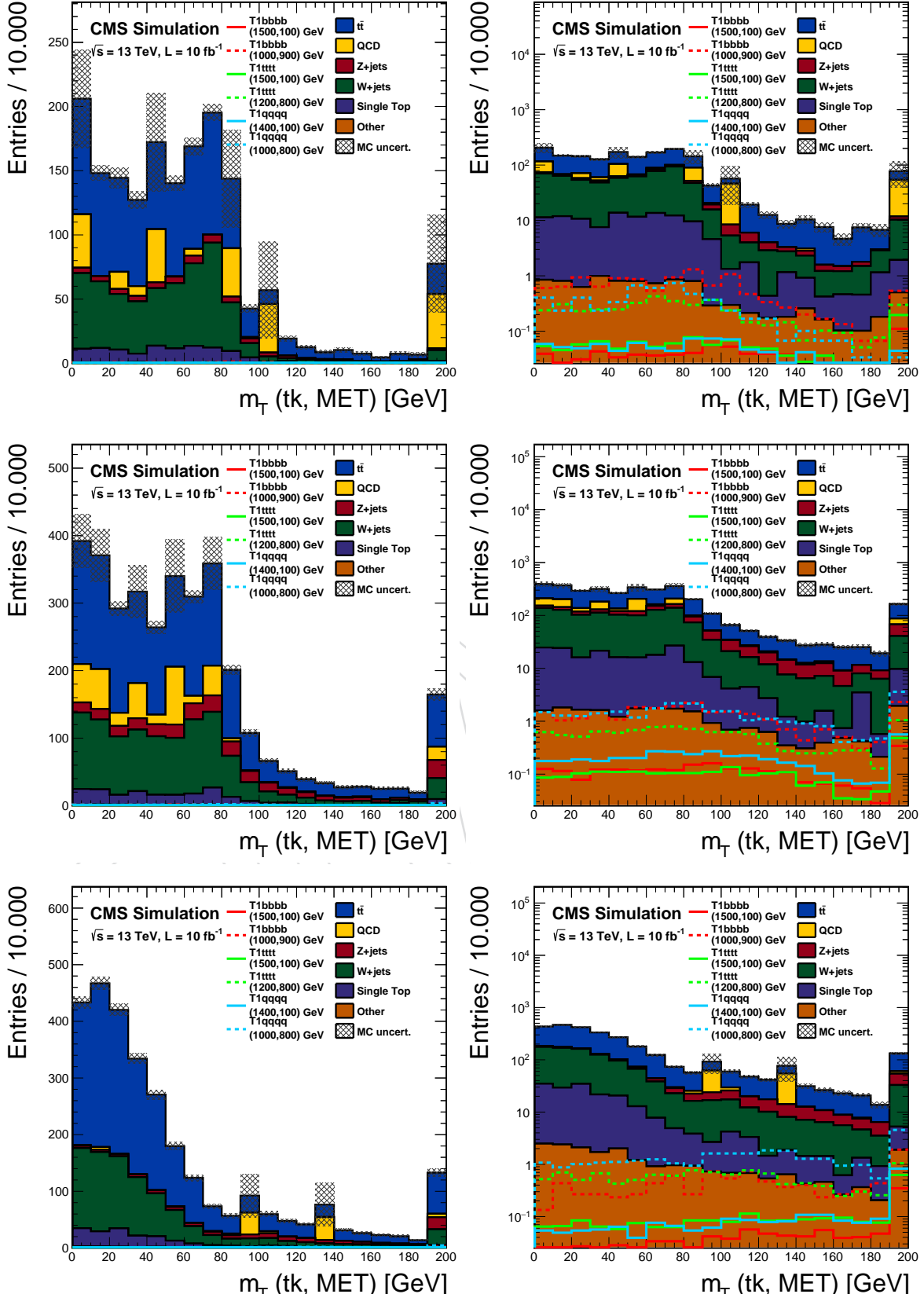


Figure 9:  $m_T(tk, E_T^{\text{miss}})$  for isolated muon, electron, and hadronic track candidates (from top-to-bottom) in signal and background events on a linear (left) and log (right) scale. These tracks all pass the corresponding isolation and  $p_T$  cuts. Tracks with  $m_T > 100$  GeV are not counted as “veto tracks,” so these events would enter our search region. The SM and signal MC samples are scaled to  $10 \text{ fb}^{-1}$ .

Table 9: SM  $\gamma + \text{jets}$  MC samples used in the analysis. The cross sections are calculated to LO.

Dataset	$\sigma$ (pb)	$\int \mathcal{L} dt$ (fb $^{-1}$ )
GJets_HT-100To200_TuneCUETP8M1_13TeV-madgraphMLM-pythia8	22010	0.23
GJets_HT-200To400_TuneCUETP8M1_13TeV-madgraphMLM-pythia8	9110	1.13
GJets_HT-400To600_TuneCUETP8M1_13TeV-madgraphMLM-pythia8	273	9.07
GJets_HT-600ToInf_TuneCUETP8M1_13TeV-madgraphMLM-pythia8	94.5	26.99

Table 10: MC FullSim samples for signal SMS model points.

Dataset	$\sigma$ (pb)	$\int \mathcal{L} dt$ (fb $^{-1}$ )
SMS-T1tttt_mGluino-1500_mLSP-100.TuneCUETP8M1_13TeV-madgraphMLM-pythia8	0.014	7268
SMS-T1tttt_mGluino-1200_mLSP-800.TuneCUETP8M1_13TeV-madgraphMLM-pythia8	0.086	1719
SMS-T1bbbb_mGluino-1500_mLSP-100.TuneCUETP8M1_13TeV-madgraphMLM-pythia8	0.014	3708
SMS-T1bbbb_mGluino-1000_mLSP-900.TuneCUETP8M1_13TeV-madgraphMLM-pythia8	0.325	438.5
SMS-T1qqqq_mGluino-1400_mLSP-100.TuneCUETP8M1_13TeV-madgraphMLM-pythia8	0.025	1958
SMS-T1qqqq_mGluino-1000_mLSP-800.TuneCUETP8M1_13TeV-madgraphMLM-pythia8	0.325	293.0

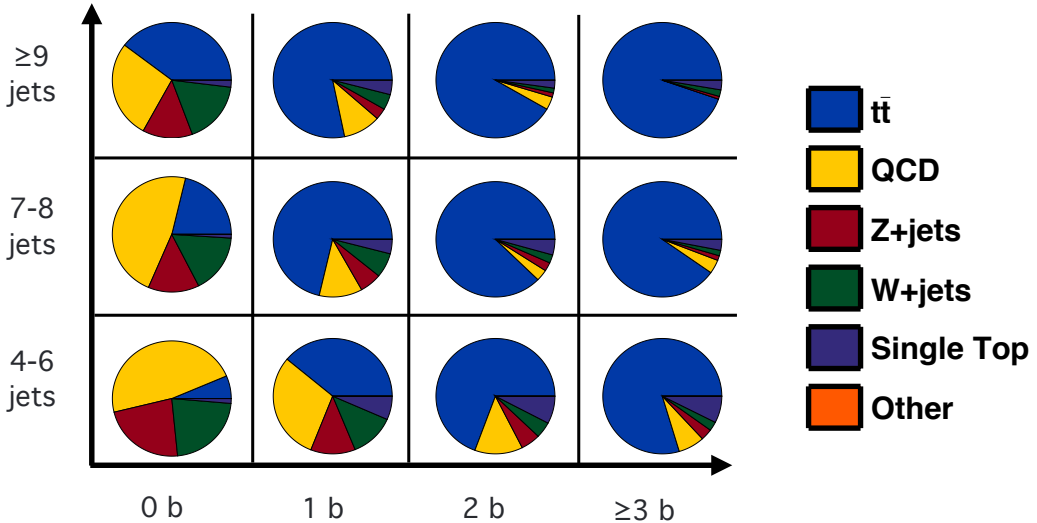


Figure 10: Relative expected contribution from each SM background in bins of  $N_{\text{jet}}$  and  $N_{\text{b-jet}}$ , integrated over all  $H_{\text{T}}^{\text{miss}} > 200$  GeV and  $H_{\text{T}} > 500$  GeV bins.

Table 11: Cutflow and expected yields at  $10 \text{ fb}^{-1}$  for SM backgrounds, with the baseline selection. The MC results are scaled using the cross sections listed in Section 3. The efficiency of each cut, calculated with respect to the previous cut, is given in parentheses after the expected yield.

Cut	$t\bar{t}$	QCD	Z+jets	W+jets	Single top	Other	Total
Start	$8 \times 10^6$	$> 10^8$	$6 \times 10^6$	$2 \times 10^7$	$2 \times 10^6$	$10^4$	$> 10^8$
$N_{\text{jet}} \geq 4$	$6 \times 10^6$	$> 10^7$	$8 \times 10^5$	$2 \times 10^6$	$5 \times 10^5$	$10^4$	$> 10^7$
$H_T > 500 \text{ GeV}$	$10^6$	$> 10^7$	$4 \times 10^4$	$3 \times 10^5$	$8 \times 10^5$	$7 \times 10^3$	$> 10^7$
$H_{\text{miss}} > 200 \text{ GeV}$	46204.02	100718.36	35208.73	6877.23	614.60)		200332.37
$\mu$ veto	31209.42 (0.68)	100424.34 (1.00)	10693.15 (1.00)	24940.95 (0.71)	4705.32 (0.68)	412.58 (0.67)	172385.76 (0.86)
$e$ veto	19116.81 (0.61)	99296.67 (0.99)	10607.60 (0.99)	15240.75 (0.61)	2862.62 (0.61)	270.28 (0.66)	147394.74 (0.86)
$\mu$ track veto	17698.28 (0.93)	97798.80 (0.98)	10538.85 (0.99)	14456.57 (0.95)	2643.27 (0.92)	255.55 (0.95)	143391.32 (0.97)
$e$ track veto	15237.88 (0.86)	93962.19 (0.96)	10272.05 (0.97)	12952.54 (0.90)	2299.85 (0.87)	229.50 (0.90)	134954.00 (0.94)
Had. track veto	12201.90 (0.80)	91628.84 (0.98)	10133.97 (0.99)	10553.74 (0.81)	1828.28 (0.79)	201.53 (0.88)	126548.26 (0.94)
$\Delta\phi$ cuts	6946.27 (0.57)	9645.15 (0.11)	7543.35 (0.74)	6101.87 (0.58)	863.79 (0.47)	138.06 (0.69)	31238.48 (0.25)
Evt. cleaning	6651.03 (0.96)	4789.70 (0.50)	7477.41 (0.99)	5803.18 (0.95)	831.93 (0.96)	133.63 (0.97)	25686.89 (0.82)
<hr/>							
Nb-jet bins							
$N_{\text{b-jet}} = 0$	982.01 (0.15)	2494.63 (0.52)	5743.30 (0.77)	4433.89 (0.76)	173.28 (0.21)	17.85 (0.13)	13844.97 (0.54)
$N_{\text{b-jet}} = 1$	2839.90 (0.43)	1575.38 (0.33)	1416.57 (0.19)	1158.09 (0.20)	393.38 (0.47)	52.14 (0.39)	7435.45 (0.29)
$N_{\text{b-jet}} = 2$	2298.84 (0.35)	466.97 (0.10)	286.99 (0.04)	190.50 (0.03)	222.79 (0.27)	45.75 (0.34)	3511.85 (0.14)
$N_{\text{b-jet}} \geq 3$	530.28 (0.08)	252.71 (0.05)	30.55 (0.00)	20.70 (0.00)	42.49 (0.05)	17.89 (0.13)	894.62 (0.03)

Table 12: Cutflow and expected yields at  $10 \text{ fb}^{-1}$  for SMS model points, with the baseline selection. The MC results are scaled using the cross sections listed in Table 10. The efficiency of each cut, calculated with respect to the previous cut, is given in parentheses after the expected yield.

Cut	T1tttt (1500, 100)	T1tttt (1200, 800)	T1bbbb (1500, 100)	T1bbbb (1000, 900)	T1qqqq (1400, 100)	T1qqqq (1000, 800)
Start	141.9	856.4	141.9	3253.8	252.9	3253
$N_{\text{jet}} \geq 4$	141.8 (1.00)	854.8 (1.00)	137.3 (0.97)	1624 (0.50)	244.9 (0.97)	2549 (0.78)
$H_T > 500 \text{ GeV}$	141.7 (1.00)	706.1 (0.83)	137.3 (1.00)	654.8 (0.40)	244.8 (1.00)	1390 (0.55)
$H_T^{\text{miss}} > 200 \text{ GeV}$	125.8 (0.89)	311.9 (0.44)	124.2 (0.91)	534.8 (0.82)	221.2 (0.90)	904.1 (0.65)
$\mu$ veto	80.49 (0.64)	202.4 (0.65)	123.1 (0.99)	521.3 (0.97)	220.8 (1.00)	902.6 (1.00)
$e$ veto	51.54 (0.64)	135.14 (0.67)	122.0 (0.99)	512.0 (0.98)	218.5 (0.99)	894.9 (0.99)
$\mu$ track veto	50.74 (0.98)	129.9 (0.96)	121.5 (1.00)	500.07 (0.98)	217.8 (1.00)	888.9 (0.99)
$e$ track veto	49.32 (0.97)	120.0 (0.92)	119.9 (0.99)	478.8 (0.96)	215.0 (0.99)	868.8 (0.98)
Had. track veto	48.27 (0.98)	112.0 (0.93)	119.4 (1.00)	472.0 (0.99)	213.9 (1.00)	852.2 (0.98)
$\Delta\phi$ cuts	39.08 (0.81)	87.76 (0.78)	95.94 (0.80)	373.1 (0.79)	173.0 (0.81)	699.6 (0.82)
Evt. cleaning	38.18 (0.98)	86.27 (0.98)	94.76 (0.99)	369.0 (0.99)	169.9 (0.98)	690.6 (0.99)
$N_{\text{b-jet}}$ bins						
0 CSVM	0.99 (0.03)	2.46 (0.03)	4.52 (0.05)	25.46 (0.07)	115.9 (0.68)	489.3 (0.71)
1 CSVM	5.31 (0.14)	13.75 (0.16)	20.89 (0.22)	110.8 (0.30)	43.59 (0.26)	163.5 (0.24)
2 CSVM	11.55 (0.30)	27.76 (0.32)	34.51 (0.36)	144.4 (0.39)	9.13 (0.05)	32.81 (0.05)
$\geq 3$ CSVM	20.33 (0.53)	42.30 (0.49)	34.84 (0.37)	88.34 (0.24)	1.38 (0.01)	5.12 (0.01)

## 366 5 Search variables and binning: $H_T$ , $H_T^{\text{miss}}$ , $N_{\text{jet}}$ , and $N_{\text{b-jet}}$

367 The search variables and corresponding binning are as follows:

- 368 •  $N_{\text{jet}}$ : 4–6, 7–8,  $\geq 9$ ;
- 369 •  $N_{\text{b-jet}}$ : 0, 1, 2,  $\geq 3$ ;
- 370 •  $H_T$ : 500–800, 800–1200,  $\geq 1200 \text{ GeV}$ ;
- 371 •  $H_T^{\text{miss}}$ : 200–500, 500–750,  $\geq 750 \text{ GeV}$ .

372 The analysis is restricted to  $N_{\text{jet}} \geq 4$  because of the focus on gluino pair production. The  
373  $H_T > 500 \text{ GeV}$  and  $H_T^{\text{miss}} > 200 \text{ GeV}$  restrictions are dictated by the trigger conditions.

374 The binning is rectangular as above, except the 12 bins with  $H_T < 800 \text{ GeV}$  and  $H_T^{\text{miss}} > 750 \text{ GeV}$   
375 are removed since  $H_T^{\text{miss}}$  cannot exceed (or be on the order of)  $H_T$  in a physical event. Addi-  
376 tionally, for  $500 < H_T^{\text{miss}} < 750 \text{ GeV}$ , a single range with  $500 < H_T < 1200 \text{ GeV}$  is used, and  
377 for  $H_T^{\text{miss}} > 750 \text{ GeV}$ , a single range with  $H_T > 800 \text{ GeV}$  is used, because of the lower expected  
378 number of events at large  $H_T^{\text{miss}}$ . The merging of these bins further reduces the bin count by 24,  
379 for a total of 72 bins. The six bins in the  $H_T$  and  $H_T^{\text{miss}}$  plane are shown visually in Fig. 11.

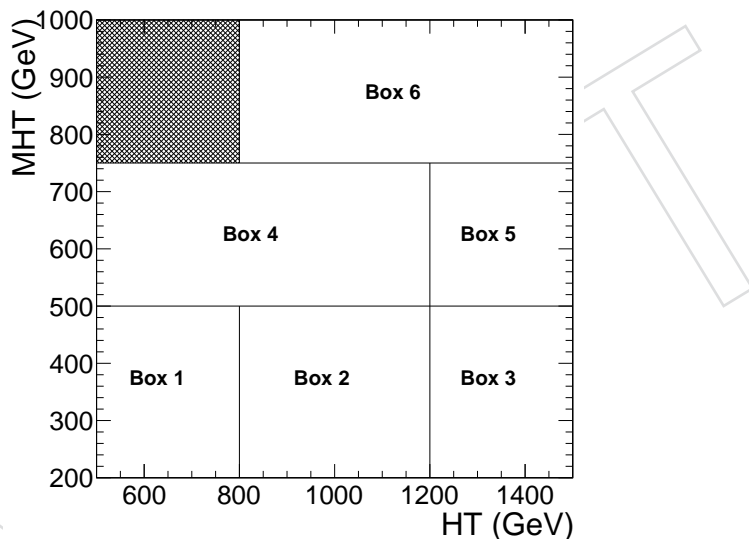


Figure 11: Two-dimensional plane in  $H_T$  and  $H_T^{\text{miss}}$  showing the signal bins. The same  $H_T$  and  $H_T^{\text{miss}}$  regions are used for each  $N_{\text{jet}}$  and  $N_{\text{b-jet}}$  count.

## 380 6 Estimation of top quark and W+jets backgrounds

381 Following the baseline kinematic selection and application of the electron and muon vetoes  
 382 (Section 4), about 50% of the expected SM background (integrated over all search bins) comes  
 383 from  $t\bar{t}$ , single-top, and W+jets events. This fraction exceeds 90% for search bins requiring  
 384 larger values of  $N_{\text{jet}}$  and  $N_{\text{b-jet}}$  (Fig. 10). This background primarily arises when a W boson  
 385 decays leptonically, yielding a neutrino (thus, genuine  $H_T^{\text{miss}}$ ) and a non-vetoed charged lepton.  
 386 The non-vetoed lepton can be an electron or muon (including an electron or muon from  $\tau$   
 387 lepton decay) that does not satisfy the electron or muon selection criteria of Section 4 (so-called  
 388 “lost leptons”), or it can be a hadronically decaying  $\tau$  lepton. The fraction of the  $t\bar{t}$ , single-  
 389 top, and W+jets background due to hadronically decaying  $\tau$  leptons is as large as 55% in some  
 390 search regions.

391 A smaller contribution to the lost-lepton background arises from dileptonic  $t\bar{t}$  events, in which  
 392 both top quarks decay to a final state with either an electron or a muon, when both leptons are  
 393 lost.

394 The MC prediction for the leptonic composition of background events after applying the selec-  
 395 tion requirements of Section 4, integrated over all search regions, is shown in Fig. 12.

396 Our evaluation of the background from lost leptons is discussed in Section 6.1 and from hadron-  
 397 ically decaying  $\tau$  leptons in Section 6.2.

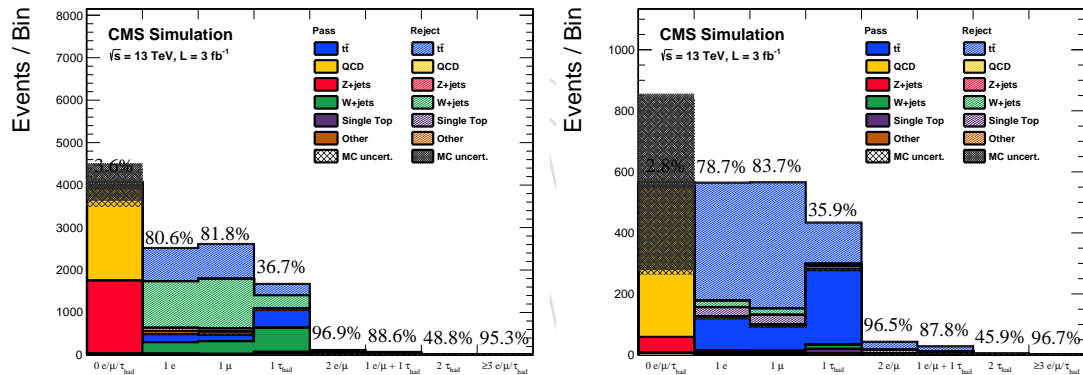


Figure 12: MC prediction for the leptonic composition of background events following the baseline event selection. The hatched part of the histogram represents the events rejected by the lepton and isolated-track vetoes. The percent of each type of leptonic event rejected by these vetoes is indicated above each bin. The solid histograms represent the background remaining in the search region after all vetoes. The left plot contains all events with  $N_{\text{b-jet}} \leq 1$ , while the right plot contains all events with  $N_{\text{b-jet}} \geq 2$ .

### 398 6.1 Classical Lost-lepton ( $e/\mu$ ) estimation method

399 Standard model events with muons or electrons can satisfy the event selection and enter the  
 400 signal sample as lost-lepton background if the requirements for any of the following analysis  
 401 steps are not satisfied (see Fig 13):

- 402 • kinematic acceptance;
- 403 • reconstruction;
- 404 • isolation.

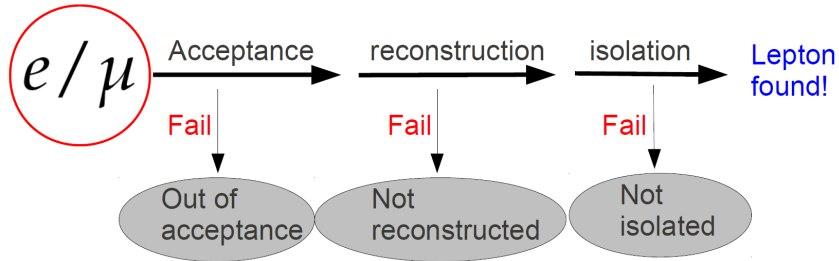


Figure 13: If an electron or muon does not satisfy one or more of the three indicated criteria, the lepton is considered to be “lost” and the event may enter the search region as background.

The basic idea of our data-driven method to evaluate the lost-lepton background is to select single-lepton control samples (CS) in the data, through inversion of the lepton vetoes, and to weight each CS event by a factor that represents the probability for a lost-lepton event to appear with the corresponding search-variable values:  $H_T$ ,  $H_T^{\text{miss}}$ ,  $N_{\text{jet}}$ , and  $N_{\text{b-jet}}$ . The weights are determined through evaluation of the efficiencies for each analysis step. The weighted distributions of the search variables, summed over the events in the CS, define the lost-lepton background prediction in the respective search regions.

In our analysis, leptons are included in the jet clustering procedure and thus in the calculation of  $H_T$  and  $H_T^{\text{miss}}$ . As a consequence, the distributions of the search variables are similar between the control and signal samples, as shown in Fig. 14. Small differences might arise from out-of-acceptance lost-lepton events. However, the lepton  $p_T$  is small for those events because, by definition, either  $p_T < 10 \text{ GeV}$ , or else  $|\eta| > 2.5$  (electrons) or 2.4 (muons), which also implies small  $p_T$ . Furthermore, differences between the control and signal samples from lost-lepton events in which the lepton is not reconstructed as *any* particle are small because the number of such particles is negligible. In the end, any deviations are accounted for through the systematic uncertainty that is assigned to account for non-closure, discussed below.

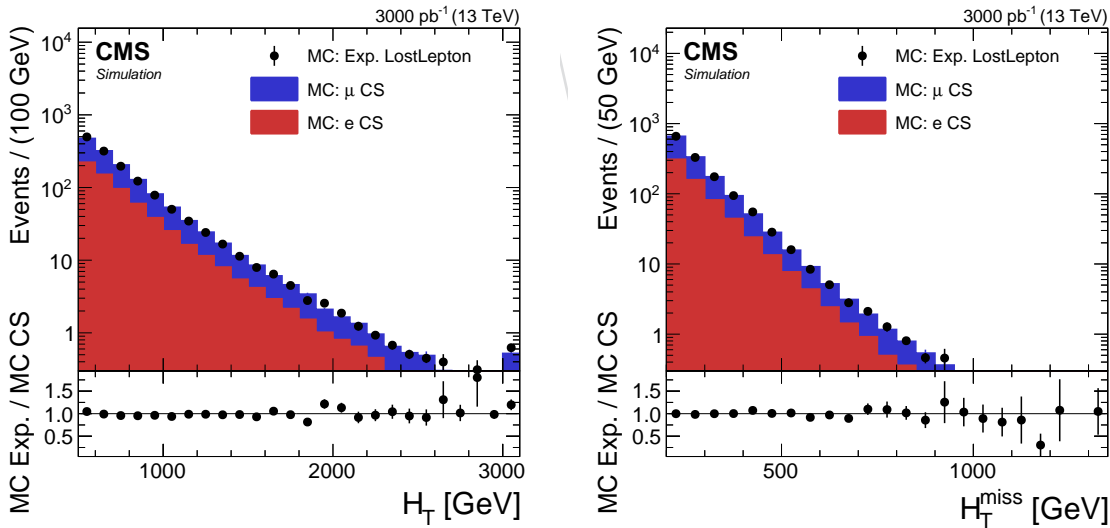


Figure 14: Distributions of the control sample events in comparison to the lost-lepton events. The CS distribution was scaled by a factor of 0.299 to match the expected number of lost-lepton events. The shape of the distributions agree on a reasonable level.

421 In the following the method is described, starting with the efficiency determinations.

422 **6.1.1 Determining the lepton efficiencies**

423 The efficiencies are determined using  $t\bar{t}$  and  $W+jets$  MC samples and single  $t$ , applying the base-

424 line selection without any lepton identification or selection criteria and without the isolated-

425 track veto.

426 For the single-muon (single-electron) efficiency determination, events with exactly one muon  
 427 (electron) are selected, using generator information, with a requirement that the lepton origi-  
 428 nate from the hard interaction. The acceptance efficiency is derived by comparing the numbers  
 429 of generator-level leptons that pass or fail the kinematic  $\eta$  and  $p_T$  requirements.

430 If a lepton satisfies the acceptance requirements, a match is performed to a reconstructed elec-  
 431 tron or muon that fulfills the reconstruction and identification criteria (except for isolation). The  
 432 numbers of leptons passing and failing the reconstruction criteria determine the reconstruction  
 433 efficiency.

434 The same procedure is followed, using the leptons that satisfy the reconstruction and identifi-  
 435 cation criteria, to determine the isolation efficiency.

436 Events that satisfy the isolation requirements are then used in an analogous manner to deter-  
 437 mine the  $m_T$  selection efficiency.

438 Dileptonic events contribute to the signal sample if both leptons ( $ee$ ,  $\mu\mu$ , or  $e\mu$ ) are lost, thus  
 439 constituting an additional source of lost-lepton background. The efficiency to lose both lep-  
 440 tons in dileptonic  $t\bar{t}$  events is calculated by requiring two generator leptons, combining the  
 441 acceptance, reconstruction, and isolation efficiencies of the two leptons into a single overall  
 442 efficiency. Dileptonic contributions to the signal sample represent less than 2% of the total  
 443 number of lost-lepton events.

444 Similarly, dileptonic events contribute to the single-lepton CS if one of the two leptons is lost.  
 445 Since the efficiency calculations are based on single-lepton generator samples, as explained  
 446 above, a correction is applied to the CS to remove the dilepton-event contamination.

447 Finally, a correction is applied to account for the isolated-track veto. This correction, which  
 448 scales down the background prediction, is obtained from simulation in each bin and is separated  
 449 into muon, electron and pion tracks. We validate the performance of this track veto and  
 450 obtain appropriate systematics on the correction factor via a tag-and-probe study in data and  
 451 simulation. This is discussed further in Section 6.3.

452 The manner in which the efficiencies are combined to obtain the total lost-lepton background  
 453 prediction is described in Section 6.1.3 (see, e.g., Eq. 18).

454 A crucial aspect of the method is the choice and binning of the parametrization variables that  
 455 define the lepton efficiency maps. Extensive studies have been performed to identify and opti-  
 456 mize these variables. The following parametrization variables have been investigated:

- 457 • search variables:  $H_T$ ,  $H_T^{\text{miss}}$ ,  $N_{\text{jet}}$ , and  $N_{\text{b-jet}}$ ;
- 458 • lepton  $p_T$ ,  $\eta$ ;
- activity around the lepton  $A_{\mu/e}$ . “Activity”  $A$  is defined as the sum of PF candidates  
 in an annulus outside standard isolation cone relative to the  $p_T$  of the lepton:

$$A_{\mu/e} := \left( \sum_{\text{PFcands}}^{R_{\text{minIso}} < r < 0.4} p_T \right) / p_T(\text{lep}) \quad (9)$$

- activity around an isolated track  $A_{\text{isoTrack}}$ . The minimum radius is fixed to 0.2 (max-

imum radius of mini isolation) and only charged PF candidates are considered:

$$A_{isoTrack} := \left( \sum_{\substack{0.2 < r < 0.4 \\ \text{PFcands} \\ (\text{charged})}} p_T \right) / p_T(\text{track}) \quad (10)$$

On the basis of our studies, the following efficiency parameterizations are used:

- lepton acceptance:  $H_T$  and  $H_T^{\text{miss}}$ , with efficiency maps determined separately for  $N_{\text{jet}} = 4, 5, 6, 7 - 8, 9 +$  (2D binning, see Figs. 15 and 16);
- lepton reconstruction:  $p_T$  and lepton activity  $A_{e,\mu}$  (2D binning, see Fig. 17);
- lepton isolation:  $p_T$  and lepton activity  $A_{e,\mu}$  (2D binning, see Fig. 18);
- purity of the single-electron control sample:  $H_T^{\text{miss}}$  and  $N_{\text{jet}}$  (2D binning, see Fig. 19);
- $m_T$  selection efficiency:  $H_T$  and  $N_{\text{jet}}$  (2D binning, see Fig. 20);
- correction  $\epsilon_{\text{singleLep}}^{\text{purity}}$  to account for the contamination of the single-lepton CS by dileptonic events:  $N_{\text{jet}}$  (1D binning, see Fig. 21);
- probability  $\epsilon_{\text{Found}}^{\text{dilep}}$  that a dileptonic event does not contribute to the signal sample:  $N_{\text{jet}}$  (1D binning, see Fig. 22);
- isolated-track veto:  $H_T$  and  $H_T^{\text{miss}}$ , with efficiency maps determined separately for  $N_{\text{jet}} = 4 - 6$  and  $N_{\text{jet}} \geq 7$  (2D binning, see Figs. 23-25).

All displayed efficiency maps are obtained from  $t\bar{t}$  & W+jets simulated events that satisfy the baseline  $H_T$ ,  $H_T^{\text{miss}}$ ,  $N_{\text{jet}}$  and  $\Delta\phi_{1,2,3}$  requirements. Due to technical limitations asymmetric uncertainties cannot be displayed. Since these efficiencies are used for the data-driven background prediction, correcting for possible differences between data and simulation is crucial. This issue is discussed in Section 6.3.

### 6.1.2 Selecting the single-lepton control sample

The single-lepton control samples are selected by requiring either exactly one isolated electron and no isolated muon (single-electron CS) or exactly one isolated muon and no isolated electron (single-muon CS), using the lepton identification and isolation criteria of Section 4, with all the other selection criteria of Section 4 applied apart from the isolated track veto. The  $m_T$  distribution (Eq. 8) for these events, except without the  $m_T$  requirement applied, is shown in Fig. 26. In Fig. 27, the number of expected lost-lepton events is shown for the 72 search bins in comparison with the expected numbers of single-muon and single-electron CS events. On average, around 3 times more total CS events are expected for each search region compared to the number of lost-lepton events (expected lost-lepton events / expected number of CS events = 0.229).

The single-electron CS is found to contain significant contamination from non-prompt electrons, reducing its purity to around 96%. A correction is applied to account for this impurity (Fig. 19). The purity of the single-muon CS exceeds 99% and so no correction for purity is required.

A correction is applied to account for dileptonic events in which one of the prompt leptons is lost, as mentioned in Section 6.1.1. The rate of these events is significantly reduced by the  $m_T < 100 \text{ GeV}$  requirement, but they still represent about 3% of the single-lepton CS (Fig. 21).

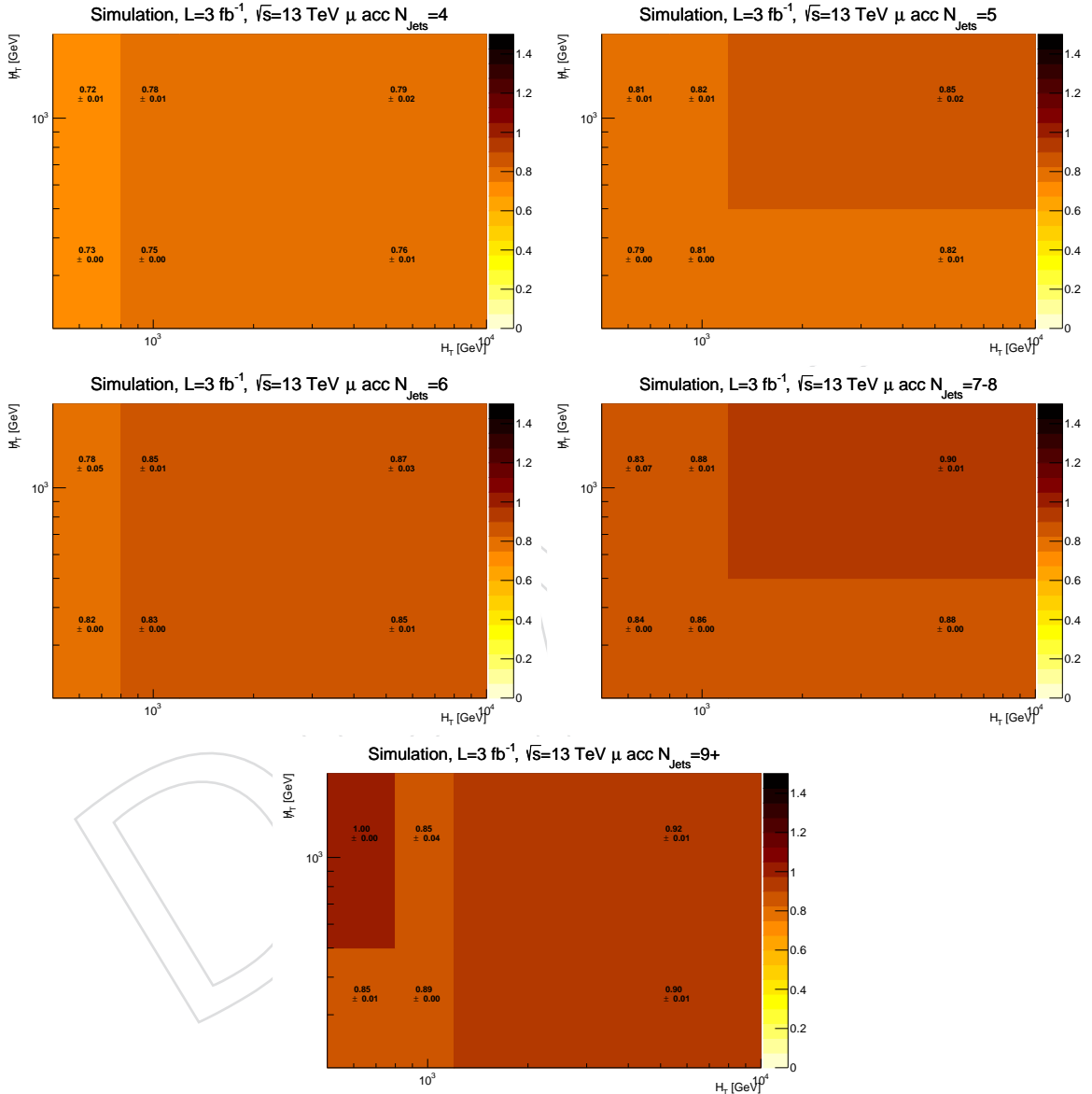


Figure 15: Muon acceptance efficiency maps: (top) for  $N_{\text{jet}} = 4, 5$ , (middle) for  $N_{\text{jet}} = 6, 7 - 8$  and (bottom)  $N_{\text{jet}} = 9 +$

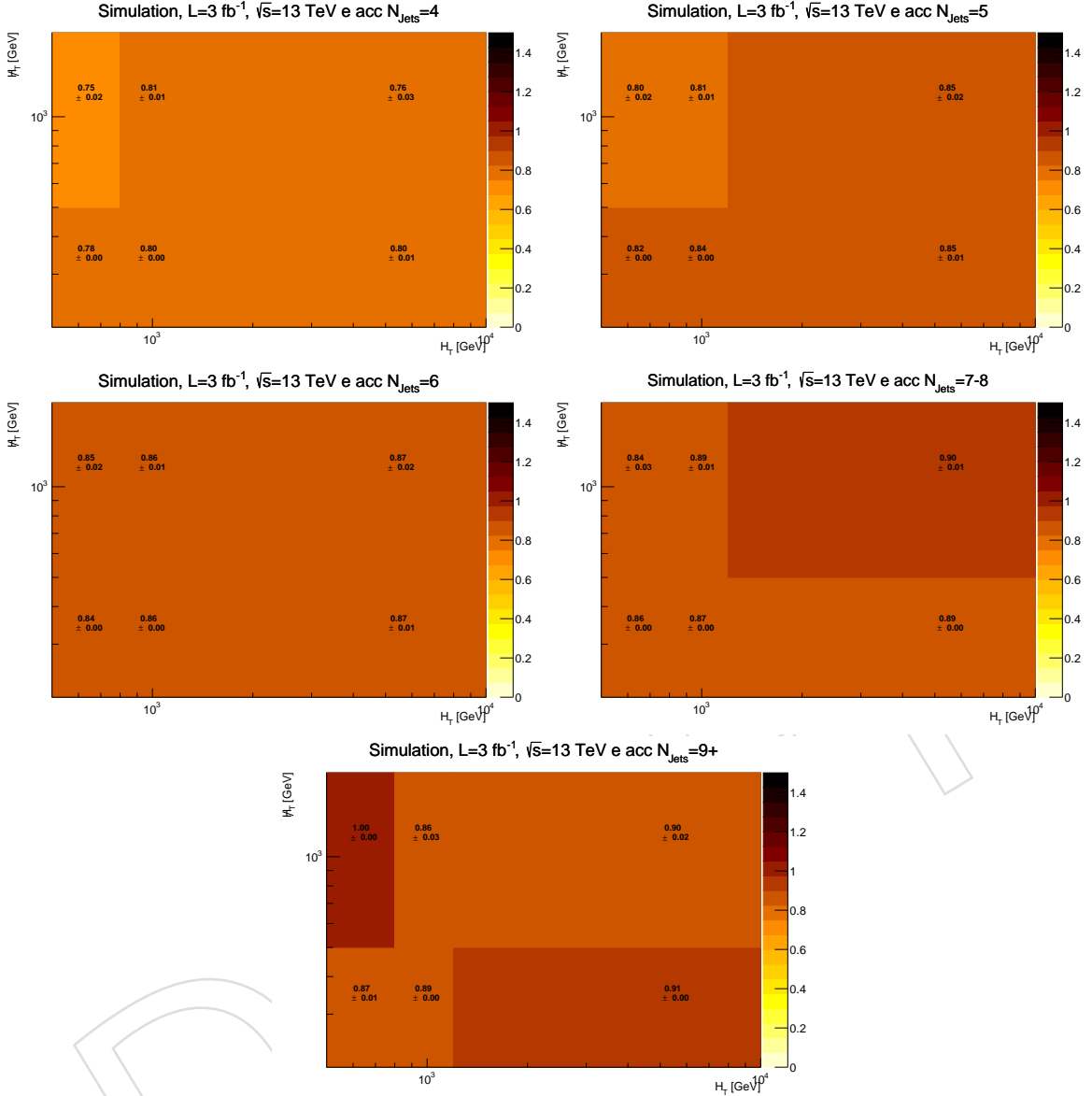


Figure 16: Electron acceptance efficiency maps: (top) for  $N_{\text{jet}} = 4, 5$ , (middle) for  $N_{\text{jet}} = 6, 7 - 8$  and (bottom)  $N_{\text{jet}} = 9 +$

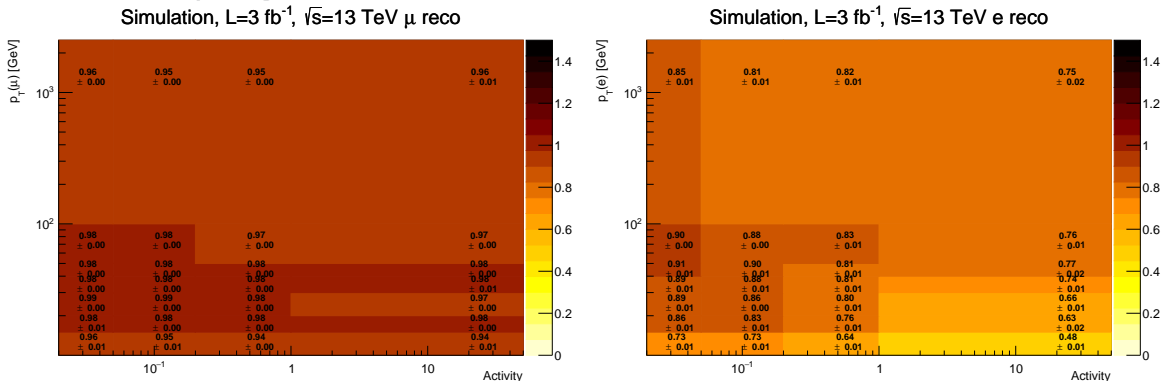


Figure 17: (left) Muon and (right) electron reconstruction efficiency maps.

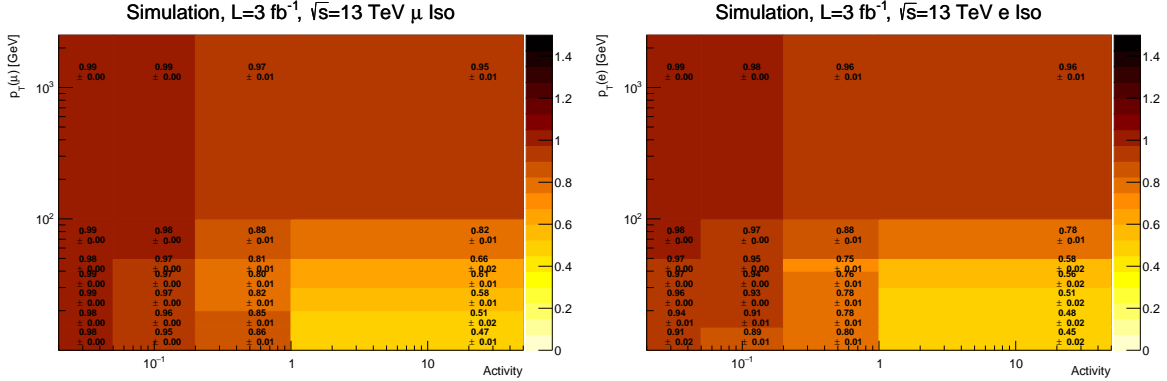


Figure 18: (left) Muon and (right) electron isolation efficiency maps.

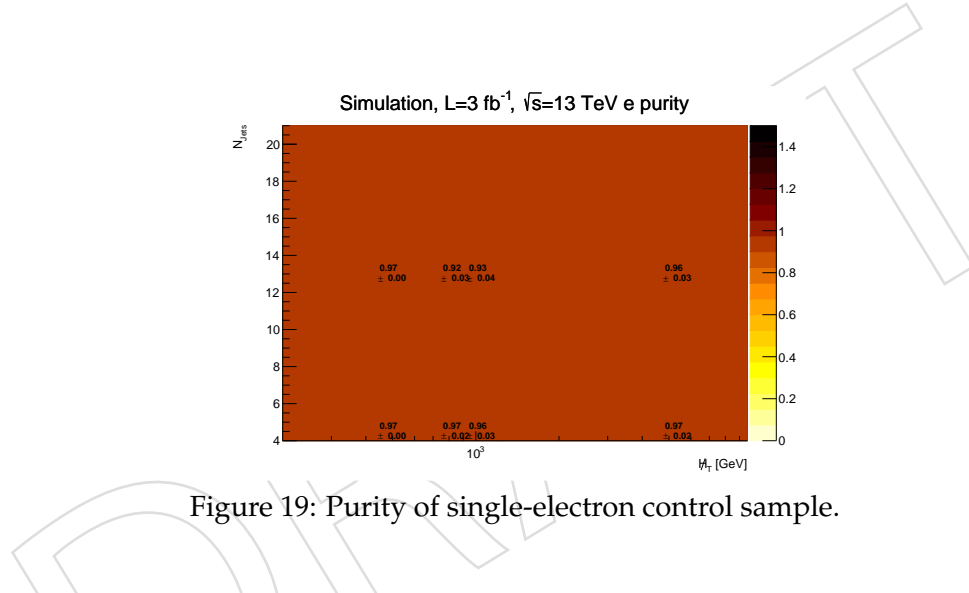
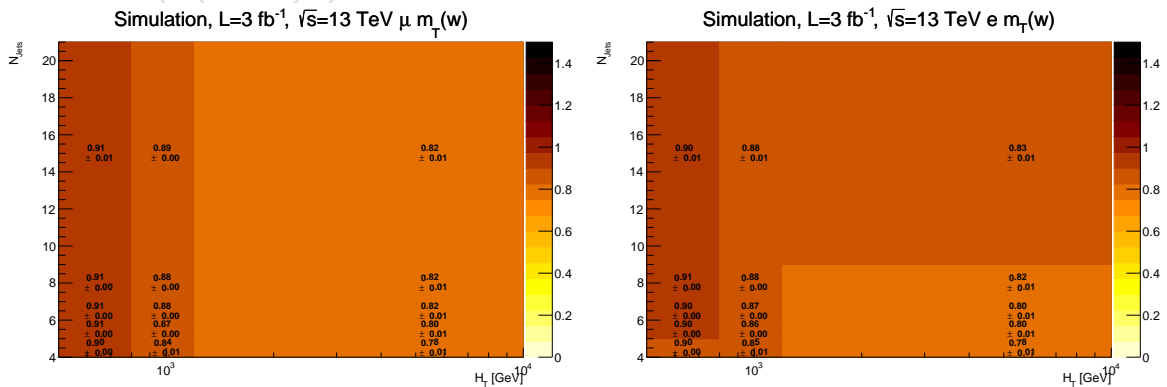


Figure 19: Purity of single-electron control sample.

Figure 20: (left) Muon and (right) electron  $m_T$ -cut efficiency maps.

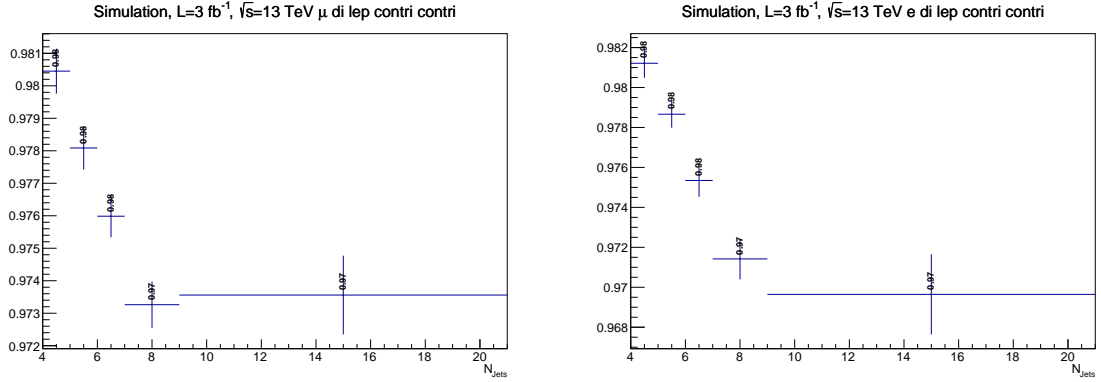


Figure 21: Single-lepton purity  $\epsilon_{\text{singleLep}}^{\text{purity}}$  of the (left) single-muon and (right) single-electron control samples. This term is applied as a correction factor to account for the contributions of dilepton events ( $ee$ ,  $e\mu$ , and  $\mu\mu$ ) to the control samples.

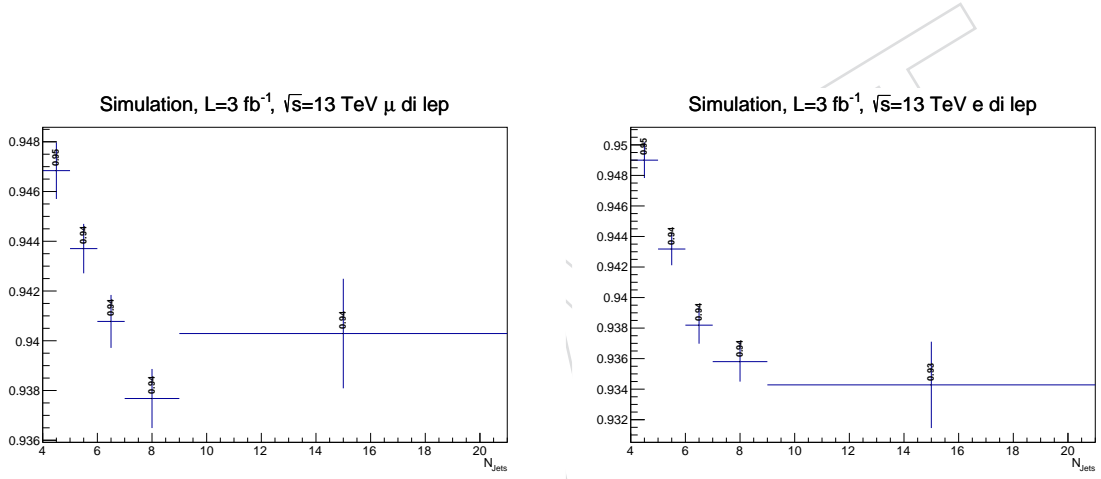


Figure 22: The probability  $\epsilon_{\text{Found}}^{\text{diLep}}$  that at most one lepton in a dilepton event ( $ee$ ,  $e\mu$ ,  $\mu\mu$ ) is lost, i.e., the probability that a dilepton event does not contribute to the lost-lepton background.

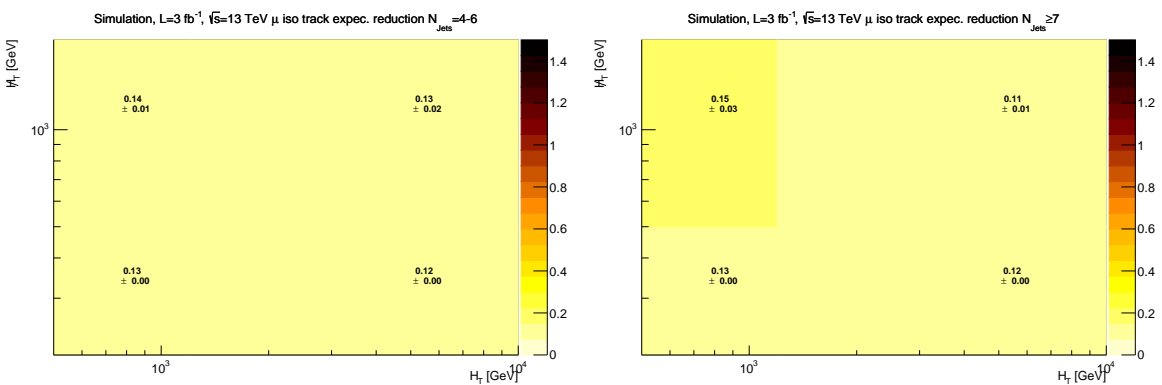


Figure 23: Isolated muon track veto event rejection efficiency: (left) for  $N_{\text{jet}} = 4 - 6$  and (right) for  $N_{\text{jet}} \geq 7$

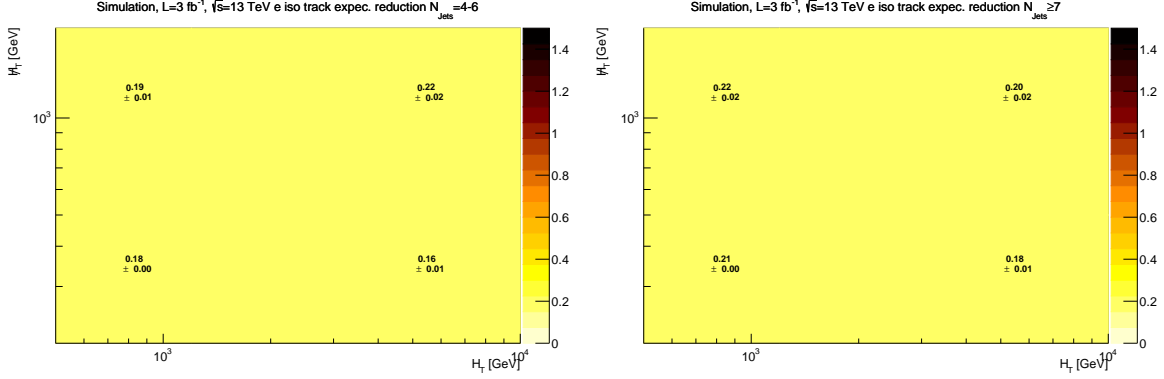


Figure 24: Isolated electron track veto event rejection efficiency: (left) for  $N_{\text{jet}} = 4 - 6$  and (right) for  $N_{\text{jet}} \geq 7$

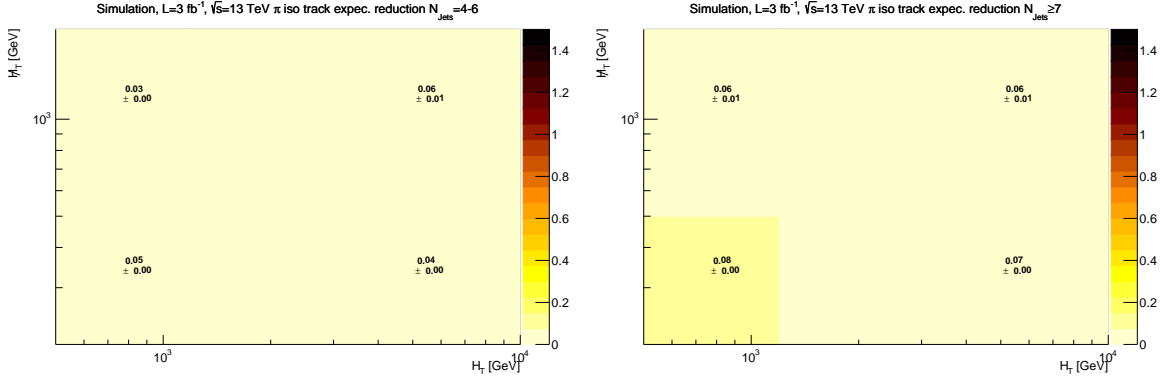


Figure 25: Isolated pion track veto event rejection efficiency: (left) for  $N_{\text{jet}} = 4 - 6$  and (right) for  $N_{\text{jet}} \geq 7$

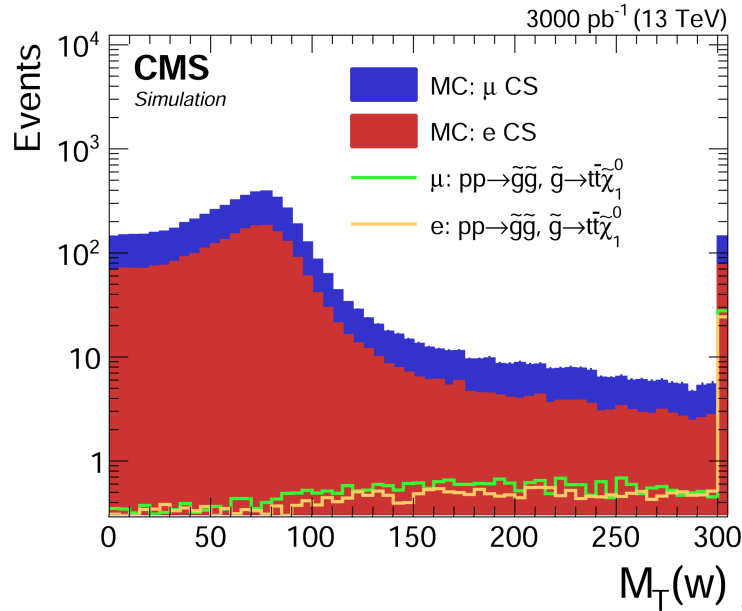


Figure 26: The  $m_T$  distribution of the single-electron and -muon control samples for simulated  $t\bar{t}$  and W+jets events together with a typical T1tttt signal distribution. For purposes of visibility, the T1tttt cross section is increased by a factor of 10.

#### 495 6.1.3 Predicting the single and dileptonic $t\bar{t}$ and W+jets background

496 After selecting and correcting the single-electron and single-muon control samples, event-by-  
497 event weights are computed based on the efficiencies.

To model the non-isolated muons, the muon control sample ( $CS^\mu$ ) is weighted according to:

$$\text{!ISO}^\mu = CS^\mu \cdot \frac{1 - \epsilon_{\text{ISO}}^\mu}{\epsilon_{\text{ISO}}^\mu}, \quad (11)$$

498 where  $\text{!ISO}^{\text{lepton}}$  is the applied weight and  $\epsilon_X^{\mu/e}$  is the efficiency of criterion X for the lepton.

The next step is to model the unreconstructed muons, taking the muon isolation and reconstruction efficiencies into account. The weight is calculated according to:

$$\text{!Reco}^\mu = CS^\mu \cdot \frac{1}{\epsilon_{\text{ISO}}^\mu} \cdot \frac{1 - \epsilon_{\text{Reco}}^\mu}{\epsilon_{\text{Reco}}^\mu}. \quad (12)$$

The last step accounts for muons that fall outside the detector acceptance. This weight, in correspondence to Eqs. 11 and 12, is:

$$\text{!Acc}^\mu = CS^\mu \cdot \frac{1}{\epsilon_{\text{ISO}}^\mu} \cdot \frac{1}{\epsilon_{\text{Reco}}^\mu} \cdot \frac{1 - \epsilon_{\text{Acc}}^\mu}{\epsilon_{\text{Acc}}^\mu}. \quad (13)$$

Lost electrons can also be modeled using the single-muon CS. This is justified because the decay of a W boson to a  $\mu$  or  $e$  has the same probability according to lepton universality. The following equations are used to model the non-isolated (Eq. 14), unreconstructed (Eq. 15), and out-of-acceptance (Eq. 16) electrons:

$$\text{!ISO}^e = CS^\mu \cdot \frac{1 - \epsilon_{\text{ISO}}^e}{\epsilon_{\text{ISO}}^\mu} \cdot \frac{\epsilon_{\text{Reco}}^e}{\epsilon_{\text{Reco}}^\mu} \cdot \frac{\epsilon_{\text{Acc}}^e}{\epsilon_{\text{Acc}}^\mu}; \quad (14)$$

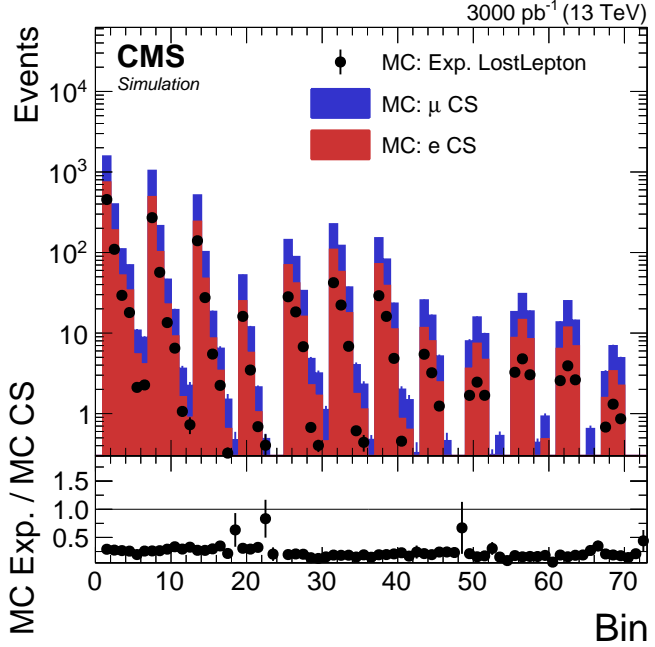


Figure 27: Expected number of lost-lepton events in the 72 search regions of the analysis compared to the number of expected single-electron and single-muon events in the corresponding control samples.

$$\text{!Reco}^e = \text{CS}^\mu \cdot \frac{1}{\epsilon_{\text{ISO}}^\mu} \cdot \frac{1 - \epsilon_{\text{Reco}}^e}{\epsilon_{\text{Reco}}^\mu} \cdot \frac{\epsilon_{\text{Acc}}^e}{\epsilon_{\text{Acc}}^\mu}; \quad (15)$$

$$\text{!Acc}^e = \text{CS}^\mu \cdot \frac{1}{\epsilon_{\text{ISO}}^\mu} \cdot \frac{1}{\epsilon_{\text{Reco}}^\mu} \cdot \frac{1 - \epsilon_{\text{Acc}}^e}{\epsilon_{\text{Acc}}^\mu}. \quad (16)$$

Furthermore, dileptonic events can also contribute to the lost-lepton background of both leptons are lost. These events are evaluated separately from the single leptonic lost-lepton events since it is by far more likely to lose one than two leptons (see Fig. 22) so these events account for less than 1% to the total lost-lepton background. The dileptonic contribution to the lost-lepton background is calculated as:

$$\text{Lost}^{dilep} = \text{CS}^\mu \cdot (1 - \epsilon_{\text{singleLep}}^{\text{purity}}) \cdot \frac{1 - \epsilon_{\text{Found}}^{\text{diLep}}}{\epsilon_{\text{Found}}^{\text{diLep}}}, \quad (17)$$

- 499 where  $(1 - \epsilon_{\text{singleLep}}^{\text{purity}})$  is the number of dilepton events with exactly one lost lepton and  
500  $\text{CS}^\mu \cdot (1 - \epsilon_{\text{Found}}^{\text{diLep}})/\epsilon_{\text{Found}}^{\text{diLep}}$  is the probability to also lose the second lepton (See Figs. 21 and 22  
501 for plots of  $\epsilon_{\text{singleLep}}^{\text{purity}}$  and  $\epsilon_{\text{Found}}^{\text{diLep}}$ , respectively.)

The total number of lost leptons is:

$$\text{Total Lost Leptons} = \epsilon_{\text{isotrk}} \cdot \sum_{i=e,\mu} \left[ \frac{[\epsilon_e^{\text{purity}}]}{\epsilon_{m_T}^i} \cdot \left( \epsilon_{\text{singleLep}}^{\text{purity}} \cdot (\text{!Iso}^i + \text{!Reco}^i + \text{!Acc}^i) + \text{Lost}^{dilep} \right) \right], \quad (18)$$

- 502 where  $\epsilon_{m_T}^i$  accounts for the  $m_T$ -selection efficiency,  $\epsilon_{\text{singleLep}}^{\text{purity}}$  for the contamination of the single-  
503 lepton CS by dilepton events, and (for electrons)  $\epsilon_e^{\text{purity}}$  for the CS purity. The  $\epsilon_{\text{isotrk}}$  term ac-  
504 counts for the probability that an event passes the isolated-track vetos and thus is not vetoed.

505 The same procedure of reweighting control sample events is also applied to the single-electron  
 506 control sample, and the two independent predictions are averaged (using the arithmetic mean)  
 507 to estimate the total number of lost leptons. A closure test in various observables for the full  
 508 method is presented in Fig. 28 for the baseline selection. Overall agreement is observed for all  
 509 search variables and no trends are observed. The remaining non-closure is expected to be of  
 510 statistical nature. In addition, a closure test for each of the search bins is shown in in Fig. 29.

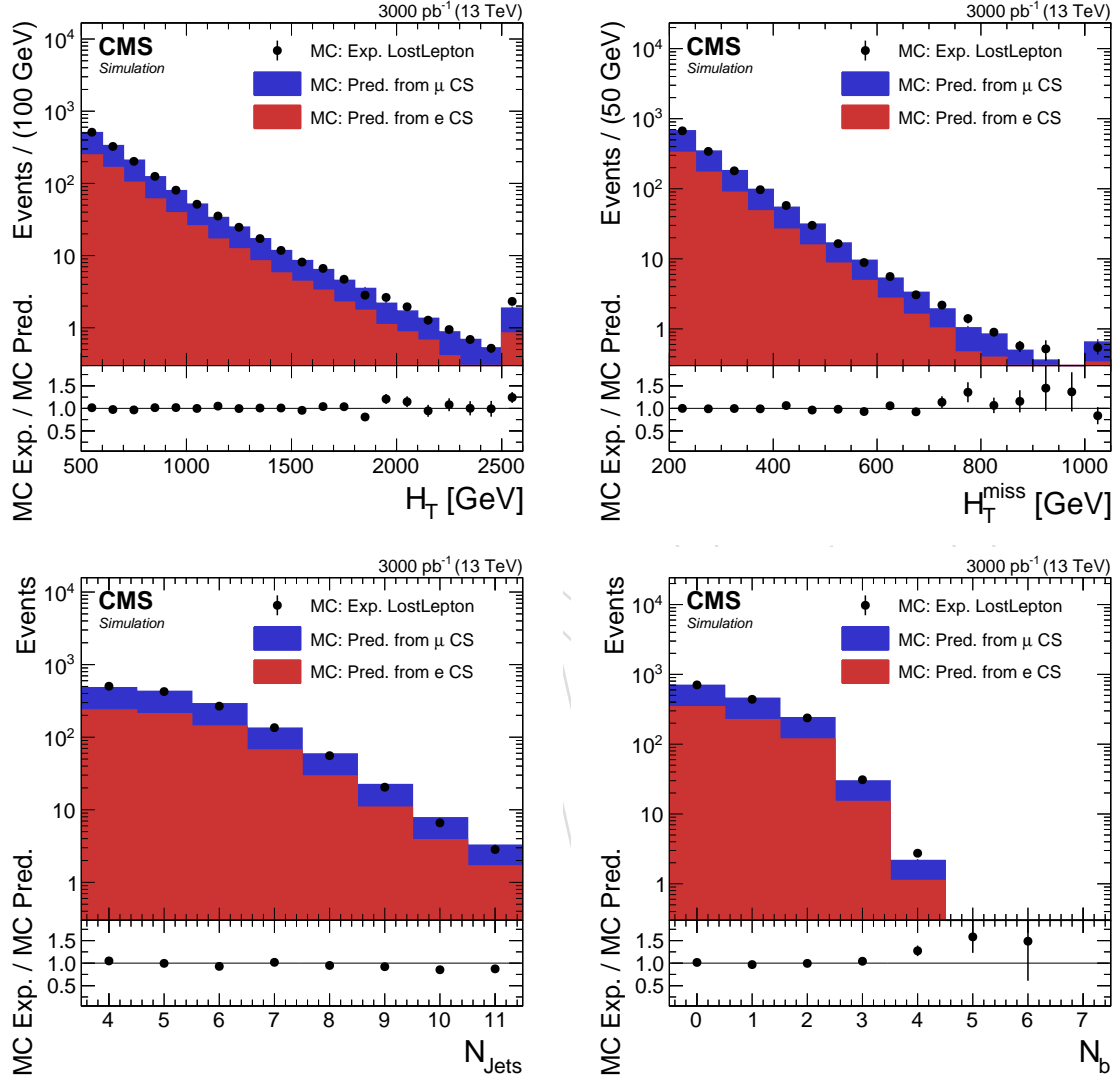


Figure 28: Comparison of the expected and predicted lost electrons and muons using both the single electron and muon control sample. Overall good agreement can be observed for all search variables. For the closure test,  $t\bar{t}$ ,  $W+jets$ , single  $t$ , and exotic events are considered (see Section 3).

511 Furthermore, we want to show that the lost lepton background estimation method is indepen-  
 512 dent of the exact composition of the background. This means that we select the control sample  
 513 in data, and the parametrization of the efficiency maps is chosen such that they reflect the ac-  
 514 tual kinematics of the process wherever possible. To illustrate this, the closure test is repeated  
 515 for the following compositions: (a) the  $t\bar{t}$  cross section is increased by 20%, (b) the  $w+jets$  cross  
 516 section is increased by 20%, (c) exotic processes are left out and (d) the cross section of exotic  
 517 processes is doubled. These plots can be found in app. C.1 and show that the composition of

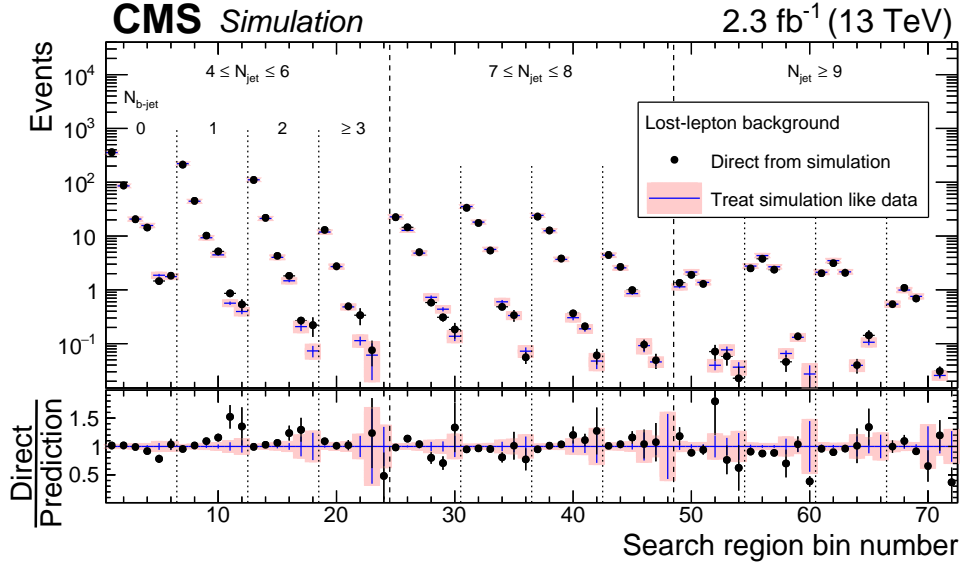


Figure 29: Comparison of prediction from single electron and single muon control sample vs expected lost-leptons in exclusive search regions. Overall reasonable agreement between expectation and combined prediction can be observed. For the closure test,  $t\bar{t}$ ,  $W+jets$ , single  $t$ , and exotic events are considered (see Table 7).

518 the background does not bias the closure test, as no trends are observed.  
 519 Additionally, the QCD background is estimated using a QCD enriched region as a control sam-  
 520 ple which is achieved by inverting the  $\Delta\Phi$  requirement. However, lost-lepton events can also  
 521 contribute to this region, so the prediction of the lost-lepton background has to be performed  
 522 here as well. This prediction is analogous to the method described in this section. The only  
 523 difference is that the QCD method relies on a finer search binning which has to be adapted by  
 524 the lost-lepton method. These closure tests in this finer binning for inverted and non-inverted  
 525  $\Delta\Phi$  cut are shown in app. C.2.

#### 526 6.1.4 Systematic uncertainties

527 The following sources of systematic uncertainty are included for the lost-lepton background  
 528 prediction. In principle we are following the approach of the 8 TeV RA2 analysis [2, 12].

- 529 • Lepton isolation efficiency:

530 The muon and electron isolation efficiencies are obtained from simulated events.  
 531 In order to estimate how well data and MC agree, Tag-and-Probe efficiencies on the  
 532 Z resonance from data and MC are used which are provided by the SUSY lepton  
 533 scalefactor groups. The uncertainty related to the difference is obtained by taking  
 534 the maximum of the relative difference between the prediction done with the Tag-  
 535 and-Probe efficiencies on MC and Data and the uncertainty on this value. Since no  
 536 systematic bias becomes visible, no correction based on data/MC scaling factors is  
 537 introduced. In addition the statistical uncertainty of the MC efficiencies are propa-  
 538 gated the same way as the Tag-and-Probe uncertainty.

- 539 • Lepton reconstruction/ID efficiency:

540 The muon and electron reconstruction and ID efficiencies are obtained from simu-  
 541 lated events. The main uncertainty here arises from possible differences between  
 542 efficiencies obtained from data and MC. By examining the reconstruction efficien-  
 543 cies as a function of the search variables it seems to be reasonable that using some

544 inclusive efficiencies also provided by the SUSY lepton scalefactor groups are suffi-  
 545 cient for deriving data/MC uncertainties (same procedure as above). Furthermore,  
 546 the statistical uncertainties from MC are propagated.

- 547 • Lepton acceptance:

548 The uncertainty of the acceptance efficiency consists of the uncertainty in the par-  
 549 ton distribution functions (PDF), the MC renormalization/factorization scale and  
 550 the uncertainty arising from the statistical precision of the efficiency maps. The PDF  
 551 uncertainties is studied by varying PDF sets used to produce the MC samples, ac-  
 552 cording to their uncertainties for the baseline selection. This procedure leads to an  
 553 uncertainty of 0.7% on the acceptance efficiency for events with  $H_T^{\text{miss}} < 500 \text{ GeV}$   
 554 and 1.9% otherwise. For the uncertainty on the acceptance due to the MC renorm-  
 555 alization/factorization scale additional 0.7% are assigned (similar procedure as for  
 556 obtaining PDF uncertainty).

- 557 • Lepton purity:

558 The purity is expected to be very high ( $> 99\%$  for muons,  $> 95\%$  for electrons) so  
 559 this only leads to a minor systematic uncertainty and a conservative uncertainty of  
 560 20% on the impurity is assigned. Furthermore, the statistical uncertainties from MC  
 561 are propagated.

- 562 • Dilepton correction:

563 Both dileptonic corrections are only minor compared to the remaining ones so a  
 564 conservative systematic uncertainty is assigned here. About 3% of the total single-  
 565 lepton control sample originates from dileptonic  $t\bar{t}$  decays (after applying the  $m_T$  cut)  
 566 and less than 2% of expected search region events. An uncertainty of 50% is assigned  
 567 on the (di-leptonic) impurity of the control sample and 20% on the probability to lose  
 568 both leptons of a dileptonic event. Furthermore, the statistical uncertainties from  
 569 MC are propagated.

- 570 •  $M_T$  cut efficiency:

571 The uncertainty associated with the  $m_T$  cut consists of two parts: the statistical un-  
 572 certainty of the efficiency map from MC and a systematic uncertainty. For the latter,  
 573 the uncertainty on the jet energy corrections (JEC) is propagated to  $E_T^{\text{miss}}$  (following  
 574 the latest recommendations of the MET group) and the efficiency of the  $M_T$  cut is  
 575 recalculated. Following this procedure, a flat, conservative uncertainty of 5% on the  
 576 inefficiency of the  $M_T$  cut is assigned as a systematic uncertainty.

- 577 • Isolated-track vetoes:

578 The isolated-track vetoes lead to a correction of about 40% in the lost-lepton back-  
 579 ground. Due to the size of this correction, it is important to study the validity of the  
 580 efficiency maps. A systematic uncertainty of 8% is assigned for muon tracks, 15%  
 581 for electron tracks and 10% for pion tracks. Furthermore, the statistical uncertain-  
 582 ties from MC are propagated. More discussion and a justification for the assigned  
 583 uncertainties is given in Section 6.3.

- 584 • MC closure:

585 Furthermore, an uncertainty on the precision of the MC closure test is assigned.  
 586 Since no true non-closure is observed (see figs. 29, 28) the larger value of the non-  
 587 closure or the stat. uncertainty on non-closure is assigned for each bin. In case this  
 588 ratio is dominated by extremely low MC statistics and a high spread in weights the  
 589 assigned non-closure uncertainty is cut off at 100%.

590 Details of the implementation of these uncertainties in the statistical framework are described  
 591 in sec. 11.

### 592 6.1.5 Lost-lepton background prediction

593 Figure 30 presents the full predictions for the lost lepton background based on  $1.28 \text{ fb}^{-1}$  of data  
 594 for 72 search bins (blue lines with green shades). The green shaded areas represent statistical  
 595 uncertainties which are not shown if no CS events were observed. The data-based predictions  
 596 are compared to the MC expectations of the lost lepton background as a reference.

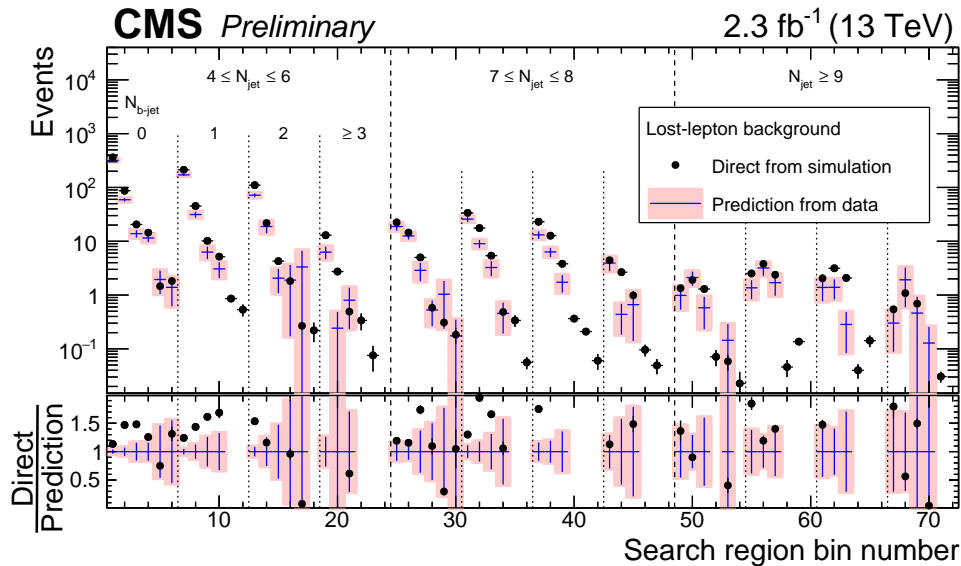


Figure 30: The lost lepton background in the 72 search bins of the analysis (intervals of  $H_T$ ,  $H_T^{\text{miss}}$ ,  $N_{\text{jet}}$ , and  $N_{b\text{-jet}}$ ) as predicted by performing the data-driven background-determination procedure on the  $1.28 \text{ fb}^{-1}$  of data (shaded regions) compared to the lost lepton background expectations from simulation (solid points). The simulation makes use of  $t\bar{t}$ ,  $W+\text{jets}$ , single-top quark and exotic event samples.

597 The efficiency weights applied to the control sample yields to produce the predictions are  
 598 shown in Fig. 31. In case no control sample events are observed an average weight from sim-  
 599 ulation is used to scale the Poisson statistical error on the zero observed, which is around 1.84  
 600 as given by the Garwood interval [13]. This average weight is calculated by the procedure in-  
 601 dicated by Eq. 18. Each event in the control sample is weighted by the various efficiency terms,  
 602 taken from the efficiency maps.

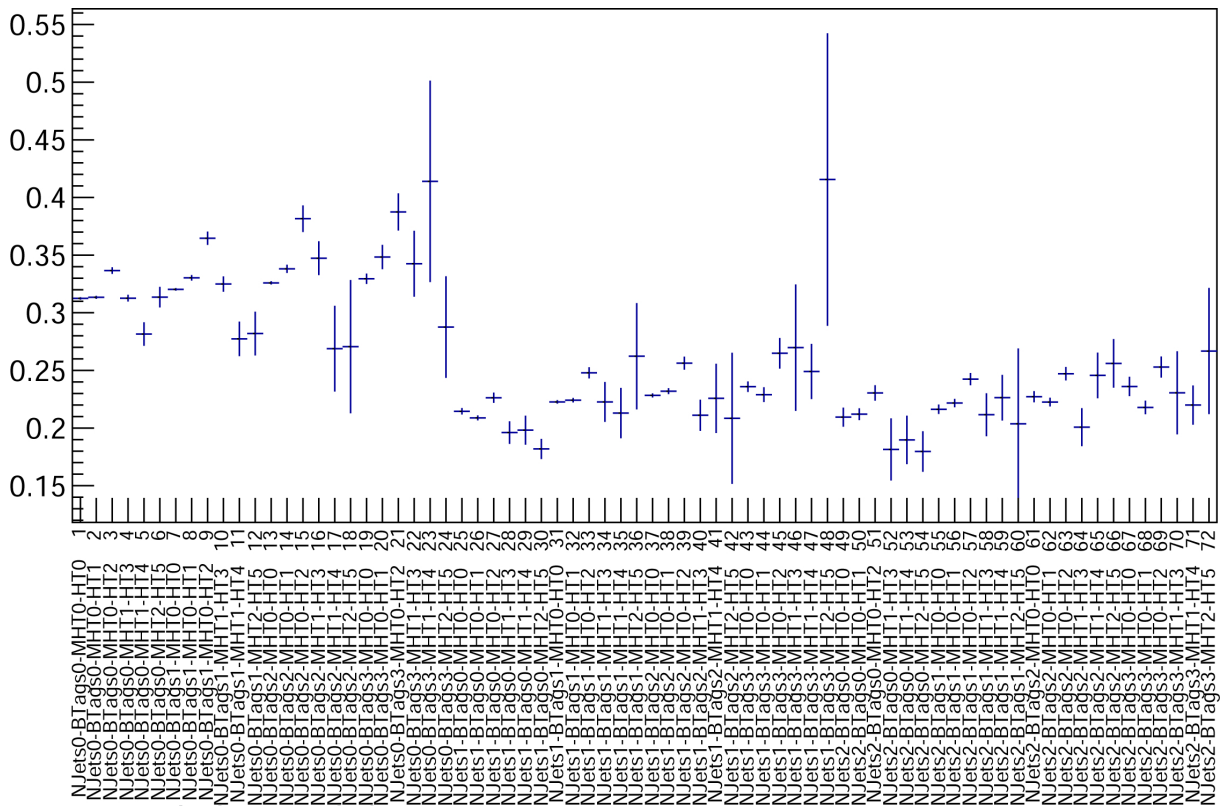


Figure 31: Average prediction weight for each search bin. The displayed uncertainty corresponds to the uncertainty on the mean.

## 603 6.2 Hadronically decaying $\tau$ lepton background estimation

604 To evaluate the  $t\bar{t}$ , single-top, and  $W+jets$  background that arises when a  $W$  boson decays to a  
 605 neutrino and a hadronically decaying  $\tau$  lepton ( $\tau_h$ ), we employ the tau-template method [2, 12,  
 606 14, 15]. In this approach, the  $\tau_h$  background is estimated from a control sample (CS) of  $\mu+jets$   
 607 events, which we select by requiring exactly one muon with  $p_T > 20 \text{ GeV}/c$  and  $|\eta| < 2.1$ . This  
 608 single-muon CS is mainly composed of  $t\bar{t}(\rightarrow \mu\nu)+jets$  and  $W(\rightarrow \mu\nu)+jets$  events. Since  $\mu+jets$   
 609 and  $\tau_h+jets$  production both arise from the same underlying process, the hadronic component  
 610 of the two event classes is expected to be the same, aside from the response of the detector to  
 611 a muon or to a  $\tau_h$  jet. The basic idea of the method is to smear the muon  $p_T$  in the CS events,  
 612 using MC-derived response functions (the “templates”), in order to emulate the  $\tau_h$  jet response.  
 613 Global hadronic variables such as  $N_{jet}$ ,  $H_T$ , and  $H_T^{\text{miss}}$  are then recomputed, and the full analysis  
 614 selection procedure is subsequently applied.

615 The smearing of muon  $p_T$  in the CS usually causes  $H_T^{\text{miss}}$  to increase. To ensure full coverage  
 616 over the  $H_T^{\text{miss}}$  range of the nominal event selection, we would like to select CS events using  
 617 a lower  $H_T^{\text{miss}}$  threshold than the nominal trigger provides. Therefore, we use a  $\mu + H_T$  cross  
 618 trigger, `HLT_Mu15_IsoVVVL_PFHT350_v` stored in the SingleMuon PD. Since this trigger was  
 619 prescaled during the 2015C period, we only use data from the 2015D period, and we scale up to  
 620 account for the luminosity of the 2015C dataset (which is only 0.7% of the 2015D dataset). The  
 621 performance of this trigger is discussed in Section 2.2. The trigger is fully efficient in terms of  
 622 the hadronic variables ( $N_{jet}$ ,  $H_T$ ,  $H_T^{\text{miss}}$ ). The muon trigger efficiency is  $\epsilon_{\text{Trig}}^{\mu} = 95.1^{+0.5}_{-0.6} \pm 1.0\%$   
 623 and we correct for it.

### 624 6.2.1 The $\tau_h$ response templates

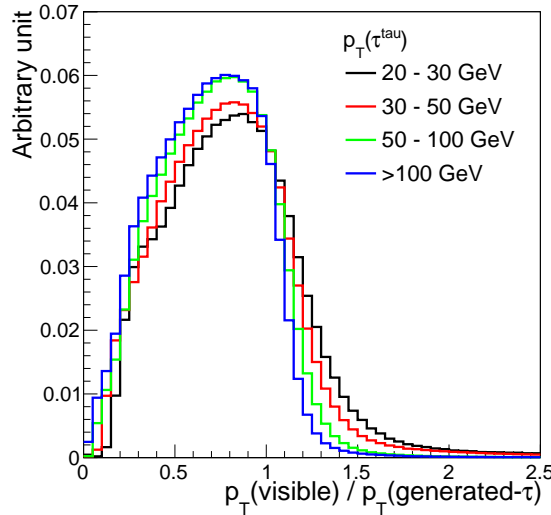


Figure 32: The  $\tau_h$  response templates: the distribution of  $p_{T,\tau_h\text{-reco}}/p_{T,\tau_h\text{-gen}}$  in intervals of  $p_{T,\tau_h\text{-gen}}$ , as determined from single  $\tau$  gun simulation.

625 The  $\tau_h$  response templates are obtained from  $t\bar{t}$  and  $W+jets$  simulation as follows. A recon-  
 626 structed jet, defined as described below, is matched to a generator-level  $\tau_h$  lepton with  $|\eta| < 2.1$   
 627 and  $p_{T,\tau_h\text{-gen}} > 20 \text{ GeV}/c$ , where  $p_{T,\tau_h\text{-gen}}$  is the  $p_T$  value of the generator-level  $\tau_h$  lepton includ-  
 628 ing the contribution of the daughter neutrino. For the purposes of this matching, the direc-  
 629 tion of the generator-level  $\tau_h$  lepton is defined by its three-momentum minus the daughter-  
 630 neutrino three-momentum. The matching criterion is  $\Delta R(\text{jet}, \tau_h\text{-gen}) = \sqrt{(\Delta\eta)^2 + (\Delta\phi)^2} < 0.1$

for  $p_{T,\tau_h\text{-gen}} > 50 \text{ GeV}$ , and  $\Delta R(\text{jet}, \tau_h\text{-gen}) < 0.2$  for  $20 < p_{T,\tau_h\text{-gen}} < 50 \text{ GeV}$ , where we use a less restrictive matching criterion in the latter case in order to maintain a high matching efficiency even for small  $p_{T,\tau_h\text{-gen}}$ . The matched detector-level jet with the smallest  $\Delta R$  is considered to be the reconstructed  $\tau_h$  jet.

We form the ratio between the  $p_T$  values of the matched detector- and generator-level  $\tau_h$  objects:  $p_{T,\tau_h\text{-reco}}/p_{T,\tau_h\text{-gen}}$ . The simulated distributions of  $p_{T,\tau_h\text{-reco}}/p_{T,\tau_h\text{-gen}}$  for different intervals of  $p_{T,\tau_h\text{-gen}}$  are shown in Fig. 32. These distributions define the  $\tau_h$  response templates. The longer tails at large  $p_{T,\tau_h\text{-reco}}/p_{T,\tau_h\text{-gen}}$  seen for smaller values of  $p_{T,\tau_h\text{-gen}}$  arise from the degradation of transverse momentum resolution at small  $p_T$ .

In the MiniAOD data sets, only jets with reconstructed  $p_T > 10 \text{ GeV}$  are stored; however, the reconstructed  $p_T$  of  $\tau_h$  jets can fluctuate to lower values, even if the underlying “true”  $p_T$  exceeds the nominal  $p_{T,\tau_h\text{-gen}} = 20 \text{ GeV}$  cutoff. Therefore, starting with PF candidates, jets are reclustered to yield jets without any  $p_T$  requirement, but with all other jet definition conditions of Section 4 applied. It is these jets that are used to build the  $\tau_h$  response templates (Fig. 32). Retaining  $\tau_h$  jets with reconstructed  $p_T < 10 \text{ GeV}$  allows us to include events in which the  $\tau_h$  lepton is merged with a nearby quark or gluon jet by the jet finder, yielding a jet that satisfies the  $p_T > 30 \text{ GeV}$  jet threshold, and events in which the properties of other objects in the event, such as the  $H_T^{\text{miss}}$  value from the neutrino in the  $W \rightarrow \tau_h\nu_\tau$  decays, allow the event selection requirements to be satisfied. We thus are able to incorporate a more inclusive  $\tau_h$  lepton sample, improving the accuracy of the response templates.

### 6.2.2 Misidentification of $\tau_h$ jets as b jets

Hadronically decaying  $\tau$  leptons have a significant probability to be erroneously identified as b jets. This misidentification must be taken into account in order to accurately predict the  $N_{\text{b-jet}}$  distribution of  $\tau_h$  background events, i.e., to assign a  $\tau_h$  background event to the most appropriate search bin.

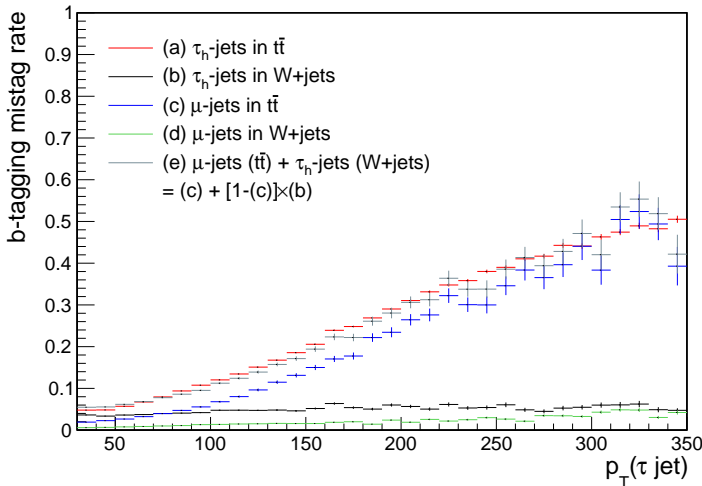


Figure 33: The rate for  $\tau_h$  jets (a,b) and muon jets (c,d) to be misidentified as a b jet as a function of jet  $p_T$  in simulated  $t\bar{t}$  and  $W+\text{jets}$  events. The distribution labeled “(e)” shows the performance of our model in which we apply the  $\tau_h$  b-mistag rate from  $W+\text{jets}$  events to muon jets in  $t\bar{t}$  events to emulate the overall  $\tau_h$  b-mistag behavior. It is similar to the MC expectation shown by distribution “(a)”.

The misidentification rates of  $\tau_h$  jets as b jets (b-mistag) in simulated  $t\bar{t}$  and  $W+\text{jets}$  events are

657 shown as a function of jet  $p_T$  in Fig. 33 by the distributions labeled “(a)” and “(b)”. The corre-  
 658 sponding results for muon jets are shown by the distributions labeled “(c)” and “(d)”, where  
 659 a “muon jet” refers to the CS muons discussed above along with all other particles clustered  
 660 with the muon into the same jet. It is this muon jet  $p_T$  that is smeared by the  $\tau_h$  response func-  
 661 tion shown in Fig. 32 to model the  $\tau_h$  background. For  $W+jets$  events, the b-mistag rate of  $\tau_h$   
 662 jets is seen to be around 4–5% independent of jet  $p_T$ . For  $t\bar{t}$  events, the b-mistag rate of  $\tau_h$  jets  
 663 is around 5% for  $p_T \lesssim 50$  GeV, but it increases to 40–50% as  $p_T$  increases. For muon jets, the  
 664 b-mistag rate is negligible for  $W+jets$  events, while for  $t\bar{t}$  events it is negligible for  $p_T \lesssim 50$  GeV  
 665 but increases to  $\sim 40\%$  at high  $p_T$ .

666 The strong increase in the b-mistag rates of  $\tau_h$  and muon jets in  $t\bar{t}$  events as  $p_T$  increases is  
 667 due to the nearby true b quark from the same top-quark decay. We consider that the intrinsic  
 668 b-mistag rate of  $\tau_h$  (muon) jets is around 5% (negligible) in both  $t\bar{t}$  and  $W+jets$  events, and that  
 669 the behavior of  $\tau_h$  and muon jet events is the same with respect to the presence of a nearby b  
 670 quark, i.e., with respect to increasing  $p_T$  in  $t\bar{t}$  events.

671 Based on these results, we construct the  $N_{b\text{-jet}}$  distribution of the  $\tau_h$  background as follows.  
 672 We model the probability  $P_{b\text{-mistag}}^{\tau_h}$  for a  $\tau_h$  jet to be b-mistagged as the probability  $P_{b\text{-mistag}}^\mu$  for  
 673 a muon jet to be b-mistagged (this accounts for b-mistagging due to proximity to a b quark),  
 674 added to the roughly 5% probability for an intrinsic  $\tau_h$  jet b-mistag, where this latter term is  
 675 taken to be the probability  $1 - P_{b\text{-mistag}}^\mu$  that a muon jet is not b-mistagged (thus making it  
 676 consistent with the expectation for muon jets in  $W+jets$  and in low- $p_T$   $t\bar{t}$  events) multiplied  
 677 by the probability  $P_{b\text{-mistag}}^{W+jets}$  for a  $\tau_h$  jet in a  $W+jets$  event or low- $p_T$   $t\bar{t}$  event to b-mistagged,  
 678 i.e.,  $P_{b\text{-mistag}}^{\tau_h} = P_{b\text{-mistag}}^\mu + (1 - P_{b\text{-mistag}}^\mu)P_{b\text{-mistag}}^{W+jets}$ , shown by the combination of distributions  
 679 (e) = (c)+[1-(c)](b) in Fig. 33 (left). We determine the b-jet multiplicity  $N_{b\text{-CS}}$  of each CS event  
 680 using the nominal b-tagging requirements (Section 4). If the muon jet in the CS event is not  
 681 b-tagged, the CS event is entered into the  $N_{b\text{-jet}}$  distribution of the  $\tau_h$  background twice: once  
 682 for  $N_{b\text{-jet}} = N_{b\text{-CS}}$  with weight  $w_{b\text{-mistag}}^{\tau_h} = 1 - P_{b\text{-mistag}}^{\tau_h}$ , and once for  $N_{b\text{-jet}} = N_{b\text{-CS}} + 1$  with  
 683 weight  $w_{b\text{-mistag}}^{\tau_h} = P_{b\text{-mistag}}^{\tau_h}$ , i.e., we adjust the number of tagged b jets contributed by the  
 684 CS event upwards by one in correspondence with the probability for the event-by-event  $\tau_h$  b-  
 685 misidentification. In contrast, if the muon jet in the CS event is b-tagged, we enter the event  
 686 into the  $\tau_h$  background distribution once, with value  $N_{b\text{-jet}} = N_{b\text{-CS}}$  and weight  $w_{b\text{-mistag}}^{\tau_h} = 1$ .  
 687 Note that  $\tau_h$  jets with  $p_{T,\tau_h\text{-reco}} < 30$  GeV are not included in the above procedure since jets  
 688 (including b jets) are required to have  $p_T > 30$  GeV in our analysis.

689 This procedure works well to emulate the  $N_{b\text{-jet}}$  distribution for the  $\tau_h$  background as shown in  
 690 the “closure” tests presented in Fig. 40(bottom right).

### 691 6.2.3 Muon control sample selection and hadronic tau background prediction

692 Events in the muon data control sample are selected using the following criteria:

- 693 • exactly one isolated muon with  $p_T > 20$  GeV/c and  $|\eta| < 2.1$ , based on the muon  
   694 isolation and ID criteria of Section 4;
- 695 • No isolated electron candidate defined according to the criteria of Section 4;
- 696 •  $m_T < 100$  GeV, to reduce potential contributions of signal events.

697 For each event in this sample, the measured muon transverse momentum  $p_{T\mu}$  is smeared ac-  
 698 cording to the  $\tau_h$  response functions of Fig. 32. The smearing is accomplished as follows. We  
 699 assume that the value of  $p_{T\mu}$  can be used to represent the generator-level  $p_{T,\tau_h\text{-gen}}$  of the simu-

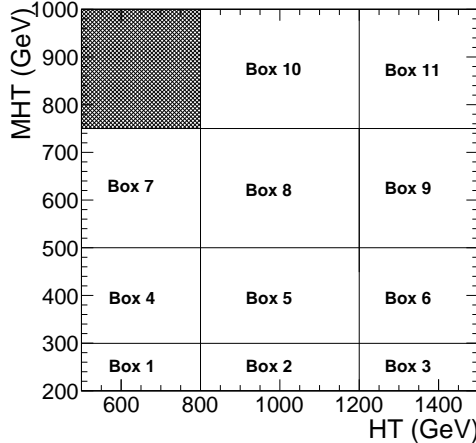


Figure 34: Two-dimensional plane in  $H_T$  and  $H_T^{\text{miss}}$  showing bins used to parametrize the acceptance ( $\epsilon_{\text{Acc}}^\mu$ ),  $m_T$  selection efficiency ( $\epsilon_{m_T}$ ), contamination of the CS by  $W \rightarrow \tau\nu_\tau \rightarrow \mu\nu_\mu\bar{\nu}_\tau\nu_\tau$  events ( $f_{\tau \rightarrow \mu}$ ), and the isolated-track veto efficiency ( $\epsilon_{\text{isotrk}}$ ) for  $N_{\text{jet}} \leq 6$ . For  $N_{\text{jet}} \geq 7$ , coarser bins in  $H_T$ - $H_T^{\text{miss}}$  as shown in Fig. 11 are used.

lated  $\tau_h$  leptons. This assumption is justified by the good momentum resolution achieved for muons in the CMS detector, i.e., the close correspondence expected between the detector-level and underlying true values of muon momentum. A  $\tau_h$  response template is chosen based on the  $p_{T,\tau_h\text{-gen}}$  interval into which  $p_{T,\mu}$  falls. For a given template, we successively choose each bin in the template, replacing  $p_{T,\mu}$  in the CS event with the value of  $p_{T,\tau_h\text{-reco}}$  corresponding to that bin. In this manner, all bins in the template are uniformly sampled. For each choice of  $p_{T,\tau_h\text{-reco}}$ , the kinematic variables in the event, viz.,  $N_{\text{jet}}$ ,  $H_T$ ,  $H_T^{\text{miss}}$ , and the  $\Delta\phi(j_i, H_T^{\text{miss}})$  variables, are calculated. A weight is then determined for the event to contribute to each bin of the kinematic distributions and thus to each search bin. We include a weight to account for the probability that a  $\tau_h$  jet is misidentified as a b jet (Section 6.2.2). The following corrections are also incorporated:

- the ratio of branching fractions  $\mathcal{B}(W \rightarrow \tau_h\nu)/\mathcal{B}(W \rightarrow \mu\nu) = 0.6476 \pm 0.0024$  [16];
- the muon reconstruction and identification efficiency  $\epsilon_{\text{Reco}}^\mu$ , and the muon isolation efficiency  $\epsilon_{\text{ISO}}^\mu$  [ $p_T$ , activity];
- the muon acceptance ( $\epsilon_{\text{Acc}}^\mu$ ) [ $N_{\text{jet}}, H_T^{\text{miss}}$ ] (see Fig. 35);
- the  $m_T$  selection efficiency ( $\epsilon_{m_T}$ ) [ $N_{\text{jet}}, H_T, H_T^{\text{miss}}$ ] (see Fig. 36);
- the contamination of the CS by  $W \rightarrow \tau\nu_\tau \rightarrow \mu\nu_\mu\bar{\nu}_\tau\nu_\tau$  events (as opposed to the assumed  $W \rightarrow \mu\nu_\mu$  events), accounted for with the correction term  $(1 - f_{\tau \rightarrow \mu})$  [ $N_{\text{jet}}, H_T, H_T^{\text{miss}}$ ] (see Fig. 37);
- the dileptonic event contamination of the CS, accounted for with the correction term  $(1 - f_{ll})$ , where  $f_{ll} = 0.02$ ;
- the isolated-track veto efficiency ( $\epsilon_{\text{isotrk}}$ ) [ $N_{\text{jet}}, H_T, H_T^{\text{miss}}$ ] (see Fig. 38).

The muon reconstruction and identification efficiency, and the muon isolation efficiency, are the same as used for the lost-lepton background determination and are discussed in Sections 6.1 and 6.3. The variables in block parentheses are those that are used to parameterize the indicated correction. For items without block parentheses, a constant correction factor is used.

About 30–40% of the  $\tau_h$  background is rejected by the isolated-track veto, which works efficiently against 1-prong  $\tau_h$  decays. The efficiency of this veto is obtained from simulated  $t\bar{t}$ ,

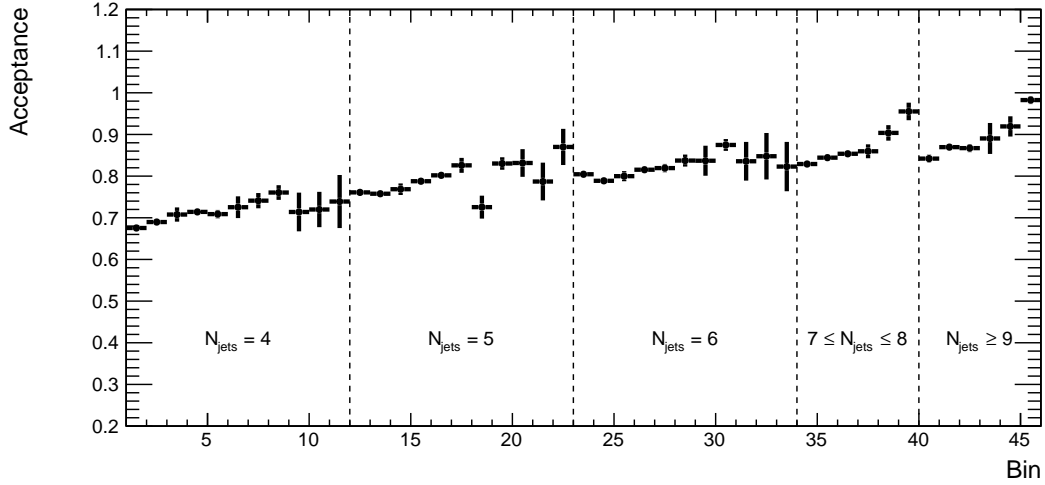


Figure 35: Acceptance  $\epsilon_{\text{Acc}}^{\mu}$  of hadronically decaying  $\tau$  leptons for  $p_T > 20 \text{ GeV}$  and  $|\eta| < 2.1$ . The results are shown for eleven (six)  $H_T$ - $H_T^{\text{miss}}$  bins as defined in Fig. 34 (11) for  $N_{\text{jet}} = 4, 5$ , and  $6$  ( $7-8, 9-$ ) bins integrated over the four bins of  $N_{\text{b-jet}}$  (in total 45 bins).

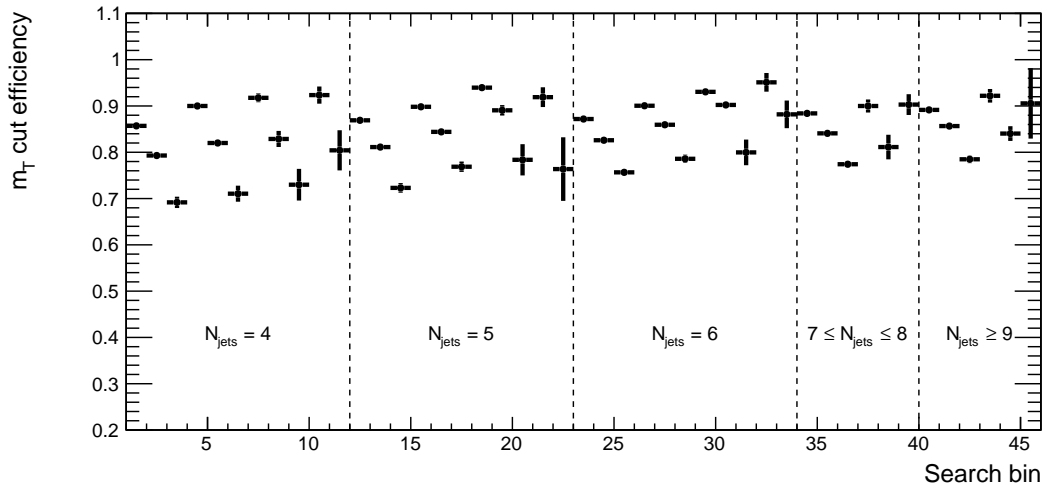


Figure 36: The efficiency  $\epsilon_{m_T}$  of the muon  $m_T$  selection. The results are shown for eleven (six)  $H_T$ - $H_T^{\text{miss}}$  bins as defined in Fig. 34 (11) for  $N_{\text{jet}} = 4, 5$ , and  $6$  ( $7-8, 9-$ ) bins integrated over the four bins of  $N_{\text{b-jet}}$  (in total 45 bins).

728 W+jets, and single-top quark event samples. The validation of this veto efficiency is discussed  
 729 in Section 6.3.

The  $\tau_h$  background is given by:

$$N_{\tau_h} = \sum_i^{N_{\text{CS}}^{\mu}} \left( \sum_j^{\text{Template bins}} \left( P_{\tau_h}^{\text{resp}} \sum_k w_{\text{b-mistag}}^{\tau_h} \right) \frac{1}{\epsilon_{\text{Trig}}^{\mu} \epsilon_{\text{Reco}}^{\mu} \epsilon_{\text{ISO}}^{\mu}} \frac{1}{\epsilon_{\text{Acc}}^{\mu} \epsilon_{m_T}^{\mu}} (1 - f_{\tau \rightarrow \mu})(1 - f_{\text{ll}}) \frac{\mathcal{B}(W \rightarrow \tau_h \nu)}{\mathcal{B}(W \rightarrow \mu \nu)} \epsilon_{\text{isotrk}} \right), \quad (19)$$

730 where the first summation is over the events in the  $\mu$ +jets control sample, the second is over the  
 731 bins of the  $\tau_h$  response template ( $P_{\tau_h}^{\text{resp}}$ ), and the third accounts for the probability to misidentify  
 732 a  $\tau_h$  jet as a b jet ( $w_{\text{b-mistag}}^{\tau_h}$ ).

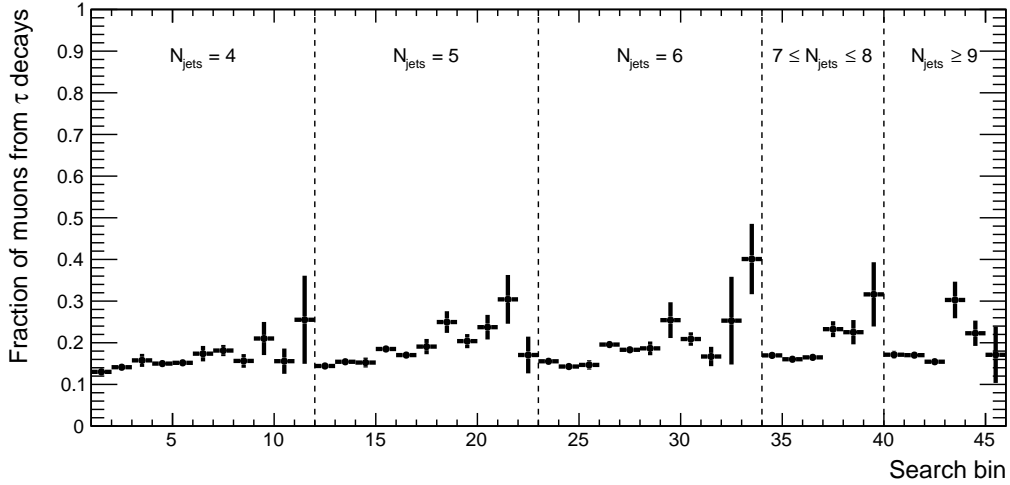


Figure 37: The fraction  $f_{\tau \rightarrow \mu}$  of muons from  $\tau$  decays in the single-muon control sample, as determined from simulation. The results are shown for eleven (six)  $H_T$ - $H_T^{\text{miss}}$  bins as defined in Fig. 34 (34) for  $N_{\text{jet}} = 4, 5$ , and  $6 (7-8, 9-)$  bins integrated over the four bins of  $N_{\text{b-jet}}$  (in total 45 bins).

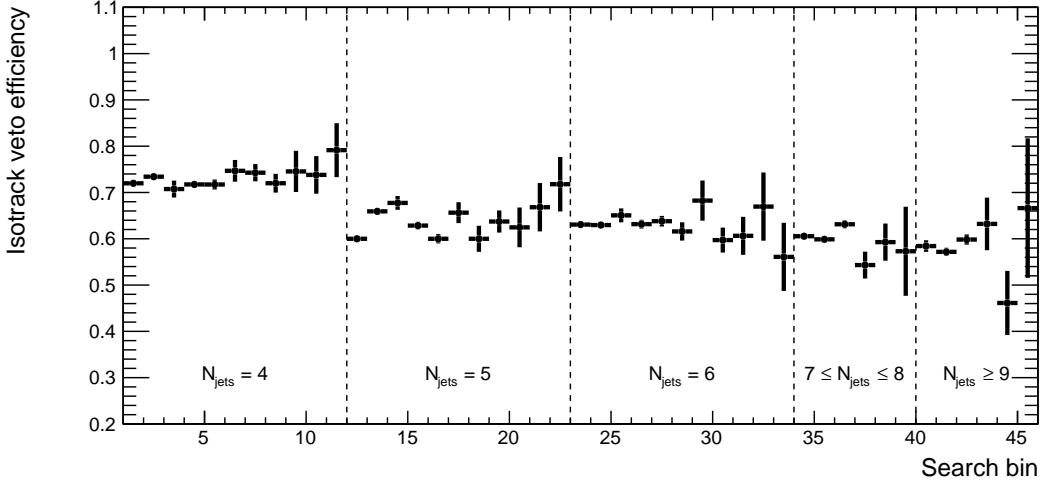


Figure 38: The isolated-track veto efficiency  $\epsilon_{\text{isotrk}}$ . The results are shown for eleven (six)  $H_T$ - $H_T^{\text{miss}}$  bins as defined in Fig. 34 (34) for  $N_{\text{jet}} = 4, 5$ , and  $6 (7-8, 9-)$  bins integrated over the four bins of  $N_{\text{b-jet}}$  (in total 45 bins).

733 Closure tests of the  $\tau_h$  background-determination method, based on simulated  $t\bar{t}$ , W+jets, single-  
 734 top, WW/WZ/ZZ, Drell-Yan samples, and other SM rare process samples are shown in Figs. 39  
 735 and 40. As shown in Fig. 39, the method closes within about 10% in most of high statistics  
 736 bins. The larger one of either statistical uncertainty of the closure test in each search bin or  
 737 the amount of the non-closure are assigned as systematic uncertainties. For QCD background  
 738 predictions, we also need  $\tau_h$  background prediction in finer bins defined by  $H_T$ ,  $H_T^{\text{miss}}$ ,  $N_{\text{jet}}$ ,  
 739 and  $N_{\text{b-jet}}$  for events passing or failing the angular cuts on  $\Delta\phi(j_{1,2,3,4}, H_T^{\text{miss}})$ . The closure test in  
 740 these binning are shown in Fig. 102.

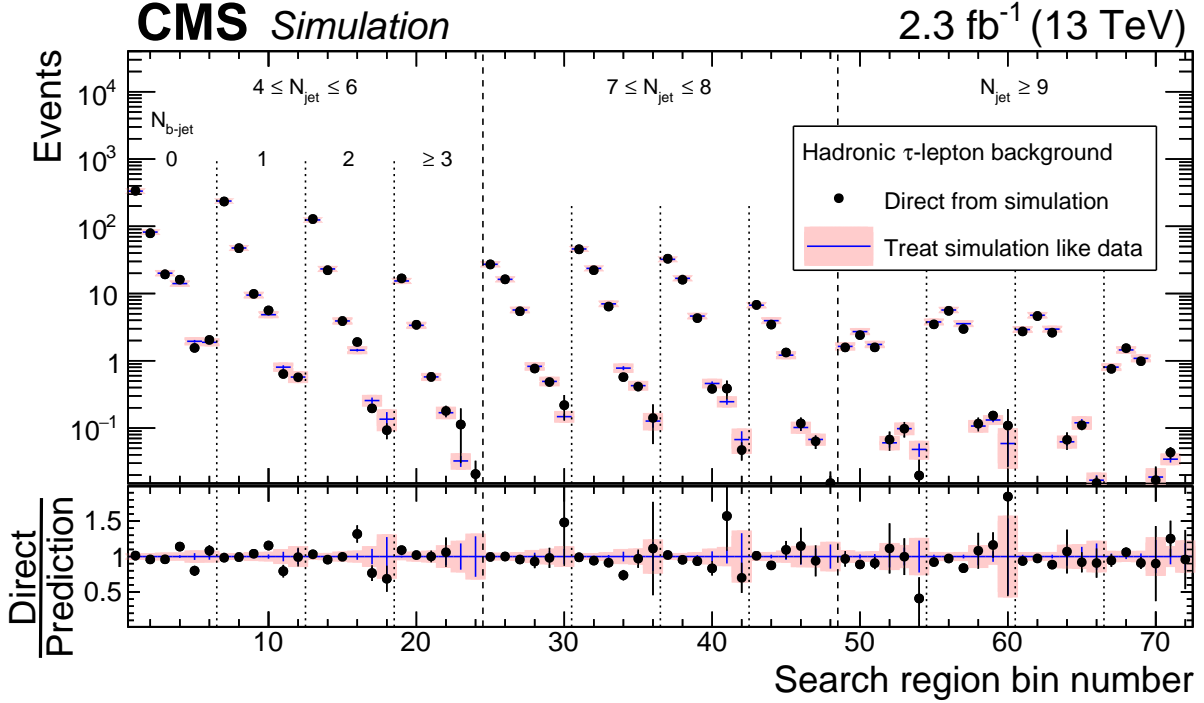


Figure 39: The  $\tau_h$  background in the 72 search bins of the analysis (intervals of  $H_T$ ,  $H_T^{\text{miss}}$ ,  $N_{\text{jet}}$ , and  $N_{\text{b-jet}}$ ) as predicted directly from simulation (solid points) and as predicted by the data-driven background-determination procedure (shaded regions). The simulation makes use of  $t\bar{t}$ ,  $W+\text{jets}$ , single-top, Drell-Yan, and other rare SM event samples listed in Table 7.

#### 6.2.4 Systematic uncertainties

The following uncertainties are considered based on the 8 TeV RA2 analysis [2, 12] and the extension of the method to include isolated track vetoes and b-tagging as an additional search variable.

- **Hadronic tau response template:** The response template of hadronic tau jets is modeled using MC simulation, so potential data-MC energy scale differences have to be considered. The uncertainty by varying the hadronic tau jet energy scale as suggested by the JetMET POG is evaluated. These are correlated across all signal bins and are modeled with a single nuisance parameter.
- **Mistagging rate of hadronic tau jet:** The b-tagging mistag rate for hadronic tau jets as measured in  $W+\text{jets}$  simulated events is used in the method as discussed earlier. We conservatively vary this mistag rate by 50% to evaluate the uncertainty after consulting with the Btag POG. These are correlated across all signal bins and are modeled with a single nuisance parameter.
- **Muon reconstruction/ID/isolation efficiency:** The uncertainties on the data/MC corrections from tag and probe studies as discussed in Section 6.3. The uncertainty from the tag-and-probe method performed on Drell-Yan events by the SUSY lepton scale factor (SF) group is considered [17]. These are correlated across all signal bins and are modeled with a single nuisance parameter.
- **Acceptance:** The uncertainty of the acceptance efficiency consists of the uncertainty in the parton distribution functions (PDF) and in the renormalization and factorization scales used for the MC generation as well as the uncertainty arising from

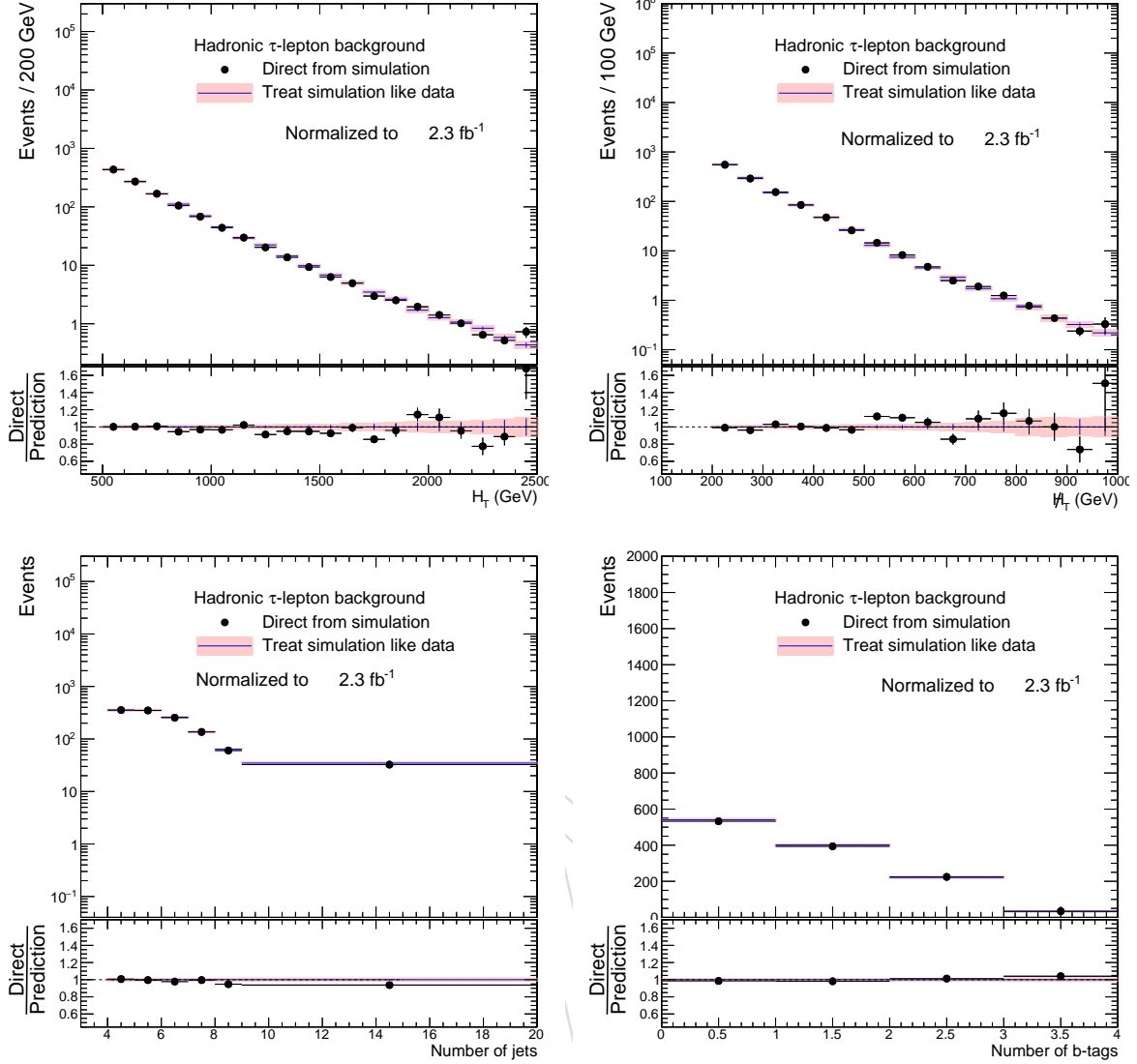


Figure 40: The  $H_T$ ,  $H_T^{\text{miss}}$ ,  $N_{\text{jet}}$ , and  $N_{\text{b-jet}}$  distributions as predicted directly from simulation (solid points) and as predicted by the data-driven background-determination procedure (shaded regions), for the baseline selection. The simulation makes use of  $t\bar{t}$ , W+jets, single-top, Drell-Yan, and other rare SM event samples listed in Table 7.

the statistical precision of the corrections. The uncertainties due to PDF are evaluated by computing the acceptance with 100 different sets of PDF weights stored in events representing uncertainties from NNPDF3.0 (100 MC replicas) and by finding the maximum variation in the acceptance. The uncertainties due to the renormalization and factorization scale are evaluated by computing the acceptance with eight different sets of renormalization and factorization scales varied by a factor of two up and down from the nominal values and by finding the maximum variation in the acceptance. These are done in  $t\bar{t}$  and W+jets, as these weights are not available in single top MC samples.

- **Dilepton correction:** This contamination is determined to be about 2% across all search regions. 100% of this subtraction is considered for systematic uncertainty.

774 •  **$m_T$  cut efficiency:** The uncertainty associated with the  $m_T$  cut comes from (1) the  
 775 statistical uncertainty of determining this efficiency from MC, and the uncertainty in  
 776 the  $E_T^{\text{miss}}$  scale.  $E_T^{\text{miss}}$  is scaled up/down by 30% and we evaluate the variations in the  
 777  $m_T$  cut efficiency. The variation of the cut efficiency is then assigned as a systematic  
 778 uncertainty. This procedure yields about 5% uncertainties across the search bins.  
 779 These uncertainties are treated as correlated across all signal bins and are modeled  
 780 with a single nuisance parameter.

781 • **Isolated track vetoes:** The isolated track veto efficiency that matters most here is the  
 782 efficiency of hadronic track vetoes on  $\tau_h$  jets. The strategy to validate and estimate  
 783 isolated hadronic track efficiency is discussed in Section 6.3.

784 • **MC closure:** The MC closure test is found to close to within 10% in most of the  
 785 search bins with high statistics except for three bins as discussed above, and in tight  
 786 search regions the statistical uncertainties of the closure test go beyond 10%. As  
 787 done for the lost-lepton background, the larger value of the non-closure or the sta-  
 788 tistical uncertainty on non-closure is assigned for each bin as bin-to-bin uncorrelated  
 789 uncertainties. In case this closure evaluation is dominated by low MC statistics and  
 790 a high spread in weights, the assigned non-closure uncertainty is cut off at 100%.

791 Many of the systematic uncertainties (muon reconstruction/ID/isolation efficiency, acceptance,  
 792 dilepton correction,  $m_T$  cut efficiency) are common with the lost-lepton background method  
 793 discussed in Section 6.1, and they will be considered fully correlated in the statistical interpre-  
 794 tation.

### 795 6.2.5 Hadronic-tau background prediction

796 Figure 41 presents the full predictions for the hadronic-tau background based on  $2.3 \text{ fb}^{-1}$  of  
 797 the single muon dataset for 72 search bins (blue lines with light-red shades). The shaded ar-  
 798 eas represent statistical uncertainties which include the extra additional uncertainty term to  
 799 account for zero observed events with high weights based on the Poisson statistical error on  
 800 the zero observed as given by the Garwood interval [13], which is 1.84, multiplied by a factor of  
 801 0.25 which gives a good coverage in statistics tests discussed in Appendix J. These data-based  
 802 predictions are compared to the MC expectations of  $\tau_h$  background as a reference. Figure 42  
 803 presents the predictions as a function of four search variables,  $H_T$ ,  $H_T^{\text{miss}}$ ,  $N_{\text{jet}}$ , and  $N_{\text{b-jet}}$ .

## 804 6.3 Lepton and isolated-track efficiency validation

805 One of the most important inputs, not only for the classical lost-lepton method but also for the  
 806 hadronic tau and  $H_T^{\text{miss}}$  extrapolation methods, are the lepton efficiencies. We use efficiencies  
 807 obtained from high-statistics MC samples and validate them using data where possible. The  
 808 efficiencies are divided into three main categories:

- 809 • electrons;
- 810 • muons;
- 811 • isolated tracks, which are further divided in  $e$ ,  $\mu$ , and  $\pi$  tracks.

812 Table 13 lists the different efficiencies and the planned validation techniques. The out-of-acceptance  
 813 terms for electrons and muons cannot be validated with data since they are by definition out  
 814 of the kinematically accessible region of the detector. The reconstruction and identification  
 815 efficiencies are combined into one term, denoted “reco”.

816 The isolation efficiency “iso” can be directly validated in data using a Tag&Probe method where  
 817 the probe object is a well-reconstructed and identified lepton on which the isolation criteria is

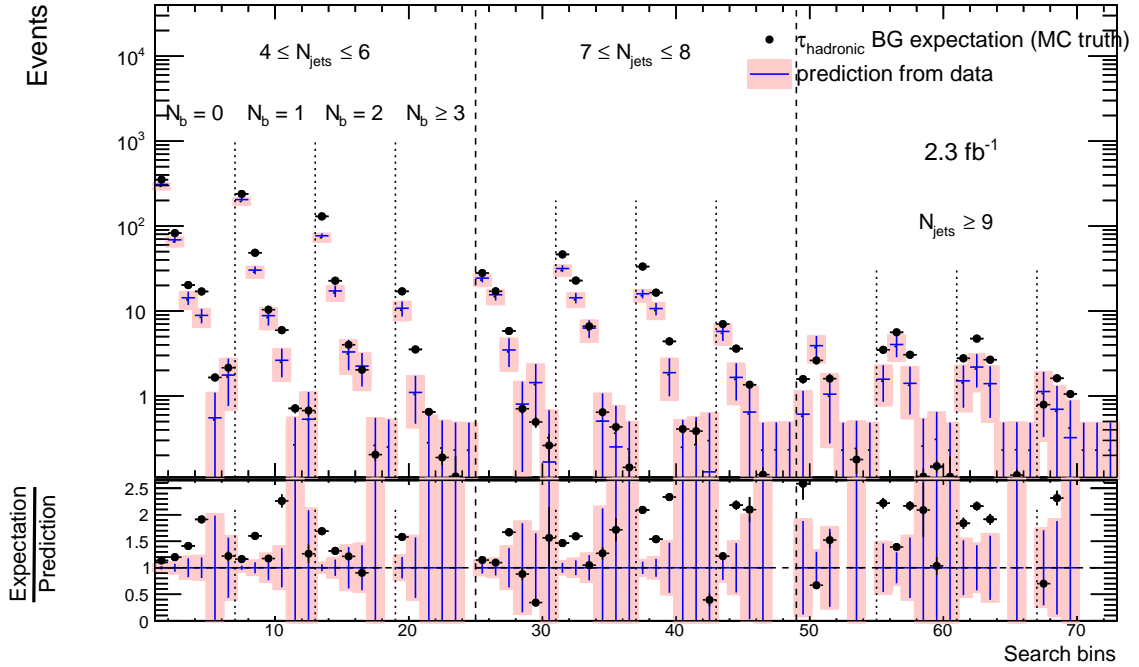


Figure 41: The  $\tau_h$  background in the 72 search bins of the analysis (intervals of  $H_T$ ,  $H_T^{\text{miss}}$ ,  $N_{\text{jet}}$ , and  $N_{\text{b-jet}}$ ) as predicted by performing the data-driven background-determination procedure on the  $2.3 \text{ fb}^{-1}$  of data (shaded regions) compared to the  $\tau_h$  background expectations from simulation (solid points). The simulation makes use of  $t\bar{t}$ , W+jets, single-top, Drell-Yan, and other rare SM event samples listed in Table 7.

Table 13: List of efficiencies for the different objects used for the  $t\bar{t}$  & W+jets background estimation methods.

Object	Parametrization	Validation in Data
$\mu$ , iso	$p_T$ , activity	Tag&Probe
$\mu$ , reco	$p_T$ , activity	Tag&Probe
$\mu$ , acc	$H_T$ , $H_T^{\text{miss}}$ , $N_{\text{jet}}$	—
e, iso	$p_T$ , activity	Tag&Probe
e, reco	$p_T$ , activity	Tag&Probe
e, acc	$H_T$ , $H_T^{\text{miss}}$ , $N_{\text{jet}}$	—
$\mu$ tracks	$H_T$ & $N_{\text{jet}}$	Tag&Probe
e tracks	$H_T$ & $N_{\text{jet}}$	Tag&Probe
$\pi$ tracks	$H_T$ & $N_{\text{jet}}$	Tag&Probe (indirect)

818 tested. This study is performed by the SUSY PAG Lepton SF group. The differences between  
 819 the isolation and efficiencies measured in data and in MC are at most a few percent [18, 19]. A  
 820 similar tag-and-probe procedure is used to validate lepton identification efficiencies directly in  
 821 data.

The predicted number of lost lepton and hadronic tau events in each search bin is scaled by a correction factor obtained from simulation:

$$\epsilon_{\text{isotrk}} = \frac{\text{Number of events remaining after lepton veto that are rejected by track veto}}{\text{Number of events remaining after lepton veto}} \quad (20)$$

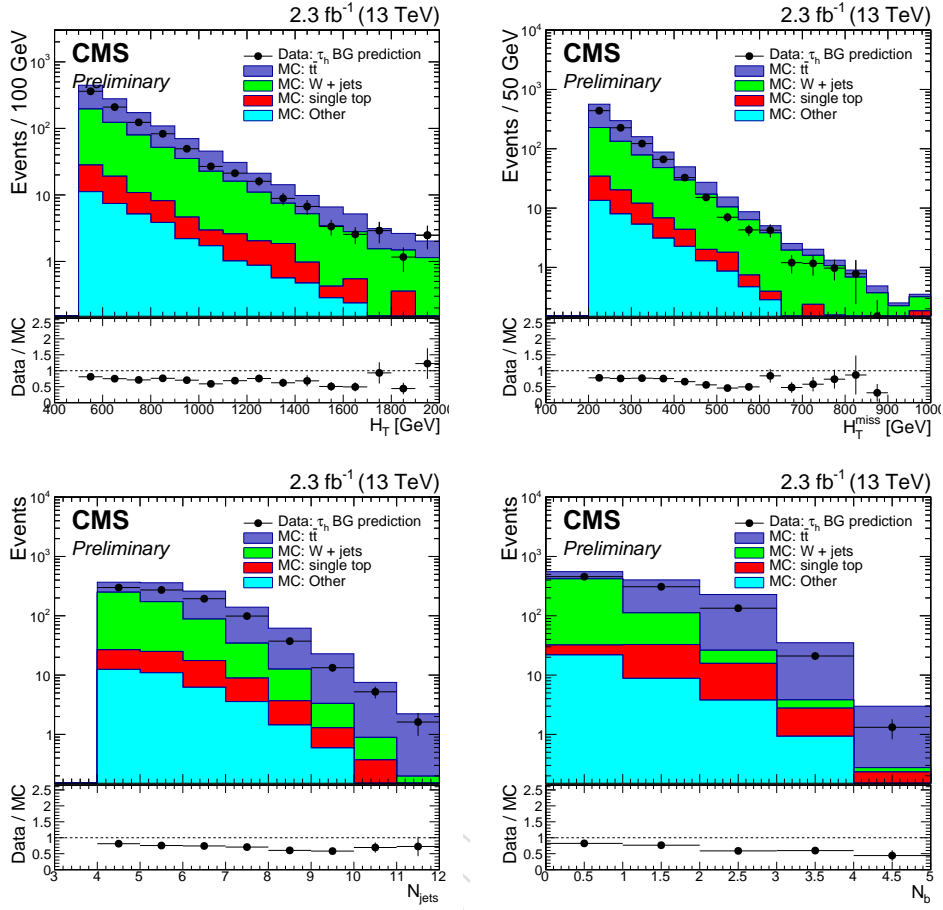


Figure 42: The  $H_T$ ,  $H_T^{\text{miss}}$ ,  $N_{\text{jets}}$ , and  $N_b$ -jet distributions as predicted by performing the data-driven background-determination procedure on the  $2.3 \text{ fb}^{-1}$  of data (shaded regions), compared to the  $\tau_h$  background expectations from simulation (solid points) for the baseline selection. The simulation makes use of  $t\bar{t}$ ,  $W+\text{jets}$ , single-top, Drell-Yan, and other rare SM event samples listed in Table 7.

- 822 The value of  $\epsilon_{\text{isotrk}}$  is relatively flat as a function of the search variables, as illustrated in Figures  
 823 43-45, and has an average value of 32%, 40%, and 35% for the lost-muon, lost-electron, and  
 824 hadronic tau backgrounds, respectively.
- 825 The biggest task in validating this correction to the backgrounds from the track veto is measur-  
 826 ing the track isolation efficiency in data and in simulation via a tag-and-probe method. This  
 827 isolation efficiency, specifically the modeling of the efficiency in simulation, is the largest source  
 828 of uncertainty on the track veto, at around 5-15% of the background prediction correction. This  
 829 accounts for around 5-10% uncertainty on the full lost lepton and hadronic tau predictions in  
 830 each search bin. The tag-and-probe study is described below.
- 831 For both the leptonic and hadronic track vetoes, smaller systematics are applied to account for  
 832 the simulation's modeling of:
- 833 • track reconstruction efficiency. This uncertainty is chosen to be a flat 3.9% for hadronic  
 834 tracks, based on measurements performed by the tracking POG in Run I [20, 21] and  
 835 1% for leptonic tracks.

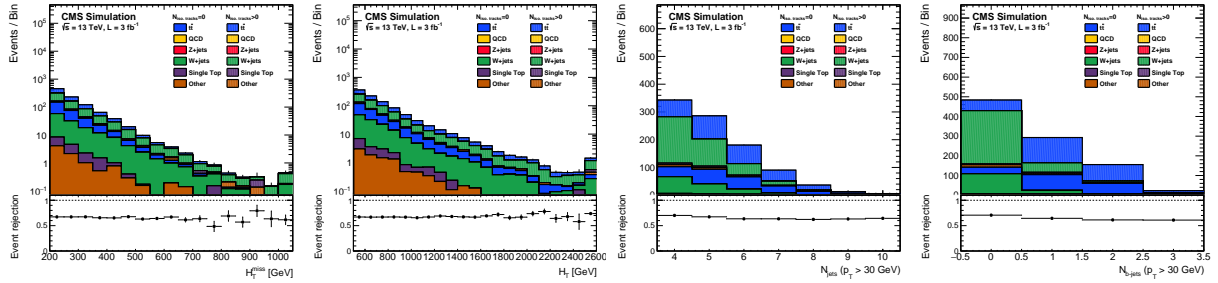


Figure 43: Performance of the isolated track veto as a function of the search variables in simulated lost-muon events. The shaded portion of the histograms represents the events in which the standard lepton veto failed to identify the muon but are rejected by the track veto. The solid portion of the histograms represents the lost-muon background remaining after both the lepton and track vetoes.

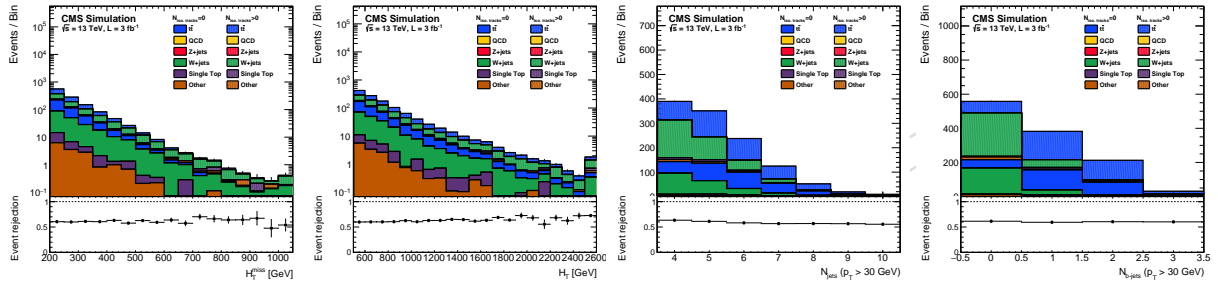


Figure 44: Performance of the isolated track veto as a function of the search variables in simulated lost-electron events. The shaded portion of the histograms represents the events in which the standard lepton veto failed to identify the electron but are rejected by the track veto. The solid portion of the histograms represents the lost-electron background remaining after both the lepton and track vetoes.

- 836 • efficiency of the  $m_T$  cut. This uncertainty is chosen to be a flat 0.1% for hadronic  
 837 tracks and 0.2% for leptonic tracks. These values are obtained by varying the jet en-  
 838 ergies within their uncertainties and propagating those variations to the  $E_T^{\text{miss}}$  and  
 839 the  $m_T$  (track,  $E_T^{\text{miss}}$ ) distributions. The effect is very small, as shown in Figure 49.  
 840 This uncertainty makes a nearly-negligible contribution to the overall track veto un-  
 841 certainty, since the efficiencies of the  $m_T$  cuts are at least 95% across the search region  
 842 (Figures 46-48).

843 A summary of all uncertainties applied to the background reduction from the track vetoes is  
 844 provided in Table 14.

#### 845 Lepton track isolation

846 To discuss the measurement of leptonic track isolation efficiency, it is useful to define the two  
 847 types of lost-lepton events that are affected by the leptonic track veto:

- 848 1. Events in which the leptons have  $5 < p_T < 10 \text{ GeV}$ —these are only affected by the track  
 849 veto.
- 850 2. Events in which the leptons have  $p_T > 10 \text{ GeV}$  but fail either the  $I_{\text{mini}}$  cut or the ID in the  
 851 standard lepton vetoes.

852 The isolation efficiency of leptons from the second type of event is difficult to measure because  
 853 the isolated track veto is applied on top of the standard lepton veto. Many of these tracks corre-

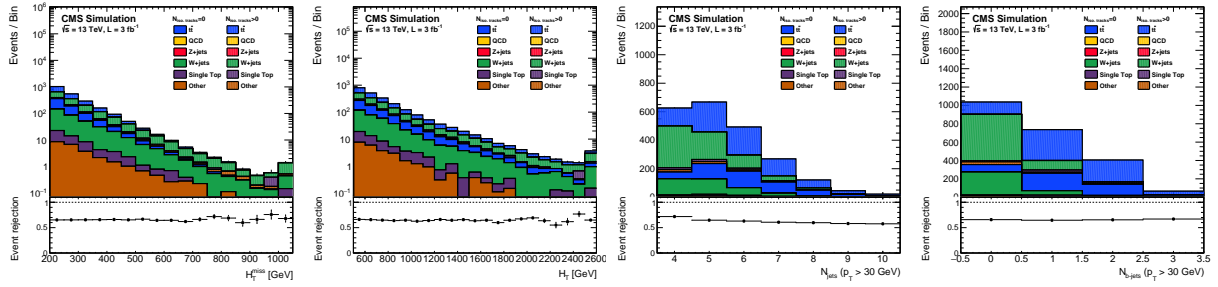


Figure 45: Performance of the isolated track veto as a function of the search variables in simulated hadronic events. The shaded portion of the histograms represents the hadronic tau events rejected by the track veto. The solid portion of the histograms represents the remaining hadronic tau background.

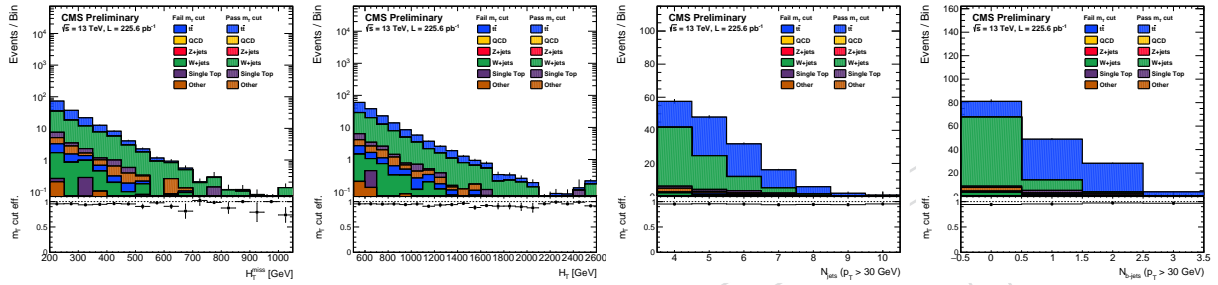


Figure 46: Efficiency of the muon track  $m_T$  cut as a function of the search variables in simulated lost-muon events. The shaded portion of the histograms represents the events in which an isolated track passes the  $m_T$  cut. The solid portion of the histograms represents the events in which an isolated track fails the  $m_T$  cut.

spond to leptons that failed the  $I_{\text{mini}}$  cut, so their isolation efficiency is biased to low values. To accurately measure the efficiency of these tracks via tag-and-probe, one must require that the probe lepton fail the standard lepton isolation or ID. This requirement depletes the statistics of the track sample.

The tag lepton is required to be well-isolated and have  $p_T > 20 \text{ GeV}$ . This measurement is performed using a single-lepton-triggered dataset. The triggers used are:

- HLT\_IsoMu20\_v\* for muon events,
- HLT\_Ele22\_eta2p1\_WP75\_Gsf\_v\* for electron events.

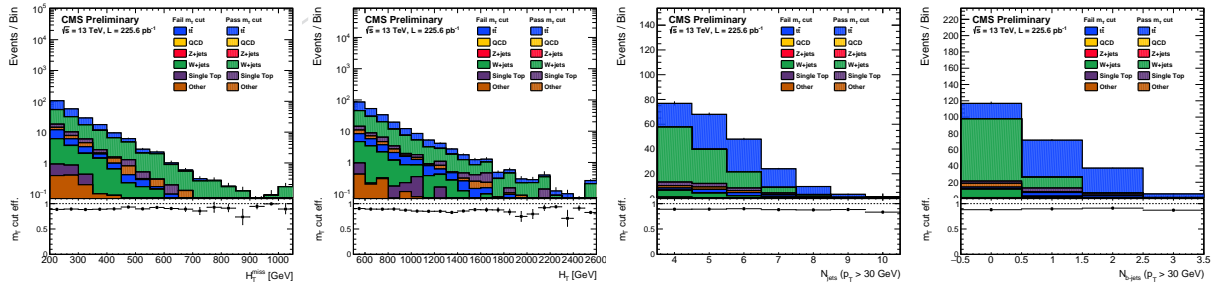


Figure 47: Efficiency of the electron track  $m_T$  cut as a function of the search variables in simulated lost-electron events. The shaded portion of the histograms represents the events in which an isolated track passes the  $m_T$  cut. The solid portion of the histograms represents the events in which an isolated track fails the  $m_T$  cut.

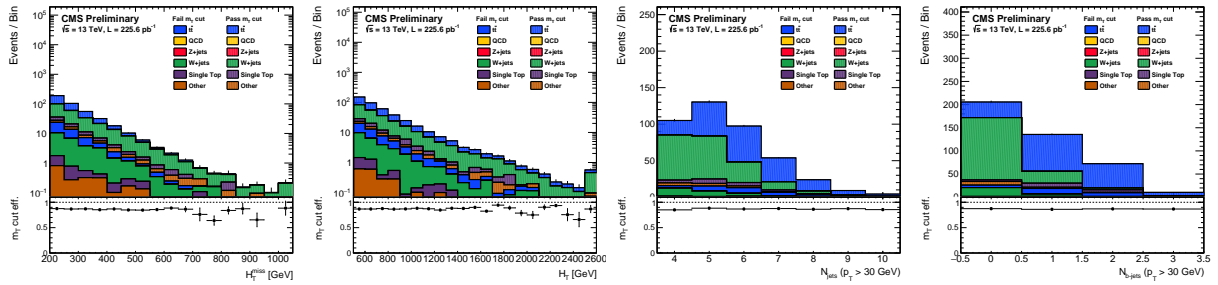


Figure 48: Efficiency of the hadronic track  $m_T$  cut as a function of the search variables in simulated hadronic-tau events. The shaded portion of the histograms represents the events in which an isolated track passes the  $m_T$  cut. The solid portion of the histograms represents the events in which an isolated track fails the  $m_T$  cut.

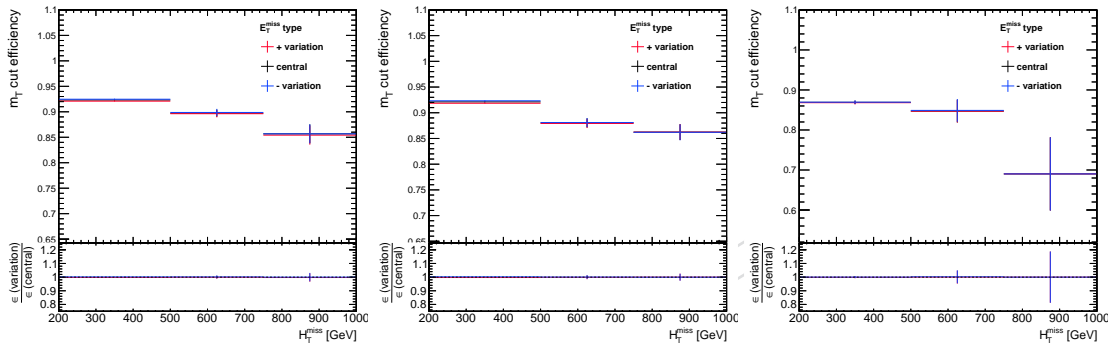


Figure 49: From left-to-right, change in efficiency of the muon, electron, and hadronic track  $m_T$  cuts from varying jet energies within their uncertainties, plotted as a function of  $H_T^{\text{miss}}$ .

862 A matching is required between the tag lepton and the HLT lepton.

863 The isolation efficiencies are parametrized in the  $p_T$  of the leptons and the charged track activity  
864 surrounding them. This activity variable is analogous to the one used to parametrize the veto  
865 lepton isolation efficiencies. The results of the tag-and-probe efficiency measurement in data  
866 and MC for leptonic tracks of both categories, as well as the ratio of the efficiencies measured  
867 in data to the efficiencies measured in MC are shown in Figures 50-51.

To translate the track-by-track isolation efficiency uncertainties reported in Figures 50-51 to search-bin-by-search-bin uncertainties on the overall reduction of the lost lepton background due to the track veto, we multiply the fraction of isolated tracks (passing isolation cut) in each  $p_T$ -activity bin by the maximum of the deviation from one of the data/MC efficiency ratio and the statistical uncertainty on that ratio in that same  $p_T$ -activity bin and sum this product over all  $p_T$ -activity bins. This procedure is performed for each of the 72 search bins:

$$\delta_{\text{search bin}}^{\text{Pred.}}(\text{Iso}) = \sum_{i=p_T-\text{bin}, j=\text{act.-bin}} f_{ij} \cdot \delta_{ij}^{\epsilon(\text{iso.})} \quad (21)$$

868 where  $\delta_{ij}^{\epsilon(\text{iso.})}$  is the maximum of the deviation from one of the data/MC efficiency ratio and the  
869 statistical uncertainty on that ratio in each  $p_T$ -activity bin. These data/MC efficiency ratios are  
870 shown in Figures 50-51. The fraction of passing tracks in bins of  $p_T$  and activity, represented by  
871  $f_{ij}$  above, is shown in Figure 52, here averaged over all 72 search bins.

872 The uncertainty on the track veto from the modeling of the track isolation efficiency in MC,  
873  $\delta_{\text{search bin}}^{\text{Pred.}}(\text{Iso})$  is added in quadrature with the flat uncertainties of the  $m_T$  and reconstruction

efficiencies to give an overall systematic on the background reduction due to each leptonic track veto. This seems to be relatively flat across search bins, as shown in Figure 58, thus we have chosen flat uncertainties of 8% and 15% on the overall muon and electron track veto systematics, respectively.

### Hadronic track isolation

We cannot validate the isolation efficiency directly for hadronic tracks; instead we must extrapolate the validation of the muon track efficiencies to the hadronic tracks. We justify the assumption that the track isolation efficiencies for muon tracks are an appropriate proxy for the track isolation efficiencies for hadronic tracks by arguing:

1. Most of the taus in the events rejected by the hadronic track veto undergo one-prong decays.
2. Since the isolation is computed by summing over neighboring charged tracks, and no neutral candidates, the isolation distributions for muon tracks should be similar to those for pions from single-prong tau decays.

The first argument is easily justified in Figure 57, which shows that the fraction of tau events vetoed that have a single-prong tau is 97% or higher across all search variables.

The second is justified by comparing the muon and pion (from one-prong tau decays) track isolation efficiencies in simulated background events, shown in Figure 55. The pion track isolation efficiencies are lower than the muon track efficiencies by less than 15%. This difference appears to be due to neutral pions from tau decays that decay into photons, which subsequently decay to electrons, whose tracks are included in the isolation sum. A comparison of the efficiencies for pion tracks from taus with and without neutral decay products is shown in Figure 56.

A conservative uncertainty of one half of the difference between the muon and pion track efficiencies shown in Figure 55 is added in quadrature with the tag-and-probe isolation efficiency defined in equation 21.

Note that the sample of muon tracks used to validate the track efficiency in data is larger in this case, as there is no equivalent hadronic tau veto applied in addition to the hadronic track veto, and thus no need to require the probe muons to fail the  $I_{\text{mini}}$  cut. The tag-and-probe efficiencies and scale factors measured for this “pre-veto” set of leptons are presented in Figures 53-54.

This uncertainty from the tag-and-probe isolation extrapolation is only applied to the 97% of MC hadronic track events that have a single-prong tau. For the few multi-prong tau events expected to be rejected by the track veto, we apply a conservative 100% uncertainty on the isolation efficiency. As in the case of the leptonic vetoes, we add these isolation efficiency uncertainties in quadrature with the reconstruction and  $m_T$  efficiency uncertainties to obtain an overall systematic on the hadronic tau background rejected by the hadronic track veto. This overall uncertainty is also shown in Figure 58. This relatively flat 5% uncertainty appears to be slightly lower than that of the leptonic track vetoes, which is due to the increase in tag-and-probe statistics we gain from using the full (pre-lepton-veto) collection of muon tracks in the tag-and-probe measurement.

Table 14: Summary of the uncertainties added in quadrature to obtain an overall uncertainty on the background reduction from the track vetoes, with approximate values.

Source	$\mu$ tracks	$e$ tracks	hadronic tracks
Isolation (tag-and-probe)	8%	15%	2%
$\mu - \pi$ extrapolation	-	-	0.2%
Multi-prong tau events	-	-	3%
Reconstruction	1%	1%	3.9%
$m_T$ cut	0.2%	0.2%	0.1%

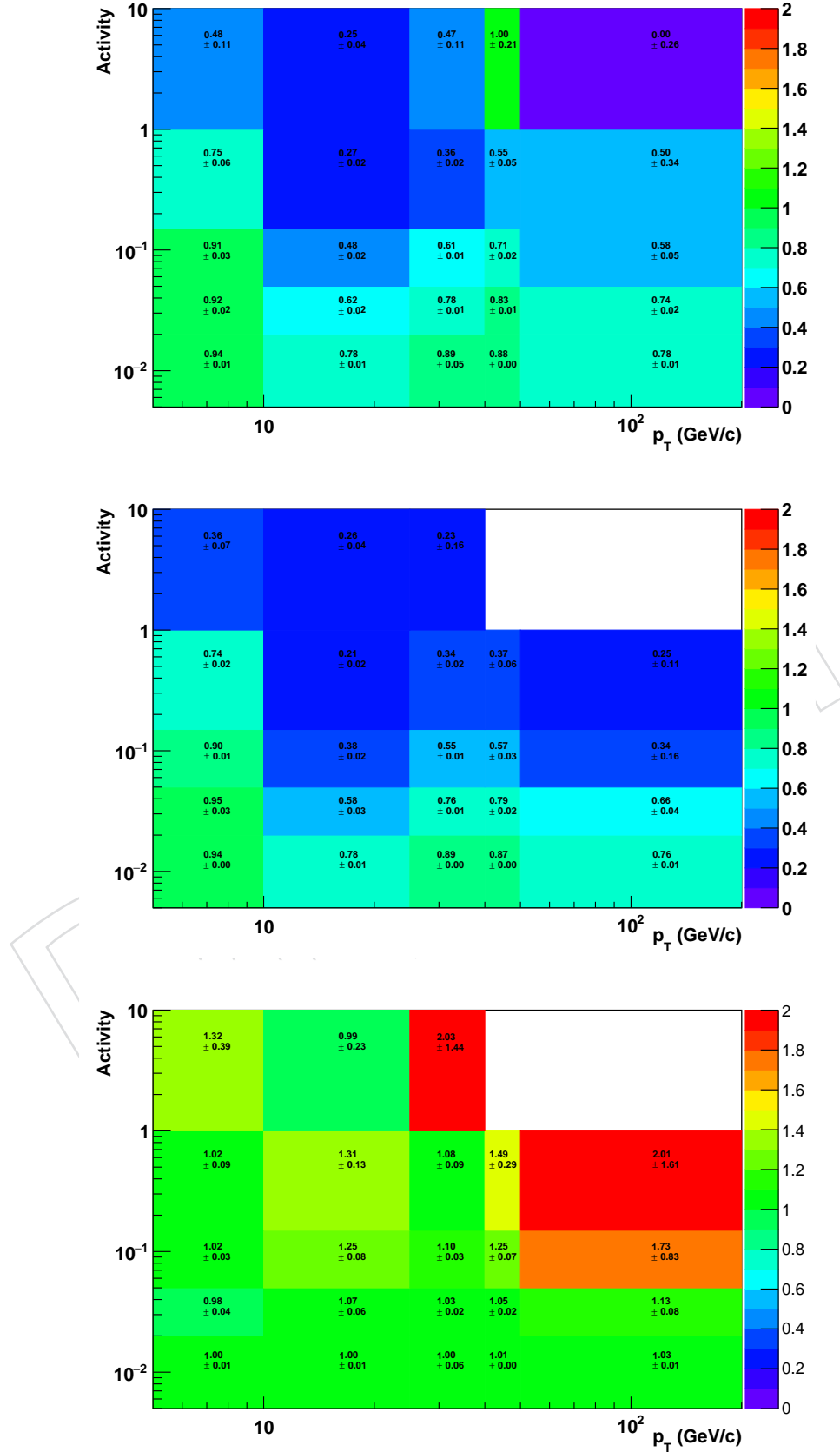


Figure 50: Tag-and-probe track isolation efficiencies for muons that fail the standard lepton veto. Top: efficiency in data; middle: efficiency in MC; bottom: ratio of efficiency in data over efficiency in MC.

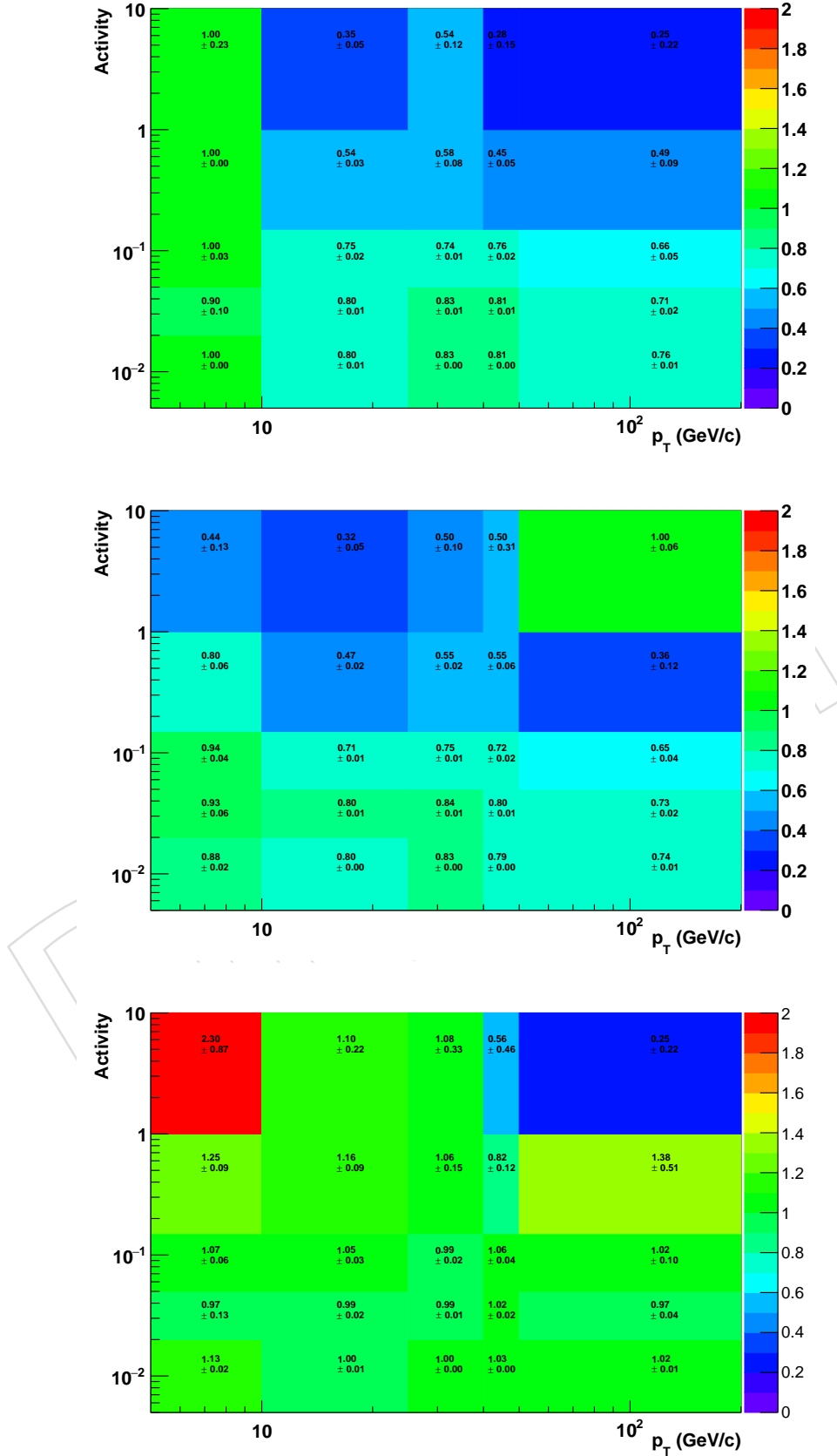


Figure 51: Tag-and-probe track isolation efficiencies for electrons that fail the standard lepton veto. Top: efficiency in data; middle: efficiency in MC; bottom: ratio of efficiency in data over efficiency in MC.

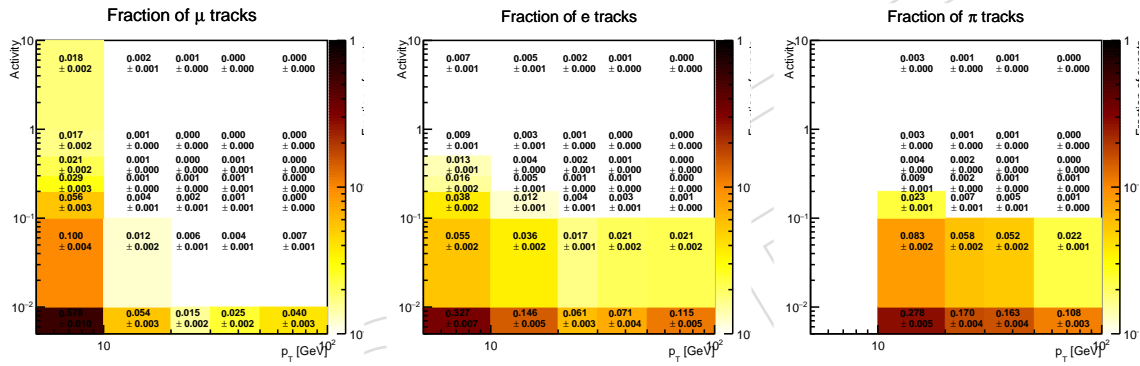


Figure 52: Fraction of passing muon (left), electron (middle) and hadronic (right) tracks in each bin of  $p_T$  and activity. The z-axis is the fraction of isolated tracks in each bin, not the isolation efficiency. These distributions are plotted after applying the lepton veto, hence the low population of the higher-lepton- $p_T$  bins.

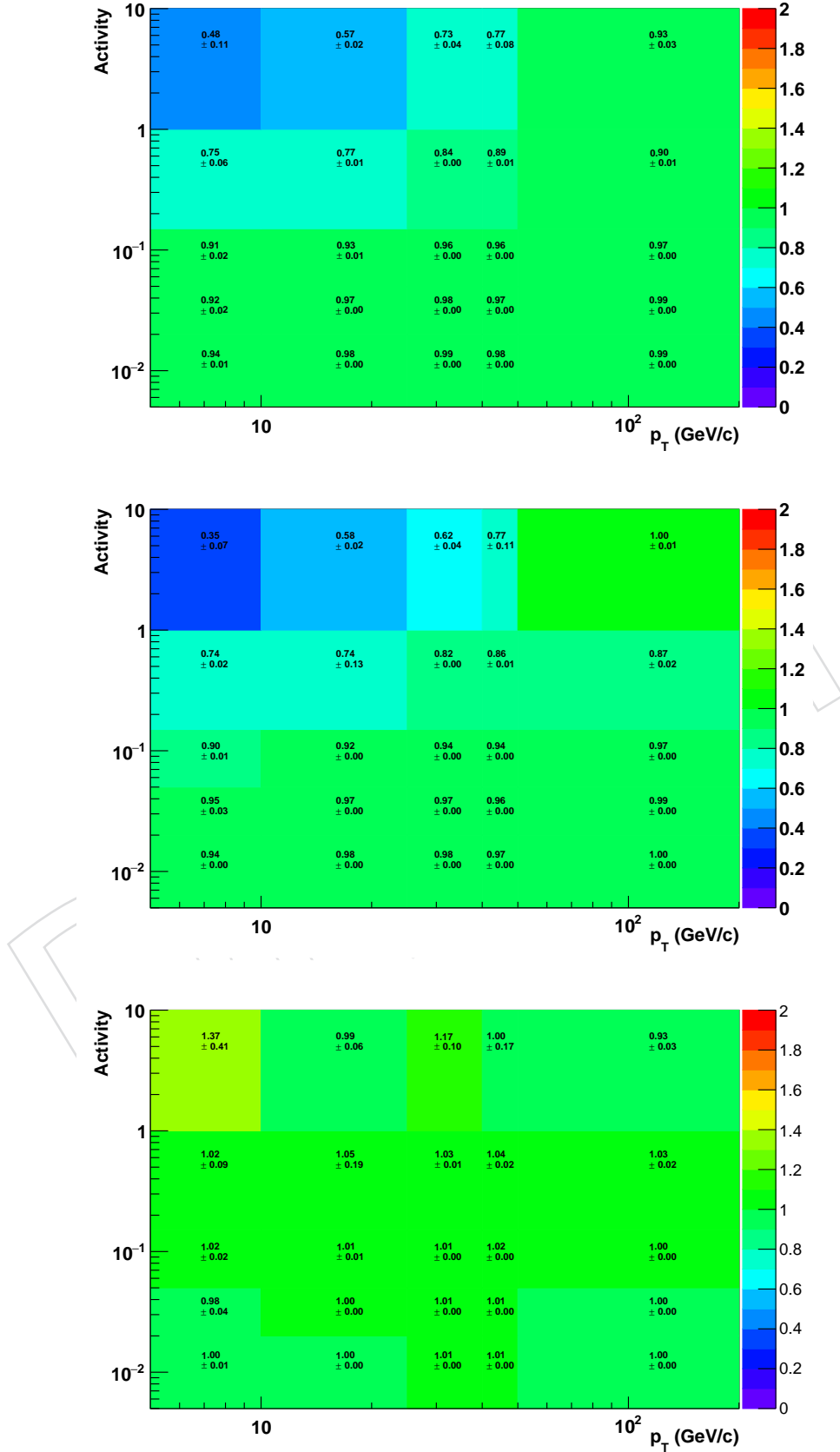


Figure 53: Tag-and-probe track isolation efficiencies for all muons. No cuts on  $I_{\text{mini}}$  nor any POG lepton ID are applied to this sample. Top: efficiency in data; middle: efficiency in MC; bottom: ratio of efficiency in data over efficiency in MC. These scale factors are used to derive an uncertainty on the track isolation efficiency for hadronic tracks from one-prong tau decays.

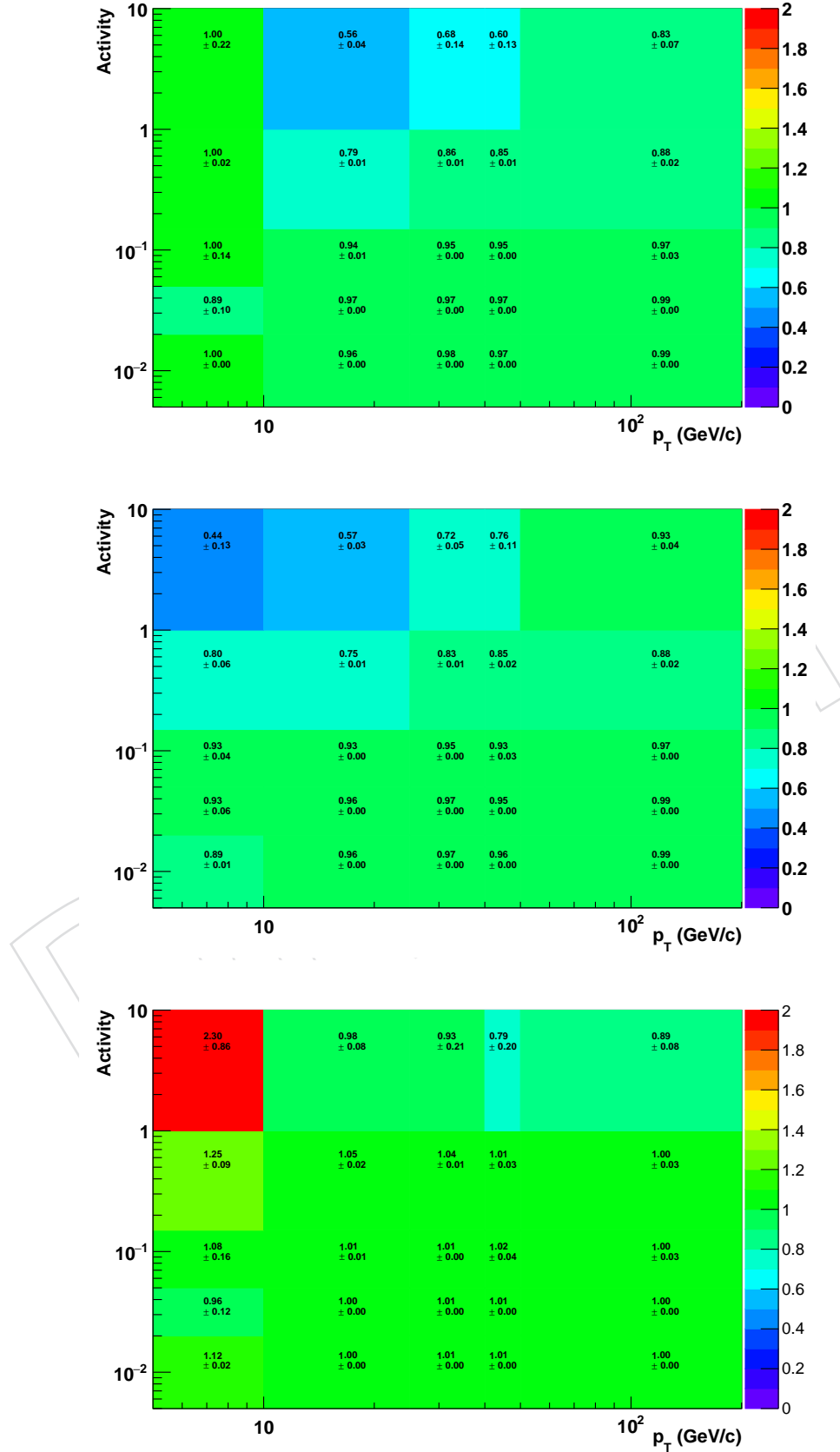


Figure 54: Tag-and-probe track isolation efficiencies for all electrons. No cuts on  $I_{\text{mini}}$  or any POG lepton ID are applied to this sample. Top: efficiency in data; middle: efficiency in MC; bottom: ratio of efficiency in data over efficiency in MC.

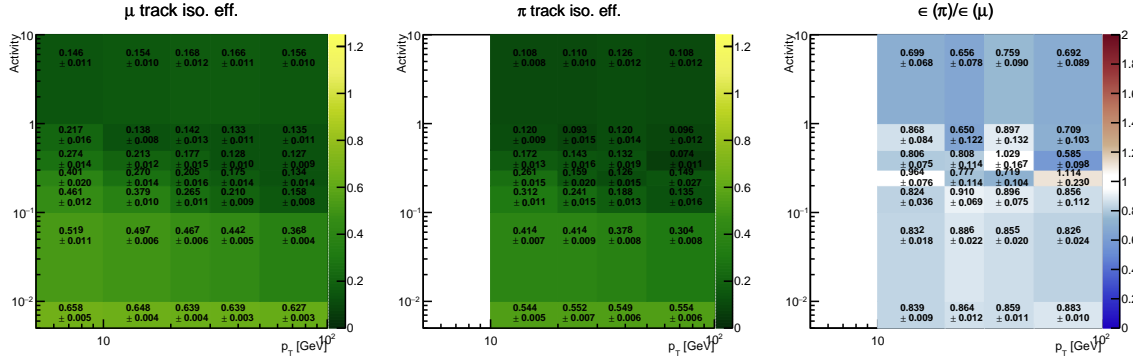


Figure 55: Left: muon track isolation efficiency; Middle: pion (from one prong tau decay) track isolation efficiency; Right: ratio of muon track efficiency to pion track efficiency—all plotted in bins of  $p_T$  and activity.

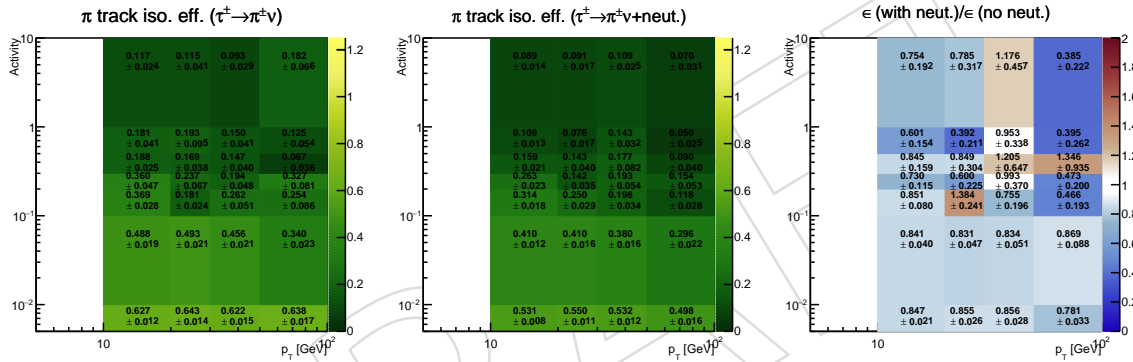


Figure 56: Left: pion (from one prong tau decay without neutral products) track isolation efficiency; Middle: pion (from one prong tau decay with neutral products) track isolation efficiency; Right: ratio of efficiency from decays without neutrals to efficiency from decays with neutrals—all plotted in bins of  $p_T$  and activity.

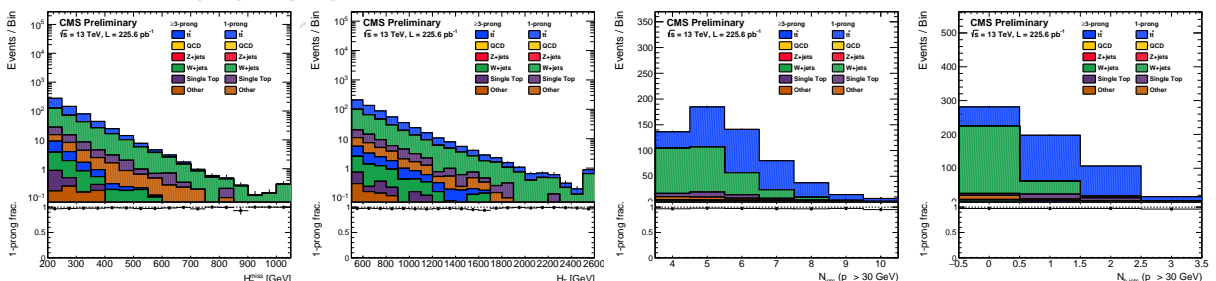


Figure 57: Fraction of hadronic tau events rejected by the hadronic track veto that have a one-prong decay, plotted as a function of the search variables. The shaded portion of the histograms includes the rejected events with one-prong decays (97% or more). The solid portion of the histograms includes the rejected events with multi-prong decays.

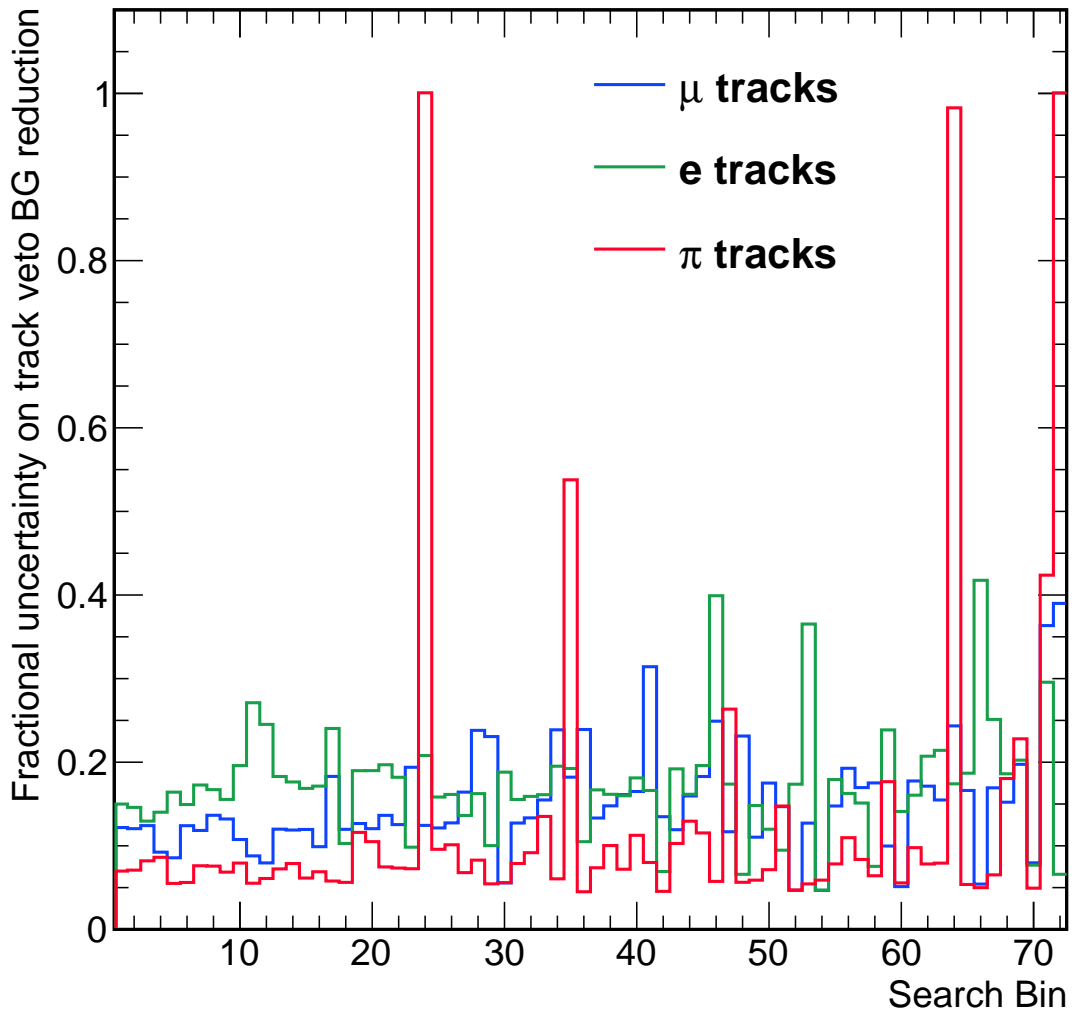


Figure 58: Fractional uncertainty on the background reduction due to each isolated track veto, defined by by Equation 21 in each search bin. These uncertainties are dominated by our somewhat-conservative estimation of the track isolation efficiency uncertainties. For the background estimations, we apply uncertainties of 8%, 15%, and 5%, respectively, on the background reduction from the muon, electron, and hadronic track vetoes, respectively.

## 913 7 Estimation of QCD multijet background

914 The QCD background is estimated using a low- $\Delta\phi_{\min}$  control sample as in [1, 22], which is  
 915 described below. Progress toward an alternative method based on the rebalance-and-smear  
 916 technique as in [2, 12] is shown in App. L, though it is not used currently in this search.

### 917 7.1 QCD background from low $\Delta\phi_{\min}$ control sample

918 **Introduction:** The  $H_T^{\text{miss}}$  in QCD multijet events is almost always due to a single mismeasured  
 919 jet in the event, thus the  $H_T^{\text{miss}}$  direction is usually close to a jet. The  $\Delta\phi_{\min}$  variable is the  
 920 minimum  $\phi$  difference between  $H_T^{\text{miss}}$  and one of the four highest  $p_T$  jets.

The low  $\Delta\phi_{\min}$  region is significantly enriched in QCD events. The sample of events with the  $\Delta\phi_{\min}$  requirement inverted (i.e.  $\Delta\phi_1 < 0.5$  or  $\Delta\phi_2 < 0.5$  or  $\Delta\phi_3 < 0.3$  or  $\Delta\phi_4 < 0.3$ ) serves as the QCD control sample. Figure 59 shows  $\Delta\phi_{\min}$  distributions for zero-lepton events passing the baseline selection in bins of  $H_T$ ,  $H_T^{\text{miss}}$ , and  $N_{\text{jet}}$ . The background at high  $\Delta\phi_{\min}$ , is estimated from the QCD yield at low  $\Delta\phi_{\min}$  and a high/low ratio  $R^{QCD}$  for the QCD component. The  $\Delta\phi_{\min}$  distributions in Fig. 59 show that the high/low ratio has some dependence on the search variables  $H_T$ ,  $H_T^{\text{miss}}$ , and  $N_{\text{jet}}$ . We model this dependence by assuming that it factorizes. That is, we assume the  $H_T$  dependence does not depend on  $H_T^{\text{miss}}$  or  $N_{\text{jet}}$  and similarly for  $H_T^{\text{miss}}$  and  $N_{\text{jet}}$ . To be explicit, we use

$$R_{i,j,k}^{QCD} = K_{HT,i}^{QCD} \cdot S_{MHT,j}^{QCD} \cdot S_{njet,k}^{QCD} \quad (22)$$

921 where  $i, j, k$  are the  $H_T$ ,  $H_T^{\text{miss}}$ , and  $N_{\text{jet}}$  bin indices. The  $K_{HT,i}^{QCD}$  parameter is the high/low ratio  
 922 for HT bin  $i$  in the first  $H_T^{\text{miss}}$  and  $N_{\text{jet}}$  bins. The  $S_{MHT,j}^{QCD}$  is a correction for  $H_T^{\text{miss}}$  bin  $j$  with respect  
 923 to the first  $H_T^{\text{miss}}$  bin. The  $S_{njet,k}^{QCD}$  is a correction for  $N_{\text{jet}}$  bin  $k$  with respect to the first  $N_{\text{jet}}$  bin.

924 We have found that the  $N_{\text{jet}}$  dependence of the high/low ratio is significant within the  $N_{\text{jet}}$  4  
 925 to 6 range, which defines the first search  $N_{\text{jet}}$  bin. If this dependence is accounted for, there  
 926 is no further dependence of the high/low ratio on  $N_{\text{b-jet}}$  within a given  $N_{\text{jet}}$  value. If we do  
 927 not subdivide the first search  $N_{\text{jet}}$  bin into separate  $N_{\text{jet}}=4$ ,  $N_{\text{jet}}=5$ , and  $N_{\text{jet}}=6$  bins, we would  
 928 have some  $N_{\text{b-jet}}$  dependence within the first search  $N_{\text{jet}}$  bin. For these reasons, we subdivide  
 929 the first search  $N_{\text{jet}}$  bin into three separate bins for the  $\Delta\phi_{\min}$  QCD BG model. We also choose  
 930 to subdivide the first search  $H_T^{\text{miss}}$  bin into two bins, [200, 300] and [300, 500], for the  $\Delta\phi_{\min}$   
 931 QCD BG model, which provides a more gradual progression in the  $H_T^{\text{miss}}$  dependence of the  
 932 high/low ratio. This also enhances the QCD fraction in the first  $H_T^{\text{miss}}$  bin, which is background  
 933 dominated for all relevant signal models. The binning used in the  $\Delta\phi_{\min}$  QCD BG model is  
 934 summarized in Table 15 and illustrated in Fig. 34.

Table 15: Binning in  $H_T$ ,  $H_T^{\text{miss}}$ , and  $N_{\text{jet}}$  used in the  $\Delta\phi_{\min}$  QCD BG model. This is illustrated in Figure 34. The data are not binned in  $N_{\text{b-jet}}$  for the  $\Delta\phi_{\min}$  QCD BG model.

	$H_T$	$H_T^{\text{miss}}$	$N_{\text{jet}}$
bin 1	[500, 800]	[200, 300]	=4
bin 2	[800, 1200]	[300, 500]	=5
bin 3	$\geq 1200$	[500, 750]	=6
bin 4	-	$\geq 750$	[7,8]
bin 5	-	-	$\geq 9$

935 **Model validation:** We test the model assumption of the factorization of the high/low ratio  $H_T$ ,  
 936  $H_T^{\text{miss}}$ , and  $N_{\text{jet}}$  dependence by directly fitting QCD Monte Carlo  $R_{i,j,k}^{QCD}$  values for the  $K^{QCD}$  and

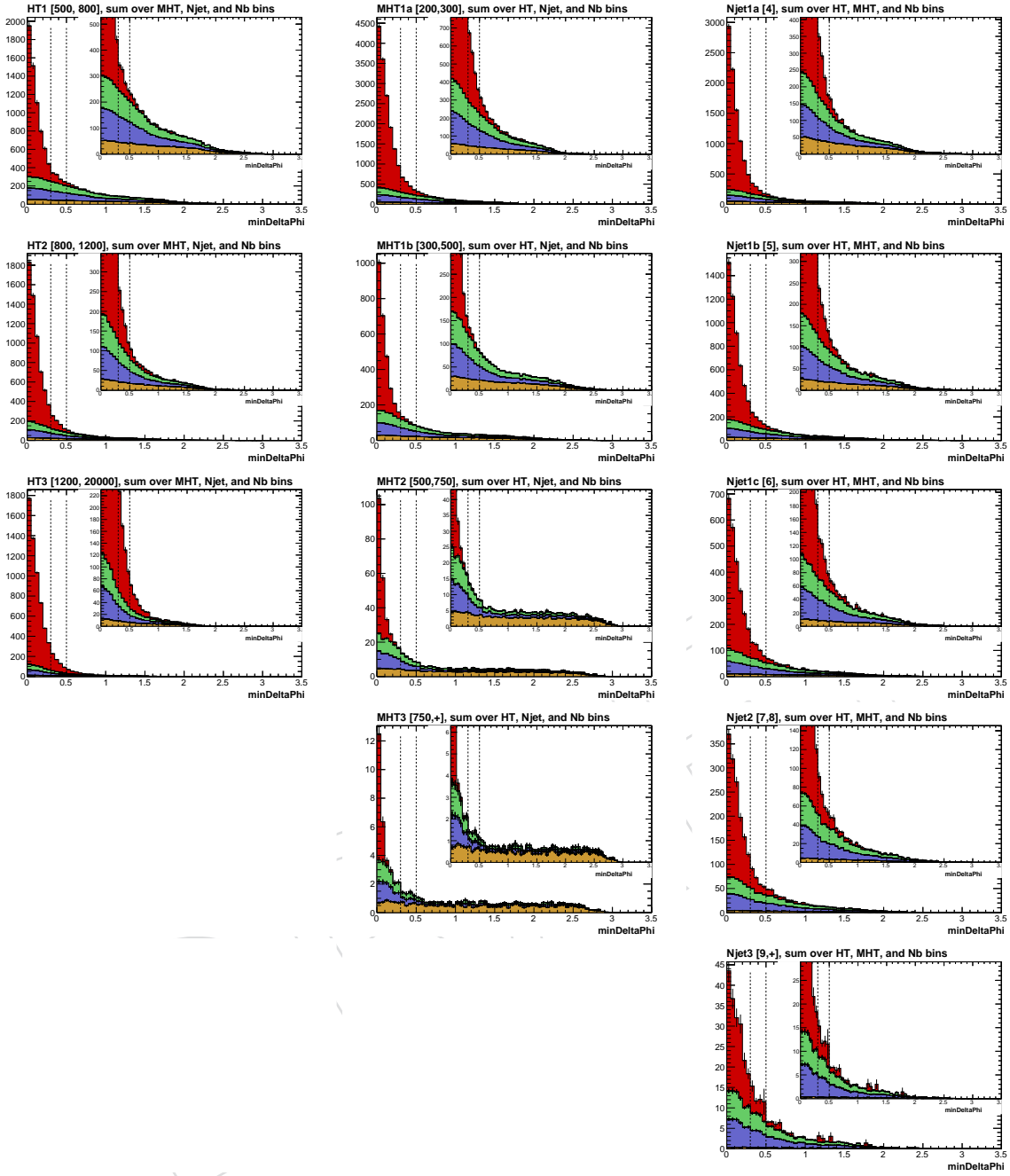


Figure 59: Distributions of  $\Delta\phi_{\min}$  in bins of one of the search variables, integrated over the other search variables. The columns are: 1 the three  $H_T$  bins; 2 the four  $H_T^{\text{miss}}$  bins used in the  $\Delta\phi_{\min}$  QCD BG analysis; and 3 the five  $N_{\text{jet}}$  bins used in the  $\Delta\phi_{\min}$  QCD BG analysis. The four background components are QCD (red), hadronic tau (green), lost-lepton (blue), and invisible Z (gold). The distributions are normalized to  $2.3 \text{ fb}^{-1}$ .

937  $S^{QCD}$  parameters and seeing if the model is able to describe all  $R_{i,j,k}^{QCD}$  values simultaneously.  
 938 The results of this test are shown in Fig. 60 and given in Table 16. Several of the bins in Fig. 60  
 939 have no black point, meaning that there weren't enough QCD MC events in that bin to define  
 940  $R^{QCD}$ . The agreement between the points and the fit is reasonable, validating the factorization  
 941 assumption, to the extent that we can with the given MC statistics. The relatively large statis-  
 942 tical errors from the  $\chi^2$  fit on the high  $H_T$  and high  $H_T^{\text{miss}}$  parameters show that our ability to

predict the high/low ratio at high  $H_T^{\text{miss}}$  and high  $N_{\text{jet}}$  is limited. However, we are able to tolerate a relatively high uncertainty on the high/low ratio without losing SUSY sensitivity, since the QCD BG is small and not the dominant BG in the most sensitive search bins.

To test for  $N_{\text{b-jet}}$  dependence, we split the 55 bins shown in Fig. 60 into the 4  $N_{\text{b-jet}}$  bins, for a total of 220 bins and repeated the fit including three  $S_{nb,l}^{QCD}$  parameters, which allow for corrections for the top 3  $N_{\text{b-jet}}$  bins relative to the first  $N_{\text{b-jet}}$  bins, where the  $N_{\text{b-jet}}$  dependence is assumed to factorize, relative to  $H_T$ ,  $N_{\text{jet}}$ , and  $H_T^{\text{miss}}$ . The  $S_{nb,l}^{QCD}$  parameters are  $0.83 \pm 0.06$ ,  $0.91 \pm 0.11$ , and  $0.73 \pm 0.11$  for  $N_{\text{b-jet}} = 1, 2, 3+$ , respectively. Details are given in Appendix O. We include systematic uncertainties of 20%, 20%, and 30% for the  $N_{\text{b-jet}} = 1, 2, 3+$  predictions, respectively.

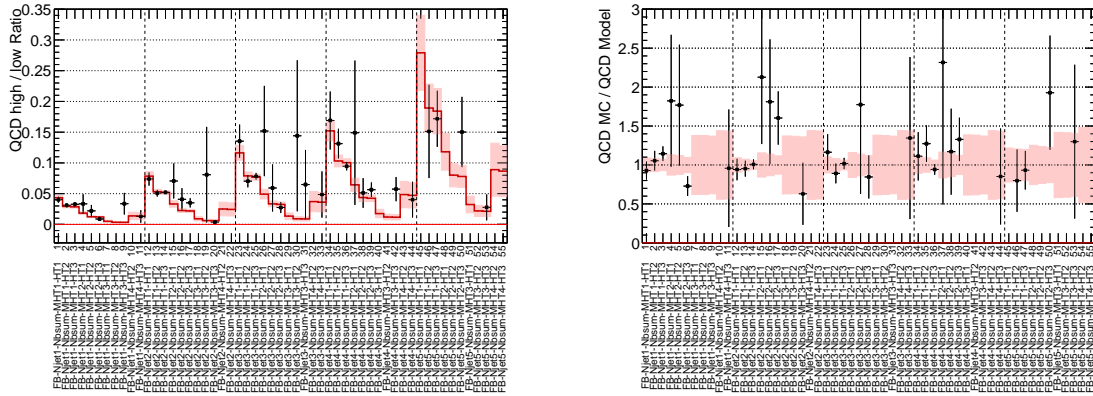


Figure 60: Left: QCD MC high/low ratio for the search  $\Delta\phi_{\text{min}}$  requirements. The red histogram with shaded errors is the  $\chi^2$  fit result, where the floating parameters in the fit were the  $K^{QCD}$  and  $S^{QCD}$  model parameters. Right: the ratio of ratios, or the QCD MC high/low ratio divided by the QCD BG model ratio. Within each plot, there are five sections of 11 bins, separated by a vertical dashed line, corresponding to the five QCD  $N_{\text{jet}}$  bins, increasing to the right. Within each  $N_{\text{jet}}$  section, the bins are grouped by  $H_T$  and  $H_T^{\text{miss}}$  both increasing to the right. The QCD sample was not split by  $N_{\text{b-jet}}$ . This fit is a test of the factorization of the  $H_T$ ,  $H_T^{\text{miss}}$ , and  $N_{\text{jet}}$  dependence of the high/low ratio, which is a key assumption of the background model.

**Determination of the QCD model parameters in data:** We perform a likelihood analysis of the data, binned as in Table 15, to determine the QCD high/low ratio model parameters, to the extent that we can. To do this, the fit includes the low- $\Delta\phi_{\text{min}}$  control sample and the high- $\Delta\phi_{\text{min}}$  sample, which corresponds to the search selection. As can be seen in Fig. 59, it is essential to have estimates of the hadronic-tau, lost-lepton, and invisible Z backgrounds in both samples in order to infer the QCD contribution. The hadronic-tau, lost-lepton, and invisible Z backgrounds are evaluated with the  $\Delta\phi_{\text{min}}$  requirement inverted using the standard techniques for those backgrounds to give the necessary input for the low- $\Delta\phi_{\text{min}}$  control sample. We currently neglect signal contamination in the data determination of the model parameters, since the events with  $H_T^{\text{miss}}$  between 200 and 300 GeV are expected to be background dominated for signal models near the current exclusion boundary. See Appendix N for details.

With the current size of the dataset, we are unable to determine the  $H_T^{\text{miss}}$  dependence of the QCD BG model from data, so we constrain these parameters to the values from the QCD MC with generous uncertainties. Appendix M describes the results of a QCD MC study, where we categorized events based on whether the worst jet in the event is or is not included in the four  $\Delta\phi$  jets. We found that the worst jet in the event is not one of the four  $\Delta\phi$  jets only 2% of the time and that this fraction does not depend on  $H_T^{\text{miss}}$ . From that study, we find  $S_{MHT,j}^{QCD}$  in Eqn. 22 to be 0.50 for  $j = 2, 3, 4$  with an uncertainties of 0.25, 0.50, and 0.50, respectively, based on varying

Table 16: Model parameters for the QCD  $\Delta\phi_{\min}$  BG evaluation. The  $\chi^2$  fit column gives the results of the direct fit of the QCD MC for the high/low ratio parameters, which is shown in Figure 60. The “MC Likelihood fit” column gives the results of the likelihood fit of a  $2.3 \text{ fb}^{-1}$  test dataset (MC) where the observed counts are set to the expected number of events from the MC, including all components (QCD, hadtau, lostlep, and znunu). The last column gives the likelihood fit results for the  $2.3 \text{ fb}^{-1}$  data sample. The likelihood fit is unable to determine the MHT2, MHT3, and MHT4 parameters so we constrain those parameters to values derived from the QCD MC as described in Appendix M. The fitted parameters are plotted in Fig 64.

QCD parameter	Bin range	$\chi^2$ Fit	MC Likelihood fit	Data Likelihood fit
$K^{QCD}, \text{HT1}$	500 to 800 GeV	$0.043 \pm 0.004$	$0.036 \pm 0.025$	$0.048 \pm 0.024$
$K^{QCD}, \text{HT2}$	800 to 1200 GeV	$0.029 \pm 0.003$	$0.031 \pm 0.007$	$0.023 \pm 0.007$
$K^{QCD}, \text{HT3}$	$>1200 \text{ GeV}$	$0.029 \pm 0.002$	$0.032 \pm 0.005$	$0.028 \pm 0.006$
$S^{QCD}, \text{MHT1}$	200 to 300 GeV	1 (fixed)	1 (fixed)	1 (fixed)
$S^{QCD}, \text{MHT2}$	300 to 500 GeV	$0.423 \pm 0.047$	not in fit	not in fit
$S^{QCD}, \text{MHT3}$	500 to 750 GeV	$0.116 \pm 0.042$	not in fit	not in fit
$S^{QCD}, \text{MHT4}$	$>750 \text{ GeV}$	$0.471 \pm 0.204$	not in fit	not in fit
$S^{QCD}, \text{Njet1}$	= 4	1 (fixed)	1 (fixed)	1 (fixed)
$S^{QCD}, \text{Njet2}$	= 5	$1.81 \pm 0.15$	$1.62 \pm 0.29$	$1.91 \pm 0.44$
$S^{QCD}, \text{Njet3}$	= 6	$2.68 \pm 0.24$	$2.36 \pm 0.48$	$2.30 \pm 0.65$
$S^{QCD}, \text{Njet4}$	7 to 8	$3.51 \pm 0.32$	$3.05 \pm 0.74$	$3.59 \pm 1.05$
$S^{QCD}, \text{Njet5}$	$\geq 9$	$6.44 \pm 1.35$	$4.89 \pm 2.30$	$3.30 \pm 1.84$

- 970 the normalization of the 2% of events where the worst jet is not in the  $\Delta\phi$  jets by 100%.
- 971 The results of fitting a test  $2.3 \text{ fb}^{-1}$  test dataset, where the observed counts were set to the MC  
972 expectations are given in Tab. 16. The likelihood fit values are consistent with the values from  
973 the direct  $\chi^2$  fit of the QCD MC. The parameter results for the fit of the  $2.3 \text{ fb}^{-1}$  data sample  
974 are given in Table 16 and shown in Fig 64. The yields of events passing the  $\Delta\phi_{\min}$  requirements  
975 (i.e. at high  $\Delta\phi_{\min}$ ) and the fit results for the  $2.3 \text{ fb}^{-1}$  data sample are shown in Fig. 61.
- 976 **QCD BG estimates in the 72 search bins:** In the final SUSY search analysis, the data are binned  
977 in the search  $N_{\text{b-jet}}$  bins in addition to the  $H_T$ ,  $H_T^{\text{miss}}$ , and  $N_{\text{jet}}$  binning for the QCD model  
978 (Tab. 15). Since the binning for the QCD model is finer than the search binning in  $H_T^{\text{miss}}$  and  
979  $N_{\text{jet}}$ , the finer bins are combined and a weighted average QCD BG ratio is used to compute the  
980 QCD BG model prediction from the control sample yield for a given search bin. The results for  
981 the MC test dataset with the observed counts set to the MC expectations are given in Fig. 62.  
982 The QCD BG model predictions are, in general, in good agreement with the QCD MC values.  
983 We see no evidence of statistically significant non-closure in Fig. 62 so we do not include a “non-  
984 closure” systematic uncertainty. The QCD BG estimates for the  $2.3 \text{ fb}^{-1}$  data sample, derived  
985 from these parameters and the low  $\Delta\phi_{\min}$  control sample are shown in Fig 63, compared to the  
986 QCD MC. The data-driven predictions are lower than the QCD MC. However, the QCD MC  
987 has not been corrected for the trigger efficiency in this plot. A full table of results is given in  
988 Appendix P.
- 989 **Discussion of uncertainties:** In the lowest search  $H_T^{\text{miss}}$  bin, the uncertainty on the data-determined  
990  $H_T$  and  $N_{\text{jet}}$  QCD model parameters give the dominant contribution. These QCD model pa-  
991 rameter uncertainties are largely from the non-QCD background uncertainty at high  $\Delta\phi$  in the  
992 data in the binned likelihood fit for the QCD model parameters. In the higher  $H_T^{\text{miss}}$  bins (for  
993  $H_T^{\text{miss}} > 500$ ), the uncertainty on the  $H_T^{\text{miss}}$  parameters, which is 100%, is a significant contribu-  
994 tion. In the highest search bins, where the low  $\Delta\phi$  control sample statistics is low, the statistical

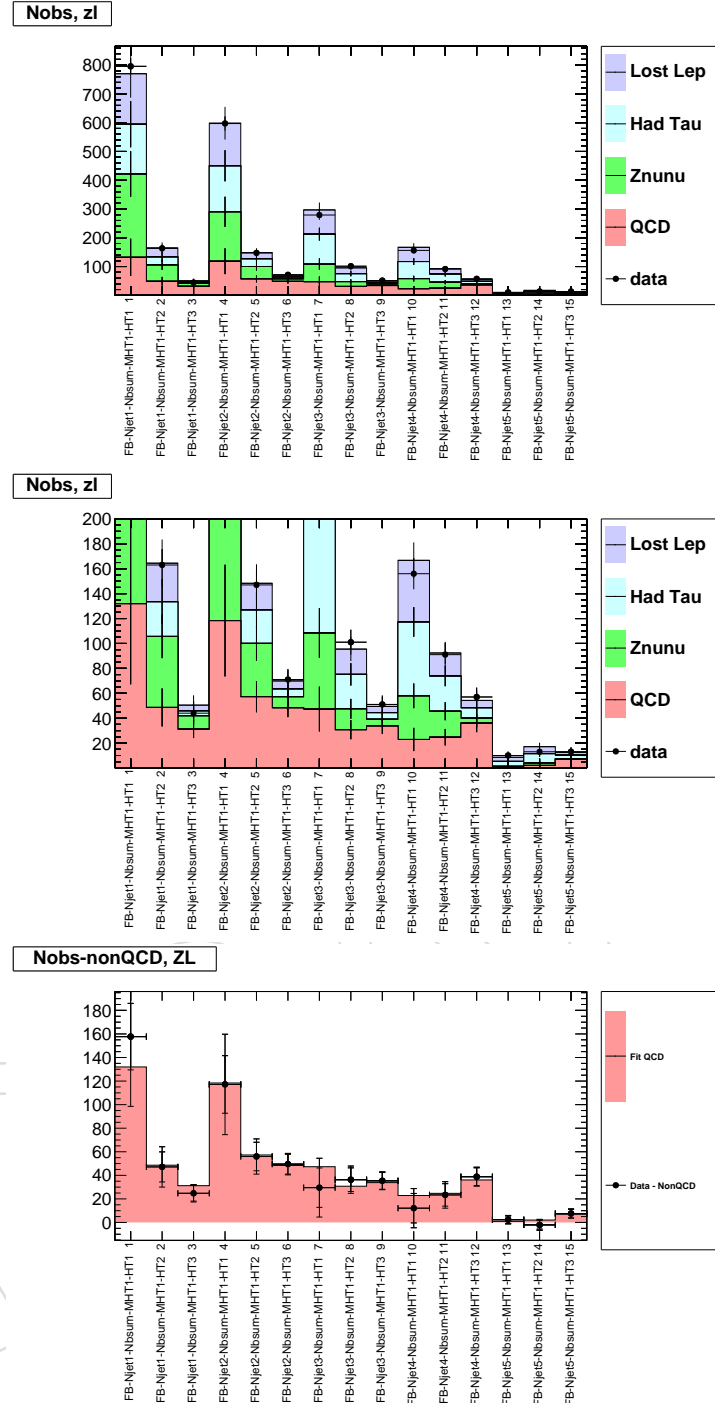


Figure 61: Yields of events passing the  $\Delta\phi_{\min}$  requirements (i.e. at high  $\Delta\phi_{\min}$ ) for the QCD bins used in the likelihood fit for the QCD background  $H_T$  and  $N_{\text{jet}}$  model parameters in the  $2.3 \text{ fb}^{-1}$  dataset. The top and middle plots show the fit results compared to the observed counts. The bottom plot shows the fit result for only the QCD component, where the points are the observed counts minus the non-QCD components. The error bars on the points in the bottom plot are  $\sqrt{N_{\text{obs}}}$  and  $\sqrt{N_{\text{obs}} + \sigma_{\text{non-QCD}}^2}$ .

995 uncertainty from the control sample becomes an important contribution.

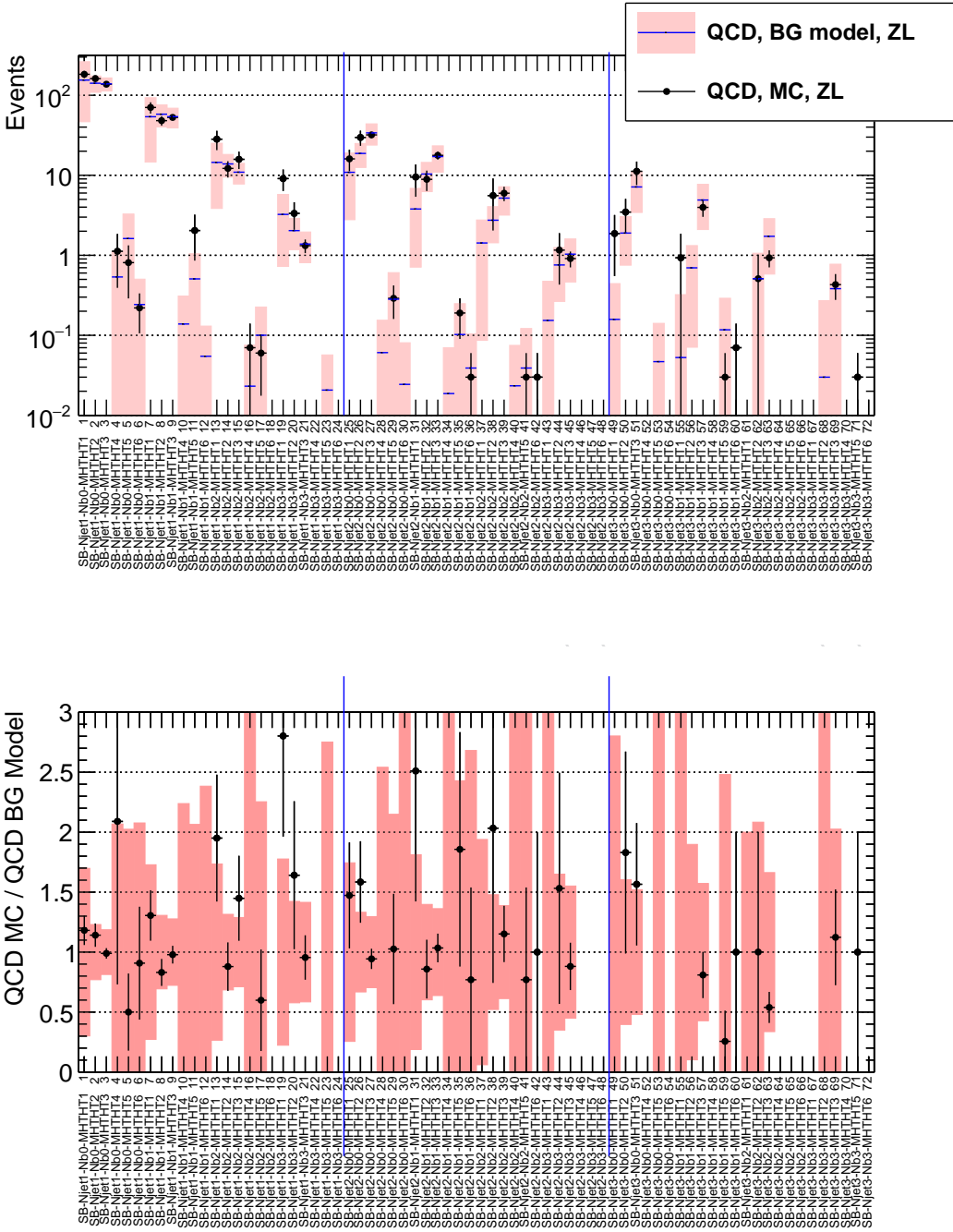


Figure 62: Comparison of the QCD background from MC (points with error bars) with the results of the  $\Delta\phi_{\min}$  QCD background analysis (solid pink histogram with solid red errors) performed on the MC test dataset in the 72 zero-lepton search bins of the analysis. The bottom plot shows the ratio of the QCD MC divided by the QCD BG model prediction (points). The shaded region in the bottom plot shows the QCD BG model uncertainty divided by the QCD BG model prediction. The plot is normalized to  $2.3 \text{ fb}^{-1}$ .

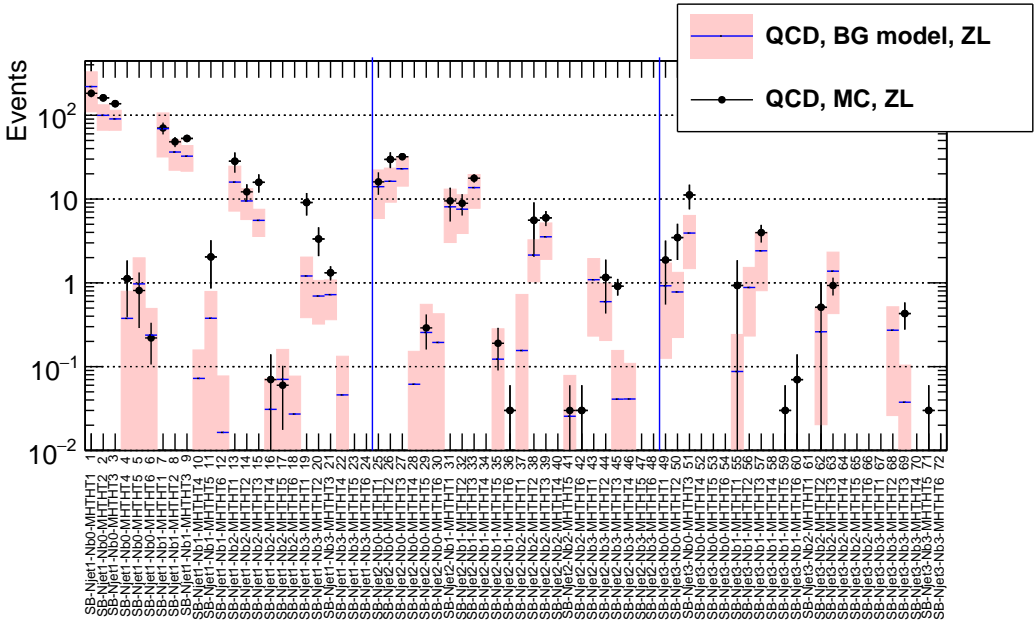


Figure 63: Comparison of results of the  $\Delta\phi_{\min}$  QCD background analysis (solid pink histogram with solid red errors) from analyzing the  $2.3 \text{ fb}^{-1}$  data sample and the QCD background from MC (points with error bars) in the 72 zero-lepton search bins of the analysis. Note that the QCD MC has not been corrected for trigger efficiency.

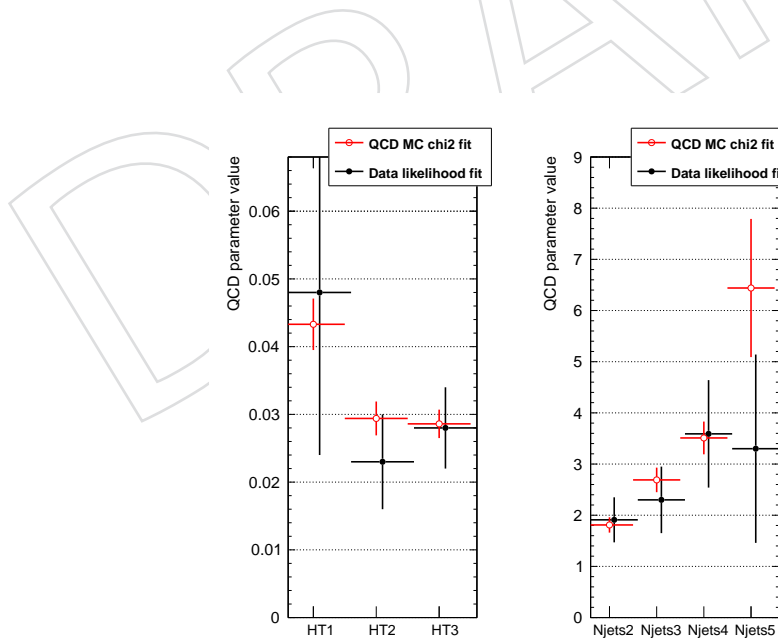


Figure 64: QCD background model parameters from the likelihood analysis of the  $2.3 \text{ fb}^{-1}$  data sample (solid black points) compared with the direct  $\chi^2$  fit of the QCD MC (open red points). The numerical values are given in Table 16.

## 996 8 Estimation of $Z \rightarrow \nu\bar{\nu}$ background

997 Events that produce a  $Z$  boson in association with jets represent an irreducible background for  
 998 our search when the  $Z$  decays to two neutrinos. The most straightforward way to measure this  
 999 background is to exploit the decays  $Z \rightarrow \ell^+\ell^-$  in which the  $Z$  boson can be reconstructed from  
 1000 the observed pair of muons or electrons. The efficiency-corrected yields from these decays can  
 1001 be translated directly into the  $Z \rightarrow \nu\bar{\nu}$  background yield by the known branching ratios. The  
 1002 limitation of this approach arises from the rather small branching ratio between the charged  
 1003 and neutral leptons, so that the transfer factor from the control sample measurement to the  
 1004 predicted background is a number larger than one (ignoring efficiencies, the branching ratio  
 1005 itself is approximately 3 when both muon and electron pairs are used).

1006 The alternative approach is to exploit the similarity to  $Z$  boson radiation of the more copious  
 1007 radiation of photons. Here the challenge is to obtain validation in data of the MC predictions  
 1008 connecting the two processes.

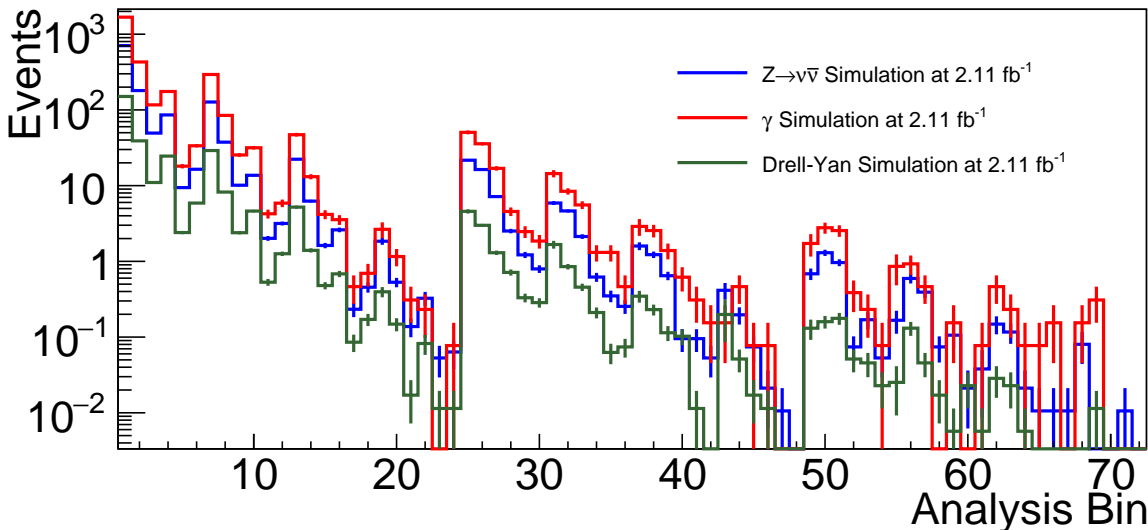


Figure 65: Yields expected at  $1.28 \text{ fb}^{-1}$  from  $Z \rightarrow \nu\bar{\nu}$  MC (blue histogram),  $\gamma + \text{jets}$  MC (red histogram), and  $Z \rightarrow \ell^+\ell^-$  MC (green histogram) in the 72 search bins. Yields are obtained using the full Spring15 MC.

1009 For insight into the quantitative problem we present in Fig. 65 the distributions among our  
 1010 search bins of the expected background from  $Z \rightarrow \nu\bar{\nu}$  together with those of the samples avail-  
 1011 able for determining it. From these we infer the following:

- 1012 • For  $N_{\text{jet}} \geq 9$  we expect at most two or so  $Z \rightarrow \nu\bar{\nu}$  events in any single bin, and in  
 1013 most bins fewer than one, at  $1.28 \text{ fb}^{-1}$ .
- 1014 • For the highest  $N_{\text{jet}}$  and  $N_{\text{b-jet}}$  bins even the MC estimates have marginal statistics.
- 1015 • The transfer factor will have a value for the  $\gamma + \text{jets}$  sample of approximately 0.6 and  
 1016 for  $Z \rightarrow \ell^+\ell^-$  about 4.

1017 The  $Z \rightarrow \ell^+\ell^-$  sample will suffer from small statistics, having one or fewer events in all of  
 1018 the highest ( $N_{\text{jet}}, N_{\text{b-jet}}$ ) bins. The  $\gamma + \text{jets}$  sample will be nearly an order of magnitude larger.  
 1019 This process differs from  $Z \rightarrow \ell^+\ell^-$  by the threshold effect caused by the  $Z$  mass, and by  
 1020 different couplings to the up-and down-type quarks; the consequences of this for systematic  
 1021 uncertainties will need to be understood, especially where the production of heavy flavor is

1022 concerned.

1023 Our baseline strategy is to use the  $\gamma + \text{jets}$  sample to determine the yields in the 18 bins corre-  
 1024 sponding to  $N_{\text{b-jet}} = 0$ . These will be compared with the  $Z \rightarrow \ell^+\ell^-$  yields in the low- $N_{\text{jet}}$  bin  
 1025 to establish the systematic uncertainty of the physics modeling of  $\gamma + \text{jets}$ , and the normaliza-  
 1026 tion corrected if necessary. The extrapolation to bins with  $N_{\text{b-jet}} > 0$  will be performed to the  
 1027 extent possible with the  $Z \rightarrow \ell^+\ell^-$  data sample, supplemented with MC information where  
 1028 necessary. Specifically, we measure the yield ratio  $R_{nb/0b} \equiv Y(N_{\text{b-jet}} = n)/Y(N_{\text{b-jet}} = 0)$  with  
 1029  $Z \rightarrow \ell^+\ell^-$  data in the well-populated lowest  $N_{\text{jet}}$  bin. We use simulation to correct the resulting  
 1030 distribution to the higher  $N_{\text{jet}}$  bins. For the systematic uncertainty of this  $N_{\text{jet}}$  extrapolation we  
 1031 use a lower bound given by taking the measured low- $N_{\text{jet}}$  distribution of  $R_{nb/0b}$  as fixed for  
 1032 all  $N_{\text{jet}}$  bins, and an upper bound from a simple model based on binomial combinatorics. The  
 1033 justification is discussed in Section 8.3 below.

1034 Some of the details specific to the  $\gamma + \text{jets}$  analysis are relegated to Appendix G, and those for  
 1035 the  $Z \rightarrow \ell^+\ell^-$  analysis to Appendix H. We are also developing each of these as stand-alone  
 1036 methods for cross checks, perhaps to be integrated as separate control samples directly via the  
 1037 COMBINE tool.

## 1038 8.1 $Z \rightarrow \nu\bar{\nu}$ measurement for $N_{\text{b-jet}} = 0$

1039 As shown in Eq. 23, we predict the number of  $Z \rightarrow \nu\nu + \text{jets}$  events contributing to each of  
 1040 the 18 0-btag analysis bins ( $N_{Z \rightarrow \nu\nu}^{\text{pred}}$ ) from the number of events in the corresponding bin of the  
 1041  $\gamma + \text{jets}$  control sample ( $N_{\gamma}^{\text{obs}}$ ), the purity of the control sample ( $\beta$ ), and the ratio of the numbers  
 1042 of  $Z \rightarrow \nu\nu + \text{jets}$  events and  $\gamma + \text{jets}$  events obtained from leading order MADGRAPH+PYTHIA  
 1043 ( $\mathcal{R}_{Z(\nu\bar{\nu})/\gamma} \cdot \mathcal{F}_{\text{dir}}$ ). Here  $\mathcal{F}_{\text{dir}}$  is the fraction of prompt photons that are direct, as explained below.

$$N_{Z \rightarrow \nu\nu}^{\text{pred}} = \mathcal{R}_{Z(\nu\bar{\nu})/\gamma} \cdot \mathcal{F}_{\text{dir}} \cdot \beta \cdot N_{\gamma}^{\text{obs}} \quad (23)$$

1044 In the rest of this section we describe each of the terms on the right-hand side of Eq. 23 and the  
 1045 systematic uncertainty related to each.

### 1046 8.1.1 $N_{\gamma}^{\text{obs}}$ and categories of photons

1047 The observed photons in the control sample come from three sources: direct prompt photons,  
 1048 fragmentation prompt photons, and non-prompt photons. Prompt photons are radiated from  
 1049 a quark; non-prompt photons come from the decay of a meson. Direct prompt photons are ra-  
 1050 diated with relatively large transverse momentum relative to the quark; fragmentation prompt  
 1051 photons are radiated with low transverse momentum relative to the quark.

1052 Direct prompt photons, which make up about 85% of the control sample, are most useful for  
 1053 predicting the  $Z \rightarrow \nu\nu$  background because their production processes most neatly map onto  
 1054 the set of  $Z$  boson production processes. Because processes producing non-prompt photons  
 1055 have no corresponding process for producing  $Z$  bosons, non-prompt photons do not contribute  
 1056 to the  $Z \rightarrow \nu\nu$  background estimation (Sec. 8.1.2). At the most basic level, the correspondence  
 1057 (or lack thereof) between fragmentation photon processes and  $Z$  processes is less straightfor-  
 1058 ward, and the special treatment of this photon category is instead motivated by practical con-  
 1059 siderations (Sec. 8.1.3).

1060 In practice, we categorize photons in the simulation as

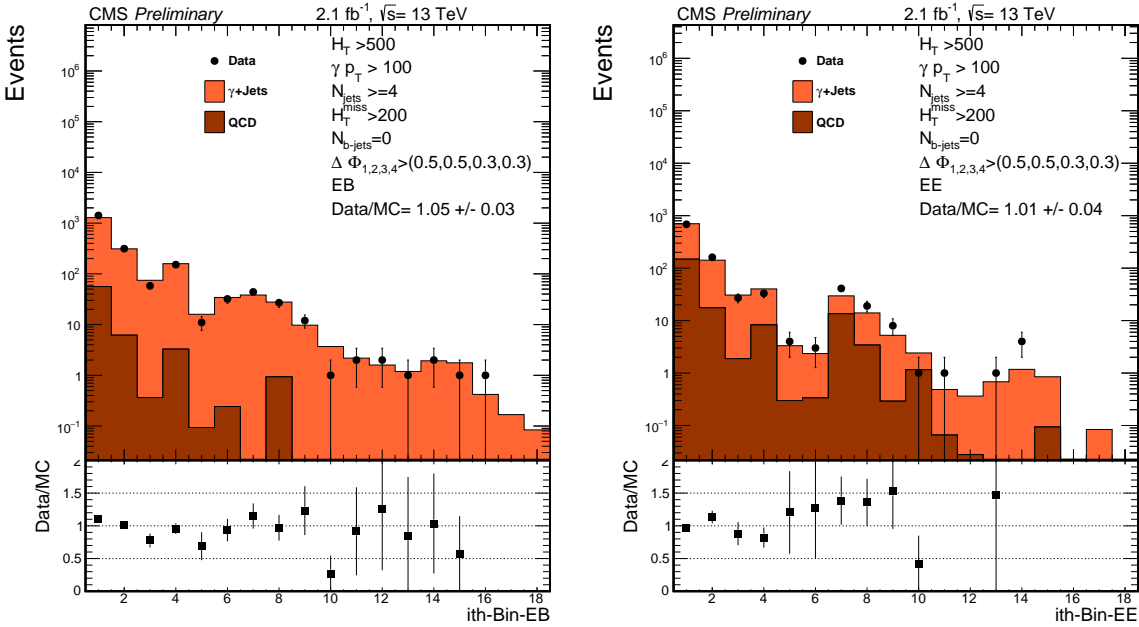


Figure 66: Numbers of observed events in the photon control samples in EB (left) and EE (right) compared to simulation.

- prompt photons: `status==1` photons with `abs(motherID) <= 22` (either a photon or a quark) or `motherID == 2212` (the incoming proton)
  - direct prompt photons: prompt photons with  $\Delta R > 0.4$  with respect to any `status=23` quarks or gluons
  - fragmentation prompt photons: all prompt photons that are not direct
- non-prompt photons: all photons that are not prompt

Any photon in the  $\gamma+\text{jets}$  or QCD samples is either non-prompt, direct prompt, or fragmentation prompt. Any prompt photon is either direct prompt or fragmentation prompt.

The numbers of observed photons in ECAL barrel (EB) and endcap (EE) are shown in Table 17, and in Fig. 66 we compare the observed numbers to the expectation from simulation for both EB and EE.

There is no systematic uncertainty on  $N_\gamma^{\text{obs}}$  because it is a simple observation. The statistical uncertainty related to this observation is included in the statistical analysis when a Poisson PDF is assigned to this variable.

### 8.1.2 Purity

The purity  $\beta$  is defined as the fraction of all photons (prompt+non-prompt) that are prompt:  $\beta = N_{\text{prompt}} / (N_{\text{prompt}} + N_{\text{non-prompt}})$ . In practice, we allow the purity to depend on photon  $p_T$ , which is essentially equivalent to event  $H_T^{\text{miss}}$ . We also explore differences in purity for ECAL barrel and endcap, but find that the EB and EE purities agree.

Prompt photons can be distinguished from non-prompt photons by the shapes of their showers in the ECAL, as described by the well known  $\sigma_{ij\eta j\eta}$  quantity. The purity is determined with a two-component fit to the  $\sigma_{ij\eta j\eta}$  distribution in the photon control sample. The PDF for the prompt component is fit directly in data using a gaussian distribution, which was motivated

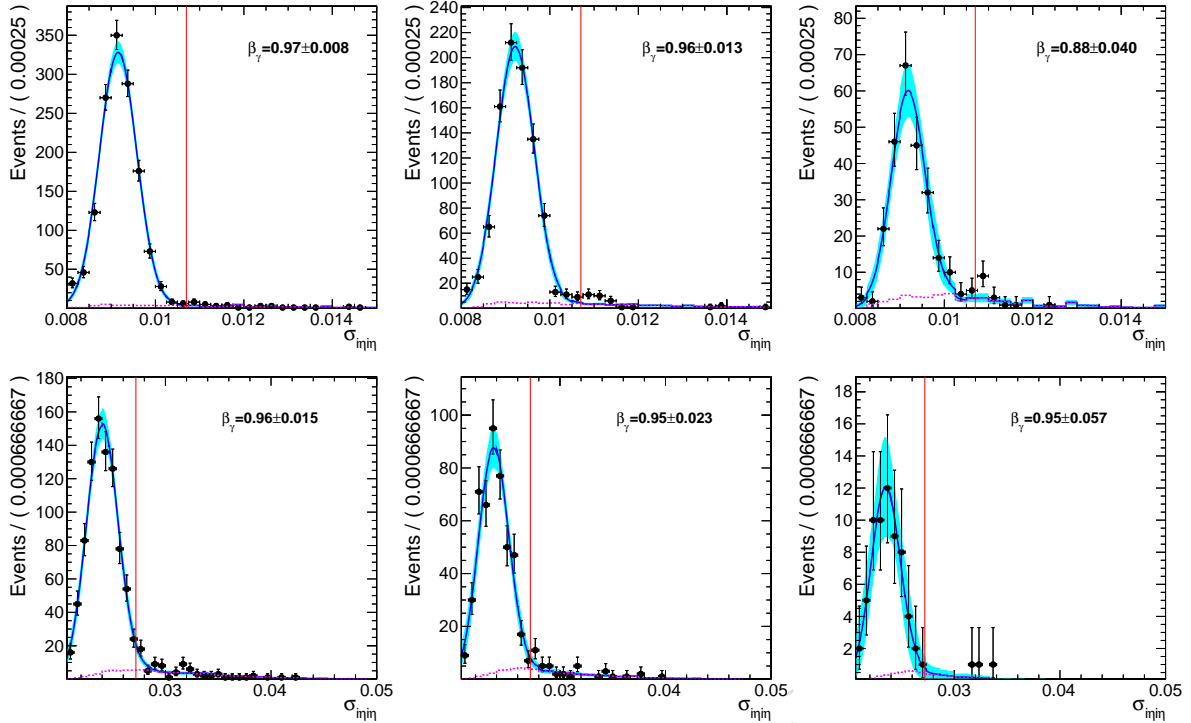


Figure 67: Fit results for purity determination in EB (top) and EE (bottom) for events with  $H_T^{\text{miss}}$  in the range 200-300, 300-500, and for  $H_T^{\text{miss}} > 500$ , respectively.  $\beta_\gamma$  is the fitted purity within the corresponding region. The red vertical line shows the  $\sigma_{\text{inj}\eta}$  requirement for the loose ID working point. The non-prompt PDF comes from the QCD simulation.

1084 by  $\gamma$ +jets MADGRAPH simulation, and the PDF for the non-prompt component comes from  
 1085 the QCD MADGRAPH simulation. The fit result is  $(96.3 \pm 0.6)\%$  for  $H_T^{\text{miss}}$  in the range 200-500  
 1086 GeV and  $(90 \pm 3)\%$  for  $H_T^{\text{miss}} > 500$  GeV.

1087 Results of the EB and EE purity fits are shown in Fig. 67.

1088 To obtain the systematic uncertainty on the purity we perform the purity fits additional times  
 1089 with alternative prompt and non-prompt PDFs, and we take the difference in resulting pu-  
 1090 rity as the systematic uncertainty. As described in App. G, the photon control sample is de-  
 1091 fined with a requirement on the charge isolation of photon candidates. For the alternative  
 1092 non-prompt PDF, we obtain a sample of mostly non-prompt photons by inverting the charge  
 1093 isolation requirement, and we use the  $\sigma_{\text{inj}\eta}$  shape from these photons as the PDF. We also con-  
 1094 sidered using a template derived from  $\gamma$ +jets simulation as an alternative prompt PDF. The  
 1095 variation in purity result for the alternative prompt PDF is negligible. The variation in purity  
 1096 result for the alternative non-prompt PDF is about 4%. We adopt the quadrature sum of the fit  
 1097 result differences and the statistical uncertainty on the nominal fit as the systematic uncertainty  
 1098 on the purity; the systematic uncertainty is uncorrelated across different MHT bins.

### 1099 8.1.3 $\mathcal{R}_{Z(\nu\bar{\nu})/\gamma}$ and $\mathcal{F}_{\text{dir}}$

1100 To account for the difference in cross sections and small differences in kinematic distribu-  
 1101 tions of  $Z$  and  $\gamma$  events, we apply a scale factor  $\mathcal{R}_{Z(\nu\bar{\nu})/\gamma}$  which is the ratio of the number of  
 1102  $Z \rightarrow \nu\nu$ +jets and  $\gamma$ +jets events computed with leading order generator-level simulation (MAD-  
 1103 GRAPH+PYTHIA) in each analysis bin. The numerator and denominator are both determined

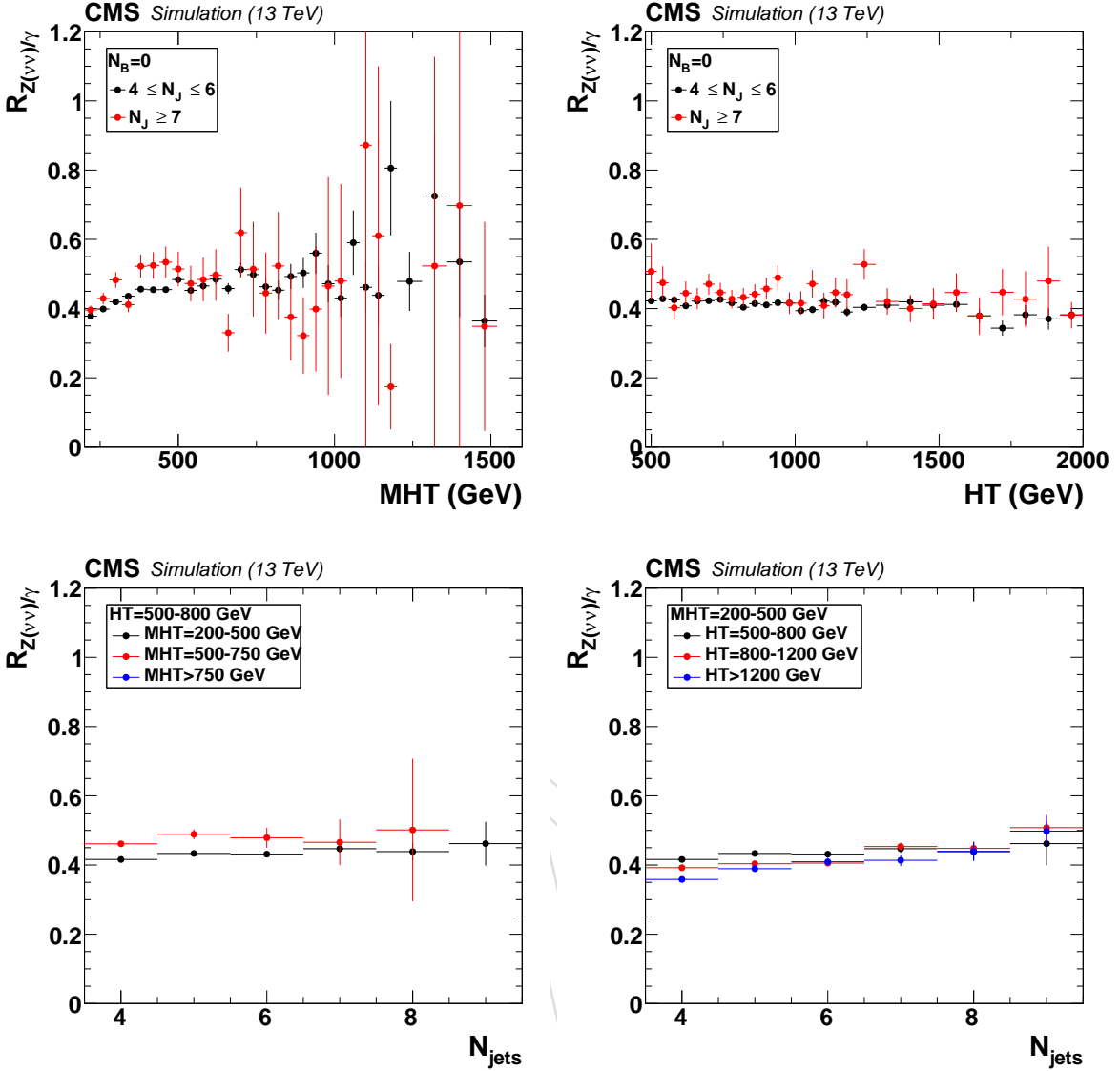


Figure 68: Plots of  $\mathcal{R}_{Z(\nu\bar{\nu})/\gamma}$  as functions of  $H_T^{\text{miss}}$ ,  $H_T$ , and  $N_{\text{jet}}$  for various binning of the data. The simulated data are from Phys14DR simulation samples processed in CMSSW 7.2. The uncertainties correspond to the full MC statistics, which vary for the different samples, but is approximately 30/fb for the smallest sample.

- 1104 after full selection with reco-level (rather than gen-level) physics objects.
- 1105 The method does not require that  $\mathcal{R}_{Z(\nu\bar{\nu})/\gamma}$  be independent of the analysis variables, but the fact  
1106 that the ratio is nearly independent of  $H_T^{\text{miss}}$ ,  $H_T$ , and  $N_{\text{jet}}$  simplifies the validation, reducing our  
1107 dependence on simulation. The most significant variation in  $\mathcal{R}_{Z(\nu\bar{\nu})/\gamma}$  is for  $H_T^{\text{miss}}$  at low boson  
1108  $p_T$  where the  $Z$  and  $\gamma$  mass difference is important. Distributions of  $\mathcal{R}_{Z(\nu\bar{\nu})/\gamma}$  as functions of  
1109  $H_T^{\text{miss}}$ ,  $H_T$ , and  $N_{\text{jet}}$  are shown in Fig. 68. (In these plots, the simulated data are from Phys14DR  
1110 simulation samples processed in CMSSW 7.2.)
- 1111 In Fig. 69, we show the exact values of  $\mathcal{R}_{Z(\nu\bar{\nu})/\gamma}$  for 18 analysis bins used in the analysis deter-  
1112 mined from the latest simulation (Sec. 3.1).

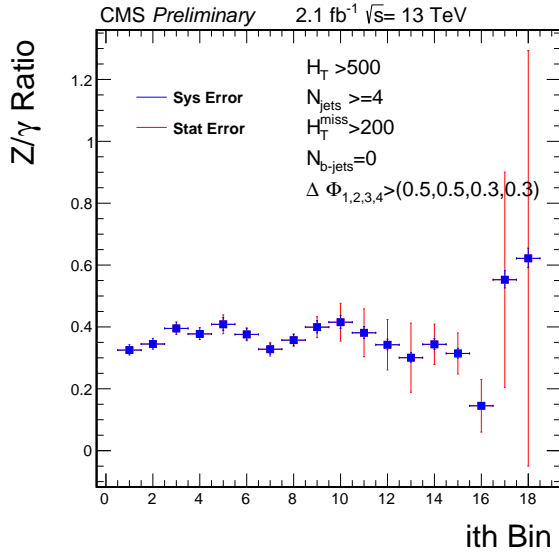


Figure 69:  $\mathcal{R}_{Z(\nu\bar{\nu})/\gamma}$  for the 18 analysis bins used in the analysis.

As introduced above, fragmentation photons must be treated carefully when computing  $\mathcal{R}_{Z(\nu\bar{\nu})/\gamma}$  primarily because the MADGRAPH  $\gamma + \text{jets}$  events that make up the  $\mathcal{R}_{Z(\nu\bar{\nu})/\gamma}$  denominator are generated with the requirement that  $\Delta R(\gamma, \text{quarks}) > 0.4$  and  $\Delta R(\gamma, \text{gluons}) > 0.4$ . Because these fragmentation prompt photons are included in the photon control sample and are experimentally indistinguishable from direct prompt photons (unlike non-prompt photons), we must correct for this missing component of the simulation. We use the prompt photons included in QCD simulation sample to determine the fraction with  $\Delta R > 0.4$ . Because this study is presently being finalized, we currently use the value determined by the MT2 analysis group (AN-15-009), which is  $0.92 \pm 0.08$ .

Because  $\mathcal{R}_{Z(\nu\bar{\nu})/\gamma}$  is determined at reco-level after full selection, we correct  $\mathcal{R}_{Z(\nu\bar{\nu})/\gamma}$  for data/MC scale factors (SFs) for efficiency related to photon reconstruction, identification, isolation, and trigger. These SFs have been computed for our selection as functions of photon  $E_T$ , photon  $\eta$ ,  $N_{\text{jet}}$ , and  $\Delta R(\gamma, \text{nearestjet})$ . Preliminary results show that the SF are independent of the analysis variables, so we correct the efficiency by the single value of  $0.98 \pm 0.05$  when computing  $\mathcal{R}_{Z(\nu\bar{\nu})/\gamma}$ , and we vary the SF by its 5% uncertainty to determine the systematic uncertainty.

#### 8.1.4 $\mathcal{R}_{Z(\nu\bar{\nu})/\gamma}$ double ratio

The dominant systematic uncertainty for the  $\gamma + \text{jets}$  method comes from our understanding of the accuracy of the leading-order modeling of  $\mathcal{R}_{Z(\nu\bar{\nu})/\gamma}$ , so we apply a correction to  $\mathcal{R}_{Z(\nu\bar{\nu})/\gamma}$  and estimate the related systematic uncertainty using  $Z \rightarrow \ell^+ \ell^-$  data. (The  $Z \rightarrow \ell^+ \ell^-$  analysis and selection is described in Sec. 8.3 and App. H.) The correction is given by the double ratio defined in Eq. 24, as was done for the 8 TeV RA2 analysis.

$$\mathcal{DR} = \frac{\mathcal{R}_{Z \rightarrow \ell^+ \ell^- / \gamma}^{\text{data}}}{\mathcal{R}_{Z \rightarrow \ell^+ \ell^- / \gamma}^{\text{MC}}} = \frac{N_{Z \rightarrow \ell^+ \ell^-}^{\text{data}}}{N_{\gamma}^{\text{data}}} \cdot \frac{N_{\gamma}^{\text{MC}}}{N_{Z \rightarrow \ell^+ \ell^-}^{\text{MC}}}. \quad (24)$$

With many data-MC differences canceling, the value of  $\mathcal{DR}$  integrated over all analysis bins is expected to be close to unity, and deviations from unity are attributed to effects of higher order processes on the overall  $\gamma + \text{jets}$  and  $Z + \text{jets}$  cross sections. In addition,  $\mathcal{DR}$  is expected to be independent of the analysis variables  $H_T^{\text{miss}}$ ,  $H_T$ , and  $N_{\text{jet}}$ . We check for significant deviations

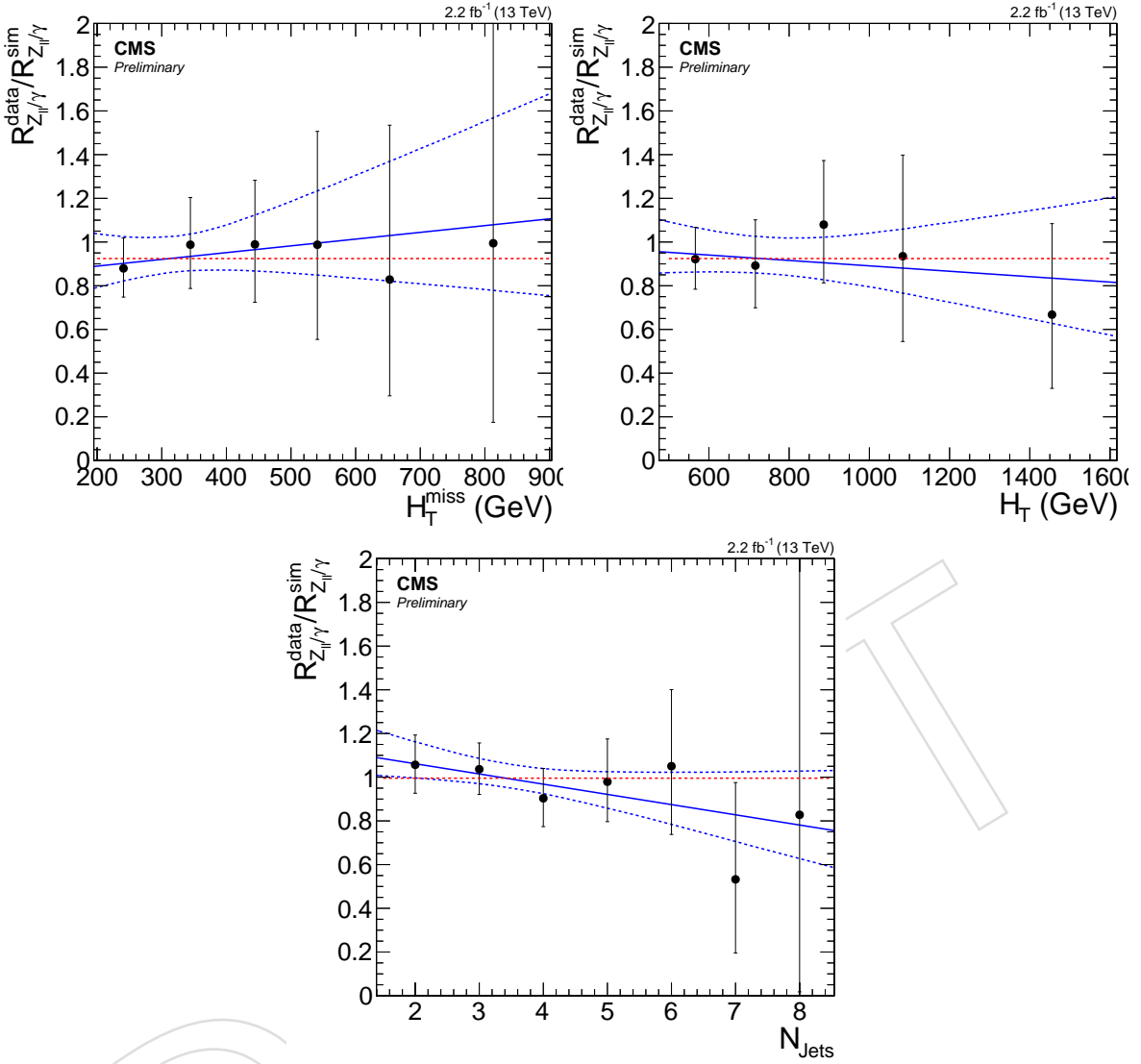


Figure 70:  $\mathcal{DR}$  vs.  $H_T^{\text{miss}}$ ,  $H_T$ , and  $N_{\text{jet}}$ . Baseline selection is applied, except that for the  $N_{\text{jet}}$  distribution we include the two additional bins  $N_{\text{jet}} = 2$  and  $3$  in the linear fit. The average value for  $N_{\text{jet}} \geq 4$  of  $0.907$  is drawn as red dashed lines on the  $H_T$  and  $H_T^{\text{miss}}$  plots.

from these assumptions in the data. As new data comes in, we reevaluate these assumptions with each new dataset by computing the overall value of  $\mathcal{DR}$  and performing linear fits of  $\mathcal{DR}$  as functions of each analysis variable. Because of limited numbers of  $Z \rightarrow \ell^+\ell^-$  events in data, we perform each fit separately in single-variable projections. These fits are shown in Fig. 70. As evidenced by the fitted slopes, no significant dependence on any analysis variable is observed. If the data-MC differences canceled perfectly, the overall value of  $\mathcal{DR}$  would be unity. We observe  $\langle \mathcal{DR} \rangle = 0.907$ , and apply this result as a multiplicative correction to the  $Z \rightarrow \nu\bar{\nu}$  background estimate, Eq. 25. The associated asymmetric systematic uncertainty is evaluated in each of the  $18 N_{\text{b-jet}} = 0$  bins by taking the largest of the deviations from the best-fit line read from the projections of Fig. 70. The uncertainty values range from about 5 to 55%.

1143 **8.2 Summary of  $\gamma + \text{jets}$  prediction and systematic uncertainty**

1144 As described above, the background prediction in each of the 18 0-btag analysis bins is de-  
 1145 termined from the numbers of control sample photons (which we split by barrel and endcap:  
 1146  $N_{\gamma, \text{EB}}^{\text{obs}}, N_{\gamma, \text{EE}}^{\text{obs}}$ ), the purity corrections as a function of  $H_T^{\text{miss}}$  ( $\beta(\text{low } H_T^{\text{miss}})$  and  $\beta(\text{high } H_T^{\text{miss}})$ ), the  
 1147 direct prompt photon correction ( $\mathcal{F}_{\text{dir}}$ ), and the MC ratio of  $Z(\nu\bar{\nu}$  and  $\gamma + \text{jets}$  events ( $\mathcal{R}_{Z(\nu\bar{\nu})/\gamma}$ ).  
 1148 To this we add the correction for  $\mathcal{DR}$  as a function of  $N_{\text{jet}}$ :

$$N_{Z \rightarrow \nu\nu}^{\text{pred}} = \mathcal{DR} \cdot \mathcal{R}_{Z(\nu\bar{\nu})/\gamma} \cdot \mathcal{F}_{\text{dir}} \cdot \beta(H_T^{\text{miss}}) \cdot N_{\gamma}^{\text{obs}}. \quad (25)$$

1149 Thus, the inputs to the 18 bins of the statistical analysis are

- 1150 •  $N_{\gamma}^{\text{obs}}$  : 18 values (from data control region), see Table 17;
- 1151 •  $\beta(\text{low } H_T^{\text{miss}}) = (96.3 \pm 3.2)\%$  with systematic uncertainty uncorrelated in the 18  
 1152 bins;
- 1153 •  $\beta(\text{high } H_T^{\text{miss}}) = (90.0 \pm 4.7)\%$  with systematic uncertainty uncorrelated in the 18  
 1154 bins;
- 1155 •  $\mathcal{R}_{Z(\nu\bar{\nu})/\gamma}$ : 18 values (from MC) with uncorrelated statistical uncertainty and corre-  
 1156 lated systematic uncertainty; see Table 17;
- 1157 •  $\mathcal{F}_{\text{dir}} = 0.92 \pm 0.08$ , with systematic uncertainty correlated in the 18 bins;
- 1158 •  $\mathcal{DR}$  : One value, with systematic uncertainty depending on  $N_{\text{jet}}$ ,  $H_T$ , and  $H_T^{\text{miss}}$ ,  
 1159 uncorrelated among these 18 bins; see Table 17.

1160 Finally, we show our prediction based on  $\gamma + \text{jets}$  data in Table 17, and in Fig. 71 we compare  
 1161 the prediction without  $\mathcal{DR}$  to the prediction from the  $Z \rightarrow \nu\nu$  simulation for the 18 0-btag  
 1162 analysis bins. The latter shows that quantifying data/MC differences in  $Z+\text{jets}$  simulation is  
 1163 the primary advantage of this background method.

Table 17:  $Z \rightarrow \nu\nu +$  jets prediction ( $N_{Z \rightarrow \nu\nu}^{\text{pred}}$ ) in the 18 0-btag analysis bins as determined with the  $\gamma +$  jets method. We show the inputs to the determination of  $N_{Z \rightarrow \nu\nu}^{\text{pred}}$  as shown in Eq. 23 that vary for the 18 bins, including  $N_{\gamma}^{\text{obs}}$  in EB and EE,  $\mathcal{R}_{Z(\nu\bar{\nu})/\gamma}$ , and  $\mathcal{DR}$ . The first uncertainty on  $\mathcal{R}_{Z(\nu\bar{\nu})/\gamma}$  comes from the statistical uncertainty on the simulation; the second (asymmetric) uncertainty on  $\mathcal{R}_{Z(\nu\bar{\nu})/\gamma}$  comes from variation of the data/MC scale factors for photon reconstruction, ID, and isolation. The purity and direct prompt fraction are described in the text.

bin	$N_{\gamma, \text{EB}}^{\text{obs}}$	$N_{\gamma, \text{EE}}^{\text{obs}}$	$\mathcal{R}_{Z(\nu\bar{\nu})/\gamma}$	$\mathcal{DR}$	$N_{Z \rightarrow \nu\nu}^{\text{pred}}$
1 ( $N_{\text{jet}} 4\text{-}6$ , MHT\_HT\_1)	1416	684	$0.35 \pm 0.00^{+0.02}_{-0.02}$	$0.91^{+0.11}_{-0.08}$	$596.4^{+13.1}_{-13.1} {}^{+96.6}_{-78.7}$
2 ( $N_{\text{jet}} 4\text{-}6$ , MHT\_HT\_2)	314	161	$0.38 \pm 0.01^{+0.02}_{-0.02}$	$0.91^{+0.13}_{-0.09}$	$143.1^{+6.6}_{-6.6} {}^{+25.6}_{-20.3}$
3 ( $N_{\text{jet}} 4\text{-}6$ , MHT\_HT\_3)	58	27	$0.43 \pm 0.01^{+0.02}_{-0.02}$	$0.91^{+0.33}_{-0.22}$	$29.3^{+3.2}_{-3.2} {}^{+11.1}_{-7.9}$
4 ( $N_{\text{jet}} 4\text{-}6$ , MHT\_HT\_4)	152	33	$0.41 \pm 0.01^{+0.02}_{-0.02}$	$0.91^{+0.24}_{-0.17}$	$57.0^{+4.2}_{-4.2} {}^{+16.6}_{-12.3}$
5 ( $N_{\text{jet}} 4\text{-}6$ , MHT\_HT\_5)	11	4	$0.44 \pm 0.03^{+0.02}_{-0.02}$	$0.91^{+0.33}_{-0.22}$	$5.0^{+1.3}_{-1.3} {}^{+1.9}_{-1.4}$
6 ( $N_{\text{jet}} 4\text{-}6$ , MHT\_HT\_6)	32	3	$0.41 \pm 0.02^{+0.02}_{-0.02}$	$0.91^{+0.49}_{-0.34}$	$10.7^{+1.8}_{-1.8} {}^{+6.0}_{-4.2}$
7 ( $N_{\text{jet}} 7\text{-}8$ , MHT\_HT\_1)	44	41	$0.36 \pm 0.02^{+0.02}_{-0.02}$	$0.91^{+0.20}_{-0.14}$	$24.4^{+2.6}_{-2.6} {}^{+6.3}_{-4.7}$
8 ( $N_{\text{jet}} 7\text{-}8$ , MHT\_HT\_2)	27	19	$0.39 \pm 0.02^{+0.02}_{-0.02}$	$0.91^{+0.20}_{-0.14}$	$14.4^{+2.1}_{-2.1} {}^{+3.6}_{-2.7}$
9 ( $N_{\text{jet}} 7\text{-}8$ , MHT\_HT\_3)	12	8	$0.43 \pm 0.04^{+0.02}_{-0.02}$	$0.91^{+0.33}_{-0.22}$	$7.0^{+1.6}_{-1.6} {}^{+2.7}_{-2.0}$
10 ( $N_{\text{jet}} 7\text{-}8$ , MHT\_HT\_4)	1	1	$0.45 \pm 0.07^{+0.02}_{-0.02}$	$0.91^{+0.24}_{-0.17}$	$0.7^{+0.5}_{-0.5} {}^{+0.2}_{-0.2}$
11 ( $N_{\text{jet}} 7\text{-}8$ , MHT\_HT\_5)	2	1	$0.41 \pm 0.08^{+0.02}_{-0.02}$	$0.91^{+0.33}_{-0.22}$	$0.9^{+0.5}_{-0.5} {}^{+0.4}_{-0.3}$
12 ( $N_{\text{jet}} 7\text{-}8$ , MHT\_HT\_6)	2	0	$0.37 \pm 0.09^{+0.02}_{-0.02}$	$0.91^{+0.49}_{-0.34}$	$0.6^{+0.4}_{-0.4} {}^{+0.3}_{-0.3}$
13 ( $N_{\text{jet}} 9+$ , MHT\_HT\_1)	1	1	$0.33 \pm 0.12^{+0.02}_{-0.02}$	$0.91^{+0.30}_{-0.20}$	$0.5^{+0.4}_{-0.4} {}^{+0.3}_{-0.2}$
14 ( $N_{\text{jet}} 9+$ , MHT\_HT\_2)	2	4	$0.37 \pm 0.07^{+0.02}_{-0.02}$	$0.91^{+0.30}_{-0.20}$	$1.8^{+0.7}_{-0.7} {}^{+0.7}_{-0.6}$
15 ( $N_{\text{jet}} 9+$ , MHT\_HT\_3)	1	0	$0.34 \pm 0.07^{+0.02}_{-0.02}$	$0.91^{+0.33}_{-0.22}$	$0.3^{+0.3}_{-0.3} {}^{+0.1}_{-0.1}$
16 ( $N_{\text{jet}} 9+$ , MHT\_HT\_4)	1	0	$0.16 \pm 0.09^{+0.01}_{-0.01}$	$0.91^{+0.30}_{-0.20}$	$0.1^{+0.1}_{-0.1} {}^{+0.1}_{-0.1}$
17 ( $N_{\text{jet}} 9+$ , MHT\_HT\_5)	0	0	$0.60 \pm 0.38^{+0.03}_{-0.03}$	$0.91^{+0.33}_{-0.22}$	$0.0^{+1.8}_{-0.0} {}^{+0.7}_{-0.7}$
18 ( $N_{\text{jet}} 9+$ , MHT\_HT\_6)	0	0	$0.68 \pm 0.73^{+0.04}_{-0.03}$	$0.91^{+0.49}_{-0.34}$	$0.0^{+1.8}_{-0.0} {}^{+1.2}_{-1.1}$

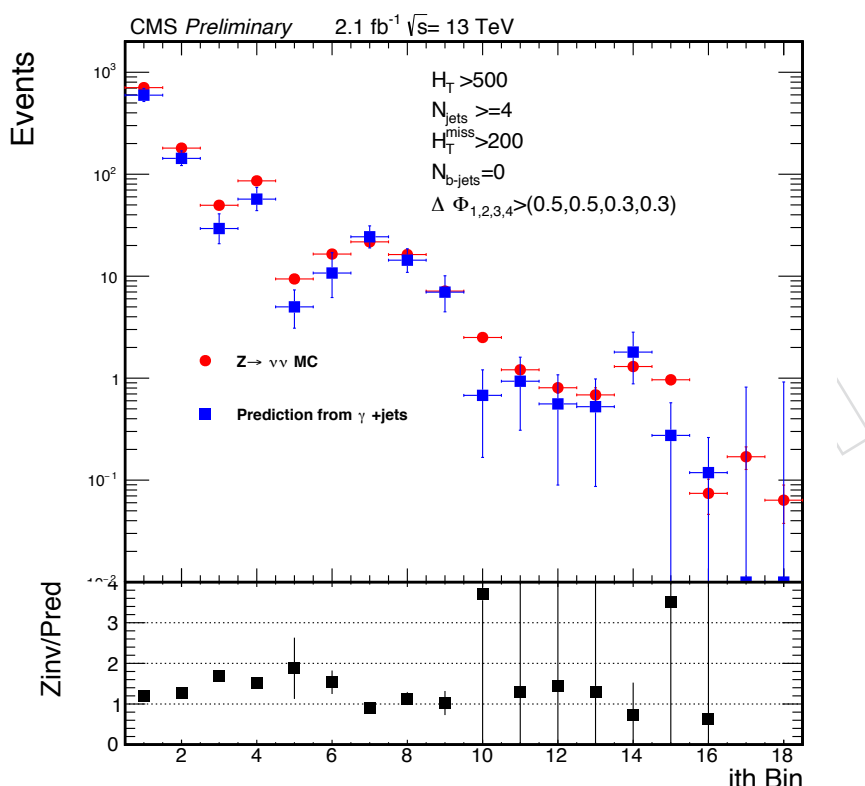


Figure 71: Data-based prediction for  $Z \rightarrow \nu\nu$  background without application of  $\mathcal{DR}$  correction (blue) compared to expectation from simulation (red).

<sup>1164</sup> **8.3  $Z \rightarrow \nu\bar{\nu}$  measurement for  $N_{\text{b-jet}} > 0$**

For a stand-alone measurement of the  $Z \rightarrow \nu\bar{\nu}$  yields directly from the  $Z \rightarrow \ell^+\ell^-$  control samples we would have

$$N(Z \rightarrow \nu\bar{\nu}) = N(Z \rightarrow \ell^+\ell^-) \cdot \mathcal{P} \cdot \mathcal{R} / (\mathcal{A} \cdot \epsilon), \quad (26)$$

<sup>1165</sup> where  $N(Z \rightarrow \ell^+\ell^-)$  is measured in each search bin,  $\mathcal{P}$  is the purity of the  $Z$  sample,  $\mathcal{R} = 5.95$   
<sup>1166</sup> [23] is the ratio of branching fractions,  $\mathcal{A}$  is the lepton acceptance, and  $\epsilon$  is the efficiency (including  
<sup>1167</sup> trigger, lepton identification, and lepton isolation efficiencies). The two independent measurements from  $Z \rightarrow e^+e^-$  and  $Z \rightarrow \mu^+\mu^-$  are combined to obtain the background prediction.  
<sup>1168</sup> We discuss the determination of the purity, acceptance, and efficiency factors in Appendix H.

<sup>1170</sup> Because of the limited statistics in these control samples for the high- $N_{\text{jet}}$  and high- $N_{\text{b-jet}}$  bins,  
<sup>1171</sup> we employ a method for projecting onto a subspace and predicting the yields in the remaining  
<sup>1172</sup> dimensions with extrapolation factors that have limited, or predictable, dependence on the sub-  
<sup>1173</sup> space variables. As described in Section 8.1 above, we gain statistics taking the  $(H_T, H_T^{\text{miss}}, N_{\text{jet}})$   
<sup>1174</sup> subspace distribution from the  $\gamma + \text{jets}$  control sample, with normalization to  $Z \rightarrow \ell^+\ell^-$  via  
<sup>1175</sup> the double ratio discussed in Section 8.1.4.

Based on our judgment of the reliability, or lack thereof, of the simulation between  $\gamma + \text{jets}$  and  $Z \rightarrow \ell^+\ell^-$ , we perform the extrapolation in the  $N_{\text{b-jet}}$  variable entirely with the  $Z \rightarrow \ell^+\ell^-$  sample. For this sample we take the  $N_{\text{b-jet}}$  distribution to be common to the bins in  $(H_T, H_T^{\text{miss}})$ ; deviations from this assumption are discussed below. On the other hand, we expect, and find in simulation, a substantial dependence of the  $N_{\text{b-jet}}$  distribution on  $N_{\text{jet}}$ . To express the shape dependence explicitly, we write

$$N(Z \rightarrow \nu\bar{\nu})_{N_{\text{jet}}, N_{\text{b-jet}}}^{H_T, H_T^{\text{miss}}} = N_{Z \rightarrow \nu\bar{\nu}}(\gamma + \text{jets})_{N_{\text{jet}}, 0}^{H_T, H_T^{\text{miss}}} \cdot \mathcal{F}_{N_{\text{jet}}, N_{\text{b-jet}}}(Z \rightarrow \ell^+\ell^-), \quad (27)$$

<sup>1176</sup> introducing the extrapolation factors  $\mathcal{F}_{N_{\text{jet}}, N_{\text{b-jet}}}$ . The prediction  $N_{Z \rightarrow \nu\bar{\nu}}(\gamma + \text{jets})_{N_{\text{jet}}, 0}^{H_T, H_T^{\text{miss}}}$  comes  
<sup>1177</sup> from Eq. 23.

We measure the extrapolation factors directly with  $Z \rightarrow \ell^+\ell^-$  data for all  $N_{\text{b-jet}} > 0$  bins in the lowest (4–6)  $N_{\text{jet}}$  bin:

$$\mathcal{F}_{N_{\text{jet}}=4-6, N_{\text{b-jet}}>0} = (N \cdot \mathcal{P})_{N_{\text{jet}}=4-6, N_{\text{b-jet}}>0} / (N \cdot \mathcal{P})_{N_{\text{jet}}=4-6, 0}. \quad (28)$$

<sup>1178</sup> The acceptance and lepton efficiencies cancel in the ratio. The purities  $\mathcal{P}$  depend on  $N_{\text{b-jet}}$   
<sup>1179</sup> because of the background from  $t\bar{t}$  in the  $Z \rightarrow \ell^+\ell^-$  control sample. They are measured by  
<sup>1180</sup> fitting the lepton-pair mass distribution in the data. We find the purities in the  $N_{\text{b-jet}} = 2$  and  
<sup>1181</sup>  $N_{\text{b-jet}} \geq 3$  bins to be around 50%. Our data estimates for  $Z$  purity are given in Table 18 and the  
<sup>1182</sup> corresponding plots are shown in Appendix H.

To extrapolate these further to the higher  $N_{\text{jet}}$  bins we need a model, the data statistics being inadequate. We thus factor the extrapolation factors as

$$\mathcal{F}_{N_{\text{jet}}>6, N_{\text{b-jet}}>0} = \mathcal{F}_{N_{\text{jet}}=4-6, N_{\text{b-jet}}>0} \cdot \mathcal{J}_{N_{\text{jet}}>6, N_{\text{b-jet}}>0}, \quad (29)$$

$$\mathcal{J}_{N_{\text{jet}}>6, N_{\text{b-jet}}>0} \equiv N_{N_{\text{jet}}>6, N_{\text{b-jet}}>0} / N_{N_{\text{jet}}=4-6, N_{\text{b-jet}}>0}, \quad (30)$$

<sup>1183</sup> where  $\mathcal{J}$  comes from the model that we discuss next.

The b-tagged jets arise from both true b quarks and mistagged light (and charm) quarks. From studies by the b-tagging POG we expect with the CSVM tagger to have mistag rates of about

1% from light quarks and 1% from charm. Thus the average number of b-mistagged jets should depend linearly on  $N_{\text{jet}}$ , and at fixed  $N_{\text{jet}}$  should obey a distribution in  $N_{\text{b-jet}}$  given by binomial combinatorics. That is, for a bin spanning  $N_{\text{jet}}$  values  $J_{\min} : J_{\max}$ , and denoting  $N_{\text{b-jet}}$  as  $b$ ,

$$\mathcal{J}_{J_{\min}, J_{\max}} \simeq \mathcal{G}_{J_{\min}, J_{\max}}^b / \mathcal{G}_{4,6}^b, \quad (31)$$

$$\mathcal{G}_{J_{\min}, J_{\max}}^b \equiv \sum_{j=J_{\min}}^{J_{\max}} \binom{j}{b} \frac{N_j}{N_{J_{\min}}} (1-p)^{j-J_{\min}}.$$

1184 This is a generalization of Eq. 40 in Section H.5. The  $N$ 's in the second equation are the yields,  
 1185 in the data, of events containing  $N$  jets.

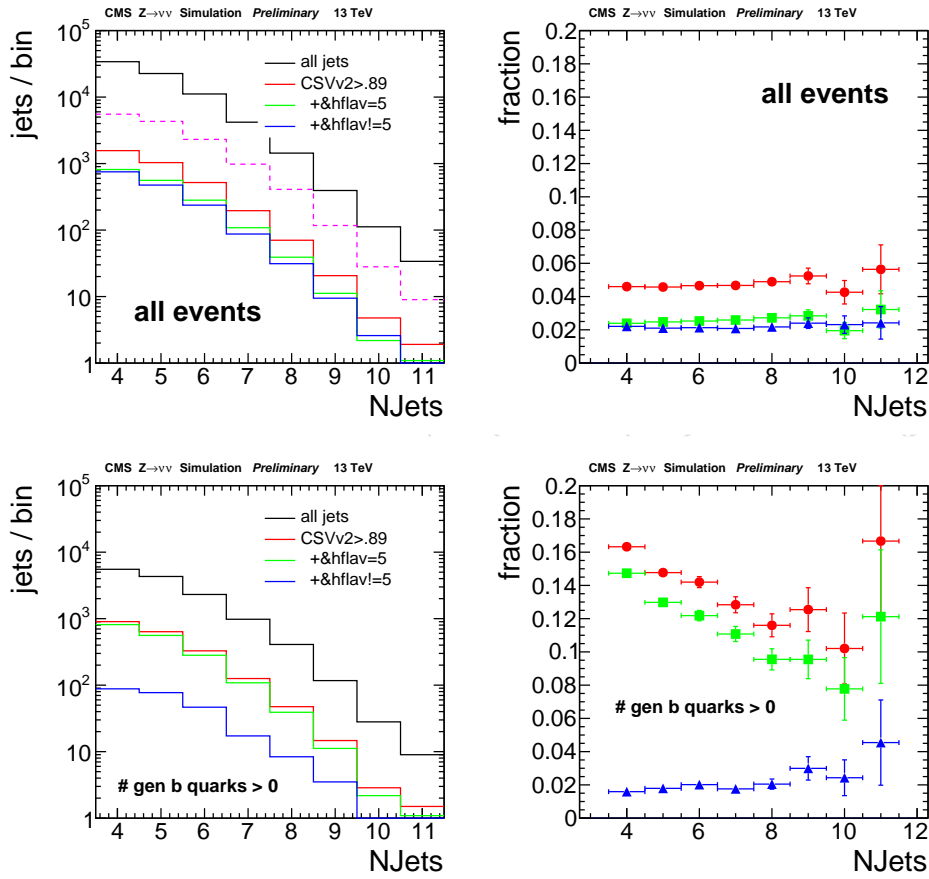


Figure 72: Distributions in  $N_{\text{jet}}$  from  $Z \rightarrow \nu\bar{\nu}$  MC (histograms on left) for all jets (black) and those tagged as a b-jet (red), tagged and truth-matched to a b-quark jet (green), or tagged but not truth-matched to a b-quark jet (blue). Points in the right-hand plots are ratios to the total. All events satisfy the baseline signal event selection. In the lower plots the event is also required to have at least one true b-quark jet. The dashed magenta histogram in the upper-left plot is a copy of the black histogram in the lower-left plot, for comparison.

1186 For true b-quark jets the situation is less clear a priori. One extreme would be that a pair  
 1187 of b quarks is produced in the hard scattering along with a modest number of jets, and the  
 1188 source of larger jet multiplicities arises primarily from the production of light quarks in the  
 1189 fragmentation. In this picture the average number of true b-quark jets would grow more slowly,  
 1190 or not at all, with  $N_{\text{jet}}$ . Use of a binomial distribution for the  $N_{\text{b-jet}}$  multiplicity would then be

inappropriate, both because the average probability for a jet to be tagged as a b-jet would not be constant with  $N_{\text{jet}}$ , and because of the pairing enforced by flavor conservation. The latter effect is, however, considerably washed out given that the jet  $p_T$  and  $\eta$  acceptance, combined with the tagging efficiency, retains only about a third of the real b-quarks.

We have studied these effects in simulation, and confirm that for events with at least one b-tagged jet the average probability for a jet to be a true and tagged b jet decreases with  $N_{\text{jet}}$ . This is shown by the green points in the lower right-hand plot of Fig. 72. We observe a similar effect in  $t\bar{t} Z$  MC. There is also a difference in the  $N_{\text{jet}}$  distributions such that when no true b-quark jet is required the  $N_{\text{jet}}$  denominator distribution falls more rapidly (black vs dashed magenta histograms in the upper-left plot of Fig. 72), so that the fractions given by the green (true b-jet) points in the upper-right plot of Fig. 72 do not show this fall-off with  $N_{\text{jet}}$ , but instead are practically constant. The same conclusion arises from fits of the binomial formula to the distribution from MC at each value of  $N_{\text{jet}}$ , as shown in Fig. 73, where the values obtained for the probability parameter  $p$  are quite independent of  $N_{\text{jet}}$ , averaging about 0.046. In data we measure  $p$  to be  $0.062 \pm 0.007$ . We also find that the fraction of jets that are true and tagged b jets is about 2.5% (green points in Fig. 72, upper right), comparable to the number that are mistagged.

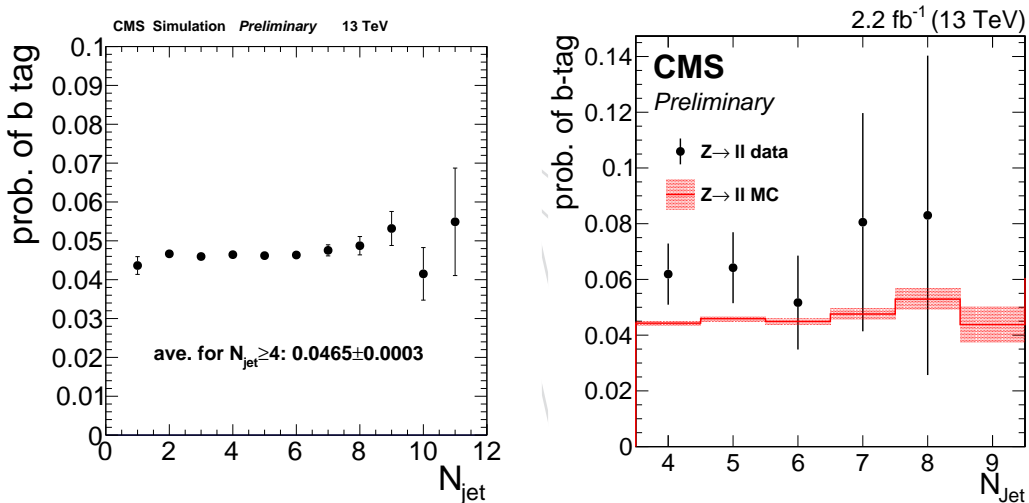


Figure 73: The b-tag probability  $p$  as a function of  $N_{\text{jet}}$ , from a fit of a binomial distribution in each  $N_{\text{jet}}$  bin as measured in  $Z \rightarrow v\bar{v}$  MC (left) and as measured in  $Z \rightarrow \ell^+\ell^-$  data compared against Drell-Yan MC (right).

From the simulation studies and the above general considerations we conclude that the  $N_{b\text{-jet}}$  distribution should be bounded from below by the distribution found in our lowest  $N_{\text{jet}}$  bin, and from above by a binomial distribution. Within errors these bounds are satisfied by the simulation we have, as can be seen in Fig. 74 which compares the direct Drell-Yan MC prediction with these two  $N_{\text{jet}}$  extrapolation procedures.

The flatness of the  $N_{\text{jet}}$  dependence observed in Fig. 72, upper right, and in Fig. 73 initially led us to propose taking the binomial model as a MC-independent estimate of the scale factors. But given these further investigations it appears that this lack of  $N_{\text{jet}}$  dependence is accidental, and so we now choose to take the factors  $\mathcal{J}_{N_{\text{jet}}>6, N_{b\text{-jet}}>0}$  from simulation, and to treat the binomial and low- $N_{\text{jet}}$  distributions as upper and lower bounds for systematic errors, respectively. To obtain 68% CL systematic errors we scale the separation between central value and bound by a factor  $1/\sqrt{3}$ .

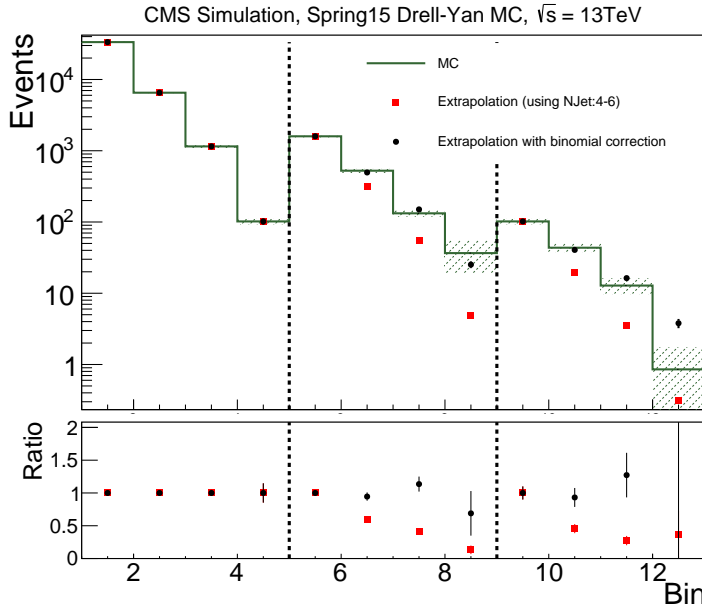


Figure 74: Distribution of yields  $Y$  in  $\text{Bin} \equiv 4(i - 1) + j$ , where  $i$  ( $j$ ) is the index of the  $N_{\text{jet}}$  ( $N_{\text{b-jet}}$ ) bin, for Drell-Yan MC (green histogram with hashed statistical error bands), and the results of projecting from the low- $N_{\text{jet}}$  bin to the higher ones with scale factors  $J_{i,j}$  derived from the binomial model (black points), or set to unity (red points).

Application of the method to the 12 bins inclusive in  $(H_{\text{T}}, H_{\text{T}}^{\text{miss}})$  is demonstrated in Fig. 75. In these plots the red points show the effect of simply scaling the distribution observed in the  $N_{\text{jet}}$  4-6 bins to the yield integrated over  $N_{\text{b-jet}}$  in the higher  $N_{\text{jet}}$  bins. As expected, the fall-off is too steep. With the correction based on the extrapolation factors of Eq. 31, we obtain the black points, which in fact lie rather close to the simulation.

Rarer electroweak processes giving rise to states such as  $t\bar{t}Z$  and  $V(V)Z$  can also contribute. We add the expectations for these from simulation to the backgrounds predicted by the procedure above. Those having  $Z \leftrightarrow \gamma$  counterparts are already counted in  $N_{\gamma}^{\text{data}}$ , and largely cancel in the ratio  $\mathcal{R}_{Z \rightarrow \nu\bar{\nu}}/\gamma$ . We find the contribution from  $t\bar{t}Z$  in the  $N_{\text{b-jet}} \geq 2$  bins to be comparable to that from  $Z + \text{jets}$ , and we add the expected yield from this process to the numerator and denominator of Eq. 30.

A number of aspects of the procedure outlined here are tested in the MC closure test presented in Fig. 76. Here  $Z \rightarrow \ell^{+}\ell^{-}$  MC data are analyzed as if the  $\gamma + \text{jets}$  measurement had exactly reproduced the MC yields in the  $N_{\text{b-jet}} = 0$  bins. The scale factors are derived from the data and  $Z \rightarrow \ell^{+}\ell^{-}$  simulation as described above and applied to the data. The results are then overlaid on the  $Z \rightarrow \nu\bar{\nu}$  MC prediction. The main source of imperfect closure is the assumption that we have no dependence on the kinematic variables. Some trend, especially with  $H_{\text{T}}$ , can be seen, although the statistical uncertainties of the MC sample dominate in many bins.

To improve the statistical precision we repeat the closure test on the larger  $Z \rightarrow \nu\bar{\nu}$  simulation. We use this comparison to extract the systematic uncertainty attributable to the kinematic dependence. We observe that this uncertainty is independent of  $N_{\text{jet}}$  and increasing with  $N_{\text{b-jet}}$ ; for the most precisely measured  $N_{\text{jet}} = 4\text{-}6$  bins we unfold the systematic uncertainty from the total RMS deviation from unity to arrive at the assigned uncertainties of 10%, 15%, and 20% for  $N_{\text{b-jet}} = 1, 2$ , and  $\geq 3$ , respectively.

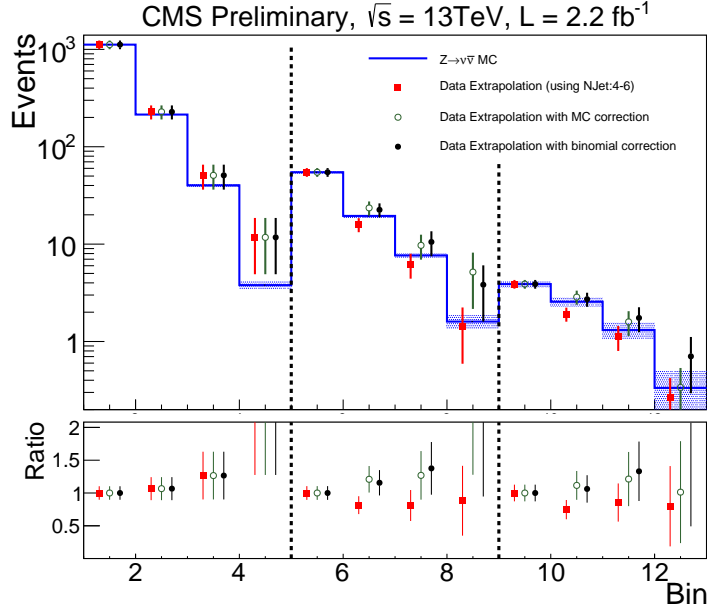


Figure 75: Distribution of yields  $Y$  in Bin  $\equiv 4(i - 1) + j$ , where  $i$  ( $j$ ) is the index of the  $N_{\text{jet}}$  ( $N_{\text{b-jet}}$ ) bin, for  $Z \rightarrow \nu\bar{\nu}$  MC (blue histogram with hashed statistical error bands), and data in bins 1-4 (points with error bars, all colors) scaled to the MC in bins 1, 5, and 9. For the remaining bins, colors distinguish the method used to derive the scale factors  $\mathcal{J}_{i,j}$ : from MC (open green points), from the binomial model (black points), or set to unity (red points).

1244 We also assign a systematic uncertainty for the purity determination. Table 18 shows the  $Z$   
 1245 sample purity as a function of  $N_{\text{b-jet}}$ . The uncertainties are dominated by the low data statistics  
 1246 used to obtain the fits. These fits are shown in Appendix H.

Table 18: Purity and absolute uncertainties obtained from data fits given in Appendix H. Low data statistics do not allow for separate purity fits for 2 and  $\geq 3 N_{\text{b-jet}}$ . Spring15 MC indicate that the sample purity is constant across the two samples for the two largest  $N_{\text{b-jet}}$  bins. We combine these bins for the  $Z$  purity estimate.

sample	$0 N_{\text{b-jet}}$	$1 N_{\text{b-jet}}$	$\geq 2 N_{\text{b-jet}}$
$Z \rightarrow \mu^+ \mu^-$	$0.96 \pm 0.06$	$0.75 \pm 0.17$	$0.64 \pm 0.25$
$Z \rightarrow e^+ e^-$	$0.98 \pm 0.06$	$0.91 \pm 0.18$	

1247 Values for the extrapolation factors and their uncertainties are given in Table 19.

## 8.4 $Z \rightarrow \nu\bar{\nu}$ background prediction

1249 To summarize, we show in Fig. 78 the background yields predicted by the procedure described  
 1250 in this section. Although not used directly, the expectation from  $Z \rightarrow \nu\bar{\nu}$  simulation is shown  
 1251 in the figure for comparison.

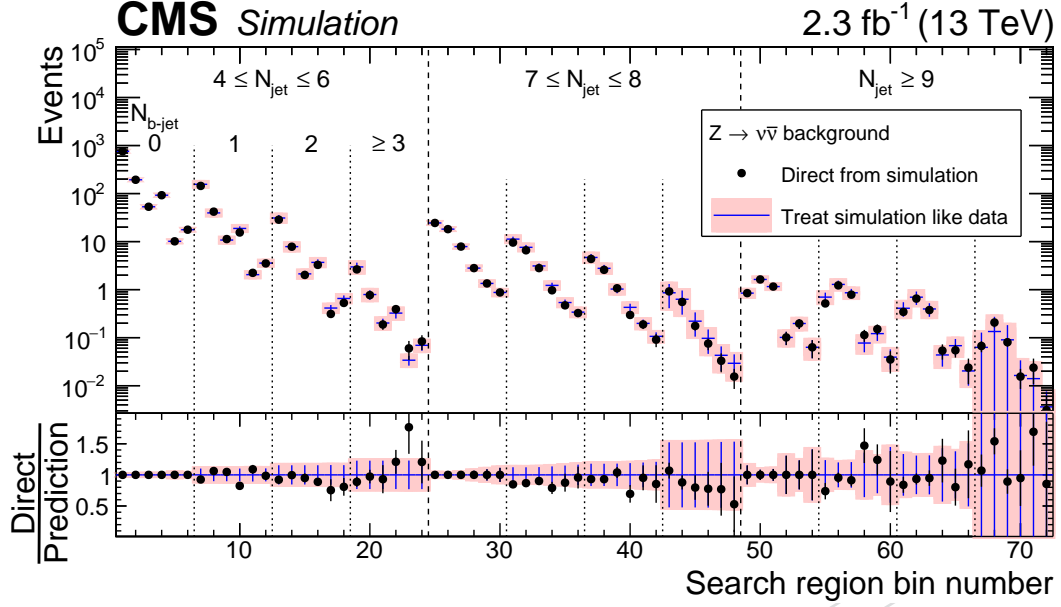


Figure 76:  $Z \rightarrow v\bar{v}$  background prediction from the  $Z \rightarrow \ell^+\ell^-$  simulation in the 72-bin search space from the procedure described in the text (histogram) compared against simulated ( $Z \rightarrow v\bar{v}$ )+jets and  $t\bar{t}Z$  events (points with error bars). The error bars and shaded boxes show the statistical uncertainties of the simulation combined with the systematic uncertainty attributable to the kinematic dependence, while the yields are scaled to the integrated luminosity of the data. For bins corresponding to  $N_{b\text{-jet}} = 0$  the agreement is exact by construction. The pink shaded bands indicate the systematic uncertainty assigned for the unmodelled dependence on the kinematic parameters.

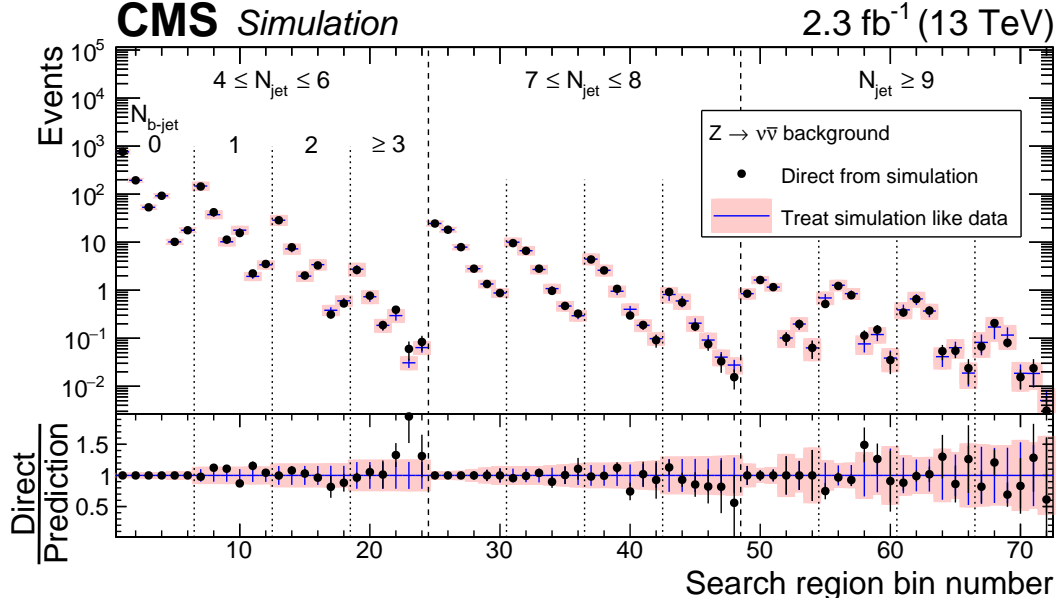


Figure 77: Same as Fig. 76 except we extract the extrapolation factors from the larger  $Z \rightarrow v\bar{v}$  simulation sample.

Table 19: Extrapolation factors for  $N_{b\text{-jet}} > 0$ , with statistical and systematic uncertainties. In the first column, bin  $\equiv 4(i - 1) + j$ , where  $i$  ( $j$ ) is the index of the  $N_{\text{jet}}$  ( $N_{b\text{-jet}}$ ) bin. Values are given for the observed dimuon yields  $N_{\mu^+\mu^-}$ , observed dielectron yields  $N_{e^+e^-}$ , extrapolation factor (0b to  $n_b$ )  $\mathcal{F}$ , its statistical uncertainty, and the systematic uncertainties attributable to the purity  $\beta_{\ell\ell}$ , to the scale factor  $\mathcal{J}$  on the  $N_{b\text{-jet}}$  shape between  $N_{\text{jet}}$  bins, and to the kinematic dependence of these. The symmetric part of the uncertainty on  $\mathcal{J}$  comes from MC statistics. All uncertainties are given in percent.

bin	$N_{\mu^+\mu^-}$	$N_{e^+e^-}$	$\mathcal{F}$	$\sigma_{\text{stat}}$	$\delta\mathcal{P}$	$\delta\mathcal{J}$	$\sigma_{\text{kin}}$
1	103	90	1.000	0	0	$\pm 0^{+0}_{-0}$	0
2	29	18	0.202	16	15	$\pm 0^{+0}_{-0}$	10
3	7	6	0.044	29	38	$\pm 0^{+0}_{-0}$	15
4	2	1	0.010	58	38	$\pm 0^{+0}_{-0}$	20
5	2	5	1.000	0	0	$\pm 0^{+0}_{-0}$	0
6	2	3	0.426	16	15	$\pm 6^{+0}_{-19}$	10
7	1	1	0.175	29	38	$\pm 9^{+6}_{-21}$	15
8	0	0	0.093	58	38	$\pm 48^{+0}_{-42}$	20
9	0	0	1.000	0	0	$\pm 0^{+0}_{-0}$	0
10	0	0	0.731	16	15	$\pm 15^{+0}_{-19}$	10
11	0	0	0.406	29	38	$\pm 26^{+6}_{-17}$	15
12	0	0	0.086	58	38	$\pm 100^{+62}_{-12}$	20

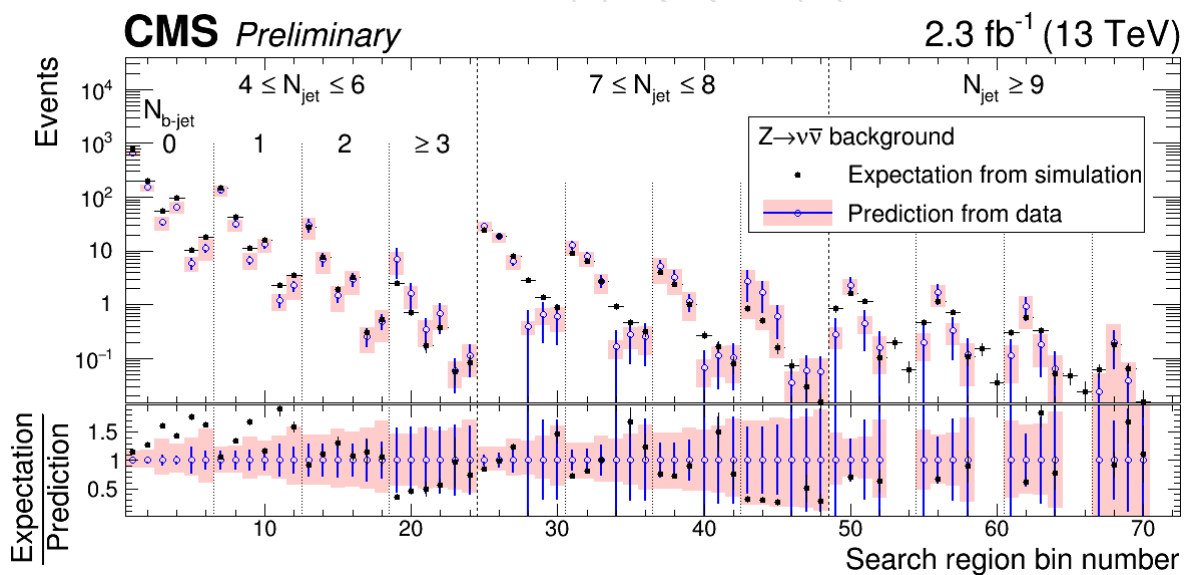


Figure 78: Predicted  $(Z \rightarrow v\bar{v}) + \text{jets}$  yields in the full 72-bin search space, from  $\gamma + \text{jets}$  data (for  $N_{b\text{-jet}} = 0$ ) combined with the extrapolation factors from  $(Z \rightarrow \ell^+\ell^-) + \text{jets}$  (for  $N_{b\text{-jet}} > 0$ ). Statistical (blue error bars) and systematic (pink shaded) uncertainties are plotted separately, and for comparison the expectation from simulation is overlaid as the black points with error bars.

## 9 Data/MC comparisons

In this chapter, we compare the distributions of search variables and other key observables in the standard model MC samples listed in Section 3.1 with all of the available data. The control samples studied in this section are summarized in Table 20. The distributions are presented in Figs. 79–85. The MC samples are normalized to the total integrated luminosity of the data. No other normalization corrections are applied to the MC samples.

In this analysis, all of the backgrounds are measured with data-driven methods. Some of these methods rely on small corrections taken from MC and validated in dedicated studies (e.g. using tag-and-probe to validate lepton and track isolation efficiencies). Thus it is not essential that the data and MC show strong shape agreement in the control or search regions. The main purpose of this chapter is understanding the limitations of the MC.

Table 20: Summary of the regions shown in this chapter and observations from the data-MC comparisons

Region	Selection	Processes	Data/MC	Observations
Single- $e$	Standard kinematic and $\Delta\phi$ cuts, exactly one isolated $e$ and no $\mu$ , do not apply track veto.	top, $W+jets$	0.762	MC over-predicts $H_T^{\text{miss}}$ and $H_T$ tails. $N_{\text{jet}}$ and $N_{\text{b-jet}}$ distributions are shifted to higher values in MC than in data. These trends may be highly-correlated.
Single- $\mu$	Standard kinematic and $\Delta\phi$ cuts, exactly one isolated $\mu$ and no $e$ , do not apply track veto.	top, $W+jets$	0.828	Same as above
Low- $\Delta\phi$	All cuts from search region, but invert $\Delta\phi(j, H_T^{\text{miss}})$ cut	QCD	0.755	Slopes of $H_T^{\text{miss}}$ and $H_T$ distributions are steeper in data. Again, $N_{\text{jet}}$ and $N_{\text{b-jet}}$ distributions are shifted to higher values in MC.
Double- $e$	Standard kinematic and $\Delta\phi$ cuts, exactly 2 isolated $e$ 's with opposite sign and invariant mass within 15 GeV of the $Z$ , zero isolated $\mu$ 's, do not apply isolated $e$ track veto.	$Z \rightarrow e^+e^-$	0.702	$N_{\text{jet}}$ and $N_{\text{b-jet}}$ distributions are shifted to higher values in MC than in data.
Double- $\mu$	Same as above with $e$ 's replaced with $\mu$ 's and vice versa.	$Z \rightarrow \mu^+\mu^-$	0.762	Same as above.
Single- $\gamma$	All cuts from search region with $N_{\text{b-jets}}=0$ , Single $\gamma$	$\gamma+jets$	1.02	Overall nice data mc agreement
Search region	All physics and event quality cuts	All BGs	0.646	No striking trends in shape comparisons

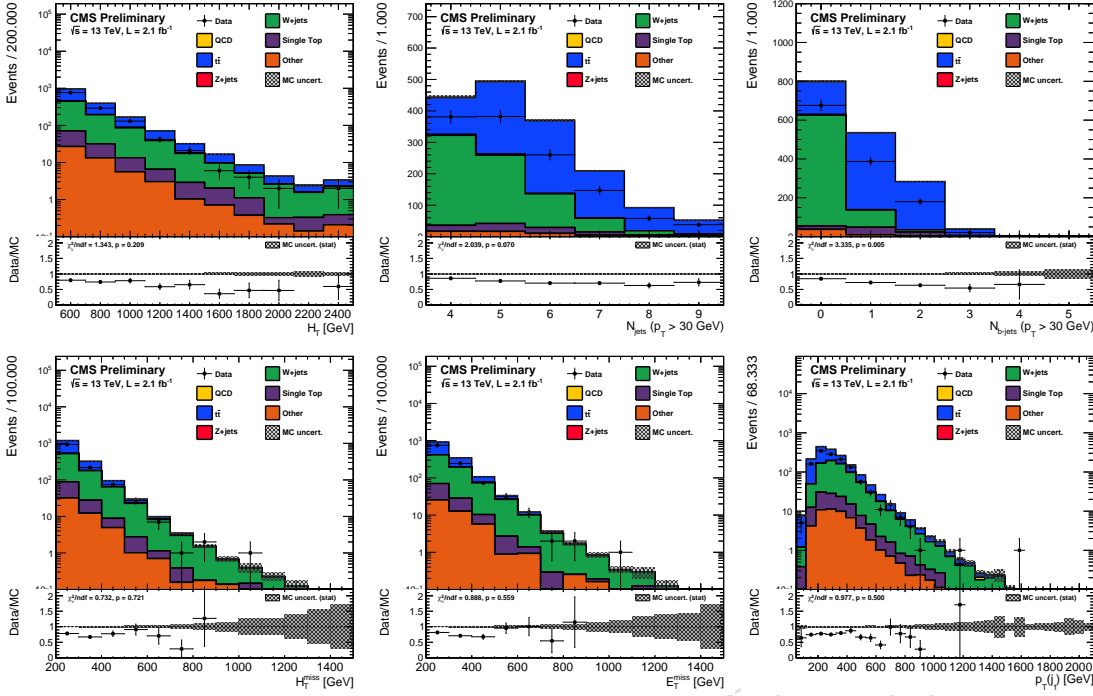


Figure 79: Distributions of the search variables, as well as the  $E_T^{\text{miss}}$  and leading jet  $p_T$  distributions, in the single-electron control region, which used to estimate the lost-lepton background (see Section 6.1)

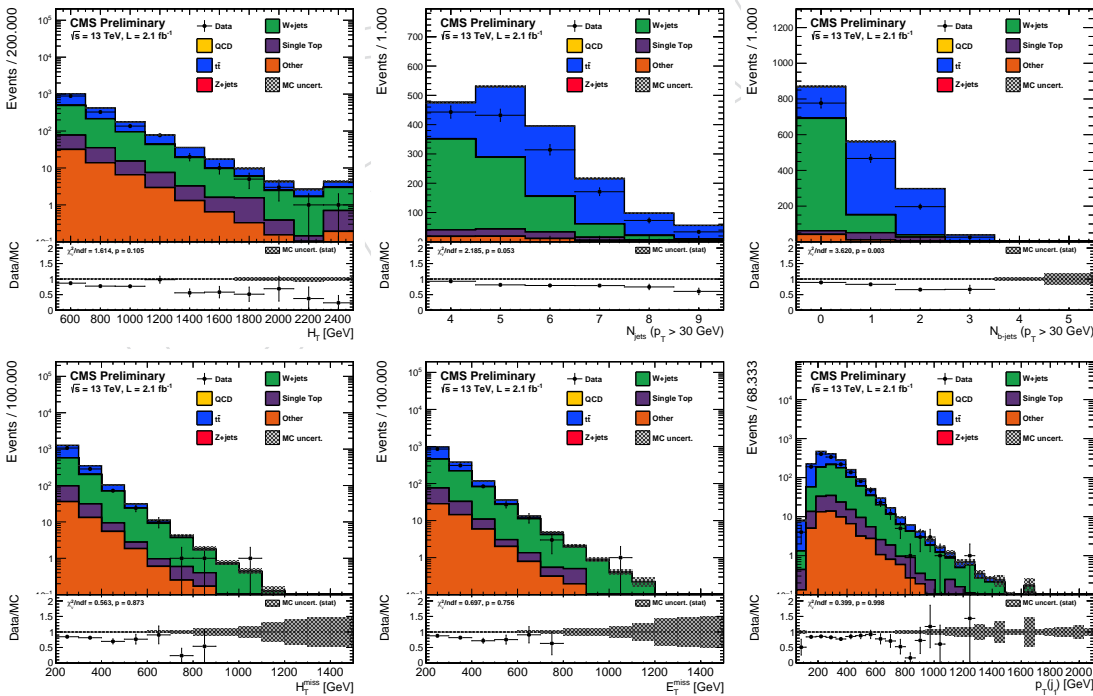


Figure 80: Distributions of the search variables, as well as the  $E_T^{\text{miss}}$  and leading jet  $p_T$  distributions, in the single-muon control region, which used to estimate the lost-lepton background (see Section 6.1)

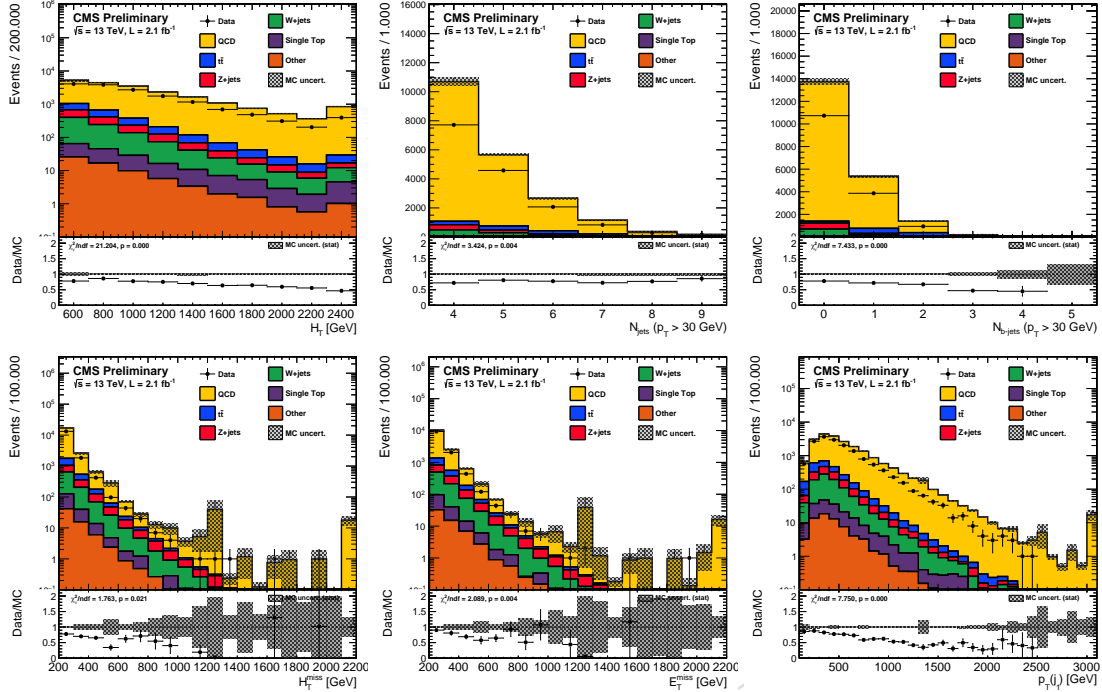


Figure 81: Distributions of the search variables, as well as the  $E_T^{\text{miss}}$  and leading jet  $p_T$  distributions, in the zero-lepton, inverted- $\Delta\phi(j, H_T^{\text{miss}})$  cut control region, which used to estimate the QCD multijet background (see Section 7.1)

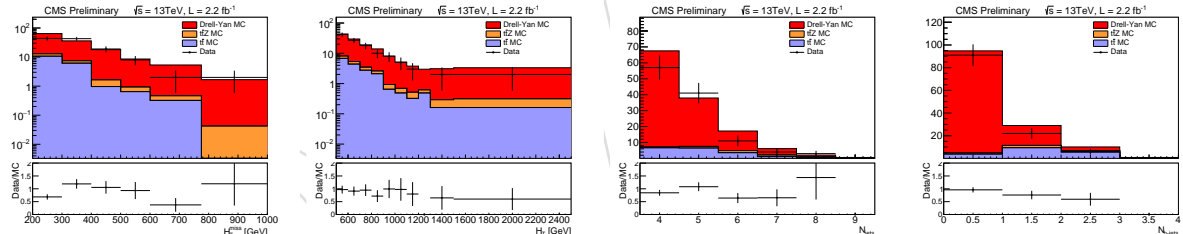


Figure 82: Distributions of the search variables in the double-electron control region, which is used, in conjunction with the double-muon and single-photon control regions, to estimate the Z invisible background (see Section 8)

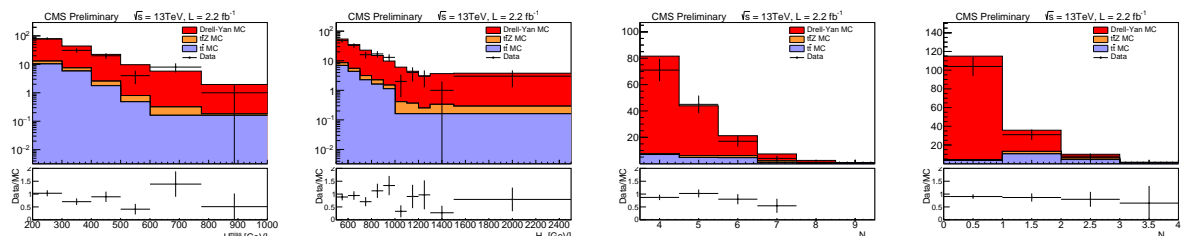


Figure 83: Distributions of the search variables in the double-muon control region, which is used, in conjunction with the double-electron and single-photon control regions, to estimate the Z invisible background (see Section 8)

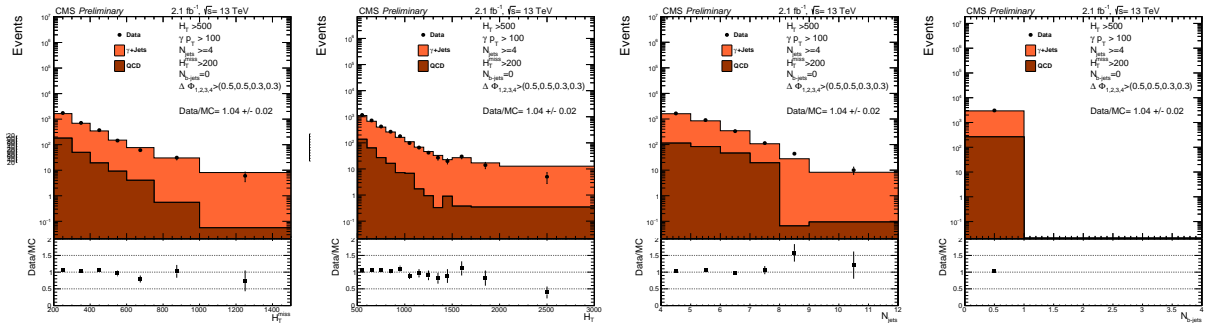


Figure 84: Distributions of the search variables in the single photon control region, which is used to estimate the z invisible background in zero btag regions.

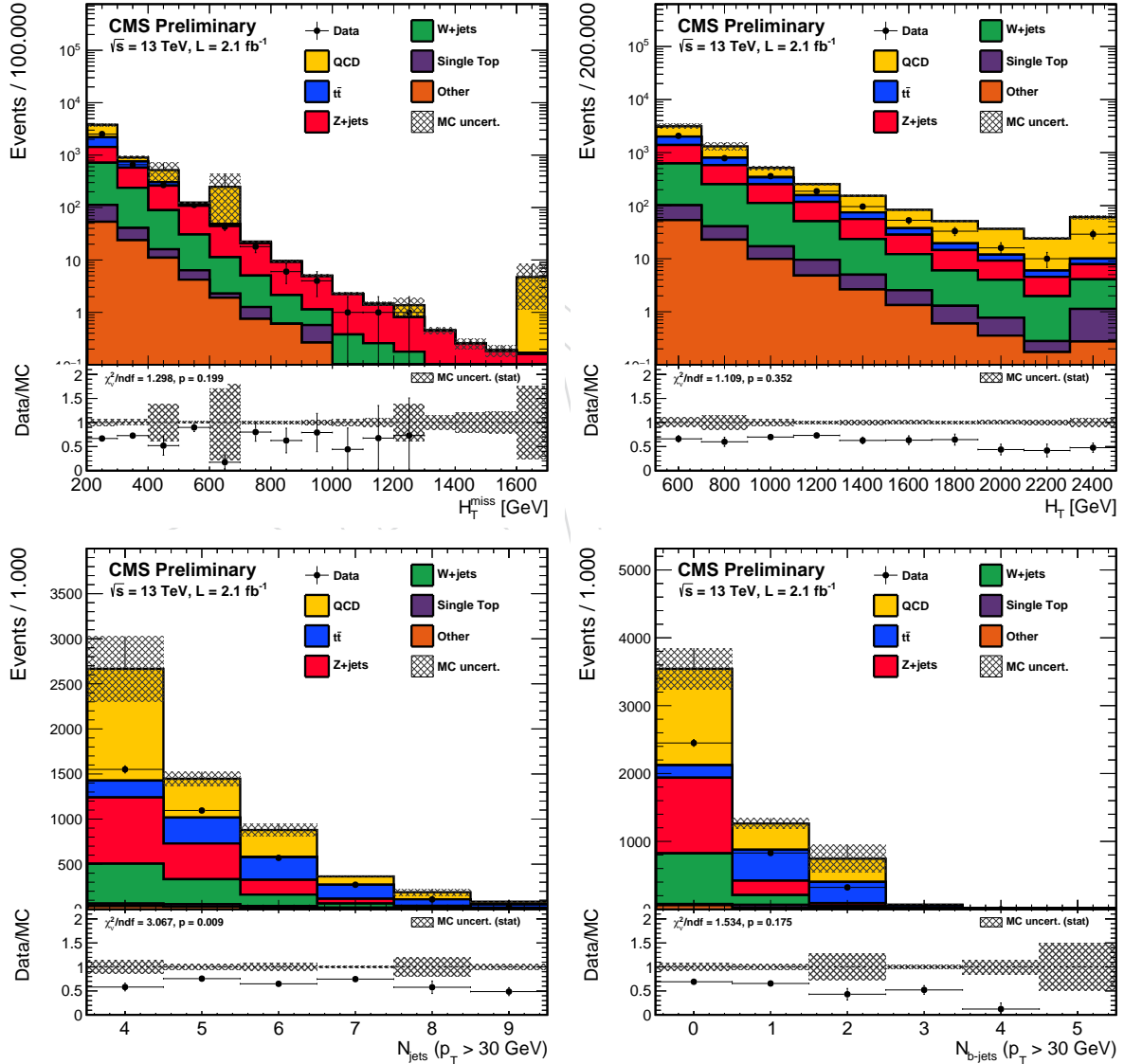


Figure 85: Distributions of the search variables in the zero-lepton search region. In the analysis, the MC are not used to estimate the backgrounds in this region.

## 1263 10 Signal Systematic Uncertainties

1264 We consider a variety of systematic uncertainties on the signal efficiency and distribution.

- 1265 • **Luminosity:** The recommendation for the full 2015 dataset is currently a flat uncer-  
1266 tainty of 4.6%.
- 1267 • **Isolated track veto:** The accuracy of the modeling of the isolated track veto efficiency  
1268 in MC is studied as described in Section 6.3. A flat uncertainty of 2% is assigned to  
1269 the T1tttt and T5qqqqVV signal samples to account for any data/MC differences,  
1270 which also covers any uncertainty from the lepton veto efficiency. The uncertainty  
1271 is negligible for the other signal models that are not expected to contain prompt  
1272 leptons or isolated tracks.
- 1273 • **PF Jet ID:** The PF Jet ID criteria, defined in Section 4, rely on numerous quantities,  
1274 some of which are not well-modeled in the fast simulation [24]. Therefore, the jet  
1275 ID criteria are not applied to the fast simulation samples. The efficiency of the event  
1276 cleaning cut on the signal samples is expected to be >99% from the full simulation,  
1277 so a correction of 0.99 is applied to the fast simulation. The uncertainty in this cor-  
1278 rection is taken to be a flat 1% uncertainty.
- 1279 • **b-tag efficiency:** The b-tagging and mistagging scale factors are functions of the jet  
1280  $p_T$  and  $\eta$ . They are applied according to the method “Event reweighting using scale  
1281 factors and MC b-tagging efficiencies ignoring the jet b-tagging status” [25]. The  
1282 scale factors are varied by their uncertainties and these variations are propagated  
1283 as migrations between the different signal bins, with no effect on the overall signal  
1284 efficiency. The b-tagging, charm-mistagging, and light flavor-mistagging scale  
1285 factors are varied independently.
- 1286 • **b-tag FastSim corrections:** The b-tagging and mistagging performance in the fast  
1287 simulation must be corrected to match the full simulation. Separate correction fac-  
1288 tors are derived for b-jets, c-jets, and light flavor jets, as functions of the jet  $p_T$  and  
1289  $\eta$  [26]. As with the scale factors above, the correction factors for each type of jet are  
1290 varied independently by their uncertainties and these variations are propagated as  
1291 migrations between the different signal bins. Currently, the correction factors and  
1292 uncertainties are derived from an average of  $t\bar{t}$  and signal events.

1293 The remaining uncertainties all affect both the signal efficiency and the shape of the signal  
1294 distributions by causing migrations between different signal bins. The PDF, scale, and ISR  
1295 uncertainty weights are normalized to maintain the total cross sections of the signal samples.

- 1296 • **MC statistics:** The signal MC sample statistical uncertainty.
- 1297 • **Trigger efficiency:** The trigger efficiencies are measured in the data (see Section 2.1).  
1298 The effect of the statistical and systematic uncertainties is at most 1.1% at low  $H_T^{\text{miss}}$ ,  
1299 and a complete tabulation is given in Table 1.
- 1300 • **Pileup reweighting:** The uncertainties in the pileup reweighting correction are de-  
1301 rived from the uncertainties in the minimum bias cross section and the difference  
1302 between the actual number of interactions and the observed number of interactions  
1303 in the data [27]. The minimum bias cross section for 13 TeV is currently estimated  
1304 to be 69 mb with an uncertainty of  $\pm 5\%$ . The correction is varied according to these  
1305 uncertainties, with a maximum effect of 0.5%.
- 1306 • **Scales:** The uncertainty is calculated using the envelope of the weights from varying  
1307 the renormalization and factorization scales,  $\mu_R$  and  $\mu_F$ , by a factor of 2 [28, 29]. The

1308 effect on the yield of non-compressed samples is less than 0.1% and on compressed  
 1309 samples ranges from 1–3%.

- **ISR:** Currently, no ISR correction is applied. Based on studies of the modeling of high- $p_T$  events in MadGraph, an uncertainty is evaluated as a function of the  $p_T$  of the gluino-gluino system:

$$\begin{aligned} 0 < p_T < 400 \text{ GeV} : 0\%, \\ 400 < p_T < 600 \text{ GeV} : 15\%, \\ 600 \text{ GeV} < p_T : 30\%. \end{aligned}$$

1310 The effect on the yield of non-compressed samples is less than 0.1% and on com-  
 1311 pressed samples ranges from 3–11%.

- **Jet Energy Corrections:** The jet energy corrections (JECs) are varied using the  $p_T$ - and  $\eta$ -dependent jet energy scale uncertainties from the official database, with a separate set of corrections for the fast simulation samples. These variations are propagated into the various jet-dependent variables, including:  $N_{\text{jet}}$ ,  $N_{\text{b-jet}}$ ,  $H_T$ ,  $H_T^{\text{miss}}$ ,  $\Delta\phi(H_T^{\text{miss}}, j_i)$ . The overall effect ranges from 0.5–4%.
- **PDFs:** The LHC4PDF prescription for the uncertainty on the total cross section is included as  $\pm 1$  sigma bands in the results plots. No additional uncertainty is considered for the uncertainty in the acceptance due to PDFs, as per SUSY group recommendation.

1321 Additionally, the effect of potential signal contamination in the control regions is considered.  
 1322 If some events observed in the control regions are in fact due to susy signal, the corresponding  
 1323 background prediction in the signal region will be too high. This effect is dealt with in the  
 1324 analysis by a corresponding reduction in the effective efficiency for the signal point. For the  
 1325 T1ttt signal the size of this reduction of effective signal efficiency is up to  $\sim 30\%$  for some  
 1326 signal bins and model points.

## 1327 11 Statistical treatment

1328 This section describes the statistical interpretation of the selected events in the search regions  
 1329 defined in Section 5. The implementation uses the Higgs Combination tool [30] to simultane-  
 1330 ously fit the signal regions and the control regions as described below.

### 1331 11.1 Implementation of background predictions

1332 Background predictions for the  $t\bar{t}$ ,  $W$ , QCD, and  $Z$  contributions are made according to the  
 1333 methods described in Sections 6.1, 6.2, 7.1, and 8. Details of the implementation of these  
 1334 methods in the statistical framework are described below.

1335 The predictions for the lost lepton and hadronic tau backgrounds in each signal bin are com-  
 1336 puted from a given number of 1 lepton control sample events which are weighted according to  
 1337 the expected contribution to the signal regions as described in Sec. 6.1 and 6.2. The statistical  
 1338 uncertainty on these backgrounds is modeled with log-normal nuisance parameters in each  
 1339 of the 72 search bins, which are taken as uncorrelated bin-to-bin. The weight applied to each  
 1340 control sample event is computed individually, which allows us to take maximal information  
 1341 from the data control sample. This procedure, however, does result in limited control sample  
 1342 statistics in some bins. To account for this uncertainty, we also include in the datacard an ad-  
 1343 dditional uncertainty modeled as a control sample with zero observed events multiplied by the

1344 average 0L/1L ratio for the given signal bin and background. Such an additional uncertainty  
 1345 is included for all 72 bins for both hadronic tau and lost lepton. We verify in toy studies that  
 1346 such an uncertainty term provides appropriate statistical coverage of background fluctuations.  
 1347 See App. J for more details.

1348 The lost lepton and hadronic tau backgrounds are predicted from partially overlapping 1 lepton  
 1349 control samples. To account for this, we take the statistical uncertainties for the hadronic tau  
 1350 and lost lepton background predictions to be 100% correlated with each other in the datacard  
 1351 in each of the 72 signal bins. This over models the true correlation, but the effect is only a small  
 1352 degradation of our sensitivity.

1353 The systematic uncertainties on the lost lepton and hadronic tau background predictions are  
 1354 described in Sec. 6.1 and 6.2. Below we describe how these uncertainties are implemented in  
 1355 the statistical framework. The MC closure test reveals no statistically significant non-closure  
 1356 and the uncertainties are treated as uncorrelated bin-to-bin. The electron and muon reconstruc-  
 1357 tion, identification, and isolation efficiencies are computed in bins of lepton  $p_T$ ,  $\eta$ , and nearby  
 1358 activity. The effect of each of these uncertainties is propagated to each search bin and the ef-  
 1359 fects are taken as a correlated shape across all search bins. Since the acceptance efficiency of  
 1360 the leptons is parametrized as a function of  $H_T, H_T^{\text{miss}}$  and  $N_{\text{jet}}$  the uncertainty on the lepton  
 1361 acceptance from MC modeling is considered correlated among  $N_{\text{b-jet}}$ . The effect of limited  
 1362 MC statistical precision for the acceptance and corrections for control region purity, dilepton  
 1363 contamination and the  $m_T$  cut efficiency are taken as uncorrelated bin-to-bin. The uncertainty  
 1364 due to the isolated track veto is taken as correlated across all search bins as the tag-and-probe  
 1365 studies used to verify the uncertainty show now significant variation. The above uncertainties  
 1366 apply to both lost lepton and hadronic tau. Additionally, the hadronic tau prediction includes  
 1367 the uncertainty due to the tau decay template modeling, which is taken as correlated across all  
 1368 search bins since template mismodeling will affect the prediction similarly in all bins. Overall,  
 1369 the largest uncertainties for the lost lepton and hadronic tau background predictions are from  
 1370 the statistical precision of the control samples.

1371 For the QCD contribution, low  $\Delta\phi_{\min}$  control regions are used to predict the signal region back-  
 1372 grounds as described in Sec. 7. The fit to determine the  $K$  and  $S$  factors, as described in Sec. 7.1,  
 1373 is performed outside of the full statistical framework. The background central values for each  
 1374 signal bin are provided as inputs to the datacard. The uncertainties on the  $K$  and  $S$  factors are  
 1375 modeled as a log-normal nuisance parameters with appropriate correlations included across  
 1376 the relevant bins. For example,  $S_{MHT,j}^{\text{QCD}}$  is correlated across the  $j$   $H_T^{\text{miss}}$  bins, but with different  
 1377 sizes of uncertainties for each bin. The  $H_T$ ,  $N_{\text{jet}}$ , and  $N_{\text{b-jet}}$  dimensions within each  $H_T^{\text{miss}}$  bin are  
 1378 100% correlated. The uncertainties on the  $K$  and  $S$  factors include the combined effect of the  
 1379 following sources of systematic uncertainty: the validity of the QCD fit model, subtraction of  
 1380 non-QCD contributions to the low  $\Delta\phi_{\min}$  control regions, limited statistical precision of the data  
 1381 in the low  $\Delta\phi_{\min}$  control regions, and limited MC statistical precision. Additional uncertainties  
 1382 are applied for potential non-closure of the method in MC and potential  $N_{\text{b-jet}}$  dependence.

1383 The Z background is derived from 18  $\gamma + \text{jets}$  control region yields corresponding to the signal  
 1384 bins with  $N_{\text{b-jet}} = 0$ . These control regions are included directly in the datacard and are multi-  
 1385 plied by the relevant factors described in Sec. 8 to arrive at the background prediction. A single  
 1386 nuisance parameter is used to model the correlated uncertainties on the  $Z/\gamma$  shape across the  
 1387 18 bins due to photon finding efficiency uncertainties. Additionally, the MC statistical uncer-  
 1388 tainty on  $Z/\gamma$  is included as uncorrelated nuisance parameters in each bin. The photon purity  
 1389 uncertainty is modeled as a correlated shape uncertainty, while the statistical uncertainty of  
 1390 the purity fits bin-by-bin are taken as uncorrelated. The uncertainty on the double ratio is in-

1391 cluded as a single correlated nuisance parameter with the same value for all bins. The  $N_{\text{b-jet}}$   
 1392 dependence of the background is determined by multiplying the  $N_{\text{b-jet}} = 0$  predictions by ap-  
 1393 propriate scale factors for  $N_{\text{b-jet}} = 1/N_{\text{b-jet}} = 0$ ,  $N_{\text{b-jet}} = 2/N_{\text{b-jet}} = 0$ , and  $N_{\text{b-jet}} = 3/N_{\text{b-jet}} = 0$ ,  
 1394 as described in Sec. 8. The uncertainties on these scale factors (also described in Sec. 8) are  
 1395 modeled as a single nuisance parameter to describe the uncertainty on the binomial factor as  
 1396 it propagates across all the signal bins and an additional uncertainty from the residual non-  
 1397 closure of the method. The non-closure uncertainty is taken as statistical in nature (no true  
 1398 non-closure of the method is observed, but the precision of the test is taken as the uncertainty)  
 1399 and separate nuisance parameters are included as uncorrelated between the bins to account for  
 1400 this uncertainty.

## 1401 11.2 Implementation of signal systematics

1402 Estimates of the various contributions to the signal efficiency systematic uncertainties are de-  
 1403 scribed in Sec. 10. Their treatment in the statistical framework is described below. All effects are  
 1404 modeled with log-normal PDFs. The jet energy scale, PDF, renormalization and factorization  
 1405 scale, ISR, MC statistics, and  $b$ -tag efficiency uncertainties are found to vary substantially as a  
 1406 function of the event kinematics and thus across the simplified model plane. Therefore we eval-  
 1407 uate these uncertainties point-by-point across the signal scans. Also, because these systematics  
 1408 affect the different bins of the analysis differently, they are evaluated separately in the various  
 1409 analysis bins, taking into account the correlations between the bins. The remaining effects are  
 1410 modeled with a single value for all signal points and correlated across all signal bins.

## 1411 11.3 Computation of signal significance and 95% C.L. exclusion Limits

The ratio of likelihood functions,  $\mathcal{L}$  is profiled to compute the expected signal significance in units of standard deviations. The likelihood is constructed as the product of Poisson PDFs of observing  $N$  events, given a mean  $n$ , where  $n$  depends on the floating parameters in the likelihood. The test statistic used in the profile likelihood calculations is given by

$$q_\mu = -2 \ln (\mathcal{L}_\mu / \mathcal{L}_{max})$$

1412 where the  $\mathcal{L}_\mu$  is the maximum likelihood at a given signal strength  $\mu$  and  $\mathcal{L}_{max}$  is the maximum  
 1413 floating all parameters. The profile likelihood signal significance is given by  $\sqrt{q_0}$  as a number  
 1414 of standard deviations. The likelihood ratio is profiled using the combine tool and is cross-  
 1415 checked with a stand alone signal strength scan in RooStats. The likelihood profiling in both  
 1416 algorithms shows good agreement and validates the significance computation done using the  
 1417 combine tool.

For setting limits, we use the LHC-style  $CL_s$  approach in the Higgs Combine tool. The CLs ratio is the ratio of confidence intervals:

$$CL_s = \frac{CL_{s+b}}{CL_b}$$

1418 where  $CL_b$  is the confidence interval in the background only region and  $CL_{s+b}$  is the confi-  
 1419 dence interval in the background region with signal. The 95% confidence level is given by the  
 1420 probability that a test statistic  $Q$  is less than the observed value in data:  $P_{95\%}(Q < Q_{obs})$ , so  
 1421 gives a probability of the data being discrepant with the background only hypothesis. The im-  
 1422 plementation of the fit technique in the Higgs Combination tool is tested against a standalone  
 1423 implementation in RooStats for a single bin, and found to demonstrate good agreement. The  
 1424 test statistic  $Q$  comes from a modified Profile Likelihood with constraints on the upper bound  
 1425 of the signal strength, so that the method gives an upper limit instead of a two-sided limit.

1426 The sensitivity of the analysis will scale with the exclusion power, so the 95% confidence level  
 1427 upper exclusion limits will decrease with increasing sensitivity to signal.

## 1428 11.4 Fit validation

1429 To ensure proper behavior of the complete fit, it is subjected to several fit validation studies.

### 1430 11.4.1 Linear fit yield response

1431 The fitted value of the signal strength is tested by producing a pseudo-dataset based on the  
 1432 expected observed counts for all observables in the fit (signal and control region bins). The test  
 1433 is performed for the 6 representative signal point with the standard model expectation based  
 1434 on  $3 \text{ fb}^{-1}$ . Signal strengths of zero through five times the expected signal are included. The  
 1435 fitted signal strength is plotted against the injected signal strength in Fig. 86. The expected  
 1436 linear performance is observed with no bias in the fitted value to within a maximum of  $\sim 20\%$   
 1437 of the fit uncertainty.

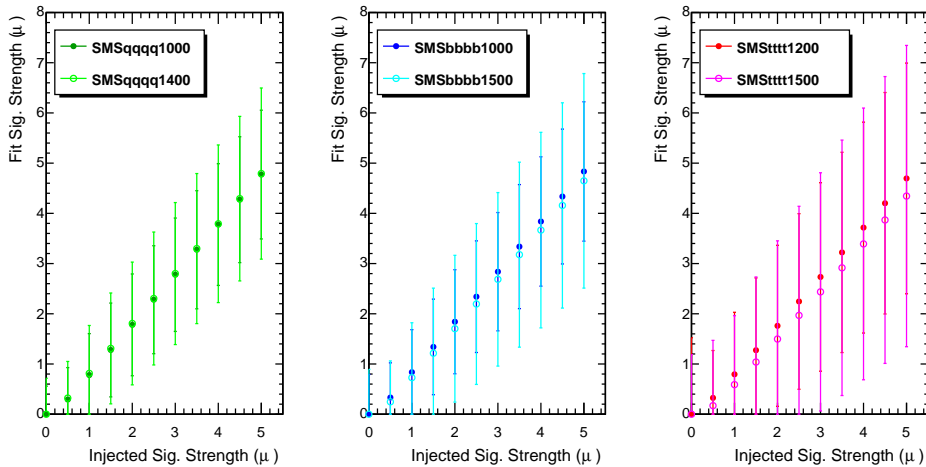


Figure 86: Fitting signal strength vs injected value for 6 representative SUSY signal points based on  $3 \text{ fb}^{-1}$ .

### 1438 11.4.2 Individual background tests

1439 An additional fit validation study is performed where the performance of each background is  
 1440 tested individually. The expected linear fit response is observed for each of QCD (fake MET),  
 1441  $Z$ , lost lepton, and hadronic tau backgrounds individually as shown in Fig. 87.

## 1442 12 Results

1443 This section contains the results of the search. The observations in the signal regions are found  
 1444 to be in generally good agreement with the predicted backgrounds. For the 72 search bins, the  
 1445 observed data and the pre-fit predictions for each background component are shown in Fig. 88  
 1446 and Tables 21, 22, and 23.

1447 Figure 89 shows the background predictions in each of the search bins from the post-fit results  
 1448 compared to the data observation in each bin.

1449 Table 24 shows the post-fit background predictions in each search bin.

Table 21: Observed number of events and pre-fit background predictions in the  $4 \leq N_{\text{jet}} \leq 6$  search bins.

Bin	$H_T^{\text{miss}}$ [GeV]	$H_T$ [GeV]	$N_{\text{jet}}$	$N_{\text{b-jet}}$	Lost- $e/\mu$	$\tau \rightarrow \text{had}$	$Z \rightarrow \nu\nu$	QCD	Total Pred.	Obs.
1	200-500	500-800	4-6	0	318.76 <sup>+11.84+28.74</sup> <sub>-11.82-27.67</sub>	310.30 <sup>+10.78+19.37</sup> <sub>-10.77-18.87</sub>	631.79 <sup>+13.20+102.80</sup> <sub>-13.20-81.76</sub>	212.06 <sup>+3.71+116.20</sup> <sub>-3.64-116.20</sub>	1472.91 <sup>+26.45+58.72</sup> <sub>-26.42-145.98</sub>	1602
2	200-500	800-1200	4-6	0	59.15 <sup>+4.33+5.47</sup> <sub>-4.29-5.28</sub>	69.08 <sup>+5.21+5.67</sup> <sub>-5.19-5.59</sub>	144.92 <sup>+6.29+25.92</sup> <sub>-6.29-20.42</sub>	98.29 <sup>+1.77+35.77</sup> <sub>-1.74-35.77</sub>	371.44 <sup>+11.57+44.84</sup> <sub>-11.51-41.90</sub>	390
3	200-500	1200+	4-6	0	13.84 <sup>+2.25+1.38</sup> <sub>-2.17-1.30</sub>	14.38 <sup>+2.57+1.56</sup> <sub>-2.53-1.51</sub>	31.36 <sup>+2.95+11.93</sup> <sub>-2.95-8.33</sub>	87.33 <sup>+1.88+25.47</sup> <sub>-1.84-25.47</sub>	146.91 <sup>+5.96+28.20</sup> <sub>-5.85-26.87</sub>	149
4	500-750	500-1200	4-6	0	11.49 <sup>+1.93+1.57</sup> <sub>-1.84-1.53</sub>	8.92 <sup>+1.72+1.33</sup> <sub>-1.66-1.32</sub>	61.62 <sup>+4.41+18.46</sup> <sub>-4.41-13.29</sub>	0.39 <sup>+0.12+0.44</sup> <sub>-0.09-0.30</sub>	82.41 <sup>+5.73+18.57</sup> <sub>-5.64-13.45</sub>	120
5	500-750	1200+	4-6	0	1.95 <sup>+1.04+0.50</sup> <sub>-0.90-0.50</sub>	0.56 <sup>+0.52+0.15</sup> <sub>-0.25-0.15</sub>	5.45 <sup>+1.32+2.12</sup> <sub>-1.32-1.51</sub>	0.94 <sup>+0.17+0.98</sup> <sub>-0.14-0.80</sub>	8.89 <sup>+2.05+2.39</sup> <sub>-1.76-1.79</sub>	13
6	750+	800+	4-6	0	1.39 <sup>+0.93+0.24</sup> <sub>-0.77-0.23</sub>	1.77 <sup>+0.99+0.34</sup> <sub>-0.88-0.33</sub>	10.35 <sup>+1.80+5.81</sup> <sub>-1.80-4.06</sub>	0.24 <sup>+0.09+0.26</sup> <sub>-0.07-0.17</sub>	13.75 <sup>+2.64+5.83</sup> <sub>-2.45-4.08</sub>	12
7	200-500	500-800	4-6	1	171.23 <sup>+8.42+16.95</sup> <sub>-8.39-16.43</sub>	205.71 <sup>+8.53+12.98</sup> <sub>-8.52-12.60</sub>	127.47 <sup>+20.90+30.82</sup> <sub>-20.90-28.14</sub>	67.01 <sup>+2.17+39.26</sup> <sub>-2.10-39.26</sub>	571.42 <sup>+27.00+54.04</sup> <sub>-26.97-52.55</sub>	499
8	200-500	800-1200	4-6	1	31.37 <sup>+3.98+2.95</sup> <sub>-3.94-2.86</sub>	30.41 <sup>+3.19+2.01</sup> <sub>-3.16-1.93</sub>	29.24 <sup>+4.92+7.40</sup> <sub>-4.92-6.66</sub>	35.79 <sup>+1.13+14.96</sup> <sub>-1.09-14.96</sub>	126.81 <sup>+8.77+17.04</sup> <sub>-8.71-16.73</sub>	123
9	200-500	1200+	4-6	1	6.29 <sup>+1.77+0.84</sup> <sub>-1.64-0.82</sub>	8.86 <sup>+2.08+0.90</sup> <sub>-2.03-0.83</sub>	6.33 <sup>+1.19+2.66</sup> <sub>-1.19-2.03</sub>	31.20 <sup>+1.18+11.20</sup> <sub>-1.13-11.20</sub>	52.67 <sup>+4.20+11.57</sup> <sub>-4.02-11.44</sub>	44
10	500-750	500-1200	4-6	1	3.07 <sup>+1.17+0.60</sup> <sub>-1.00-0.59</sub>	2.64 <sup>+0.96+0.49</sup> <sub>-0.85-0.48</sub>	12.43 <sup>+2.21+4.34</sup> <sub>-2.21-3.48</sub>	0.07 <sup>+0.04+0.09</sup> <sub>-0.02-0.05</sub>	18.21 <sup>+3.07+4.40</sup> <sub>-2.88-3.57</sub>	22
11	500-750	1200+	4-6	1	0.00 <sup>+0.52+0.00</sup> <sub>-0.42-0.00</sub>	0.07 <sup>+0.46+0.02</sup> <sub>-0.04-0.02</sub>	1.10 <sup>+0.32+0.47</sup> <sub>-0.32-0.36</sub>	0.37 <sup>+0.12+0.41</sup> <sub>-0.09-0.28</sub>	1.54 <sup>+1.04+0.62</sup> <sub>-1.04-0.46</sub>	1
12	750+	800+	4-6	1	0.00 <sup>+0.50+0.00</sup> <sub>-0.00-0.00</sub>	0.54 <sup>+0.56+0.13</sup> <sub>-0.32-0.13</sub>	2.09 <sup>+0.50+1.23</sup> <sub>-0.50-0.90</sub>	0.02 <sup>+0.06+0.05</sup> <sub>-0.00-0.02</sub>	2.64 <sup>+1.18+1.24</sup> <sub>-0.59-0.91</sub>	2
13	200-500	500-800	4-6	2	71.85 <sup>+6.08+7.16</sup> <sub>-6.05-6.67</sub>	77.18 <sup>+4.98+5.48</sup> <sub>-4.96-5.34</sub>	28.08 <sup>+8.07+12.45</sup> <sub>-8.07-12.14</sub>	15.29 <sup>+1.11+9.10</sup> <sub>-1.04-9.10</sub>	192.40 <sup>+13.73+17.63</sup> <sub>-13.69-17.41</sub>	202
14	200-500	800-1200	4-6	2	18.80 <sup>+4.79+2.53</sup> <sub>-4.75-2.20</sub>	17.30 <sup>+2.67+1.29</sup> <sub>-2.63-1.25</sub>	6.44 <sup>+1.87+2.81</sup> <sub>-1.87-2.81</sub>	9.25 <sup>+0.62+3.94</sup> <sub>-0.58-3.94</sub>	51.80 <sup>+7.71+5.51</sup> <sub>-7.63-5.46</sub>	45
15	200-500	1200+	4-6	2	2.06 <sup>+1.20+0.23</sup> <sub>-0.98-0.22</sub>	3.31 <sup>+1.28+0.34</sup> <sub>-1.20-0.32</sub>	1.39 <sup>+0.42+0.78</sup> <sub>-0.42-0.68</sub>	5.50 <sup>+0.53+2.08</sup> <sub>-0.48-2.08</sub>	12.26 <sup>+2.58+2.26</sup> <sub>-2.27-2.22</sub>	15
16	500-750	500-1200	4-6	2	1.90 <sup>+1.84+0.65</sup> <sub>-1.72-0.17</sub>	2.26 <sup>+0.94+0.86</sup> <sub>-0.82-0.86</sub>	2.74 <sup>+0.81+1.40</sup> <sub>-0.81-1.27</sub>	0.03 <sup>+0.02+0.04</sup> <sub>-0.01-0.02</sub>	6.92 <sup>+2.90+1.65</sup> <sub>-2.67-1.54</sub>	5
17	500-750	1200+	4-6	2	3.33 <sup>+3.37+1.35</sup> <sub>-3.33-0.00</sub>	0.07 <sup>+0.46+0.02</sup> <sub>-0.45-0.01</sub>	0.24 <sup>+0.09+0.14</sup> <sub>-0.09-0.12</sub>	0.07 <sup>+0.08+0.09</sup> <sub>-0.04-0.03</sub>	3.71 <sup>+3.83+0.16</sup> <sub>-3.38-0.12</sub>	0
18	750+	800+	4-6	2	0.00 <sup>+0.46+0.00</sup> <sub>-0.00-0.00</sub>	0.04 <sup>+0.46+0.02</sup> <sub>-0.03-0.01</sub>	0.46 <sup>+0.15+0.32</sup> <sub>-0.15-0.26</sub>	0.03 <sup>+0.06+0.04</sup> <sub>-0.02-0.01</sub>	0.53 <sup>+0.93+0.32</sup> <sub>-0.16-0.26</sub>	1
19	200-500	500-800	4-6	3+	6.27 <sup>+1.76+0.79</sup> <sub>-1.65-0.78</sub>	10.82 <sup>+2.17+1.66</sup> <sub>-2.12-1.62</sub>	6.48 <sup>+3.77+3.00</sup> <sub>-3.77-2.71</sub>	1.26 <sup>+0.38+0.90</sup> <sub>-0.29-0.90</sub>	24.83 <sup>+5.46+3.61</sup> <sub>-5.34-3.37</sub>	17
20	200-500	800-1200	4-6	3+	0.24 <sup>+0.67+0.03</sup> <sub>-0.24-0.00</sub>	1.10 <sup>+0.61+0.15</sup> <sub>-0.40-0.14</sub>	1.49 <sup>+0.87+0.70</sup> <sub>-0.87-0.62</sub>	0.71 <sup>+0.20+0.39</sup> <sub>-0.16-0.39</sub>	3.54 <sup>+1.56+0.81</sup> <sub>-1.09-0.75</sub>	7
21	200-500	1200+	4-6	3+	0.80 <sup>+0.91+0.13</sup> <sub>-0.57-0.13</sub>	0.11 <sup>+0.46+0.02</sup> <sub>-0.05-0.02</sub>	0.32 <sup>+0.19+0.19</sup> <sub>-0.19-0.13</sub>	0.72 <sup>+0.23+0.37</sup> <sub>-0.18-0.37</sub>	1.95 <sup>+1.40+0.43</sup> <sub>-0.67-0.41</sub>	3
22	500-750	500-1200	4-6	3+	0.00 <sup>+0.63+0.00</sup> <sub>-0.00-0.00</sub>	0.03 <sup>+0.46+0.01</sup> <sub>-0.01-0.01</sub>	0.63 <sup>+0.37+0.33</sup> <sub>-0.37-0.26</sub>	0.05 <sup>+0.11+0.08</sup> <sub>-0.04-0.01</sub>	0.71 <sup>+1.15+0.34</sup> <sub>-0.37-0.26</sub>	0
23	500-750	1200+	4-6	3+	0.00 <sup>+0.77+0.00</sup> <sub>-0.00-0.00</sub>	0.00 <sup>+0.46+0.00</sup> <sub>-0.00-0.00</sub>	0.06 <sup>+0.04+0.03</sup> <sub>-0.04-0.02</sub>	0.00 <sup>+0.05+0.01</sup> <sub>-0.00-0.00</sub>	0.06 <sup>+1.23+0.03</sup> <sub>-0.04-0.02</sub>	0
24	750+	800+	4-6	3+	0.00 <sup>+0.58+0.00</sup> <sub>-0.00-0.00</sub>	0.00 <sup>+0.46+0.00</sup> <sub>-0.00-0.00</sub>	0.11 <sup>+0.06+0.08</sup> <sub>-0.06-0.04</sub>	0.00 <sup>+0.04+0.02</sup> <sub>-0.00-0.00</sub>	0.11 <sup>+1.04+0.08</sup> <sub>-0.06-0.04</sub>	93

## 12 Results

Table 22: Observed number of events and pre-fit background predictions in the  $7 \leq N_{\text{jet}} \leq 8$  search bins.

Bin	$H_T^{\text{miss}}$ [GeV]	$H_T$ [GeV]	$N_{\text{jet}}$	$N_{\text{b-jet}}$	$\text{Lost-}e/\mu$	$\tau \rightarrow \text{had}$	$Z \rightarrow \nu\nu$	QCD	Total Pred.	Obs.
25	200-500	500-800	7-8	0	$18.78^{+3.08+2.31}_{-3.05-2.20}$	$24.50^{+2.68+2.02}_{-2.64-2.00}$	$27.40^{+2.78+6.72}_{-2.78-5.14}$	$13.75^{+1.68+8.72}_{-1.50-8.72}$	$84.42^{+6.61+11.40}_{-6.51-10.55}$	85
26	200-500	800-1200	7-8	0	$12.53^{+1.83+2.19}_{-1.79-2.17}$	$15.60^{+2.26+1.27}_{-2.22-1.25}$	$17.29^{+2.25+4.19}_{-2.25-3.17}$	$15.03^{+1.14+7.08}_{-1.06-7.08}$	$60.46^{+4.81+8.60}_{-4.72-8.15}$	60
27	200-500	1200+	7-8	0	$2.88^{+1.15+0.32}_{-1.07-0.31}$	$3.50^{+1.29+0.31}_{-1.20-0.30}$	$6.03^{+1.29+2.34}_{-1.29-1.66}$	$21.78^{+1.50+8.94}_{-1.40-8.94}$	$34.19^{+3.14+9.25}_{-2.96-9.10}$	42
28	500-750	500-1200	7-8	0	$0.53^{+0.45+0.14}_{-0.26-0.13}$	$0.81^{+0.66+0.19}_{-0.47-0.19}$	$0.36^{+0.36+0.12}_{-0.36-0.00}$	$0.06^{+0.10+0.09}_{-0.04-0.02}$	$1.75^{+1.17+0.28}_{-0.82-0.23}$	1
29	500-750	1200+	7-8	0	$1.03^{+0.88+0.33}_{-0.80-0.24}$	$1.44^{+0.93+0.29}_{-0.80-0.29}$	$0.60^{+0.43+0.26}_{-0.43-0.18}$	$0.25^{+0.17+0.29}_{-0.11-0.14}$	$3.33^{+1.87+0.54}_{-1.66-0.43}$	1
30	750+	800+	7-8	0	$0.17^{+0.38+0.09}_{-0.17-0.00}$	$0.17^{+0.49+0.11}_{-0.17-0.00}$	$0.56^{+0.40+0.34}_{-0.40-0.16}$	$0.19^{+0.15+0.22}_{-0.09-0.10}$	$1.09^{+0.97+0.41}_{-0.53-0.19}$	1
31	200-500	500-800	7-8	1	$25.79^{+2.93+3.13}_{-2.90-3.04}$	$31.75^{+2.96+2.34}_{-2.93-2.30}$	$11.68^{+2.24+3.63}_{-2.24-3.82}$	$7.61^{+1.31+5.13}_{-1.13-5.13}$	$76.83^{+6.44+7.35}_{-6.34-7.44}$	63
32	200-500	800-1200	7-8	1	$9.01^{+1.63+1.28}_{-1.58-1.10}$	$14.38^{+2.02+1.35}_{-1.97-1.34}$	$7.37^{+1.54+2.27}_{-1.54-2.39}$	$7.26^{+0.83+3.76}_{-0.74-3.76}$	$38.03^{+4.05+4.72}_{-3.94-4.78}$	43
33	200-500	1200+	7-8	1	$3.25^{+1.12+0.36}_{-1.01-0.34}$	$6.33^{+1.49+0.67}_{-1.42-0.66}$	$2.57^{+0.69+1.11}_{-0.69-0.99}$	$12.84^{+1.16+5.91}_{-1.07-5.91}$	$24.99^{+2.94+6.06}_{-2.75-6.04}$	29
34	500-750	500-1200	7-8	1	$0.46^{+0.49+0.11}_{-0.27-0.11}$	$0.51^{+0.55+0.11}_{-0.29-0.11}$	$0.15^{+0.16+0.06}_{-0.15-0.00}$	$0.00^{+0.11+0.03}_{-0.00-0.00}$	$1.12^{+1.06+0.17}_{-0.58-0.16}$	2
35	500-750	1200+	7-8	1	$0.00^{+0.40+0.00}_{-0.00-0.00}$	$0.25^{+0.49+0.05}_{-0.18-0.05}$	$0.26^{+0.19+0.12}_{-0.19-0.07}$	$0.12^{+0.14+0.15}_{-0.07-0.05}$	$0.63^{+0.92+0.20}_{-0.27-0.10}$	2
36	750+	800+	7-8	1	$0.00^{+0.45+0.00}_{-0.00-0.00}$	$0.02^{+0.46+0.01}_{-0.01-0.00}$	$0.24^{+0.17+0.15}_{-0.17-0.07}$	$0.00^{+0.08+0.02}_{-0.00-0.00}$	$0.25^{+0.93+0.15}_{-0.17-0.07}$	1
37	200-500	500-800	7-8	2	$13.15^{+2.16+1.54}_{-2.11-1.51}$	$16.03^{+1.87+1.20}_{-1.81-1.18}$	$4.79^{+1.46+2.36}_{-1.46-2.43}$	$0.20^{+0.34+0.59}_{-0.05-0.15}$	$34.17^{+4.29+3.10}_{-4.18-3.10}$	32
38	200-500	800-1200	7-8	2	$6.33^{+1.29+0.74}_{-1.22-0.71}$	$10.73^{+1.82+0.89}_{-1.76-0.88}$	$3.03^{+0.95+1.48}_{-0.95-1.53}$	$2.10^{+0.47+1.16}_{-0.39-1.16}$	$22.19^{+3.29+2.20}_{-3.15-2.23}$	17
39	200-500	1200+	7-8	2	$1.73^{+0.79+0.20}_{-0.62-0.19}$	$1.89^{+0.88+0.18}_{-0.75-0.18}$	$1.06^{+0.38+0.61}_{-0.38-0.58}$	$3.30^{+0.61+1.61}_{-0.52-1.61}$	$7.97^{+1.81+1.74}_{-1.51-1.73}$	4
40	500-750	500-1200	7-8	2	$0.00^{+0.39+0.00}_{-0.00-0.00}$	$0.04^{+0.46+0.01}_{-0.02-0.01}$	$0.06^{+0.07+0.03}_{-0.06-0.00}$	$0.00^{+0.11+0.03}_{-0.00-0.00}$	$0.10^{+0.86+0.05}_{-0.06-0.01}$	0
41	500-750	1200+	7-8	2	$0.00^{+0.43+0.00}_{-0.00-0.00}$	$0.07^{+0.47+0.04}_{-0.07-0.00}$	$0.11^{+0.08+0.06}_{-0.08-0.02}$	$0.03^{+0.10+0.05}_{-0.03-0.00}$	$0.21^{+0.90+0.08}_{-0.11-0.03}$	1
42	750+	800+	7-8	2	$0.00^{+0.34+0.00}_{-0.00-0.00}$	$0.13^{+0.48+0.06}_{-0.13-0.00}$	$0.10^{+0.07+0.07}_{-0.07-0.02}$	$0.00^{+0.08+0.02}_{-0.00-0.00}$	$0.23^{+0.82+0.08}_{-0.15-0.02}$	0
43	200-500	500-800	7-8	3+	$3.93^{+1.25+0.46}_{-1.23-0.45}$	$5.78^{+1.31+0.68}_{-1.23-0.67}$	$2.54^{+1.50+1.76}_{-1.50-1.04}$	$1.06^{+0.60+0.88}_{-0.40-0.66}$	$13.31^{+3.03+2.13}_{-2.85-1.47}$	3
44	200-500	800-1200	7-8	3+	$0.44^{+0.49+0.05}_{-0.25-0.05}$	$1.66^{+0.96+0.26}_{-0.60-0.26}$	$1.60^{+0.96+1.11}_{-0.96-0.65}$	$0.58^{+0.30+0.40}_{-0.21-0.37}$	$4.28^{+1.60+1.21}_{-1.30-0.79}$	4
45	200-500	1200+	7-8	3+	$0.66^{+0.72+0.12}_{-0.52-0.12}$	$0.65^{+0.61+0.10}_{-0.40-0.10}$	$0.56^{+0.35+0.42}_{-0.33-0.21}$	$0.05^{+0.18+0.11}_{-0.00-0.05}$	$1.92^{+1.39+0.46}_{-0.99-0.27}$	1
46	500-750	500-1200	7-8	3+	$0.00^{+0.52+0.00}_{-0.00-0.00}$	$0.00^{+0.45+0.00}_{-0.00-0.00}$	$0.03^{+0.04+0.02}_{-0.03-0.01}$	$0.04^{+0.09+0.06}_{-0.03-0.01}$	$0.07^{+0.98+0.06}_{-0.05-0.01}$	0
47	500-750	1200+	7-8	3+	$0.00^{+0.47+0.00}_{-0.00-0.00}$	$0.00^{+0.46+0.00}_{-0.00-0.00}$	$0.06^{+0.05+0.04}_{-0.05-0.00}$	$0.00^{+0.09+0.01}_{-0.00-0.00}$	$0.06^{+0.94+0.04}_{-0.05-0.00}$	0
48	750+	800+	7-8	3+	$0.00^{+0.61+0.00}_{-0.00-0.00}$	$0.01^{+0.45+0.01}_{-0.01-0.00}$	$0.05^{+0.05+0.05}_{-0.05-0.00}$	$0.00^{+0.08+0.02}_{-0.00-0.00}$	$0.06^{+1.07+0.05}_{-0.05-0.00}$	0

Table 23: Observed number of events and pre-fit background predictions in the  $N_{\text{jet}} \geq 9$  search bins.

Bin	$H_T^{\text{miss}}$ [GeV]	$H_T$ [GeV]	$N_{\text{jet}}$	$N_{\text{b-jet}}$	Lost-e/ $\mu$	$\tau \rightarrow \text{had}$	$Z \rightarrow \nu\nu$	QCD	Total Pred.	Obs.
49	200-500	500-800	9+	0	0.99 $^{+0.59+0.21}_{-0.45-0.21}$	0.61 $^{+0.52+0.09}_{-0.23-0.09}$	0.26 $^{+0.26+0.12}_{-0.26-0.00}$	0.84 $^{+0.49+0.77}_{-0.32-0.52}$	2.69 $^{+1.24+0.81}_{-0.80-0.57}$	2
50	200-500	800-1200	9+	0	2.12 $^{+0.72+0.33}_{-0.62-0.33}$	3.92 $^{+1.17+0.41}_{-1.08-0.41}$	2.14 $^{+0.81+0.81}_{-0.81-0.64}$	0.71 $^{+0.29+0.54}_{-0.21-0.50}$	8.89 $^{+2.08+1.11}_{-1.90-0.97}$	12
51	200-500	1200+	9+	0	0.58 $^{+0.54+0.08}_{-0.35-0.08}$	1.05 $^{+0.76+0.16}_{-0.61-0.15}$	0.42 $^{+0.30+0.18}_{-0.30-0.12}$	3.46 $^{+0.59+2.31}_{-0.51-2.31}$	5.51 $^{+1.46+2.32}_{-1.12-2.32}$	8
52	500-750	500-1200	9+	0	0.00 $^{+0.34+0.00}_{-0.00-0.00}$	0.00 $^{+0.46+0.00}_{-0.00-0.00}$	0.15 $^{+0.15+0.11}_{-0.15-0.00}$	0.00 $^{+0.10+0.04}_{-0.00-0.00}$	0.15 $^{+0.82+0.11}_{-0.15-0.00}$	0
53	500-750	1200+	9+	0	0.14 $^{+0.36+0.05}_{-0.14-0.00}$	0.02 $^{+0.46+0.01}_{-0.02-0.00}$	0.00 $^{+0.76+0.00}_{-0.00-0.00}$	0.00 $^{+0.08+0.04}_{-0.00-0.00}$	0.17 $^{+1.13+0.04}_{-0.17-0.00}$	0
54	750+	800+	9+	0	0.00 $^{+0.28+0.00}_{-0.00-0.00}$	0.00 $^{+0.46+0.00}_{-0.00-0.00}$	0.00 $^{+0.79+0.00}_{-0.00-0.00}$	0.00 $^{+0.07+0.04}_{-0.00-0.00}$	0.00 $^{+1.09+0.04}_{-0.00-0.00}$	0
55	200-500	500-800	9+	1	1.36 $^{+0.66+0.20}_{-0.53-0.19}$	1.58 $^{+0.71+0.19}_{-0.54-0.19}$	0.19 $^{+0.19+0.10}_{-0.19-0.00}$	0.08 $^{+0.20+0.13}_{-0.07-0.01}$	3.21 $^{+1.39+0.31}_{-1.08-0.27}$	6
56	200-500	800-1200	9+	1	3.19 $^{+0.99+0.53}_{-0.91-0.52}$	4.05 $^{+1.17+0.37}_{-1.08-0.36}$	1.57 $^{+0.64+0.70}_{-0.64-0.67}$	0.75 $^{+0.30+0.58}_{-0.22-0.53}$	9.55 $^{+2.27+1.11}_{-2.10-1.06}$	4
57	200-500	1200+	9+	1	1.70 $^{+0.85+0.25}_{-0.73-0.25}$	1.41 $^{+0.79+0.25}_{-0.65-0.25}$	0.31 $^{+0.22+0.15}_{-0.22-0.08}$	2.20 $^{+0.49+1.56}_{-0.40-1.56}$	5.62 $^{+1.72+1.61}_{-1.45-1.60}$	3
58	500-750	500-1200	9+	1	0.00 $^{+0.40+0.00}_{-0.00-0.00}$	0.05 $^{+0.46+0.02}_{-0.05-0.00}$	0.11 $^{+0.11+0.08}_{-0.11-0.00}$	0.00 $^{+0.10+0.03}_{-0.00-0.00}$	0.16 $^{+0.87+0.09}_{-0.12-0.00}$	0
59	500-750	1200+	9+	1	0.00 $^{+0.41+0.00}_{-0.00-0.00}$	0.15 $^{+0.48+0.04}_{-0.14-0.00}$	0.00 $^{+0.66+0.00}_{-0.00-0.00}$	0.00 $^{+0.08+0.02}_{-0.00-0.00}$	0.15 $^{+1.11+0.02}_{-0.14-0.00}$	1
60	750+	800+	9+	1	0.00 $^{+0.33+0.00}_{-0.00-0.00}$	0.00 $^{+0.46+0.00}_{-0.00-0.00}$	0.00 $^{+0.68+0.00}_{-0.00-0.00}$	0.00 $^{+0.07+0.02}_{-0.00-0.00}$	0.00 $^{+1.05+0.02}_{-0.00-0.00}$	0
61	200-500	500-800	9+	2	1.38 $^{+0.74+0.18}_{-0.62-0.17}$	1.51 $^{+0.77+0.15}_{-0.61-0.15}$	0.10 $^{+0.11+0.07}_{-0.10-0.00}$	0.00 $^{+0.20+0.08}_{-0.00-0.00}$	3.00 $^{+1.53+0.25}_{-1.23-0.23}$	3
62	200-500	800-1200	9+	2	1.39 $^{+0.68+0.20}_{-0.57-0.20}$	2.20 $^{+0.92+0.20}_{-0.80-0.20}$	0.87 $^{+0.41+0.54}_{-0.41-0.46}$	0.24 $^{+0.20+0.23}_{-0.12-0.12}$	4.70 $^{+1.67+0.65}_{-1.43-0.55}$	1
63	200-500	1200+	9+	2	0.28 $^{+0.48+0.04}_{-0.20-0.04}$	1.40 $^{+0.83+0.19}_{-0.70-0.19}$	0.17 $^{+0.13+0.11}_{-0.13-0.04}$	1.23 $^{+0.40+0.90}_{-0.31-0.90}$	3.09 $^{+1.39+0.93}_{-0.96-0.92}$	2
64	500-750	500-1200	9+	2	0.00 $^{+0.36+0.00}_{-0.00-0.00}$	0.00 $^{+0.46+0.00}_{-0.00-0.00}$	0.06 $^{+0.06+0.05}_{-0.06-0.00}$	0.00 $^{+0.10+0.03}_{-0.00-0.00}$	0.06 $^{+0.83+0.06}_{-0.06-0.00}$	0
65	500-750	1200+	9+	2	0.00 $^{+0.45+0.00}_{-0.00-0.00}$	0.01 $^{+0.46+0.00}_{-0.01-0.00}$	0.00 $^{+0.52+0.00}_{-0.00-0.00}$	0.00 $^{+0.08+0.02}_{-0.00-0.00}$	0.01 $^{+1.05+0.02}_{-0.01-0.00}$	0
66	750+	800+	9+	2	0.00 $^{+0.43+0.00}_{-0.00-0.00}$	0.00 $^{+0.46+0.00}_{-0.00-0.00}$	0.00 $^{+0.52+0.00}_{-0.00-0.00}$	0.00 $^{+0.07+0.02}_{-0.00-0.00}$	0.00 $^{+1.04+0.02}_{-0.00-0.00}$	0
67	200-500	500-800	9+	3+	0.30 $^{+0.48+0.05}_{-0.21-0.05}$	1.13 $^{+0.79+0.16}_{-0.64-0.16}$	0.02 $^{+0.03+0.03}_{-0.02-0.00}$	0.00 $^{+0.20+0.05}_{-0.00-0.00}$	1.46 $^{+1.28+0.18}_{-0.85-0.17}$	0
68	200-500	800-1200	9+	3+	1.92 $^{+1.38+0.33}_{-1.33-0.32}$	0.70 $^{+0.60+0.09}_{-0.38-0.09}$	0.18 $^{+0.13+0.24}_{-0.13-0.06}$	0.25 $^{+0.20+0.23}_{-0.11-0.14}$	3.06 $^{+1.99+0.47}_{-1.72-0.37}$	1
69	200-500	1200+	9+	3+	0.46 $^{+0.64+0.06}_{-0.46-0.00}$	0.32 $^{+0.54+0.05}_{-0.28-0.04}$	0.04 $^{+0.03+0.05}_{-0.03-0.00}$	0.03 $^{+0.09+0.06}_{-0.03-0.00}$	0.85 $^{+1.19+0.09}_{-0.75-0.04}$	0
70	500-750	500-1200	9+	3+	0.13 $^{+0.47+0.05}_{-0.13-0.00}$	0.00 $^{+0.46+0.00}_{-0.00-0.00}$	0.01 $^{+0.02+0.02}_{-0.01-0.00}$	0.00 $^{+0.10+0.02}_{-0.00-0.00}$	0.14 $^{+0.93+0.03}_{-0.13-0.00}$	0
71	500-750	1200+	9+	3+	0.00 $^{+0.41+0.00}_{-0.00-0.00}$	0.00 $^{+0.46+0.00}_{-0.00-0.00}$	0.00 $^{+0.30+0.00}_{-0.00-0.00}$	0.00 $^{+0.08+0.01}_{-0.00-0.00}$	0.00 $^{+0.92+0.01}_{-0.00-0.00}$	0
72	750+	800+	9+	3+	0.00 $^{+0.44+0.00}_{-0.00-0.00}$	0.00 $^{+0.46+0.00}_{-0.00-0.00}$	0.00 $^{+0.28+0.00}_{-0.00-0.00}$	0.00 $^{+0.07+0.02}_{-0.00-0.00}$	0.00 $^{+0.95+0.02}_{-0.00-0.00}$	0

bin	Lost lepton ( $e/\mu$ )	hadronic $\tau$	$Z \rightarrow \nu\nu$	QCD	Total	Observed
1	$314.80 \pm 22.20$	$306.49 \pm 16.55$	$736.91 \pm 59.90$	$176.87 \pm 50.11$	$1535.07 \pm 82.86$	1566.0
2	$57.59 \pm 4.81$	$68.88 \pm 5.26$	$159.24 \pm 18.25$	$94.87 \pm 17.22$	$380.59 \pm 26.09$	382.0
3	$13.39 \pm 1.93$	$14.07 \pm 2.10$	$33.11 \pm 9.88$	$84.58 \pm 10.01$	$145.15 \pm 14.35$	145.0
4	$12.12 \pm 1.97$	$9.62 \pm 1.84$	$88.42 \pm 9.08$	$0.16 \pm 0.18$	$110.32 \pm 9.47$	119.0
5	$2.28 \pm 0.84$	$0.75 \pm 0.29$	$6.39 \pm 2.01$	$0.74 \pm 0.65$	$10.16 \pm 2.30$	13.0
6	$1.34 \pm 0.51$	$1.71 \pm 0.58$	$9.57 \pm 2.61$	$0.16 \pm 0.16$	$12.77 \pm 2.73$	12.0
7	$157.76 \pm 11.21$	$190.82 \pm 10.09$	$112.75 \pm 18.20$	$51.66 \pm 14.83$	$512.99 \pm 27.91$	484.0
8	$29.24 \pm 3.09$	$30.96 \pm 2.59$	$25.95 \pm 5.37$	$33.33 \pm 6.27$	$119.48 \pm 9.19$	122.0
9	$5.76 \pm 1.12$	$7.77 \pm 1.37$	$5.34 \pm 1.83$	$29.63 \pm 3.62$	$48.50 \pm 4.43$	43.0
10	$3.22 \pm 0.91$	$2.71 \pm 0.79$	$14.48 \pm 2.36$	$0.02 \pm 0.05$	$20.43 \pm 2.65$	22.0
11	$0.00 \pm 0.00$	$0.08 \pm 0.01$	$1.03 \pm 0.35$	$0.27 \pm 0.25$	$1.37 \pm 0.43$	0.0
12	$0.00 \pm 0.00$	$0.55 \pm 0.08$	$1.55 \pm 0.46$	$0.00 \pm 0.01$	$2.10 \pm 0.47$	2.0
13	$72.91 \pm 6.58$	$77.91 \pm 5.19$	$28.10 \pm 9.39$	$10.20 \pm 3.16$	$189.11 \pm 12.97$	198.0
14	$17.24 \pm 2.75$	$15.77 \pm 1.69$	$5.89 \pm 2.18$	$7.95 \pm 1.56$	$46.86 \pm 4.20$	45.0
15	$2.52 \pm 0.87$	$3.29 \pm 0.92$	$1.24 \pm 0.65$	$5.01 \pm 0.85$	$12.05 \pm 1.65$	15.0
16	$1.44 \pm 0.85$	$1.89 \pm 0.60$	$3.24 \pm 1.02$	$0.01 \pm 14.52$	$6.57 \pm 1.46$	5.0
17	$1.39 \pm 0.91$	$0.04 \pm 0.03$	$0.24 \pm 0.11$	$0.06 \pm 0.16$	$1.72 \pm 0.93$	0.0
18	$0.00 \pm 0.00$	$0.04 \pm 0.01$	$0.36 \pm 0.14$	$0.02 \pm 0.11$	$0.42 \pm 0.18$	1.0
19	$5.19 \pm 1.03$	$9.01 \pm 1.57$	$4.80 \pm 2.29$	$0.74 \pm 0.37$	$19.74 \pm 2.98$	17.0
20	$0.53 \pm 0.25$	$2.36 \pm 1.11$	$1.08 \pm 0.53$	$0.52 \pm 0.20$	$4.49 \pm 1.27$	7.0
21	$0.94 \pm 0.50$	$0.10 \pm 0.03$	$0.22 \pm 0.12$	$0.68 \pm 0.22$	$1.94 \pm 0.56$	3.0
22	$0.00 \pm 0.00$	$0.03 \pm 0.00$	$0.58 \pm 0.24$	$0.04 \pm 0.10$	$0.65 \pm 0.26$	0.0
23	$0.00 \pm 0.00$	$0.00 \pm 0.00$	$0.04 \pm 0.02$	$0.00 \pm 0.00$	$0.05 \pm 0.02$	0.0
24	$0.00 \pm 0.00$	$0.00 \pm 0.00$	$0.06 \pm 0.03$	$0.00 \pm 0.00$	$0.06 \pm 0.03$	0.0
25	$17.87 \pm 2.55$	$24.59 \pm 2.19$	$27.26 \pm 5.75$	$11.77 \pm 3.97$	$81.50 \pm 7.75$	82.0
26	$11.64 \pm 1.90$	$15.42 \pm 1.62$	$18.20 \pm 3.74$	$15.24 \pm 3.86$	$60.50 \pm 5.93$	57.0
27	$2.97 \pm 0.81$	$3.70 \pm 0.89$	$8.14 \pm 2.68$	$22.96 \pm 4.26$	$37.77 \pm 5.18$	40.0
28	$0.37 \pm 0.14$	$0.75 \pm 0.27$	$0.32 \pm 0.48$	$0.04 \pm 0.21$	$1.48 \pm 0.61$	1.0
29	$0.70 \pm 0.45$	$1.09 \pm 0.44$	$0.77 \pm 0.79$	$0.22 \pm 0.25$	$2.78 \pm 1.04$	1.0
30	$0.17 \pm 0.14$	$0.16 \pm 0.14$	$0.65 \pm 0.60$	$0.19 \pm 0.25$	$1.18 \pm 0.68$	1.0
31	$23.53 \pm 2.50$	$29.73 \pm 2.05$	$8.54 \pm 2.58$	$5.44 \pm 2.34$	$67.24 \pm 4.75$	62.0
32	$9.33 \pm 1.50$	$15.33 \pm 1.58$	$5.78 \pm 1.68$	$6.33 \pm 1.75$	$36.77 \pm 3.26$	42.0
33	$3.51 \pm 0.79$	$6.54 \pm 1.17$	$2.57 \pm 0.95$	$13.03 \pm 2.31$	$25.64 \pm 2.87$	29.0
34	$0.46 \pm 0.22$	$0.42 \pm 0.22$	$0.10 \pm 0.15$	$0.00 \pm 0.00$	$0.98 \pm 0.34$	1.0
35	$0.00 \pm 0.00$	$0.25 \pm 0.03$	$0.24 \pm 0.27$	$0.09 \pm 0.22$	$0.58 \pm 0.35$	2.0
36	$0.00 \pm 0.00$	$0.02 \pm 0.01$	$0.21 \pm 0.20$	$0.00 \pm 0.00$	$0.22 \pm 0.21$	1.0
37	$12.50 \pm 1.58$	$15.14 \pm 1.26$	$3.55 \pm 1.49$	$0.00 \pm 563.16$	$31.19 \pm 2.51$	30.0
38	$5.72 \pm 0.84$	$9.99 \pm 1.16$	$2.36 \pm 0.94$	$1.42 \pm 0.53$	$19.49 \pm 1.80$	17.0
39	$1.20 \pm 0.32$	$1.36 \pm 0.38$	$1.05 \pm 0.55$	$2.83 \pm 0.68$	$6.45 \pm 1.01$	4.0
40	$0.00 \pm 0.00$	$0.04 \pm 0.01$	$0.04 \pm 0.06$	$0.00 \pm 0.00$	$0.08 \pm 0.06$	0.0
41	$0.00 \pm 0.00$	$0.10 \pm 0.04$	$0.10 \pm 0.12$	$0.04 \pm 0.32$	$0.24 \pm 0.34$	1.0
42	$0.00 \pm 0.00$	$0.12 \pm 0.04$	$0.09 \pm 0.10$	$0.00 \pm 0.00$	$0.21 \pm 0.10$	0.0
43	$2.26 \pm 0.50$	$4.28 \pm 0.67$	$1.16 \pm 0.73$	$0.60 \pm 0.73$	$8.31 \pm 1.33$	3.0
44	$0.50 \pm 0.20$	$1.80 \pm 0.49$	$0.80 \pm 0.53$	$0.45 \pm 0.28$	$3.54 \pm 0.80$	5.0
45	$0.58 \pm 0.33$	$0.55 \pm 0.22$	$0.35 \pm 0.23$	$0.00 \pm 35.40$	$1.49 \pm 0.46$	1.0
46	$0.00 \pm 0.00$	$0.00 \pm 0.00$	$0.01 \pm 0.02$	$0.04 \pm 0.11$	$0.06 \pm 0.12$	0.0
47	$0.00 \pm 0.00$	$0.01 \pm 0.00$	$0.03 \pm 0.05$	$0.00 \pm 0.00$	$0.04 \pm 0.05$	0.0
48	$0.00 \pm 0.00$	$0.01 \pm 0.00$	$0.03 \pm 0.04$	$0.00 \pm 0.00$	$0.03 \pm 0.04$	0.0
49	$0.76 \pm 0.32$	$0.60 \pm 0.15$	$0.29 \pm 0.66$	$0.67 \pm 0.52$	$2.33 \pm 0.92$	2.0
50	$2.27 \pm 0.51$	$4.32 \pm 0.85$	$2.01 \pm 1.09$	$0.56 \pm 0.31$	$9.16 \pm 1.51$	11.0
51	$0.66 \pm 0.27$	$1.24 \pm 0.49$	$0.25 \pm 0.43$	$3.16 \pm 1.16$	$5.30 \pm 1.36$	7.0
52	$0.00 \pm 0.00$	$0.00 \pm 0.00$	$0.12 \pm 0.31$	$0.00 \pm 0.00$	$0.12 \pm 0.31$	0.0
53	$0.13 \pm 0.10$	$0.02 \pm 0.02$	$0.00 \pm 0.05$	$0.00 \pm 0.02$	$0.15 \pm 0.11$	0.0
54	$0.00 \pm 0.00$	$0.00 \pm 0.00$	$0.00 \pm 0.00$	$0.00 \pm 0.00$	$0.00 \pm 0.00$	0.0
55	$1.65 \pm 0.41$	$1.96 \pm 0.44$	$0.15 \pm 0.34$	$0.02 \pm 0.77$	$3.78 \pm 1.04$	6.0
56	$2.46 \pm 0.56$	$3.22 \pm 0.59$	$1.06 \pm 0.59$	$0.54 \pm 0.28$	$7.28 \pm 1.04$	4.0
57	$1.47 \pm 0.39$	$1.28 \pm 0.38$	$0.13 \pm 0.26$	$1.86 \pm 0.74$	$4.74 \pm 0.95$	3.0
58	$0.00 \pm 0.00$	$0.05 \pm 0.01$	$0.06 \pm 0.17$	$0.00 \pm 0.00$	$0.12 \pm 0.17$	0.0
59	$0.00 \pm 0.00$	$0.14 \pm 0.02$	$0.00 \pm 0.02$	$0.00 \pm 0.00$	$0.15 \pm 0.03$	1.0
60	$0.00 \pm 0.00$	$0.00 \pm 0.00$	$0.00 \pm 0.00$	$0.00 \pm 0.00$	$0.00 \pm 0.00$	0.0
61	$1.34 \pm 0.38$	$1.60 \pm 0.40$	$0.09 \pm 0.23$	$0.00 \pm 0.02$	$3.03 \pm 0.59$	3.0
62	$1.08 \pm 0.29$	$1.74 \pm 0.40$	$0.60 \pm 0.39$	$0.12 \pm 0.17$	$3.54 \pm 0.65$	1.0
63	$0.26 \pm 0.12$	$1.31 \pm 0.42$	$0.07 \pm 0.13$	$0.97 \pm 0.44$	$2.61 \pm 0.63$	2.0
64	$0.00 \pm 0.00$	$0.00 \pm 0.00$	$0.04 \pm 0.08$	$0.00 \pm 0.00$	$0.04 \pm 0.08$	0.0
65	$0.00 \pm 0.00$	$0.01 \pm 0.00$	$0.00 \pm 0.02$	$0.00 \pm 0.00$	$0.01 \pm 0.02$	0.0
66	$0.00 \pm 0.00$	$0.00 \pm 0.00$	$0.00 \pm 0.00$	$0.00 \pm 0.00$	$0.00 \pm 0.00$	0.0
67	$0.22 \pm 0.10$	$0.87 \pm 0.30$	$0.01 \pm 0.04$	$0.00 \pm 0.00$	$1.11 \pm 0.31$	0.0
68	$1.40 \pm 0.59$	$0.50 \pm 0.17$	$0.10 \pm 0.12$	$0.18 \pm 0.18$	$2.19 \pm 0.65$	1.0
69	$0.35 \pm 0.21$	$0.24 \pm 0.15$	$0.01 \pm 0.04$	$0.01 \pm 0.22$	$0.61 \pm 0.34$	0.0
70	$0.12 \pm 0.08$	$0.00 \pm 0.00$	$0.01 \pm 0.03$	$0.00 \pm 0.00$	$0.12 \pm 0.09$	0.0
71	$0.00 \pm 0.00$	$0.00 \pm 0.00$	$0.00 \pm 0.00$	$0.00 \pm 0.00$	$0.00 \pm 0.00$	0.0
72	$0.00 \pm 0.00$	$0.00 \pm 0.00$	$0.00 \pm 0.00$	$0.00 \pm 0.00$	$0.00 \pm 0.00$	0.0

Table 24: Results of the data-driven background predictions for each of the background components,  $t\bar{t}$ ,  $W$ , QCD, and  $Z$ , compared to data in the 72 search bins.

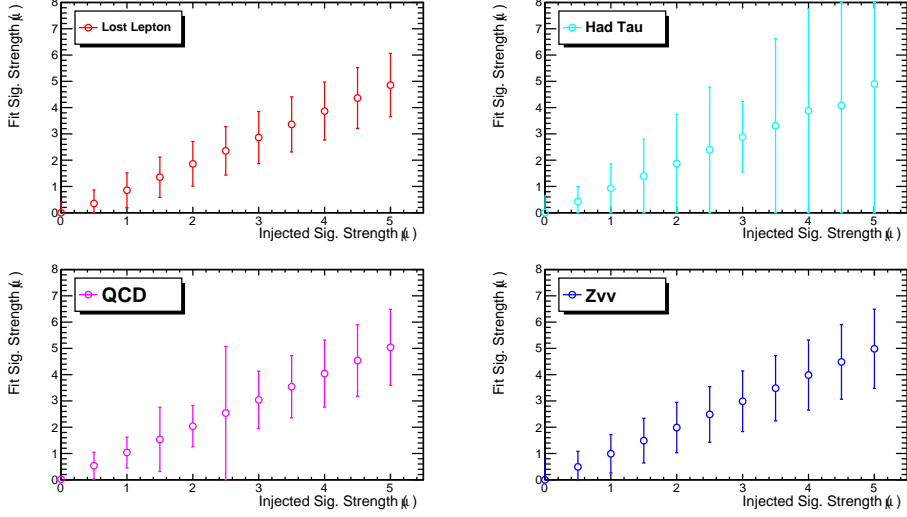


Figure 87: Fitting signal strength vs injected value for each background component individually based on  $3 \text{ fb}^{-1}$ .

1450 The search results are interpreted as 95% CL upper limits on a variety of signal models. Table 25  
 1451 shows the observed and expected ULs for six signal benchmark points. Table 26 shows the  
 1452 expected signal significance for six signal benchmark points. Figure 90 shows the observed and  
 1453 expected 95% CL upper limits for the T1bbbb SUSY scenario. Figure 91 shows the observed and  
 1454 expected 95% CL upper limits for the T1tttt SUSY scenario. Figure 93 shows the observed and  
 1455 expected 95% CL upper limits for the T1qqqq SUSY scenario.

Model	Expected 95% CL UL	Observed 95% CL UL
T1qqqq(1400, 100)	0.71	0.60
T1qqqq(1000, 900)	0.79	0.77
T1bbbb(1500, 100)	0.51	0.50
T1bbbb(1000, 800)	0.70	0.49
T1tttt(1500, 100)	0.74	0.75
T1tttt(1200, 800)	1.26	0.62

Table 25: Observed and Expected Upper Limit exclusion at 95% CL for six SUSY scenarios. Results are given in terms of the expected signal strength ( $\mu$ ) for each SMS based on  $2.1 \text{ fb}^{-1}$ .

1456 Additional SMS models will be added as the scans are available.

1457 As an aide in understanding which search bins are driving the limits, we include the expected  
 1458 amount of BG and several signal models (BG from data-driven predictions) in each search bin,  
 1459 as well as the local  $Q$  figure-of-merit for each model in each bin in Figure 94. Additionally,  
 1460 figure 95 presents one-dimensional projections of the results in  $H_T^{\text{miss}}$  or  $H_T$  after criteria are  
 1461 imposed, as indicated in the legends, to select intervals of the search-region phase space par-  
 1462 ticularly sensitive to the T1bbbb, T1tttt, or T1qqqq scenarios.

## 1463 13 Summary

1464 In this note we've show data-driven background estimation techniques for a hadronic multi-  
 1465 jet search for new physics. Sensitivities with  $2.2 \text{ fb}^{-1}$  of integrated luminosity with  $\sqrt{s} =$

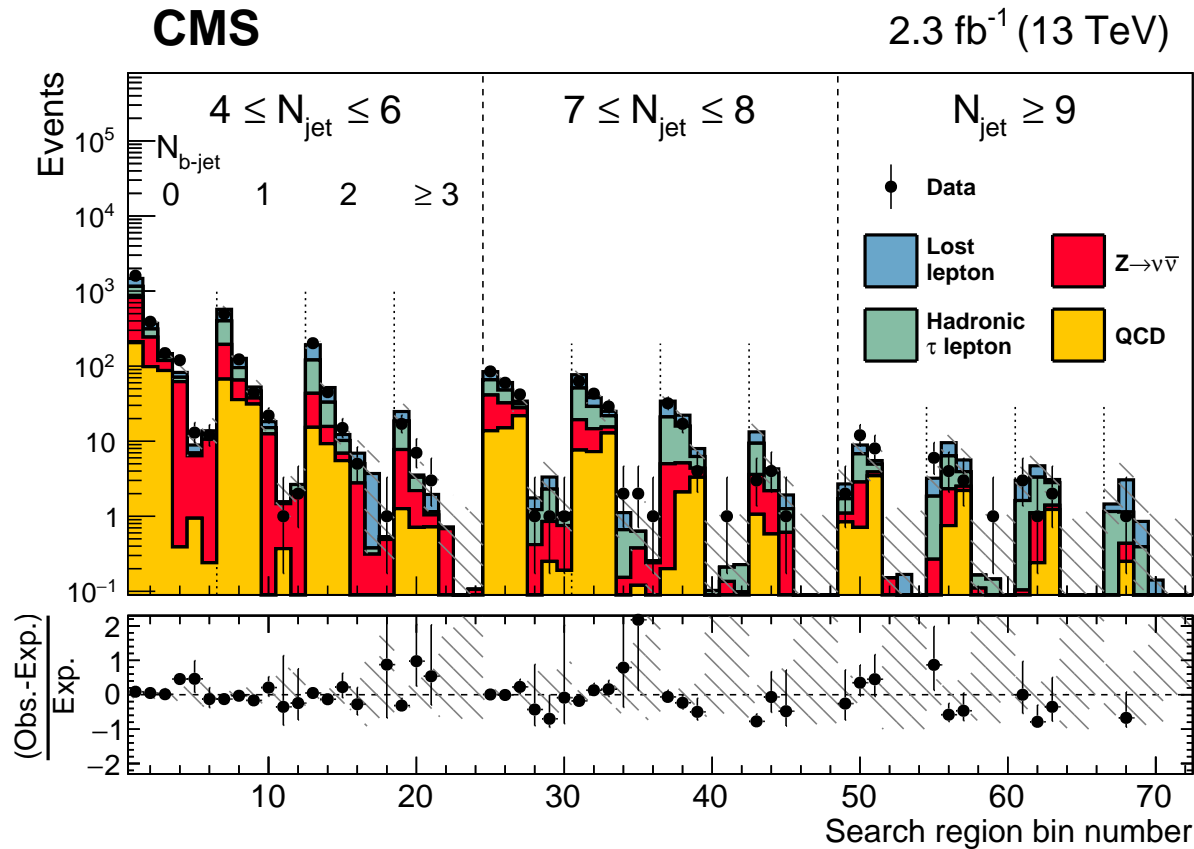


Figure 88: Observed number of events and pre-fit background predictions in the all search bins.

Model	Expected significance ( $\sigma$ )
T1qqqq(1400, 100)	2.4
T1qqqq(1000, 900)	2.5
T1bbbb(1500, 100)	3.2
T1bbbb(1000, 800)	2.7
T1tttt(1500, 100)	2.5
T1tttt(1200, 800)	1.9

Table 26: Expected signal significance for six SUSY scenarios based on  $1.3 \text{ fb}^{-1}$ .

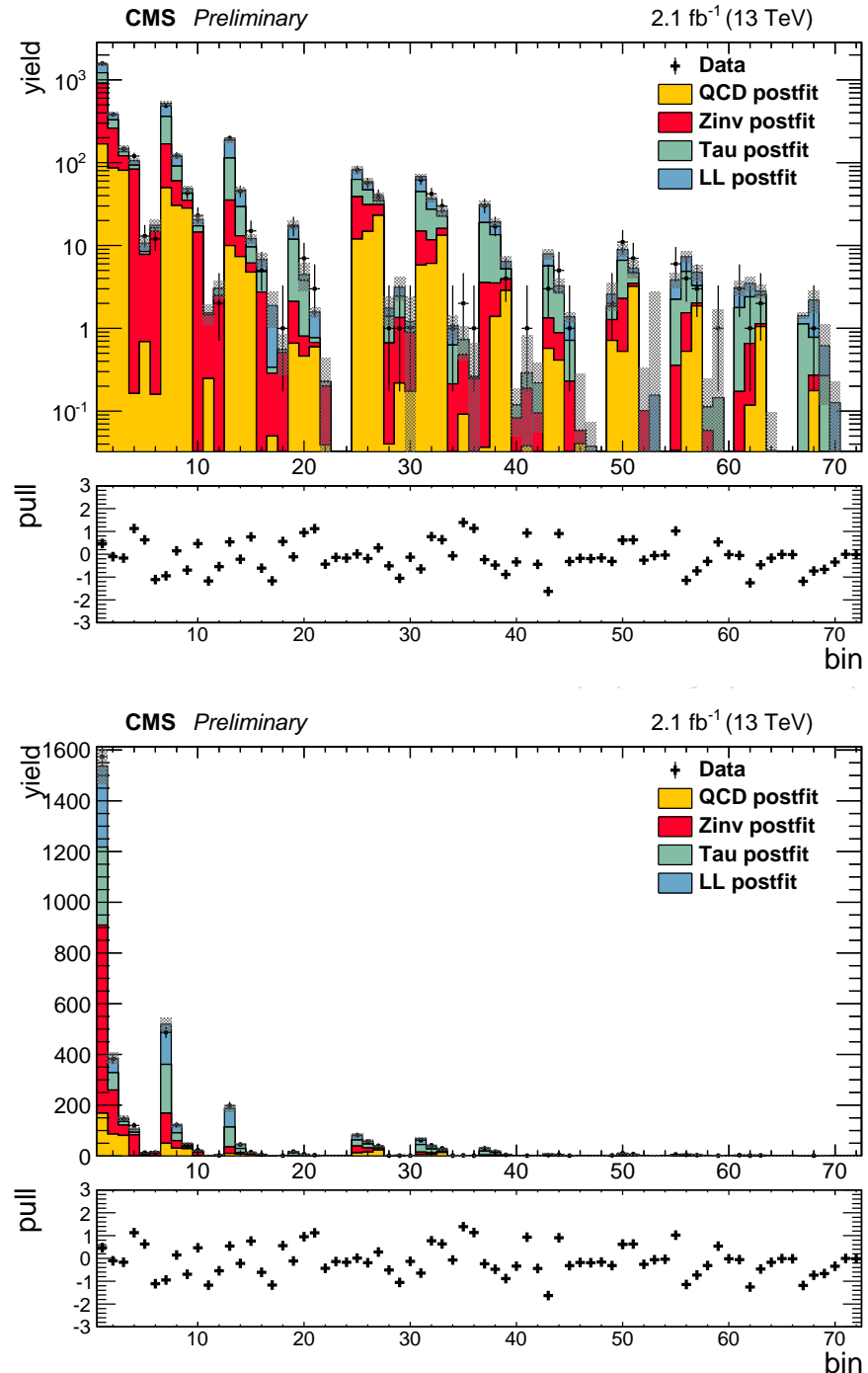


Figure 89: Results of the data-driven background predictions (post-fit) for each of the background components,  $t\bar{t}$ ,  $W$ , QCD, and  $Z$ , compared to data and SUSY signal benchmark points. Upper plot is log scale. Lower plot is linear scale.

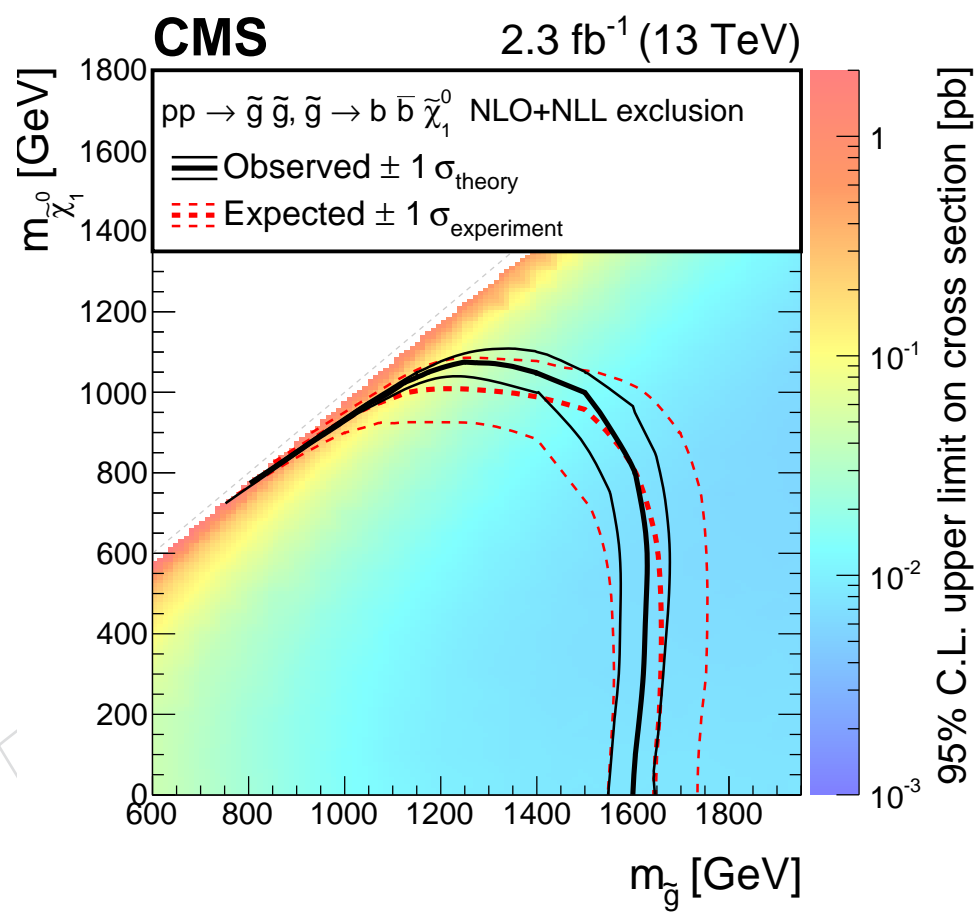


Figure 90: Observed and Expected Upper Limit exclusion at 95% CL for T1bbbb.

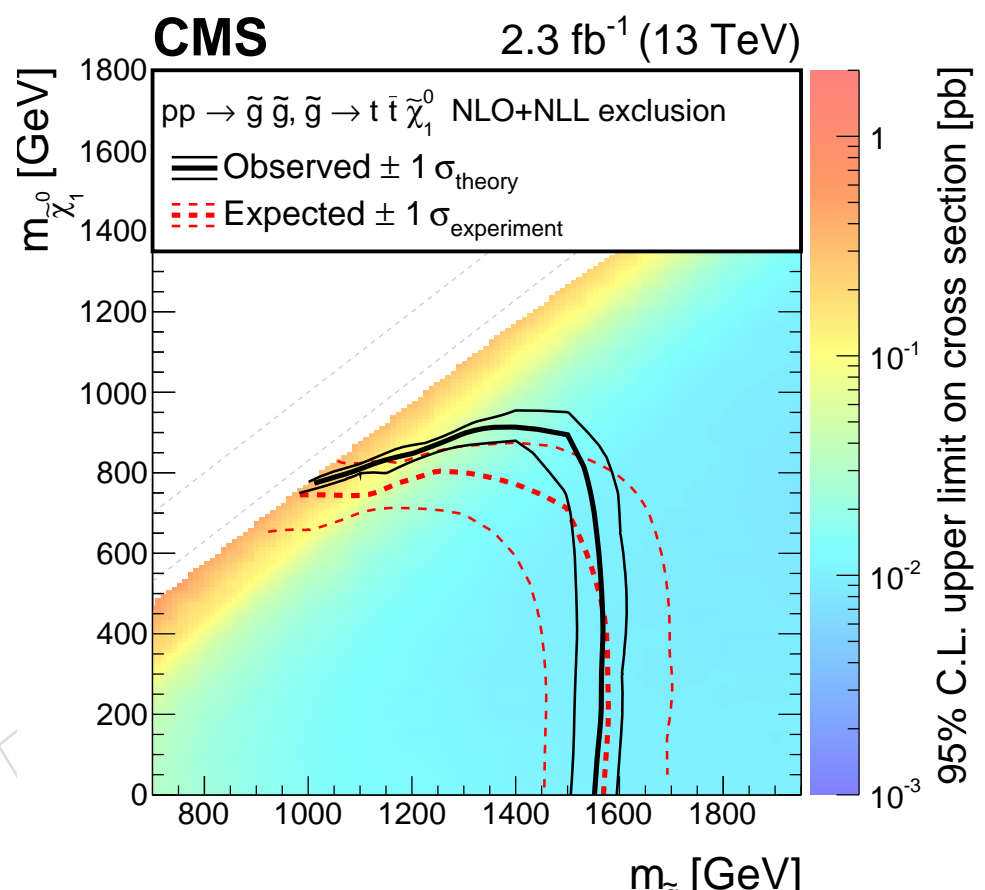


Figure 91: Observed and Expected Upper Limit exclusion at 95% CL for T1tttt.

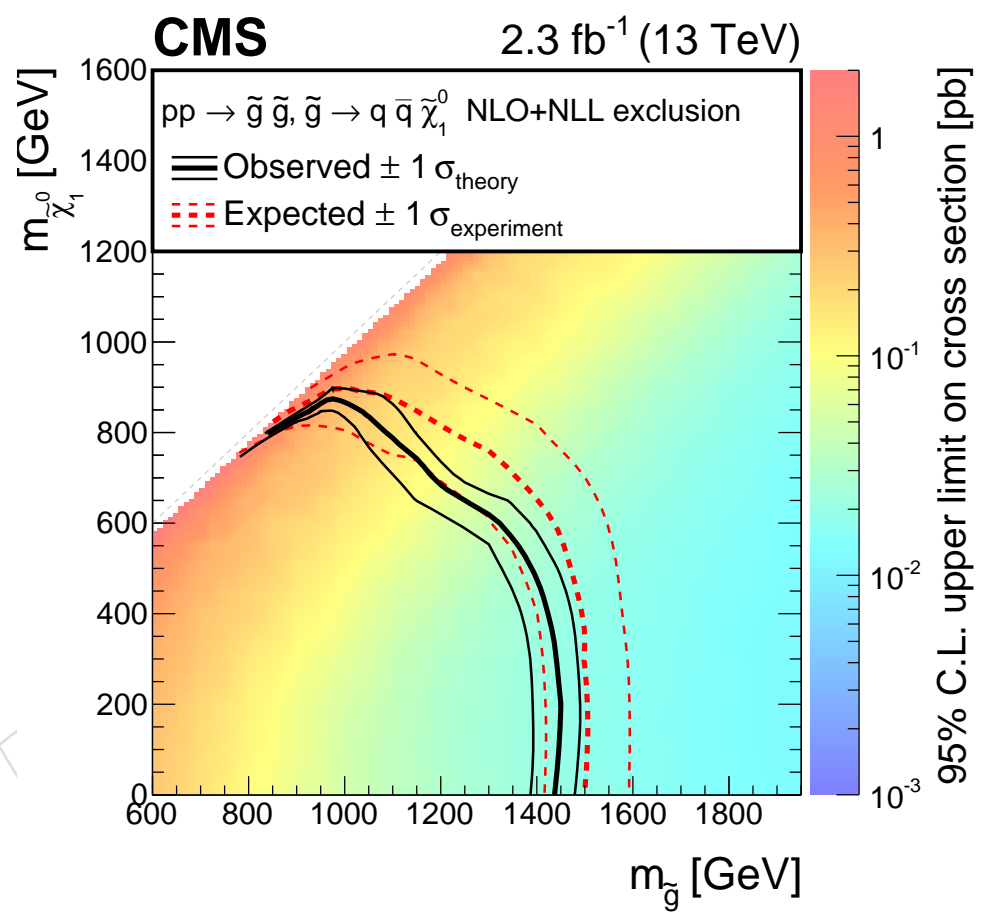


Figure 92: Observed and Expected Upper Limit exclusion at 95% CL for T1qqqq.

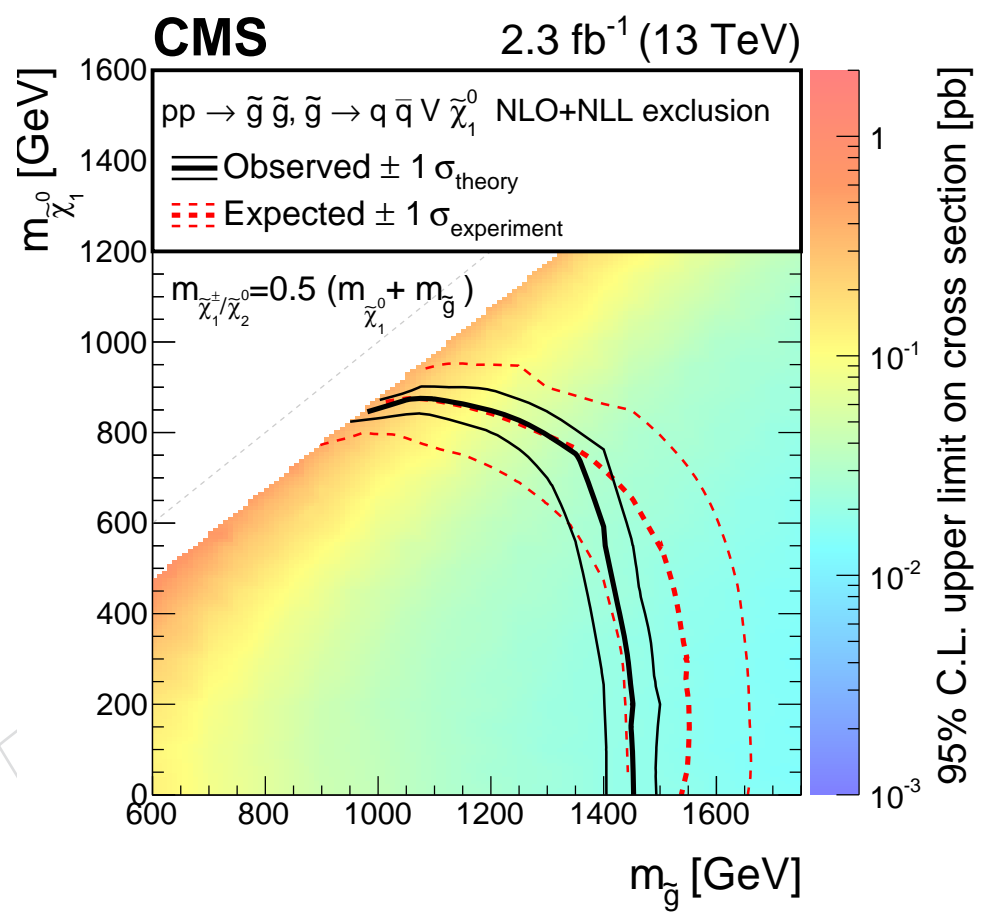


Figure 93: Observed and Expected Upper Limit exclusion at 95% CL for T5qqqqVV.

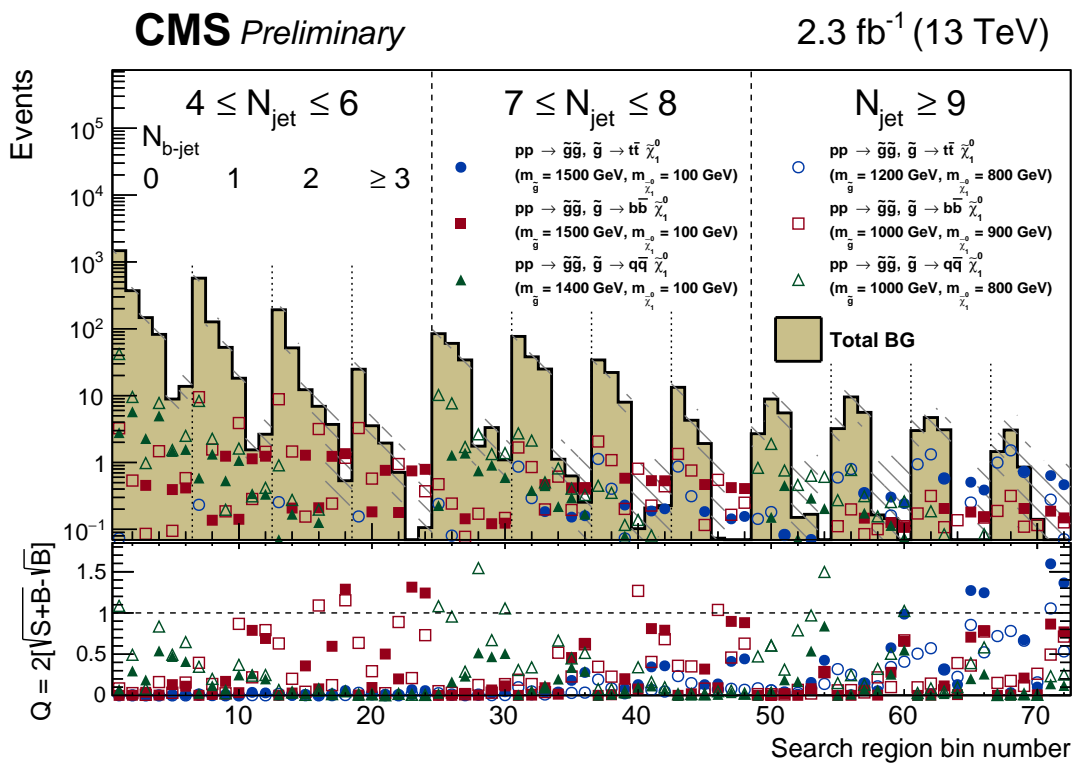


Figure 94: Expected number of background and signal events for 6 different FastSim signal points. The BG values are taken from the pre-fit data-driven predictions. The lower panel of the plot shows the local  $Q$  figure-of-merit for each model in each bin.

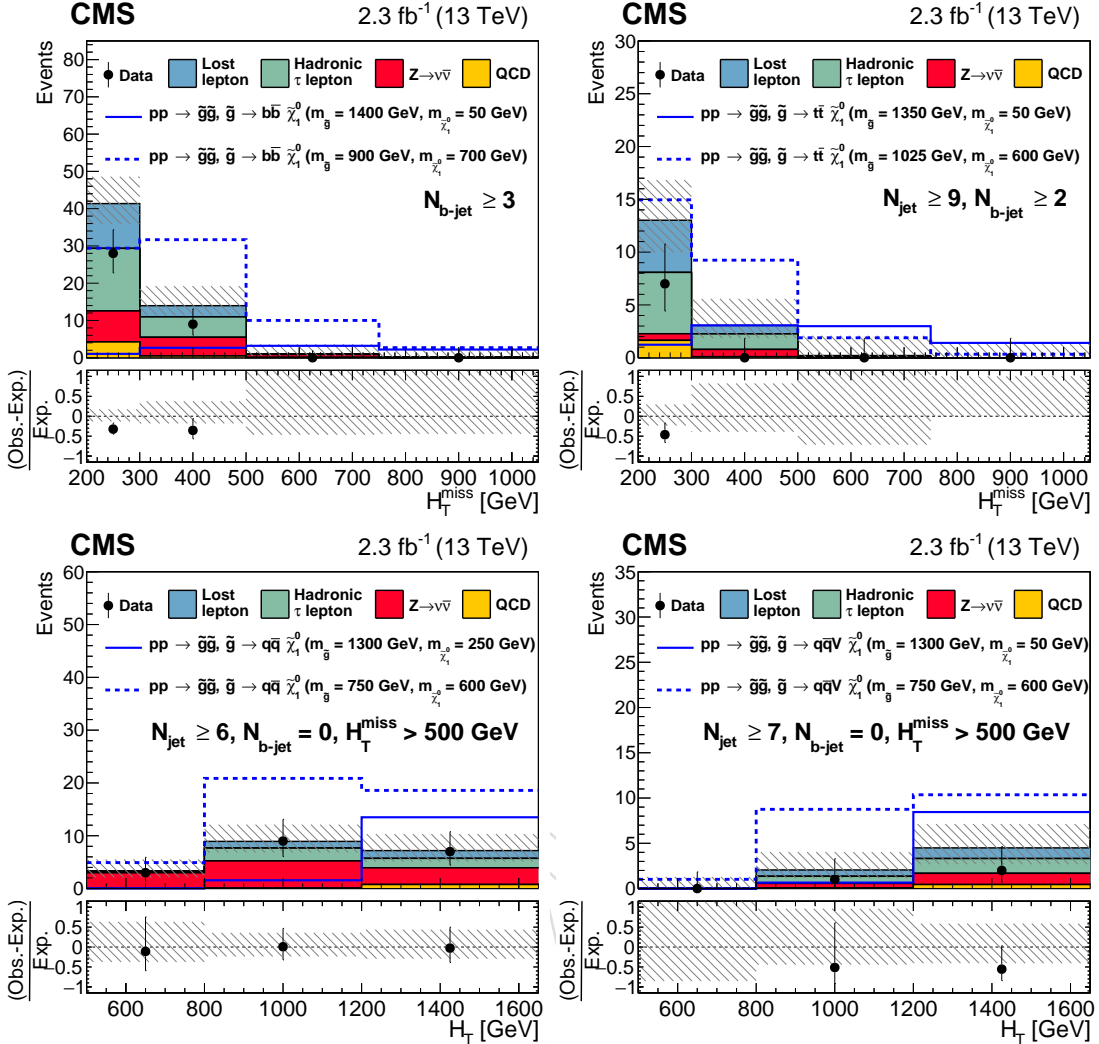


Figure 95: Observed numbers of events and corresponding SM background predictions for intervals of the search-region phase space particularly sensitive to the (top left) T1tttt, (top right) T1bbbb, (bottom left) T1qqqq, and (bottom right) T5qqqqVV scenarios. The selection requirements are given in the figure legends. The hatched regions indicate the total uncertainties in the background predictions. The (unstacked) results for two example signal scenarios are shown in each instance, one with  $m_{\tilde{g}} >> m_{\tilde{\chi}_1^0}$  and the other with  $m_{\tilde{\chi}_1^0} \approx m_{\tilde{g}}$ . Note that for purposes of presentation, the four-bin scheme discussed in Section 7 is used for the  $H_T^{\text{miss}}$  variable.

1466 13 TeV already greatly exceed those from the corresponding 8 TeV results for various gluino  
 1467 production models.

## 1468 References

- 1469 [1] CMS Collaboration, "Search for gluino mediated bottom- and top-squark production in  
 1470 multijet final states in pp collisions at 8 TeV", *Phys. Lett. B* **725** (2013) 243–270,  
 1471 doi:10.1016/j.physletb.2013.06.058.
- 1472 [2] CMS Collaboration, "Search for new physics in the multijet and missing transverse  
 1473 momentum final state in proton-proton collisions at  $\sqrt{s} = 8$  TeV", *JHEP* **06** (2014) 055,  
 1474 doi:10.1007/JHEP06(2014)055.
- 1475 [3] Rohan Bhandari, Adam Dishaw, Ryan Heller, Ana Ovcharova, Jeffrey Richman, Manuel  
 1476 Franco Sevilla, David Stuart, Chris West, Jae Hyeok Yoo, "Search for supersymmetry in  
 1477 pp collisions at  $\sqrt{s} = 13$  TeV in the single-lepton final state using the sum of masses of  
 1478 large radius jets", *CMS Analysis Note AN-15-139* (2015).
- 1479 [4] C. Borschensky et al., "Squark and gluino production cross sections in pp collisions at  
 1480  $\sqrt{s} = 13, 14, 33$  and 100 TeV", *Eur. Phys. J. C* **74** (2014), no. 12,  
 1481 doi:10.1140/epjc/s10052-014-3174-y, arXiv:1407.5066.
- 1482 [5] M. Cacciari, G. P. Salam, and G. Soyez, "The anti- $k_t$  jet clustering algorithm", *JHEP* **04**  
 1483 (2008) 063, doi:10.1088/1126-6708/2008/04/063, arXiv:0802.1189.
- 1484 [6] CMS Collaboration, "Particle-Flow Event Reconstruction in CMS and Performance for  
 1485 Jets, Taus, and  $E_T^{\text{miss}}$ ", CMS Physics Analysis Summary CMS-PAS-PFT-09-001, CERN,  
 1486 2009.
- 1487 [7] CMS Collaboration, "Determination of jet energy calibration and transverse momentum  
 1488 resolution in CMS", *JINST* **6** (2011) P11002,  
 1489 doi:10.1088/1748-0221/6/11/P11002, arXiv:1107.4277.
- 1490 [8] CMS JetMET POG, "Jet Energy Corrections: Official Software Tools for applying JEC  
 1491 Corrections and Uncertainties". <https://twiki.cern.ch/twiki/bin/view/CMS/WorkBookJetEnergyCorrections>.
- 1493 [9] Harel, A. and Schieferdecker, P., "Jet Identification", (2010).  
 1494 <https://twiki.cern.ch/twiki/bin/view/CMS/JetID>.
- 1495 [10] CMS Muon POG, "Baseline muon selections for 2012 data (CMSSW 52X and above)",  
 1496 (2012). <https://twiki.cern.ch/twiki/bin/view/CMS/WorkBookMuonId#The2012Data>.
- 1498 [11] CMS E/gamma POG, "Cut Based Electron ID for Run 2", (2014). <https://twiki.cern.ch/twiki/bin/viewauth/CMS/CutBasedElectronIdentificationRun2>.
- 1500 [12] The RA2 Group, "Search for new physics in multijets and missing momentum final state  
 1501 at 8 TeV", *CMS Analysis Note AN-12-350* (2012).
- 1502 [13] CMS Statistics Committee, "Asymmetric Error Bars for Poisson Event Counts", (2015).  
 1503 <https://twiki.cern.ch/twiki/bin/view/CMS/PoissonErrorBars>.
- 1504 [14] CMS Collaboration, "Search for new physics in the multijet and missing transverse  
 1505 momentum final state in proton-proton collisions at  $\sqrt{s} = 7$  TeV", *Phys. Rev. Lett.* **109**  
 1506 (2012) 171803, doi:10.1103/PhysRevLett.109.171803, arXiv:1207.1898.

- 1507 [15] CMS Collaboration, “Search for New Physics with Jets and Missing Transverse  
1508 Momentum in  $pp$  collisions at  $\sqrt{s} = 7$  TeV”, *JHEP* **1108** (2011) 155,  
1509 doi:10.1007/JHEP08(2011)155, arXiv:1106.4503.
- 1510 [16] Particle Data Group Collaboration, “Review of Particle Physics (RPP)”, *Phys. Rev. D* **86**  
1511 (2012) 010001, doi:10.1103/PhysRevD.86.010001.
- 1512 [17] SUS Data/MC Lepton Scale Factor Group, “SUS Data/MC Lepton Scale Factors –  
1513 Muons”, (2015).  
1514 [https://twiki.cern.ch/twiki/bin/view/CMS/SUSLeptonSF#Muons\\_AN1](https://twiki.cern.ch/twiki/bin/view/CMS/SUSLeptonSF#Muons_AN1).
- 1515 [18] G. Perrin and L. Perrozzi, “Status Report on Muon SF extraction for the SUSY PAG”,  
1516 (October, 2015). <https://indico.cern.ch/event/455555/session/0/contribution/3/attachments/1175994/1700195/SFMuon.pdf>.
- 1518 [19] A. Dishaw et al., “Preliminary Scale Factors for SUSY Electron Isolation Working Points”,  
1519 (October, 2015). [https://indico.cern.ch/event/455555/session/0/contribution/4/attachments/1175983/1700123/2015\\_10\\_22\\_tnp.pdf](https://indico.cern.ch/event/455555/session/0/contribution/4/attachments/1175983/1700123/2015_10_22_tnp.pdf).
- 1521 [20] CMS Collaboration, “Description and performance of track and primary-vertex  
1522 reconstruction with the CMS tracker”, *JINST* **9** (2014), no. 10, P10009,  
1523 doi:10.1088/1748-0221/9/10/P10009, arXiv:1405.6569.
- 1524 [21] CMS Collaboration, “Measurement of Tracking Efficiency”, CMS Physics Analysis  
1525 Summary CMS-PAS-TRK-10-002, CERN, 2010.
- 1526 [22] The RA2b Group, “Search for supersymmetry in  $pp$  collisions at 8 TeV using the shape of  
1527  $H_T$ ,  $E_T^{\text{miss}}$ , and b-quark jet multiplicity distributions”, *CMS Analysis Note AN-12-081*  
1528 (2012).
- 1529 [23] Particle Data Group, “Review of Particle Physics”, *Chinese Physics C* **38** (2014) 090001,  
1530 doi:10.1088/1674-1137/38/9/090001.
- 1531 [24] CMS JetMET POG, “Inefficiency in PFJetID in FastSim”, (2015). <https://hypernews.cern.ch/HyperNews/CMS/get/jet-algorithms/379.html>.
- 1533 [25] CMS B-tag POG, “Methods to apply b-tagging efficiency scale factors”, (2015).  
1534 <https://twiki.cern.ch/twiki/bin/viewauth/CMS/BTagSFMETHODS>.
- 1535 [26] CMS B-tag POG, “2015 FastSim Correction Factors”, (2015). <https://twiki.cern.ch/twiki/bin/viewauth/CMS/Btag2015FastSimCorrectionFactors>.
- 1537 [27] CMS Physics Validation Team, “Estimating Systematic Errors Due to Pileup Modeling”,  
1538 (2013).  
1539 <https://twiki.cern.ch/twiki/bin/view/CMS/PileupSystematicErrors>.
- 1540 [28] M. Cacciari et al., “The  $t\bar{t}$  cross-section at 1.8 TeV and 1.96 TeV: A Study of the systematics  
1541 due to parton densities and scale dependence”, *JHEP* **04** (2004) 068,  
1542 doi:10.1088/1126-6708/2004/04/068, arXiv:hep-ph/0303085.
- 1543 [29] S. Catani, D. de Florian, M. Grazzini, and P. Nason, “Soft gluon resummation for Higgs  
1544 boson production at hadron colliders”, *JHEP* **07** (2003) 028,  
1545 doi:10.1088/1126-6708/2003/07/028, arXiv:hep-ph/0306211.

- 1546 [30] CMS Higgs Combination Group, “Documentation of the RooStats-based statistics tools  
1547 for Higgs PAG”, (2015). [https://twiki.cern.ch/twiki/bin/viewauth/CMS/  
1548 SWGuideHiggsAnalysisCombinedLimit](https://twiki.cern.ch/twiki/bin/viewauth/CMS/SWGuideHiggsAnalysisCombinedLimit).
- 1549 [31] J. Alwall et al., “The automated computation of tree-level and next-to-leading order  
1550 differential cross sections, and their matching to parton shower simulations”, *JHEP* **1407**  
1551 (2014) 079, doi:10.1007/JHEP07(2014)079, arXiv:1405.0301.
- 1552 [32] T. Sjstrand et al., “An Introduction to PYTHIA 8.2”, arXiv:1410.3012.
- 1553 [33] Giovanni Zevi Della Porta, “ECAL and HCAL reconstruction for 25ns bunch spacing”,  
1554 (2014). [https://indico.cern.ch/event/339666/session/2/contribution/  
1555 20/material/slides/0.pdf](https://indico.cern.ch/event/339666/session/2/contribution/20/material/slides/0.pdf).
- 1556 [34] The RA2b Group, “Search for New Physics in Events with b-Jets and Missing Transverse  
1557 Energy with the full 2011 Data Sample”, *CMS Analysis Note AN-11-409* (2011).
- 1558 [35] A. Czarnecki, J. Korner, and J. Piclum, “Helicity fractions of W bosons from top quark  
1559 decays at NNLO in QCD”, *Phys. Rev. D* **81** (2010) 111503,  
1560 doi:10.1103/PhysRevD.81.111503.

DRAFT

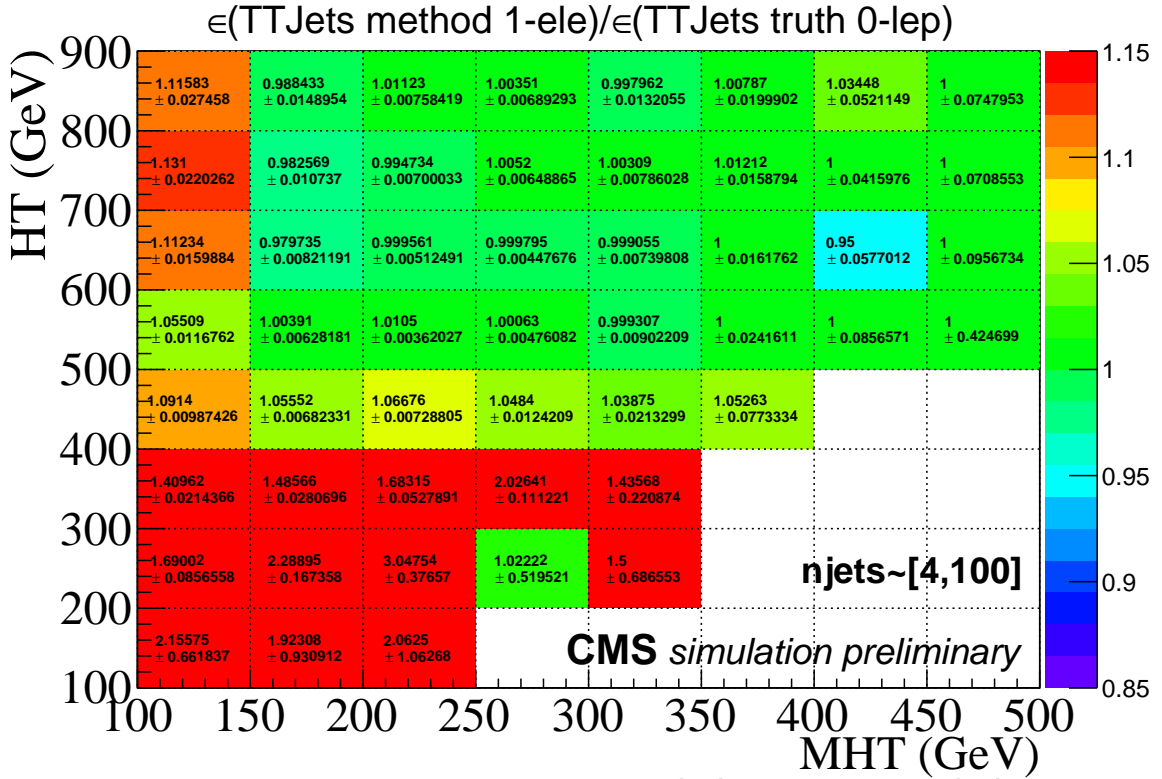


Figure 96: The ratio of the trigger efficiency for events passing the single electron reference trigger to the true efficiency for 0-lepton events in  $t\bar{t}$  simulation, as a function of the offline  $H_T$  and  $H_T^{\text{miss}}$ . The ratio is consistent with 1 within the region of the baseline selection of  $H_T > 500 \text{ GeV}$  and  $H_T^{\text{miss}} > 200 \text{ GeV}$ .

## A Supplemental information on the triggers

The method for estimating the primary trigger efficiency using single electron events has been studied, and we determine that the method provides an unbiased estimate of the true efficiency in the signal region to within the statistical uncertainty of the samples studied. Because the turn-on of the  $H_T$  and  $H_T^{\text{miss}}$  legs are measured in events selected by the same single electron reference trigger, it is natural to examine the efficiency in the  $H_T$ - $H_T^{\text{miss}}$  plane. Figure 96 shows the ratio of the efficiency using the single electron method in a simulated sample of  $t\bar{t}$  events to the true efficiency in the 0-lepton region taken from the same sample. The ratio is consistent with unity for  $H_T^{\text{miss}} > 150 \text{ GeV}$  and  $H_T > 500 \text{ GeV}$ .

The trigger turn-on is significantly slower for events with fake  $E_T^{\text{miss}}$  than for real  $E_T^{\text{miss}}$ . The efficiency is shown in Figure 97 in a sample of fake  $E_T^{\text{miss}}$ -enriched events selected by the HLT\_PFT800 trigger that are required to satisfy an inverted  $\Delta\phi$  selection (see section 4 for details of the  $\Delta\phi$  control region selection). This efficiency is applied to simulated QCD events in background studies.

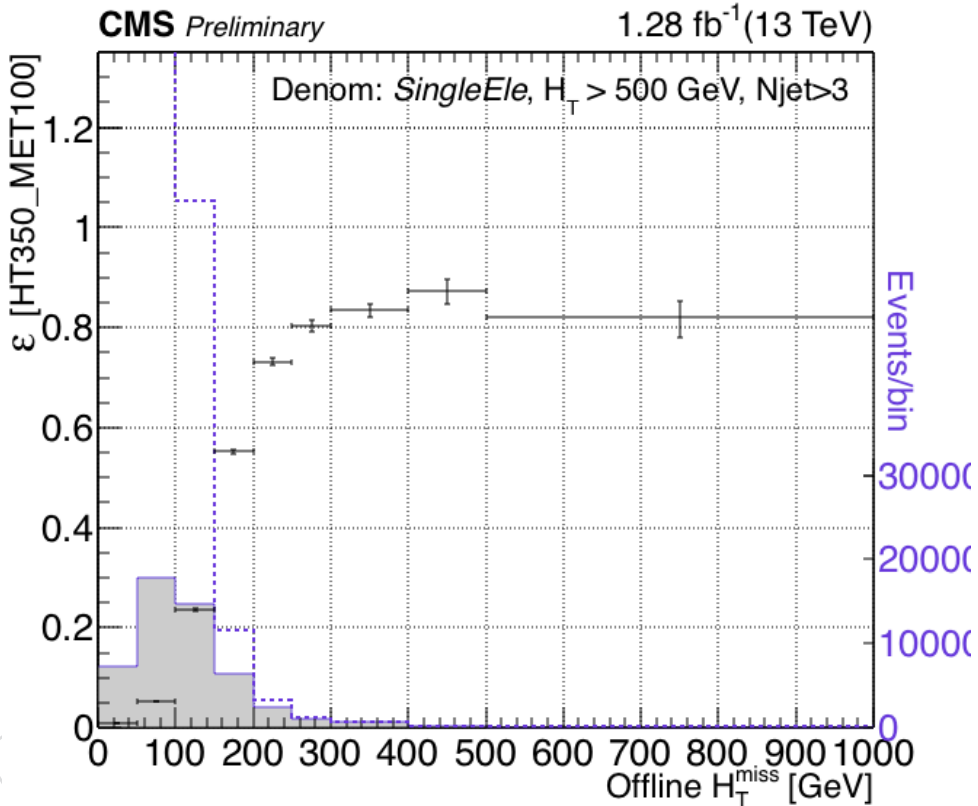


Figure 97: The trigger efficiency vs the offline  $H_T^{\text{miss}}$  for data events in the QCD control region with an offline  $H_T > 500$  GeV. The low plateau is thought to come about as a result of large discrepancies between the online calorimeter-based  $E_T^{\text{miss}}$  and the particle flow  $E_T^{\text{miss}}$ . A matching between these objects is being considered as an analysis-level selection and will be implemented as we try to understand the behavior of the primary trigger in QCD events.

## 1575 B Comparison of QCD samples

1576 As part of the Phys14 MC production campaign, two sets of QCD samples were produced:

- 1577 1. Samples binned in generator-level  $H_T$ , generated with Madgraph [31]
- 1578 2. Samples binned in generator-level  $\hat{p}_T$ , generated with Pythia 8 [32]

1579 The Phys14 Madgraph samples more closely resemble the QCD MC that will be used through-  
 1580 out the upcoming run, but they have insufficient statistics for studying the closure of the QCD  
 1581 background estimation methods described in Section 7. Thus we use the Phys14 Pythia 8 sam-  
 1582 ples in those studies. Here we present a few basic comparisons between the Phys14 Madgraph  
 1583 and Pythia 8 samples and their CSA14 (CMSSW\_7\_0\_6\_patch1) versions.

1584 Table 27 includes a baseline event selection cutflow comparison of the four sets of samples. Af-  
 1585 ter baseline selection, in particular the QCD-suppressing cut on  $\Delta\hat{\phi}_{\min}$ , the expected yields from  
 1586 the two sets of Phys14 samples agree within statistical uncertainty. The expected yields from  
 1587 the CSA14 samples are consistently larger than the corresponding Phys14 yields. These dis-  
 1588 agreements may be explained by known differences in reconstruction between CMSSW\_7\_0\_6\_patch1  
 1589 and CMSSW\_7\_2\_0\_patch1, including the improved mitigation of out-of-time pileup effects in  
 1590 CMSSW\_7\_2\_0\_patch1 [33].

Table 27: Comparison of cutflow and expected yields at  $4 \text{ fb}^{-1}$  for QCD samples after baseline selection. Note that the CSA14 samples are reconstructed with CMSSW\_7\_0\_6\_patch1, while the Phys14 samples are reconstructed with CMSSW\_7\_2\_0\_patch1.

Cut	CSA14 Pythia	CSA14 Madgraph	Phys14 Pythia	Phys14 Madgraph
Start	$33065553 \pm 18251$	$2792038900 \pm 3315130$	$33065553 \pm 21286$	$2792038930 \pm 1642779$
$H_T > 500 \text{ GeV}$	$30667176 \pm 17512$	$94910354 \pm 282016$	$30196895 \pm 20254$	$65239789 \pm 71885$
$N_{\text{jet}} \geq 4$	$15725313 \pm 12459$	$60902673 \pm 249387$	$13472302 \pm 13420$	$36841661 \pm 62033$
$H_T^{\text{miss}} > 200 \text{ GeV}$	$51028 \pm 598$	$30294 \pm 5897$	$36371 \pm 532$	$23871 \pm 1123$
Muon veto	$50843 \pm 597$	$30276 \pm 5897$	$36322 \pm 532$	$23850 \pm 1123$
Electron veto	$34988 \pm 466$	$29946 \pm 5896$	$35479 \pm 525$	$23332 \pm 1119$
$\Delta\hat{\phi}_{\min} > 4$	$6018 \pm 209$	$7600 \pm 4126$	$4892 \pm 216$	$5144 \pm 1039$

## 1591 C Supplemental materials for lost-lepton background estimation

### 1592 C.1 Closure test with varied MC cross sections

1593 We show closure tests of the methods for determination of the lost-lepton background in Fig. 98  
 1594 for the nominal simulation model, and in Figs. 99 and 100 for variations of the model.

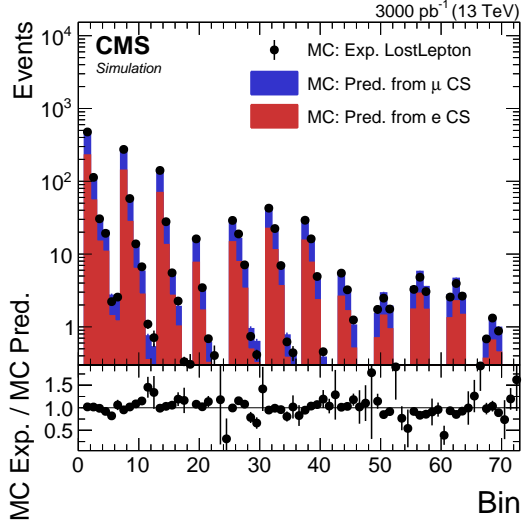


Figure 98: Comparison of the expected and predicted lost electrons and muons using both the single electron and muon control sample. For the closure test,  $t\bar{t}$ ,  $W$ -jets, single  $t$ , and exotic events are considered (see Section 3) and nominal MC cross sections are used.

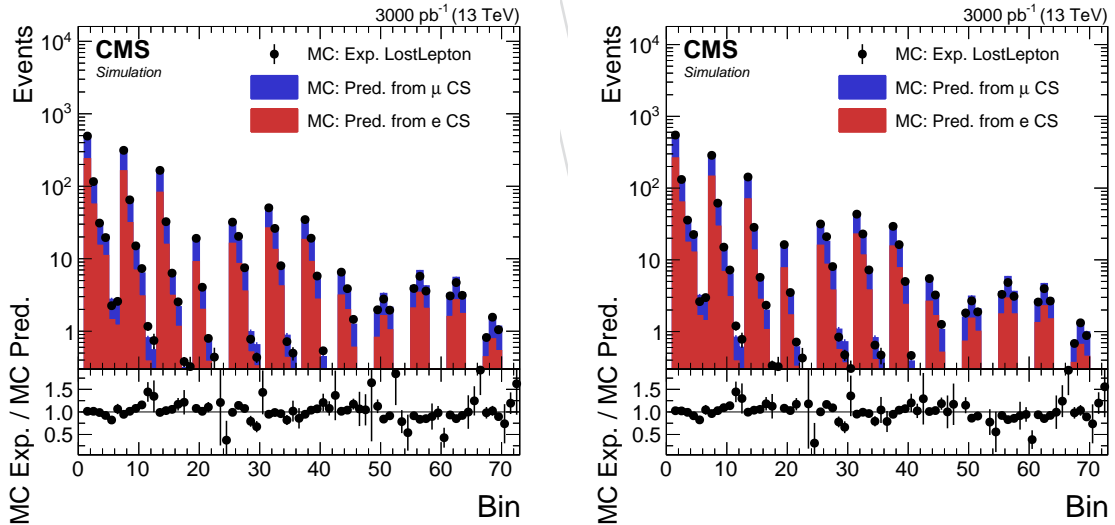


Figure 99: Same as Fig. 98, but with (left) the  $t\bar{t}$  cross section increased by 20% and (right) the  $w$ -jets cross section increased by 20%.

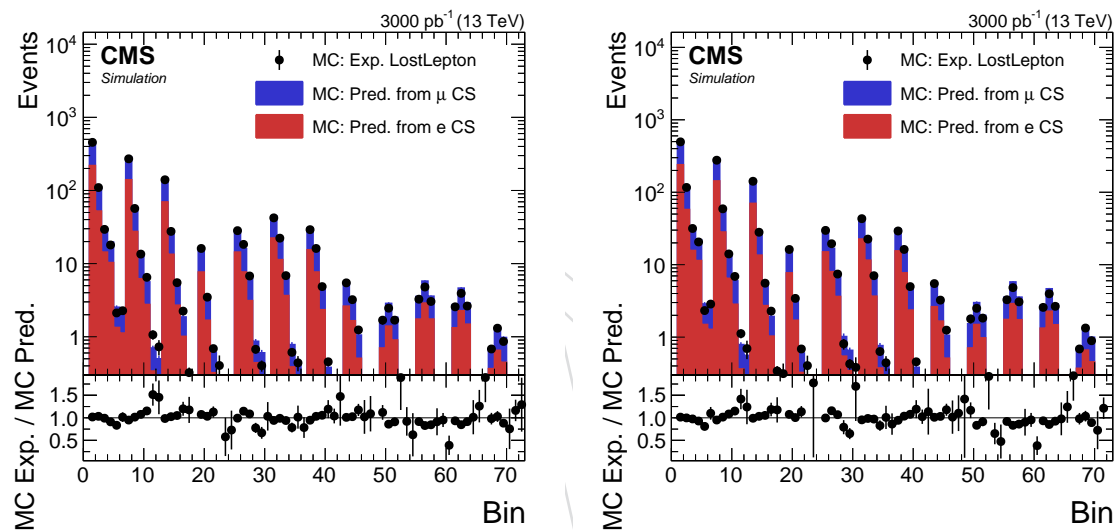


Figure 100: Same as Fig. 98, but (left) without the rare processes ( $t\bar{t}$ ,  $w+jets$  and single  $t$  only), and (right), with the cross sections of the rare processes increased by 100%.

1595 **C.2 Closure test in QCD binning**

1596 We show closure tests of the methods for determination of the lost-lepton background in Fig. 101  
 1597 in finer binning which is required by the QCD background estimation method. This test is per-  
 1598 formed in the search region and in a QCD enriched region which is achieved by inverting the  
 1599  $\Delta\Phi$  requirement.

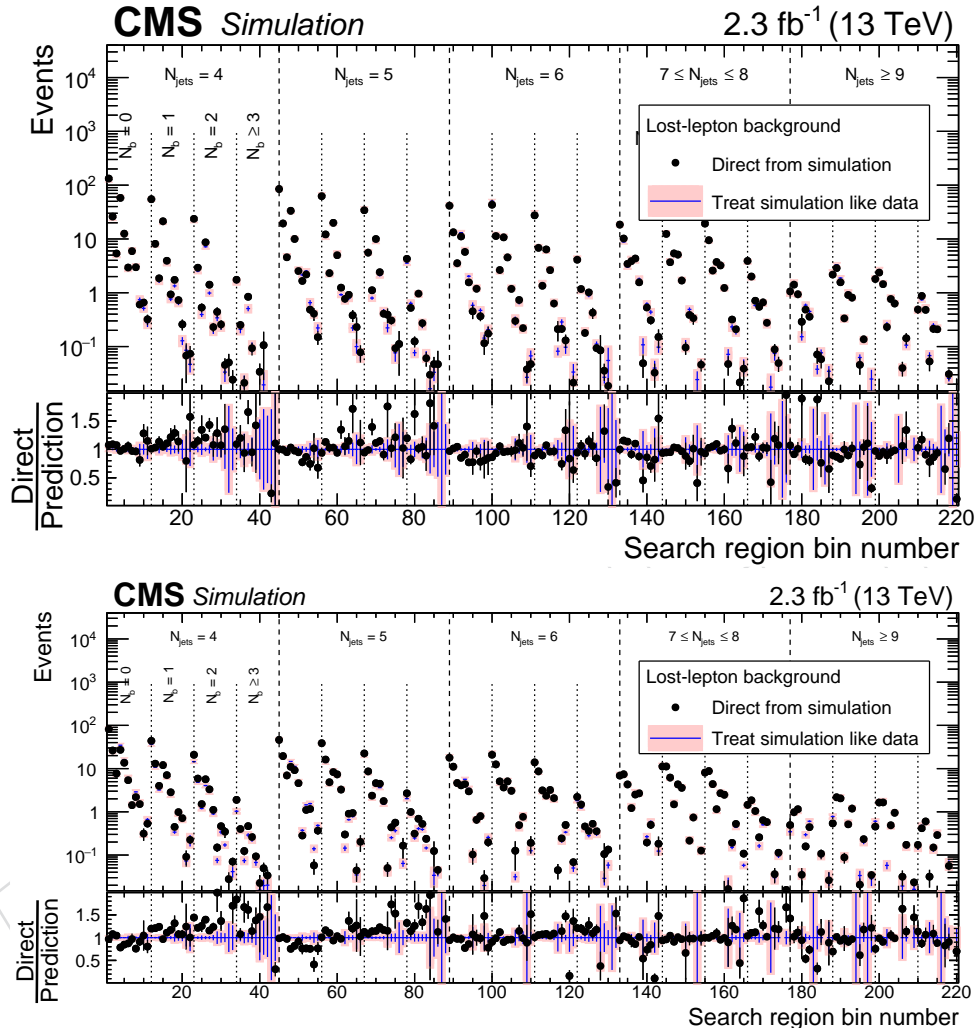


Figure 101: Comparison of prediction from single electron and single muon control sample vs expected lost-leptons for finer QCD binning. The top plot shows the closure test in the non-inverted  $\Delta\Phi$  region, the bottom plot in the inverted  $\Delta\Phi$  region.

1600 **D Supplemental materials for hadronically-decaying  $\tau$  background  
1601 estimation**

1602 We show closure tests of the methods for determination of the  $\tau_h$  background in Fig. 102 in finer  
1603 binning which is required by the QCD background estimation method described in Section 7.  
1604 This test is performed in the search region and in a QCD enriched region which is achieved by  
1605 inverting the  $\Delta\phi(j_{1,2,3,4}, H_T^{\text{miss}})$  requirement.

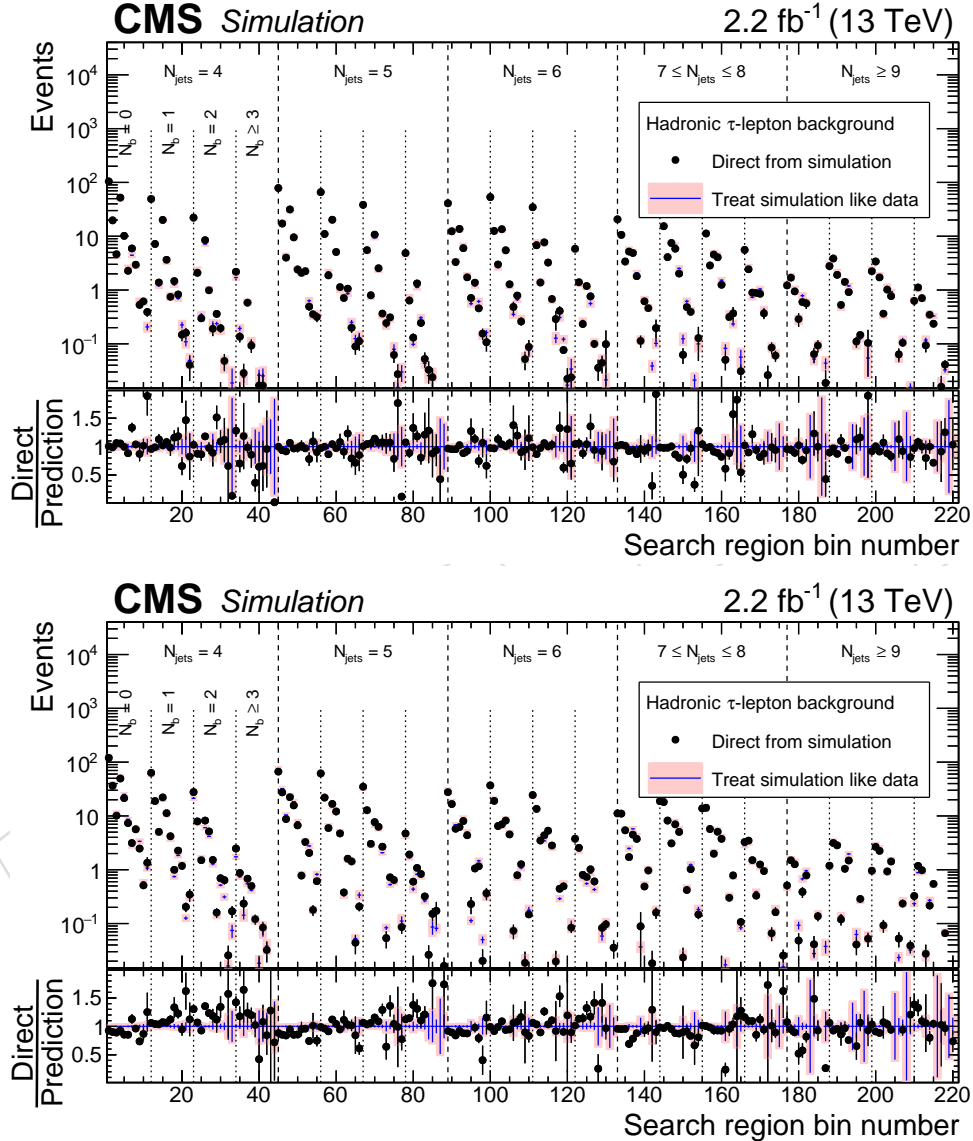


Figure 102: The  $\tau_h$  background for events (top) passing and (bottom) failing the angular cuts on  $\Delta\phi(j_{1,2,3,4}, H_T^{\text{miss}})$  in fine 220 bins defined in terms of search variables (i.e.  $H_T$ ,  $H_T^{\text{miss}}$ ,  $N_{\text{jet}}$ , and  $N_{\text{b-jet}}$ ) as predicted directly from simulation (solid points) and as predicted by the data-driven background-determination procedure (shaded regions). The binning is based on eleven  $H_T$ - $H_T^{\text{miss}}$  bins as defined in Fig. 34 for five  $N_{\text{jet}}$  and four  $N_{\text{b-jet}}$  regions. These are used as inputs to QCD background predictions. The simulation makes use of  $t\bar{t}$ ,  $W+\text{jets}$ , and single-top quark event samples.

1606 Also, here we show in Fig. 103 the closure test plots in the 72 search bins before we included  
1607 rare SM processes. These rare SM processes contribute about 4% compared to the total of

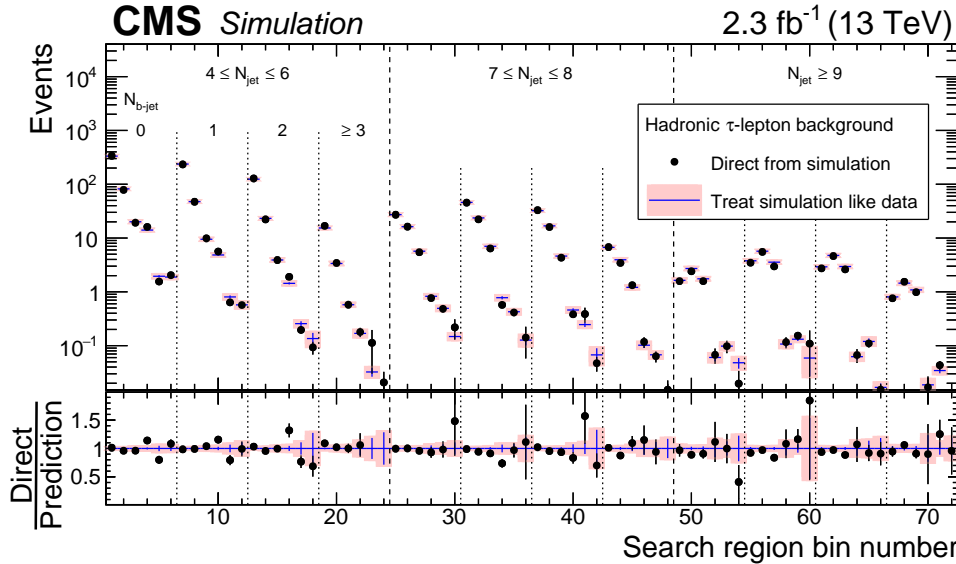


Figure 103: The  $\tau_h$  background in the 72 search bins of the analysis (intervals of  $H_T$ ,  $H_T^{\text{miss}}$ ,  $N_{\text{jet}}$ , and  $N_{\text{b-jet}}$ ) as predicted directly from simulation (solid points) and as predicted by the data-driven background-determination procedure (shaded regions). The simulation makes use of  $t\bar{t}$ ,  $W+\text{jets}$ , and single-top quark event samples only in contrast to Fig. 39 which makes use of  $t\bar{t}$ ,  $W+\text{jets}$ , single-top, Drell-Yan, and other rare SM event samples listed in Table 7.

1608     $t\bar{t}$ ,  $W+\text{jets}$ , and single-top quark event samples, but it contributes to both “expectation” (pre-  
 1609    diction directly from simulation) and “prediction” (predicted by the data-driven background-  
 1610    determination procedure), so the closure does not get affected much by inclusion of Drell-Yan  
 1611    and SM rare process samples from WW/WZ/ZZ,  $t\bar{t}V$  ( $V=W, Z, h$ ), and other rare SM event  
 1612    samples listed in Table 7.

## 1613    E Other track veto efficiency validation studies

### 1614    E.1 Effect of the $m_T$ cut on track isolation efficiency

1615    The  $m_T$  cut disregarding events with tracks with  $m_T > 100 \text{ GeV}$  is important to preserve signal  
 1616    selection efficiency while reduces the  $t\bar{t}$  &  $W+\text{jets}$  background significantly. The  $m_T$  variable  
 1617    aims to reconstruct the transverse  $W$  mass from the lepton candidate and the neutrino. The  
 1618    neutrino is reconstructed indirectly as the missing transverse momentum, computed from the  
 1619    recoil of the hadronic activity in the event including the lepton momentum. In the validation  
 1620    region, which is based on  $Z \rightarrow ll$  events, no neutrino is present as a genuine source of  $\vec{p}_T^{\text{miss}}$ .  
 1621    In order to mimic a  $W$  decay, the tag lepton is subtracted from the computed  $\vec{p}_T^{\text{miss}}$  and the  $m_T$   
 1622    variable is calculated. Here the nominal maximum transverse mass does not peak at  $80 \text{ GeV}$   
 1623    ( $W$  mass) but rather at  $91 \text{ GeV}$  ( $Z$  mass): thus the cut value of  $100 \text{ GeV}$  is increased by  $11 \text{ GeV}$  to  
 1624     $111 \text{ GeV}$  in order to compensate. Comparison distributions of calculated  $m_T$  using recalculated  
 1625     $E_T^{\text{miss}}$  including the tag lepton  $p_T$  and  $m_T$  distributions from  $t\bar{t}$  &  $W+\text{jets}$  are shown in Figs. 104.  
 1626    for the important threshold effect relative to the to be cut on mass. This  $m_T$  cut is shown in to  
 1627    have very little impact on the isolation efficiency, so ultimately the tag-and-probe measurement  
 1628    is performed without the modified  $m_T$  cut on the probe lepton.

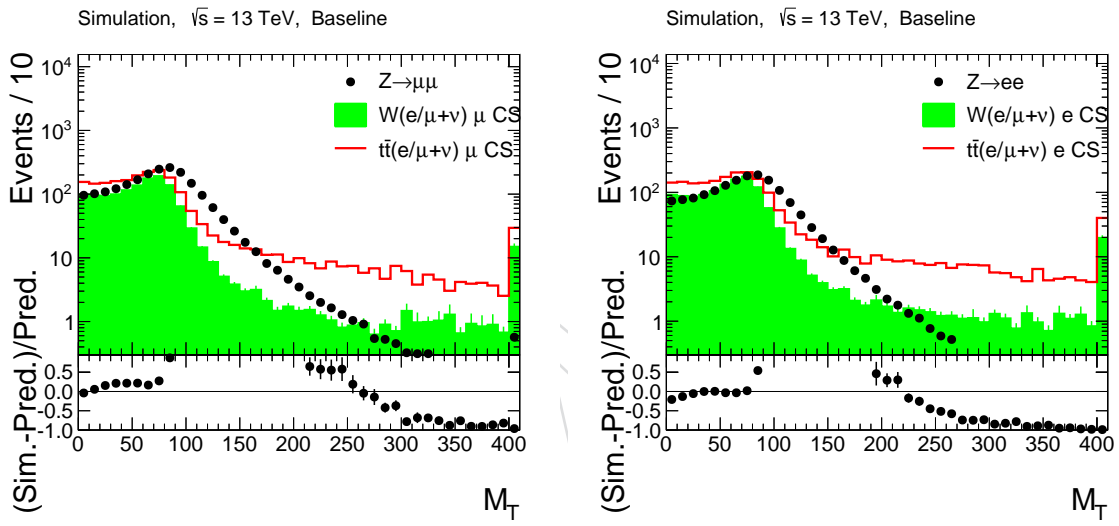


Figure 104: These plots show comparisons between  $m_T$  calculated from  $t\bar{t}$  &  $W$ +jets single  $\mu$  (left) & electron (right) control sample and  $m_T$  calculated in DY events treating the tag lepton as neutrino by adding it to the in the event already existing  $E_T^{\text{miss}}$ . Reasonable agreement between  $W$ +jets and DY can be observed while the  $t\bar{t}$  show significant longer tails to high  $m_T$  due to di-leptonic decays. Also from these plots one can see the expected shift of the peak  $m_T$  in DY events as expected due to the higher  $M_Z$ .

**F Full Table of Event Yields**

1629 Table 28 shows the event yields in the signal region weighted by cross section for the four main  
1630 backgrounds (QCD, W, Z and TTbar) and the six signal points used in the analysis. Table 29  
1631 shows the yields control region with zero leptons and low  $\Delta\hat{\phi}_{\min}$  and Table 30 shows yields in  
1632 the single lepton region with one muon or one electron.  
1633

DRAFT

Table 28: Event Yields Weighted by Cross-Section and scaled to  $4\text{ fb}^{-1}$  for the main Backgrounds and the signal points used in the analysis.

Signal and Background Yields										
	QCD	ttbar	Z	W	T1tttt $M_{glu}, M_\chi$ 1500,100	T1tttt $M_{glu}, M_\chi$ 1200,800	T1qqqq $M_{glu}, M_\chi$ 1400,100	T1qqqq $M_{glu}, M_\chi$ 1000,800	T1bbbb $M_{glu}, M_\chi$ 1500,100	T1bbbb $M_{glu}, M_\chi$ 1200,900
HT-MHTBin1 jetbin1 btag0	29457.36	412.13	1132.98	1090.20	0.01	0.12	0.27	76.47	0.01	5.13
HT-MHTBin2 jetbin1 btag0	2250.38	81.35	261.34	274.44	0.01	0.02	1.59	21.12	0.05	0.95
HT-MHTBin3 jetbin1 btag0	313.66	13.03	56.03	60.43	0.02	0.00	8.40	2.14	0.35	0.07
HT-MHTBin4 jetbin1 btag0	18.45	10.47	122.45	63.32	0.01	0.00	1.63	14.19	0.06	2.44
HT-MHTBin5 jetbin1 btag0	18.45	3.36	13.74	9.16	0.03	0.00	8.70	3.27	0.37	0.11
HT-MHTBin6 jetbin1 btag0	135.20	1.19	22.75	9.43	0.02	0.00	8.93	5.34	0.36	0.96
HT-MHTBin1 jetbin1 btag1	6117.89	1103.13	266.82	263.21	0.01	0.44	0.07	21.45	0.06	21.52
HT-MHTBin2 jetbin1 btag1	753.30	236.38	69.93	78.96	0.03	0.08	0.52	6.69	0.24	3.51
HT-MHTBin3 jetbin1 btag1	129.15	40.64	16.55	18.19	0.09	0.03	2.76	0.81	1.56	0.39
HT-MHTBin4 jetbin1 btag1	9.23	19.05	28.37	15.75	0.04	0.03	0.50	4.55	0.24	8.43
HT-MHTBin5 jetbin1 btag1	9.23	5.26	3.91	3.25	0.08	0.02	2.90	1.13	1.61	0.51
HT-MHTBin6 jetbin1 btag1	0.00	1.63	6.18	3.02	0.10	0.01	2.83	1.48	1.58	3.51
HT-MHTBin1 jetbin1 btag2	1081.63	821.95	51.77	42.12	0.02	0.71	0.01	3.38	0.08	25.89
HT-MHTBin2 jetbin1 btag2	236.68	186.86	13.27	12.17	0.06	0.16	0.09	1.18	0.47	4.15
HT-MHTBin3 jetbin1 btag2	18.45	27.17	3.03	3.05	0.16	0.01	0.48	0.19	2.37	0.36
HT-MHTBin4 jetbin1 btag2	0.00	12.29	5.03	2.59	0.06	0.05	0.09	0.75	0.48	9.97
HT-MHTBin5 jetbin1 btag2	0.00	3.75	0.62	0.51	0.15	0.02	0.50	0.16	2.50	0.79
HT-MHTBin6 jetbin1 btag2	0.00	1.90	1.02	0.38	0.16	0.03	0.46	0.20	2.63	4.35
HT-MHTBin1 jetbin1 btag3	135.20	149.44	4.79	3.44	0.01	0.54	0.00	0.28	0.08	11.99
HT-MHTBin2 jetbin1 btag3	18.45	36.32	1.41	1.28	0.04	0.10	0.01	0.13	0.55	2.32
HT-MHTBin3 jetbin1 btag3	9.23	6.63	0.29	0.44	0.14	0.02	0.05	0.03	1.95	0.25
HT-MHTBin4 jetbin1 btag3	0.00	1.60	0.45	0.23	0.05	0.03	0.01	0.12	0.49	4.07
HT-MHTBin5 jetbin1 btag3	0.00	1.08	0.07	0.02	0.13	0.02	0.04	0.01	2.18	0.33
HT-MHTBin6 jetbin1 btag3	0.00	0.25	0.08	0.05	0.13	0.02	0.04	0.03	2.35	1.85
HT-MHTBin1 jetbin2 btag0	1324.36	75.63	32.74	38.09	0.01	0.31	0.02	20.72	0.00	0.78
HT-MHTBin2 jetbin2 btag0	418.01	26.79	20.88	26.23	0.02	0.12	0.29	14.84	0.00	0.42
HT-MHTBin3 jetbin2 btag0	27.68	6.43	6.79	8.11	0.04	0.01	3.46	3.00	0.13	0.07
HT-MHTBin4 jetbin2 btag0	0.00	0.63	3.05	1.85	0.01	0.01	0.23	5.03	0.00	0.28
HT-MHTBin5 jetbin2 btag0	0.00	0.25	1.51	1.30	0.04	0.02	3.62	3.34	0.12	0.03
HT-MHTBin6 jetbin2 btag0	9.23	0.19	0.88	0.44	0.05	0.01	3.14	2.73	0.10	0.19
HT-MHTBin1 jetbin2 btag1	261.18	212.16	11.96	12.60	0.01	1.28	0.00	7.74	0.00	3.67
HT-MHTBin2 jetbin2 btag1	46.13	91.27	8.25	10.77	0.08	0.59	0.13	6.49	0.03	1.96
HT-MHTBin3 jetbin2 btag1	9.23	20.18	2.96	3.99	0.28	0.14	1.65	1.37	0.58	0.46
HT-MHTBin4 jetbin2 btag1	0.00	1.66	1.12	0.85	0.06	0.07	0.09	1.95	0.03	1.33
HT-MHTBin5 jetbin2 btag1	0.00	2.11	0.59	0.28	0.26	0.10	1.64	1.40	0.62	0.48
HT-MHTBin6 jetbin2 btag1	0.00	0.82	0.43	0.28	0.23	0.05	1.32	1.29	0.55	0.78
HT-MHTBin1 jetbin2 btag2	0.00	184.69	3.47	3.50	0.03	2.39	0.00	1.70	0.00	6.04
HT-MHTBin2 jetbin2 btag2	0.00	94.07	2.62	2.38	0.14	1.06	0.04	1.44	0.07	2.76
HT-MHTBin3 jetbin2 btag2	0.00	18.04	0.88	1.03	0.55	0.20	0.40	0.35	1.04	0.70
HT-MHTBin4 jetbin2 btag2	0.00	2.33	0.26	0.16	0.12	0.11	0.03	0.43	0.07	2.36
HT-MHTBin5 jetbin2 btag2	0.00	1.23	0.18	0.16	0.50	0.14	0.38	0.31	1.10	0.78
HT-MHTBin6 jetbin2 btag2	0.00	0.30	0.11	0.05	0.45	0.09	0.33	0.26	1.01	1.51
HT-MHTBin1 jetbin2 btag3	0.00	60.69	0.59	0.51	0.03	2.47	0.00	0.26	0.01	4.84
HT-MHTBin2 jetbin2 btag3	125.98	30.94	0.48	0.72	0.20	1.25	0.01	0.31	0.11	2.81
HT-MHTBin3 jetbin2 btag3	0.00	5.89	0.18	0.28	0.78	0.19	0.07	0.12	1.25	0.36
HT-MHTBin4 jetbin2 btag3	0.00	0.51	0.06	0.03	0.16	0.09	0.00	0.13	0.09	1.92
HT-MHTBin5 jetbin2 btag3	0.00	0.89	0.03	0.08	0.74	0.20	0.07	0.09	1.26	0.66
HT-MHTBin6 jetbin2 btag3	0.00	0.13	0.03	0.02	0.65	0.10	0.06	0.07	1.18	0.91
HT-MHTBin1 jetbin3 btag0	0.00	4.61	0.96	1.26	0.00	0.14	0.00	1.75	0.00	0.07
HT-MHTBin2 jetbin3 btag0	144.43	6.02	1.52	2.08	0.01	0.21	0.05	4.58	0.00	0.09
HT-MHTBin3 jetbin3 btag0	9.23	2.58	0.99	1.13	0.09	0.12	1.14	1.84	0.03	0.04
HT-MHTBin4 jetbin3 btag0	0.00	0.13	0.15	0.11	0.01	0.01	0.02	0.88	0.00	0.04
HT-MHTBin5 jetbin3 btag0	0.00	0.14	0.20	0.18	0.09	0.05	1.21	1.67	0.04	0.05
HT-MHTBin6 jetbin3 btag0	0.00	0.00	0.09	0.10	0.05	0.02	0.99	0.86	0.02	0.03
HT-MHTBin1 jetbin3 btag1	0.00	16.81	0.34	0.50	0.00	0.82	0.00	0.77	0.00	0.19
HT-MHTBin2 jetbin3 btag1	9.23	19.60	0.78	1.03	0.05	1.22	0.02	2.19	0.00	0.35
HT-MHTBin3 jetbin3 btag1	0.00	6.57	0.57	0.97	0.47	0.55	0.67	1.08	0.21	0.19
HT-MHTBin4 jetbin3 btag1	0.00	0.25	0.06	0.03	0.05	0.04	0.01	0.40	0.00	0.13
HT-MHTBin5 jetbin3 btag1	0.00	0.93	0.06	0.08	0.45	0.28	0.64	0.93	0.20	0.12
HT-MHTBin6 jetbin3 btag1	0.00	0.13	0.04	0.02	0.32	0.13	0.53	0.55	0.18	0.19
HT-MHTBin1 jetbin3 btag2	0.00	19.15	0.13	0.07	0.01	1.65	0.00	0.40	0.00	0.71
HT-MHTBin2 jetbin3 btag2	0.00	20.33	0.22	0.28	0.16	2.76	0.00	0.61	0.01	0.76
HT-MHTBin3 jetbin3 btag2	0.00	9.10	0.18	0.36	1.13	1.30	0.24	0.34	0.36	0.40
HT-MHTBin4 jetbin3 btag2	0.00	0.31	0.02	0.00	0.09	0.12	0.00	0.08	0.01	0.39
HT-MHTBin5 jetbin3 btag2	0.00	0.76	0.05	0.02	1.03	0.74	0.23	0.31	0.39	0.32
HT-MHTBin6 jetbin3 btag2	0.00	0.00	0.03	0.02	0.75	0.26	0.17	0.16	0.33	0.28
HT-MHTBin1 jetbin3 btag3	0.00	5.26	0.04	0.08	0.01	2.93	0.00	0.04	0.00	0.64
HT-MHTBin2 jetbin3 btag3	0.00	10.17	0.08	0.20	0.27	4.73	0.00	0.16	0.01	1.29
HT-MHTBin3 jetbin3 btag3	0.00	3.82	0.05	0.10	2.37	2.36	0.05	0.08	0.55	0.38
HT-MHTBin4 jetbin3 btag3	0.00	0.13	0.01	0.00	0.15	0.23	0.00	0.01	0.01	0.44
HT-MHTBin5 jetbin3 btag3	0.00	0.30	0.00	0.00	2.10	1.24	0.06	0.05	0.60	0.42
HT-MHTBin6 jetbin3 btag3	0.00	0.00	0.00	0.00	1.38	0.44	0.04	0.05	0.49	0.40

	Signal and Background Yields										
	QCD	tbar	Z	W	T1ttt $M_{glu}, M_{\chi}$ 1500,100	T1ttt $M_{glu}, M_{\chi}$ 1200,800	T1qqq $M_{glu}, M_{\chi}$ 1400,100	T1qqq $M_{glu}, M_{\chi}$ 1000,800	T1bbbb $M_{glu}, M_{\chi}$ 1500,100	T1bbbb $M_{glu}, M_{\chi}$ 1200,900	
HT-MHTBin1 jetbin1 btag0	75021.52	173.41	149.14	271.06	0.00	0.01	0.02	6.39	0.00	0.50	
HT-MHTBin2 jetbin1 btag0	14380.24	77.94	81.42	149.66	0.00	0.01	0.30	4.07	0.01	0.17	
HT-MHTBin3 jetbin1 btag0	4262.10	38.22	36.43	67.79	0.01	0.00	4.81	1.02	0.25	0.09	
HT-MHTBin4 jetbin1 btag0	166.06	1.49	3.79	6.17	0.00	0.00	0.07	0.74	0.00	0.11	
HT-MHTBin5 jetbin1 btag0	18.45	2.30	3.28	5.09	0.01	0.00	1.42	0.69	0.08	0.05	
HT-MHTBin6 jetbin1 btag0	9.23	0.53	0.94	1.20	0.00	0.00	0.45	0.44	0.02	0.04	
HT-MHTBin1 jetbin1 btag1	19718.59	446.68	35.63	70.85	0.00	0.05	0.01	1.68	0.01	2.09	
HT-MHTBin2 jetbin1 btag1	4821.05	200.13	22.16	43.74	0.00	0.03	0.09	1.40	0.05	0.74	
HT-MHTBin3 jetbin1 btag1	1937.32	100.17	11.04	22.92	0.06	0.01	1.66	0.36	0.98	0.11	
HT-MHTBin4 jetbin1 btag1	46.13	2.43	1.03	1.63	0.00	0.01	0.02	0.22	0.01	0.39	
HT-MHTBin5 jetbin1 btag1	27.68	6.56	0.90	1.69	0.01	0.00	0.44	0.31	0.31	0.07	
HT-MHTBin6 jetbin1 btag1	0.00	0.74	0.24	0.67	0.01	0.00	0.13	0.15	0.11	0.27	
HT-MHTBin1 jetbin1 btag2	3294.20	310.65	7.10	11.58	0.00	0.08	0.00	0.27	0.01	2.63	
HT-MHTBin2 jetbin1 btag2	965.48	158.78	4.13	7.36	0.01	0.03	0.02	0.38	0.09	0.91	
HT-MHTBin3 jetbin1 btag2	341.34	75.65	2.05	4.12	0.07	0.01	0.25	0.05	1.35	0.21	
HT-MHTBin4 jetbin1 btag2	27.68	2.01	0.11	0.30	0.00	0.00	0.00	0.01	0.02	0.55	
HT-MHTBin5 jetbin1 btag2	0.00	3.94	0.14	0.26	0.03	0.00	0.08	0.05	0.46	0.13	
HT-MHTBin6 jetbin1 btag2	0.00	0.25	0.03	0.16	0.01	0.00	0.02	0.01	0.15	0.25	
HT-MHTBin1 jetbin1 btag3	451.74	59.61	0.79	1.04	0.00	0.06	0.00	0.01	0.00	1.07	
HT-MHTBin2 jetbin1 btag3	156.83	32.18	0.52	0.71	0.00	0.03	0.00	0.00	0.09	0.48	
HT-MHTBin3 jetbin1 btag3	64.58	13.10	0.25	0.39	0.07	0.00	0.03	0.00	1.02	0.07	
HT-MHTBin4 jetbin1 btag3	0.00	0.25	0.01	0.07	0.00	0.00	0.00	0.00	0.01	0.27	
HT-MHTBin5 jetbin1 btag3	0.00	0.72	0.03	0.00	0.03	0.00	0.01	0.01	0.33	0.07	
HT-MHTBin6 jetbin1 btag3	0.00	0.13	0.00	0.00	0.01	0.00	0.00	0.00	0.13	0.11	
HT-MHTBin1 jetbin2 btag0	7742.12	32.53	3.76	7.19	0.00	0.02	0.00	1.18	0.00	0.03	
HT-MHTBin2 jetbin2 btag0	1819.96	29.01	5.73	11.24	0.00	0.03	0.04	2.44	0.00	0.05	
HT-MHTBin3 jetbin2 btag0	827.10	17.93	4.80	8.95	0.03	0.01	2.25	1.20	0.10	0.07	
HT-MHTBin4 jetbin2 btag0	9.23	0.13	0.11	0.16	0.00	0.00	0.00	0.19	0.00	0.01	
HT-MHTBin5 jetbin2 btag0	0.00	0.89	0.34	0.51	0.01	0.00	0.63	0.59	0.02	0.01	
HT-MHTBin6 jetbin2 btag0	0.00	0.05	0.05	0.11	0.00	0.00	0.18	0.19	0.01	0.03	
HT-MHTBin1 jetbin2 btag1	1659.35	109.08	1.37	2.33	0.00	0.11	0.00	0.58	0.00	0.16	
HT-MHTBin2 jetbin2 btag1	777.80	85.82	2.37	4.61	0.01	0.13	0.02	0.90	0.00	0.29	
HT-MHTBin3 jetbin2 btag1	405.92	54.02	2.33	4.53	0.15	0.07	0.98	0.51	0.44	0.12	
HT-MHTBin4 jetbin2 btag1	0.00	0.25	0.03	0.02	0.00	0.00	0.00	0.12	0.00	0.01	
HT-MHTBin5 jetbin2 btag1	0.00	1.53	0.14	0.25	0.05	0.03	0.27	0.24	0.12	0.00	
HT-MHTBin6 jetbin2 btag1	0.00	0.25	0.03	0.05	0.01	0.00	0.08	0.19	0.04	0.05	
HT-MHTBin1 jetbin2 btag2	405.61	101.82	0.39	0.67	0.00	0.18	0.00	0.09	0.00	0.33	
HT-MHTBin2 jetbin2 btag2	175.28	82.61	0.64	1.25	0.01	0.25	0.01	0.20	0.01	0.52	
HT-MHTBin3 jetbin2 btag2	175.28	48.41	0.65	1.22	0.28	0.06	0.24	0.15	0.66	0.19	
HT-MHTBin4 jetbin2 btag2	0.00	0.40	0.01	0.05	0.00	0.01	0.00	0.03	0.00	0.07	
HT-MHTBin5 jetbin2 btag2	0.00	1.69	0.05	0.08	0.09	0.06	0.07	0.11	0.21	0.08	
HT-MHTBin6 jetbin2 btag2	0.00	0.13	0.00	0.03	0.02	0.01	0.02	0.01	0.06	0.08	
HT-MHTBin1 jetbin2 btag3	125.98	29.38	0.08	0.15	0.00	0.26	0.00	0.01	0.00	0.42	
HT-MHTBin2 jetbin2 btag3	153.65	25.32	0.14	0.18	0.02	0.29	0.00	0.04	0.02	0.51	
HT-MHTBin3 jetbin2 btag3	27.68	15.80	0.11	0.23	0.35	0.10	0.04	0.01	0.69	0.19	
HT-MHTBin4 jetbin2 btag3	0.00	0.13	0.00	0.00	0.00	0.02	0.00	0.01	0.00	0.12	
HT-MHTBin5 jetbin2 btag3	0.00	0.63	0.02	0.02	0.12	0.03	0.01	0.00	0.22	0.11	
HT-MHTBin6 jetbin2 btag3	0.00	0.14	0.00	0.00	0.03	0.02	0.01	0.00	0.06	0.08	
HT-MHTBin1 jetbin3 btag0	0.00	3.67	0.10	0.21	0.00	0.01	0.00	0.07	0.00	0.00	
HT-MHTBin2 jetbin3 btag0	101.48	6.21	0.43	0.94	0.00	0.02	0.01	0.42	0.00	0.00	
HT-MHTBin3 jetbin3 btag0	101.48	4.25	0.64	1.69	0.03	0.03	0.82	0.82	0.03	0.00	
HT-MHTBin4 jetbin3 btag0	0.00	0.13	0.01	0.02	0.00	0.00	0.00	0.00	0.00	0.00	
HT-MHTBin5 jetbin3 btag0	0.00	0.27	0.05	0.05	0.01	0.01	0.22	0.15	0.01	0.01	
HT-MHTBin6 jetbin3 btag0	0.00	0.00	0.01	0.02	0.00	0.00	0.07	0.07	0.00	0.01	
HT-MHTBin1 jetbin3 btag1	251.96	9.30	0.01	0.13	0.00	0.06	0.00	0.03	0.00	0.00	
HT-MHTBin2 jetbin3 btag1	27.68	19.35	0.19	0.21	0.01	0.28	0.00	0.34	0.00	0.04	
HT-MHTBin3 jetbin3 btag1	73.80	15.45	0.36	0.57	0.22	0.21	0.48	0.48	0.17	0.09	
HT-MHTBin4 jetbin3 btag1	0.00	0.27	0.00	0.00	0.00	0.00	0.00	0.00	0.00	0.03	
HT-MHTBin5 jetbin3 btag1	0.00	0.17	0.02	0.07	0.06	0.08	0.15	0.15	0.05	0.01	
HT-MHTBin6 jetbin3 btag1	0.00	0.13	0.00	0.00	0.01	0.02	0.03	0.11	0.02	0.01	
HT-MHTBin1 jetbin3 btag2	0.00	10.77	0.01	0.02	0.00	0.13	0.00	0.03	0.00	0.01	
HT-MHTBin2 jetbin3 btag2	0.00	21.02	0.09	0.08	0.02	0.52	0.00	0.12	0.00	0.08	
HT-MHTBin3 jetbin3 btag2	0.00	15.26	0.18	0.30	0.51	0.41	0.14	0.08	0.27	0.13	
HT-MHTBin4 jetbin3 btag2	0.00	0.13	0.00	0.00	0.00	0.01	0.00	0.00	0.00	0.01	
HT-MHTBin5 jetbin3 btag2	0.00	0.33	0.01	0.00	0.14	0.12	0.06	0.05	0.08	0.01	
HT-MHTBin6 jetbin3 btag2	0.00	0.13	0.00	0.00	0.05	0.04	0.02	0.01	0.02	0.04	
HT-MHTBin1 jetbin3 btag3	0.00	5.20	0.00	0.00	0.00	0.20	0.00	0.00	0.00	0.04	
HT-MHTBin2 jetbin3 btag3	18.45	6.84	0.03	0.00	0.02	0.73	0.00	0.00	0.00	0.15	
HT-MHTBin3 jetbin3 btag3	0.00	7.35	0.02	0.08	1.04	0.85	0.03	0.01	0.35	0.12	
HT-MHTBin4 jetbin3 btag3	0.00	0.00	0.00	0.00	0.00	0.00	0.00	0.00	0.00	0.00	
HT-MHTBin5 jetbin3 btag3	0.00	0.13	0.00	0.00	0.29	0.26	0.02	0.00	0.10	0.01	
HT-MHTBin6 jetbin3 btag3	0.00	0.00	0.00	0.00	0.08	0.06	0.00	0.00	0.04	0.03	

Table 29: Low  $\Delta\hat{\phi}_{\min}$  Control Region Table

	Signal and Background Yields									
	QCD	tbar	Z	W	T1ttt $M_{glu}, M_\chi$ 1500,100	T1ttt $M_{glu}, M_\chi$ 1200,800	T1qqq $M_{glu}, M_\chi$ 1400,100	T1qqq $M_{glu}, M_\chi$ 1000,800	T1bbbb $M_{glu}, M_\chi$ 1500,100	T1bbbb $M_{glu}, M_\chi$ 1200,900
HT-MHTBin1 jetbin1 btag0	251.96	66.19	14.44	150.98	0.00	0.01	0.01	1.00	0.00	0.12
HT-MHTBin2 jetbin1 btag0	153.65	13.60	3.20	36.40	0.01	0.00	0.02	0.27	0.00	0.01
HT-MHTBin3 jetbin1 btag0	9.23	1.17	0.61	7.23	0.02	0.00	0.09	0.01	0.01	0.00
HT-MHTBin4 jetbin1 btag0	0.00	2.16	1.23	9.99	0.01	0.01	0.03	0.19	0.00	0.11
HT-MHTBin5 jetbin1 btag0	0.00	0.43	0.14	0.99	0.02	0.00	0.09	0.07	0.01	0.01
HT-MHTBin6 jetbin1 btag0	0.00	0.25	0.20	1.15	0.02	0.00	0.09	0.05	0.00	0.04
HT-MHTBin1 jetbin1 btag1	0.00	180.87	3.83	33.12	0.03	0.09	0.00	0.34	0.00	0.62
HT-MHTBin2 jetbin1 btag1	18.45	32.27	0.97	9.06	0.04	0.02	0.01	0.13	0.00	0.09
HT-MHTBin3 jetbin1 btag1	0.00	5.73	0.20	2.10	0.07	0.00	0.03	0.00	0.01	0.00
HT-MHTBin4 jetbin1 btag1	0.00	3.34	0.38	2.15	0.04	0.01	0.01	0.04	0.00	0.31
HT-MHTBin5 jetbin1 btag1	0.00	1.14	0.04	0.46	0.06	0.00	0.03	0.03	0.02	0.00
HT-MHTBin6 jetbin1 btag1	0.00	0.09	0.06	0.30	0.09	0.00	0.03	0.01	0.02	0.09
HT-MHTBin1 jetbin1 btag2	0.00	125.96	0.75	5.28	0.04	0.11	0.00	0.05	0.00	0.64
HT-MHTBin2 jetbin1 btag2	0.00	27.09	0.17	1.76	0.07	0.03	0.00	0.01	0.01	0.11
HT-MHTBin3 jetbin1 btag2	0.00	5.29	0.02	0.28	0.12	0.00	0.00	0.01	0.03	0.00
HT-MHTBin4 jetbin1 btag2	0.00	2.12	0.06	0.36	0.08	0.01	0.00	0.00	0.01	0.24
HT-MHTBin5 jetbin1 btag2	0.00	0.13	0.01	0.05	0.12	0.00	0.00	0.00	0.03	0.01
HT-MHTBin6 jetbin1 btag2	0.00	0.13	0.01	0.03	0.14	0.00	0.00	0.01	0.02	0.05
HT-MHTBin1 jetbin1 btag3	0.00	18.76	0.07	0.39	0.02	0.08	0.00	0.01	0.00	0.25
HT-MHTBin2 jetbin1 btag3	0.00	5.41	0.03	0.11	0.07	0.03	0.00	0.00	0.01	0.08
HT-MHTBin3 jetbin1 btag3	0.00	0.76	0.00	0.13	0.11	0.00	0.00	0.00	0.02	0.00
HT-MHTBin4 jetbin1 btag3	0.00	0.27	0.01	0.03	0.06	0.00	0.00	0.00	0.01	0.07
HT-MHTBin5 jetbin1 btag3	0.00	0.13	0.00	0.00	0.11	0.00	0.00	0.00	0.02	0.01
HT-MHTBin6 jetbin1 btag3	0.00	0.00	0.00	0.00	0.11	0.00	0.00	0.00	0.03	0.00
HT-MHTBin1 jetbin2 btag0	0.00	11.85	0.54	5.27	0.00	0.05	0.00	0.40	0.00	0.00
HT-MHTBin2 jetbin2 btag0	9.23	4.05	0.36	3.38	0.01	0.01	0.01	0.28	0.00	0.01
HT-MHTBin3 jetbin2 btag0	0.00	1.19	0.07	1.12	0.04	0.00	0.05	0.07	0.00	0.00
HT-MHTBin4 jetbin2 btag0	0.00	0.00	0.04	0.30	0.02	0.01	0.01	0.08	0.00	0.00
HT-MHTBin5 jetbin2 btag0	0.00	0.14	0.01	0.25	0.03	0.00	0.06	0.05	0.00	0.00
HT-MHTBin6 jetbin2 btag0	0.00	0.00	0.01	0.13	0.03	0.00	0.04	0.08	0.00	0.01
HT-MHTBin1 jetbin2 btag1	0.00	30.57	0.22	1.58	0.03	0.15	0.00	0.20	0.00	0.05
HT-MHTBin2 jetbin2 btag1	0.00	14.66	0.13	1.51	0.10	0.05	0.00	0.09	0.00	0.04
HT-MHTBin3 jetbin2 btag1	0.00	3.44	0.05	0.39	0.23	0.01	0.02	0.01	0.01	0.00
HT-MHTBin4 jetbin2 btag1	0.00	0.65	0.00	0.11	0.07	0.01	0.00	0.01	0.00	0.03
HT-MHTBin5 jetbin2 btag1	0.00	0.00	0.01	0.07	0.20	0.01	0.02	0.04	0.01	0.00
HT-MHTBin6 jetbin2 btag1	0.00	0.17	0.00	0.02	0.19	0.01	0.02	0.04	0.01	0.01
HT-MHTBin1 jetbin2 btag2	0.00	25.01	0.06	0.57	0.04	0.32	0.00	0.01	0.00	0.29
HT-MHTBin2 jetbin2 btag2	0.00	12.18	0.05	0.31	0.19	0.17	0.00	0.01	0.00	0.07
HT-MHTBin3 jetbin2 btag2	0.00	2.34	0.01	0.16	0.43	0.02	0.00	0.00	0.02	0.01
HT-MHTBin4 jetbin2 btag2	0.00	0.13	0.00	0.03	0.17	0.02	0.00	0.00	0.00	0.04
HT-MHTBin5 jetbin2 btag2	0.00	0.13	0.00	0.02	0.41	0.03	0.00	0.00	0.02	0.04
HT-MHTBin6 jetbin2 btag2	0.00	0.00	0.00	0.00	0.35	0.03	0.01	0.00	0.02	0.03
HT-MHTBin1 jetbin2 btag3	0.00	8.82	0.01	0.08	0.04	0.36	0.00	0.03	0.00	0.17
HT-MHTBin2 jetbin2 btag3	0.00	2.68	0.02	0.05	0.24	0.17	0.00	0.03	0.00	0.03
HT-MHTBin3 jetbin2 btag3	0.00	0.43	0.00	0.02	0.61	0.02	0.00	0.00	0.03	0.00
HT-MHTBin4 jetbin2 btag3	0.00	0.00	0.00	0.00	0.20	0.03	0.00	0.00	0.00	0.05
HT-MHTBin5 jetbin2 btag3	0.00	0.00	0.00	0.00	0.55	0.02	0.00	0.00	0.02	0.01
HT-MHTBin6 jetbin2 btag3	0.00	0.00	0.00	0.00	0.47	0.02	0.00	0.00	0.02	0.04
HT-MHTBin1 jetbin3 btag0	0.00	0.38	0.03	0.05	0.00	0.01	0.00	0.03	0.00	0.00
HT-MHTBin2 jetbin3 btag0	0.00	1.39	0.03	0.31	0.01	0.03	0.00	0.12	0.00	0.00
HT-MHTBin3 jetbin3 btag0	0.00	0.63	0.01	0.23	0.05	0.01	0.02	0.04	0.00	0.00
HT-MHTBin4 jetbin3 btag0	0.00	0.00	0.00	0.02	0.01	0.00	0.00	0.01	0.00	0.00
HT-MHTBin5 jetbin3 btag0	0.00	0.00	0.00	0.00	0.06	0.00	0.02	0.01	0.00	0.00
HT-MHTBin6 jetbin3 btag0	0.00	0.00	0.00	0.02	0.04	0.01	0.02	0.01	0.00	0.00
HT-MHTBin1 jetbin3 btag1	0.00	2.28	0.00	0.11	0.01	0.10	0.00	0.01	0.00	0.00
HT-MHTBin2 jetbin3 btag1	0.00	3.77	0.02	0.13	0.07	0.13	0.00	0.04	0.00	0.04
HT-MHTBin3 jetbin3 btag1	0.00	0.89	0.01	0.08	0.33	0.05	0.01	0.01	0.00	0.01
HT-MHTBin4 jetbin3 btag1	0.00	0.13	0.00	0.00	0.04	0.01	0.00	0.03	0.00	0.00
HT-MHTBin5 jetbin3 btag1	0.00	0.13	0.00	0.00	0.30	0.05	0.02	0.04	0.00	0.04
HT-MHTBin6 jetbin3 btag1	0.00	0.00	0.00	0.00	0.21	0.01	0.01	0.00	0.01	0.00
HT-MHTBin1 jetbin3 btag2	0.00	2.03	0.00	0.06	0.01	0.16	0.00	0.01	0.00	0.01
HT-MHTBin2 jetbin3 btag2	0.00	2.79	0.00	0.16	0.18	0.31	0.00	0.04	0.00	0.00
HT-MHTBin3 jetbin3 btag2	0.00	1.14	0.00	0.03	0.80	0.13	0.00	0.01	0.01	0.01
HT-MHTBin4 jetbin3 btag2	0.00	0.00	0.00	0.00	0.09	0.02	0.00	0.00	0.00	0.00
HT-MHTBin5 jetbin3 btag2	0.00	0.13	0.00	0.03	0.76	0.08	0.01	0.00	0.01	0.01
HT-MHTBin6 jetbin3 btag2	0.00	0.00	0.00	0.00	0.45	0.02	0.00	0.00	0.00	0.01
HT-MHTBin1 jetbin3 btag3	0.00	1.05	0.00	0.00	0.01	0.33	0.00	0.00	0.00	0.00
HT-MHTBin2 jetbin3 btag3	0.00	1.17	0.00	0.02	0.30	0.53	0.00	0.00	0.00	0.03
HT-MHTBin3 jetbin3 btag3	0.00	0.51	0.00	0.00	1.55	0.18	0.00	0.00	0.01	0.01
HT-MHTBin4 jetbin3 btag3	0.00	0.00	0.00	0.00	0.17	0.05	0.00	0.00	0.00	0.01
HT-MHTBin5 jetbin3 btag3	0.00	0.00	0.00	0.00	1.38	0.09	0.00	0.00	0.00	0.03
HT-MHTBin6 jetbin3 btag3	0.00	0.00	0.00	0.00	0.91	0.05	0.00	0.00	0.01	0.03

Table 30: Single Lepton Control Region

## 1634 G Estimating ( $Z \rightarrow \nu\nu$ )+jets background with $\gamma$ +jets

1635 The missing transverse momentum in  $Z \rightarrow \nu\nu + \text{jets}$  events is dominated by the invisible,  
 1636 high- $p_T$   $Z$  boson. A single photon control sample with  $H_T^{\text{miss}}$  recalculated while neglecting the  
 1637 photon can be used to predict the  $Z \rightarrow \nu\nu$  background because the two processes have similar  
 1638 kinematics for high  $p_T$  bosons and because differing kinematics for lower  $p_T$  bosons can be  
 1639 corrected with a combination of simulation and data.

### 1640 G.1 Datasets

1641 The simulated samples used to study this background estimation method include sets of  $\gamma$ +jet,  
 1642  $Z \rightarrow \nu\nu$ , and  $Z \rightarrow \mu\mu$  events generated with MADGRAPH+PYTHIA programs in bins of  $H_T$ .  
 1643 All samples are from the Phys14DR-PU20bx25\_PHYS14\_25\_V1-v1 production campaign.  
 1644 These samples along with their cross sections and number of events simulated are shown in  
 1645 Table 31.

Table 31: Datasets used in  $\gamma$ +jets method.

Dataset	Events Sim.	$\sigma [\text{pb}]$
GJets_HT-400to600_Tune4C_13TeV-madgraph-tauola	4802346	62.05
GJets_HT-600toInf_Tune4C_13TeV-madgraph-tauola	4341179	20.87
ZJetsToNuNu_HT-400to600_Tune4C_13TeV-madgraph-tauola	4158549	11.99
ZJetsToNuNu_HT-600toInf_Tune4C_13TeV-madgraph-tauola	4201502	4.11
DYJetsToLL_M-50_HT-200to400_Tune4C_13TeV-madgraph-tauola	4931372	6.546
DYJetsToLL_M-50_HT-600toInf_Tune4C_13TeV-madgraph-tauola	4493574	2.179

### 1646 G.2 Photon reconstruction

1647 For the single photon control sample, we require at least one well identified and isolated photon  
 1648 candidate having at least 100 GeV of transverse momentum and pseudorapidity  $|\eta| < 2.5$ ,  
 1649 excluding the barrel/endcap transition,  $1.4442 < |\eta| < 1.566$ . Identification and isolation  
 1650 requirements intended to reject electrons and pions misreconstructed as photons are adopted  
 1651 from the Egamma POG's recommendations for 8 TeV data and 13 TeV data/simulation, where  
 1652 available. The identification criteria, which include requirements for low hadronic activity  
 1653 ( $H/E$ ), a shower shape ( $\sigma_{\eta\eta}$ ) consistent with a photon, and an associated pixel seed veto, are  
 1654 shown in Table 32 for events with a photon in the barrel or endcap.

1655 The isolation requirements restrict the energy sum from particle flow (PF) candidates within  
 1656 a cone of  $\Delta R < 0.3$  around the momentum vector of the photon candidate. Specifically, we  
 1657 require that the energy from charged hadrons ( $\text{Iso}_{\text{pfCh.}}$ ), neutral hadrons ( $\text{Iso}_{\text{pfNu.}}$ ), and elec-  
 1658 tromagnetic particles  $\text{Iso}_{\text{pfGa.}}$  not exceed the  $p_T$ -dependent thresholds shown in Table 32. The  
 1659 isolation energy from each of the three particle species is corrected for pileup with the per-  
 1660 event average pileup energy density ( $\rho$ ) and per-photon  $\eta$ -dependent effective areas shown in  
 1661 Table 33.

### 1662 G.3 Photon reconstruction efficiencies and purity

1663 As shown in Eq. 23, we correct the observed number of  $\gamma$ +jets events ( $N_\gamma^{\text{obs}}$ ) for the reconstruc-  
 1664 tion efficiencies ( $\epsilon_{\text{ID}}$ ,  $\epsilon_{\text{ISO}}$ ) and the purity of the sample ( $\beta_{\text{purity}}$ ).

1665 Simulation-based efficiencies for the ID ( $\epsilon_{\text{ID}}$ ) and isolation ( $\epsilon_{\text{ISO}}$ ) requirements are shown in  
 1666 Figs. 105 and 106 as functions of the variables used for analysis binning:  $H_T$ ,  $H_T^{\text{miss}}$ ,  $N_{\text{jets}}$ , and

Table 32: Photon identification and isolation requirements for events with photons in the barrel and endcap.

Variable	Barrel	Endcap
Pixel Seed Veto	Yes	Yes
H/E	<0.05	<0.05
$\sigma_{ij\eta j\eta}$	<0.011	<0.031
$\max(\text{Iso}_{\text{pfCh.}} - \text{EA} \cdot \rho, 0)$	<0.7	<0.5
$\max(\text{Iso}_{\text{pfNu.}} - \text{EA} \cdot \rho, 0)$	$<0.4 + 0.04 \cdot p_T$	$<1.5 + 0.04 \cdot p_T$
$\max(\text{Iso}_{\text{pfGa.}} - \text{EA} \cdot \rho, 0)$	$<0.5 + 0.005 \cdot p_T$	$<1.0 + 0.005 \cdot p_T$

Table 33: Effective areas used in pileup correction as a function of photon pseudorapidity.

$ \eta $	pfCh.	pfNu.	pfGa.
0.0 - 1.0	0.012	0.030	0.148
1.0 - 1.479	0.010	0.057	0.130
1.479 - 2.0	0.014	0.039	0.112
2.0 - 2.2	0.012	0.015	0.216
2.2 - 2.3	0.016	0.024	0.262
2.3 - 2.4	0.020	0.039	0.260
> 2.4	0.012	0.072	0.266

1667  $N_{\text{b-tags}}$ . The ID efficiency is computed relative to events passing generator-level acceptance,  
 1668  $\epsilon_{\text{ID}} = N_{\text{ID}} / N_{\text{acc}}$ , while the isolation efficiency is computed relative to the ID efficiency,  $\epsilon_{\text{iso}} =$   
 1669  $N_{\text{iso}} / N_{\text{ID}}$ . In both cases, the expected general trend is observed: efficiencies increase with  $H_{\text{T}}^{\text{miss}}$   
 1670 (because it is effectively the photon  $p_{\text{T}}$  in this method), increase with  $H_{\text{T}}$  because of its strong  
 1671 correlation with photon  $p_{\text{T}}$ , and decreases with jet multiplicity because of the higher probability  
 1672 for photon-jet overlap. The  $C_{\text{data/MC}}$  factors that correct these simulation-based efficiencies ( $\epsilon_{\text{ID}}$   
 1673 and  $\epsilon_{\text{iso}}$ ), which will be measured in 13 TeV data using tag-and-probe methods, are currently  
 1674 assumed to be unity.

1675 The  $\beta_{\text{purity}}$  correction for misreconstructed photons is measured in data with a two-component  
 1676 fit of the  $\sigma_{ij\eta j\eta}$  distribution. The prompt-photon PDF for this fit comes from simulation, the  
 1677 non-prompt-photon PDF comes from data with a photon candidate failing exactly one of the  
 1678 isolation criteria.

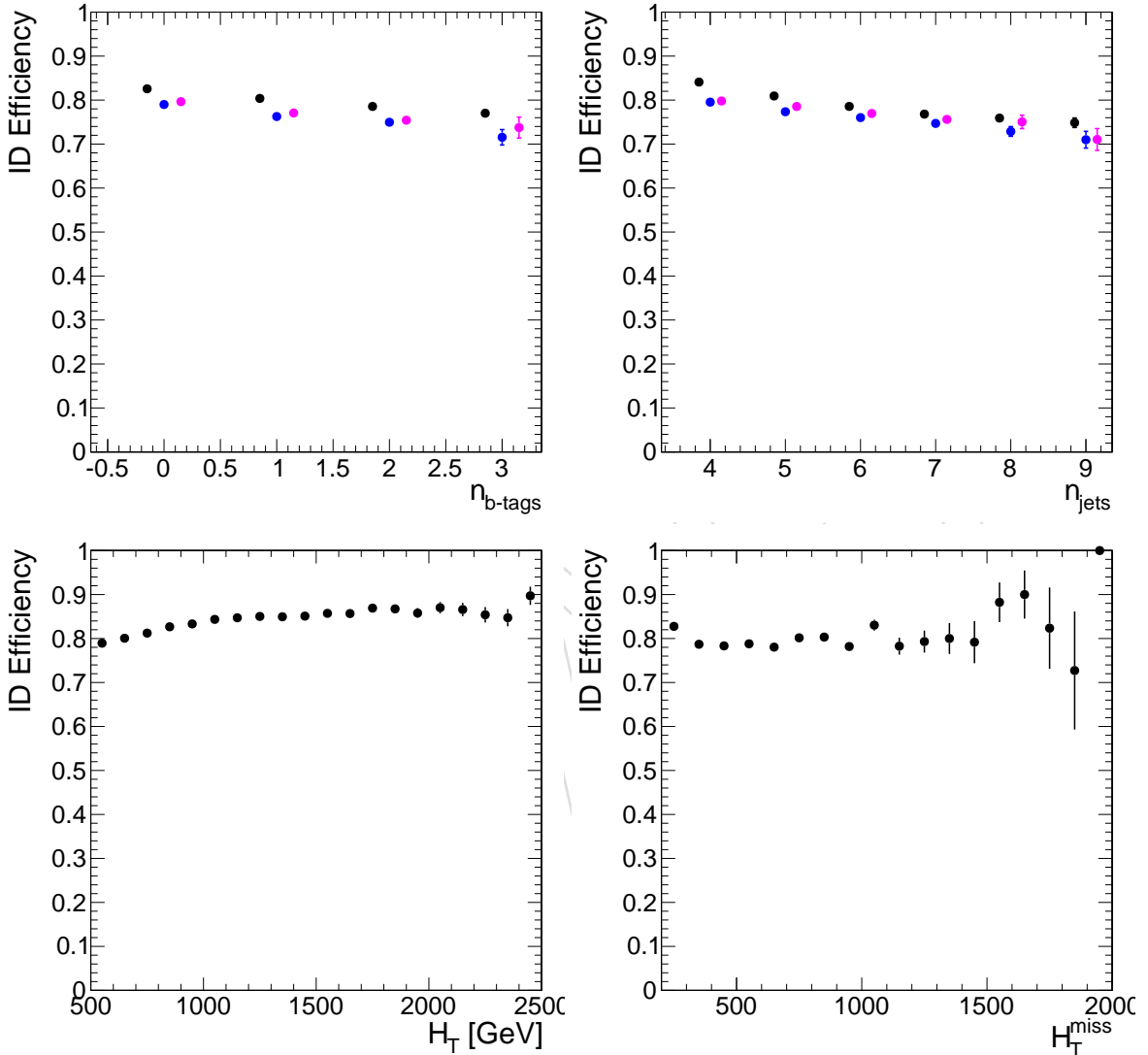


Figure 105: Efficiency of photon ID requirements versus kinematic variables. The top row shows distributions of events with low ( $200 < H_T^{\text{miss}} < 350$  GeV), medium ( $350 < H_T^{\text{miss}} < 500$  GeV), and high ( $H_T^{\text{miss}} > 500$  GeV) missing transverse momentum in black, blue, and magenta, respectively.

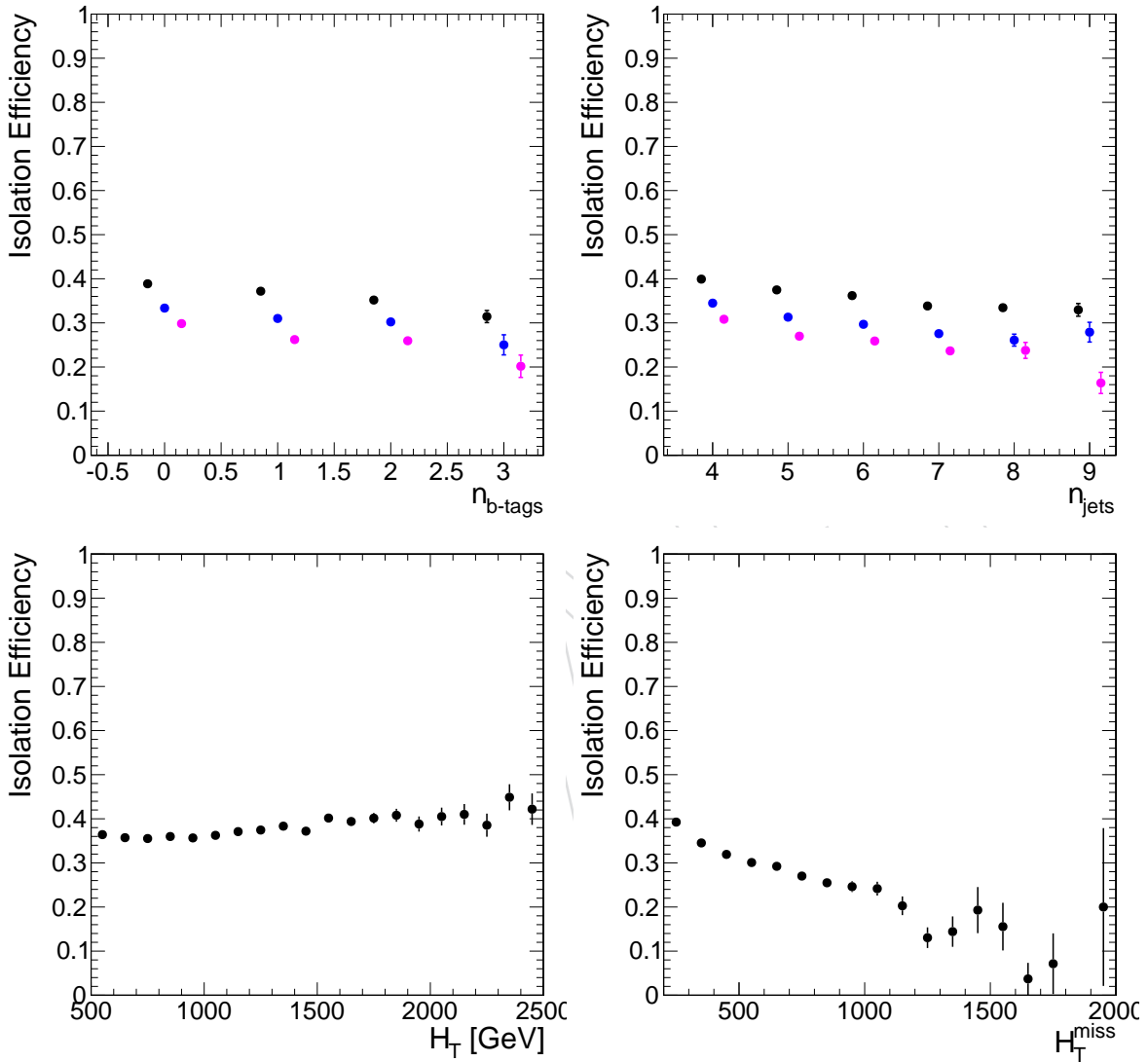


Figure 106: Efficiency of isolation requirements versus kinematic variables. The top row shows distributions of events with low ( $200 < H_T^{\text{miss}} < 350 \text{ GeV}$ ), medium ( $350 < H_T^{\text{miss}} < 500 \text{ GeV}$ ), and high ( $H_T^{\text{miss}} > 500 \text{ GeV}$ ) missing transverse momentum in black, blue, and magenta, respectively.

<sup>1679</sup> **G.4 Efficiencies for photon method**

<sup>1680</sup> The computed efficiencies ( $\epsilon_{acc}$ ,  $\epsilon_{ID}$ , and  $\epsilon_{iso}$ ) are shown in Tables 34, 35, and 36.

	$i^{th}$ Bin	$\epsilon_{acc}$	$\epsilon_{ID}$	$\epsilon_{iso}$
$N_{b\text{-tags}} = 0$	1	$0.9473 \pm 0.00045$	$0.8074 \pm 0.00073$	$0.37 \pm 0.0012$
	2	$0.9469 \pm 0.00081$	$0.862 \pm 0.0013$	$0.394 \pm 0.002$
	3	$0.947 \pm 0.0017$	$0.88 \pm 0.0026$	$0.446 \pm 0.0042$
	4	$0.948 \pm 0.0012$	$0.79 \pm 0.0021$	$0.309 \pm 0.0029$
	5	$0.952 \pm 0.0036$	$0.86 \pm 0.006$	$0.314 \pm 0.0087$
	6	$0.957 \pm 0.0025$	$0.811 \pm 0.0048$	$0.259 \pm 0.006$
$N_{b\text{-tags}} = 1$	7	$0.9464 \pm 0.00088$	$0.782 \pm 0.0015$	$0.351 \pm 0.0023$
	8	$0.949 \pm 0.0015$	$0.842 \pm 0.0025$	$0.375 \pm 0.0037$
	9	$0.953 \pm 0.0029$	$0.871 \pm 0.0047$	$0.424 \pm 0.0075$
	10	$0.944 \pm 0.0023$	$0.765 \pm 0.0043$	$0.263 \pm 0.0053$
	11	$0.941 \pm 0.007$	$0.84 \pm 0.011$	$0.31 \pm 0.015$
	12	$0.954 \pm 0.0046$	$0.775 \pm 0.0094$	$0.23 \pm 0.011$
$N_{b\text{-tags}} = 2$	13	$0.948 \pm 0.002$	$0.769 \pm 0.0036$	$0.333 \pm 0.0053$
	14	$0.946 \pm 0.0036$	$0.814 \pm 0.0062$	$0.363 \pm 0.0085$
	15	$0.954 \pm 0.0066$	$0.84 \pm 0.012$	$0.42 \pm 0.017$
	16	$0.946 \pm 0.0054$	$0.75 \pm 0.01$	$0.27 \pm 0.013$
	17	$0.93 \pm 0.017$	$0.85 \pm 0.025$	$0.28 \pm 0.034$
	18	$0.96 \pm 0.011$	$0.75 \pm 0.023$	$0.21 \pm 0.025$
$N_{b\text{-tags}} \geq 3$	19	$0.941 \pm 0.0063$	$0.75 \pm 0.011$	$0.3 \pm 0.016$
	20	$0.95 \pm 0.01$	$0.82 \pm 0.019$	$0.3 \pm 0.024$
	21	$0.95 \pm 0.021$	$0.8 \pm 0.038$	$0.45 \pm 0.053$
	22	$0.95 \pm 0.014$	$0.74 \pm 0.03$	$0.2 \pm 0.032$
	23	$1.0 \pm 0.0$	$0.58 \pm 0.097$	$0.3 \pm 0.11$
	24	$0.96 \pm 0.029$	$0.83 \pm 0.056$	$0.16 \pm 0.059$

Table 34: Acceptance, identification, and isolation efficiencies computed in various analysis bins of the low jet multiplicity region ( $4 \leq N_{\text{jets}} \leq 6$ ). Errors account for statistical uncertainties of the MC only. Errors are always reported to two significant figures and central values are quoted to the most significant figure of the error.

	$i^{th}$ Bin	$\epsilon_{acc}$	$\epsilon_{ID}$	$\epsilon_{iso}$
$N_{b\text{-tags}} = 0$	25	$0.948 \pm 0.0025$	$0.742 \pm 0.0046$	$0.321 \pm 0.0066$
	26	$0.944 \pm 0.0027$	$0.79 \pm 0.0048$	$0.322 \pm 0.0062$
	27	$0.939 \pm 0.0047$	$0.829 \pm 0.0076$	$0.36 \pm 0.011$
	28	$0.946 \pm 0.0062$	$0.75 \pm 0.012$	$0.24 \pm 0.014$
	29	$0.946 \pm 0.0096$	$0.79 \pm 0.018$	$0.23 \pm 0.021$
	30	$0.963 \pm 0.0098$	$0.79 \pm 0.021$	$0.19 \pm 0.023$
$N_{b\text{-tags}} = 1$	31	$0.946 \pm 0.0041$	$0.726 \pm 0.0077$	$0.31 \pm 0.011$
	32	$0.941 \pm 0.0042$	$0.763 \pm 0.0078$	$0.32 \pm 0.0099$
	33	$0.938 \pm 0.0072$	$0.8 \pm 0.012$	$0.39 \pm 0.017$
	34	$0.95 \pm 0.0095$	$0.71 \pm 0.021$	$0.3 \pm 0.026$
	35	$0.96 \pm 0.013$	$0.81 \pm 0.027$	$0.21 \pm 0.031$
	36	$0.97 \pm 0.014$	$0.77 \pm 0.033$	$0.25 \pm 0.039$
$N_{b\text{-tags}} = 2$	37	$0.945 \pm 0.0074$	$0.73 \pm 0.015$	$0.29 \pm 0.02$
	38	$0.94 \pm 0.0078$	$0.75 \pm 0.015$	$0.31 \pm 0.018$
	39	$0.92 \pm 0.014$	$0.81 \pm 0.021$	$0.35 \pm 0.028$
	40	$0.91 \pm 0.023$	$0.67 \pm 0.039$	$0.26 \pm 0.044$
	41	$0.89 \pm 0.036$	$0.79 \pm 0.05$	$0.17 \pm 0.052$
	42	$0.98 \pm 0.021$	$0.74 \pm 0.065$	$0.24 \pm 0.073$
$N_{b\text{-tags}} \geq 3$	43	$0.94 \pm 0.02$	$0.7 \pm 0.033$	$0.21 \pm 0.042$
	44	$0.95 \pm 0.016$	$0.77 \pm 0.031$	$0.29 \pm 0.038$
	45	$0.96 \pm 0.024$	$0.7 \pm 0.055$	$0.35 \pm 0.069$
	46	$1.0 \pm 0.0$	$0.5 \pm 0.1$	$0.3 \pm 0.13$
	47	$0.94 \pm 0.054$	$0.82 \pm 0.092$	$0.2 \pm 0.11$
	48	$0.8 \pm 0.1$	$0.92 \pm 0.08$	$0.3 \pm 0.13$

Table 35: Acceptance, identification, and isolation efficiencies computed in various analysis bins of the low jet multiplicity region ( $7 \leq N_{\text{jets}} \leq 8$ ). Errors account for statistical uncertainties of the MC only. Errors are always reported to two significant figures and central values are quoted to the most significant figure of the error.

	$i^{th}$ Bin	$\epsilon_{acc}$	$\epsilon_{ID}$	$\epsilon_{iso}$
$N_{b\text{-tags}} = 0$	49	$0.96 \pm 0.012$	$0.7 \pm 0.028$	$0.35 \pm 0.042$
	50	$0.938 \pm 0.0093$	$0.75 \pm 0.017$	$0.31 \pm 0.022$
	51	$0.94 \pm 0.011$	$0.78 \pm 0.021$	$0.37 \pm 0.028$
	52	$0.96 \pm 0.025$	$0.72 \pm 0.056$	$0.21 \pm 0.06$
	53	$0.97 \pm 0.02$	$0.75 \pm 0.053$	$0.16 \pm 0.051$
	54	$1.0 \pm 0.0$	$0.7 \pm 0.075$	$0.12 \pm 0.063$
$N_{b\text{-tags}} = 1$	55	$0.94 \pm 0.02$	$0.7 \pm 0.04$	$0.22 \pm 0.047$
	56	$0.93 \pm 0.014$	$0.74 \pm 0.025$	$0.28 \pm 0.031$
	57	$0.93 \pm 0.017$	$0.77 \pm 0.029$	$0.34 \pm 0.037$
	58	$1.0 \pm 0.0$	$0.7 \pm 0.067$	$0.18 \pm 0.067$
	59	$0.95 \pm 0.028$	$0.63 \pm 0.064$	$0.19 \pm 0.066$
	60	$0.91 \pm 0.087$	$0.8 \pm 0.13$	$0.1 \pm 0.12$
$N_{b\text{-tags}} = 2$	61	$0.97 \pm 0.022$	$0.72 \pm 0.073$	$0.37 \pm 0.097$
	62	$0.97 \pm 0.017$	$0.74 \pm 0.042$	$0.28 \pm 0.053$
	63	$0.93 \pm 0.027$	$0.75 \pm 0.047$	$0.34 \pm 0.059$
	64	$1.0 \pm 0.0$	$0.75 \pm 0.097$	$0.2 \pm 0.1$
	65	$0.93 \pm 0.064$	$0.6 \pm 0.13$	$0.0 \pm 0.0$
	66	$0.91 \pm 0.087$	$0.8 \pm 0.13$	$0.1 \pm 0.12$
$N_{b\text{-tags}} \geq 3$	67	$1.0 \pm 0.0$	$0.7 \pm 0.18$	$0.3 \pm 0.18$
	68	$0.92 \pm 0.044$	$0.66 \pm 0.08$	$0.22 \pm 0.086$
	69	$0.96 \pm 0.039$	$0.63 \pm 0.099$	$0.3 \pm 0.12$
	70	$1.0 \pm 0.0$	$1.0 \pm 0.0$	$0.0 \pm 0.0$
	71	$1.0 \pm 0.0$	$0.7 \pm 0.19$	$0.0 \pm 0.0$
	72	$0.0 \pm 0.0$	$0.0 \pm 0.0$	$0.0 \pm 0.0$

Table 36: Acceptance, identification, and isolation efficiencies computed in various analysis bins of the low jet multiplicity region ( $N_{\text{jets}} \leq 9$ ). Errors account for statistical uncertainties of the MC only. Errors are always reported to two significant figures and central values are quoted to the most significant figure of the error.

## 1681 H $Z \rightarrow \ell^+ \ell^-$ with $\ell = e, \mu$

1682 Here we present the specifics of the  $Z \rightarrow \ell^+ \ell^-$  analysis.

1683 We select  $Z \rightarrow \ell^+ \ell^-$  candidates in the Spring15  $H_T$  binned Drell-Yan (DY) MC sample listed in  
 1684 Table 8. Unlike what we expect from a Double Lepton triggered data sample, the reconstructed  
 1685  $Z$  purity in the DY sample is very nearly 100%. To more closely model the data, we perform  
 1686 our data driven estimate on a MC dataset which includes DY and  $t\bar{t}$  MC.

1687 Leptons are identified with the same criteria as lepton vetoes described in Section 4. Oppositely-  
 1688 signed pairs of selected leptons are combined to form  $Z$  candidates in the invariant mass range  
 1689  $91.188 \pm 15$  GeV. Jets that correspond to these leptons are removed from the jet collection prior  
 1690 to the computation of  $H_T$ ,  $H_T^{\text{miss}}$ ,  $\Delta\phi_{\min}$ , and  $N_{\text{jet}}$ . The same cuts are applied to this sample as  
 1691 given in Section 4, including the requirement that the event contain no leptons other than those  
 1692 from  $Z$  decay.

In some bins of the search space we observe very few events. To deal with this we assume that the dependence on at least some of the observables factorizes. For example, for a stand-alone measurement we start with the assumption that the kinematic shapes in each of the  $N_{\text{jet}}$  and  $N_{\text{b-jet}}$  bins agree with the kinematic shapes inclusive in  $N_{\text{jet}}$  and  $N_{\text{b-jet}}$  bins. To determine  $Z \rightarrow \ell^+ \ell^-$  yields in any of the 72 bins, we count the events in each  $H_T$ ,  $H_T^{\text{miss}}$  bin and scale the observed counts by the extrapolation factor  $\mathcal{F}_{N_{\text{jet}}, N_{\text{b-jet}}} = \frac{N(Z \rightarrow \ell^+ \ell^-)_{N_{\text{jet}}, N_{\text{b-jet}}}}{N(Z \rightarrow \ell^+ \ell^-)_{\text{Inclusive}}}$ , where yields in the numerator and denominator are integrated over  $H_T^{\text{miss}}$  and  $H_T$ . Then to compute the  $Z \rightarrow \nu\bar{\nu}$  background, we use:

$$N(Z \rightarrow \nu\bar{\nu})_{N_{\text{jet}}, N_{\text{b-jet}}}^{H_T, H_T^{\text{miss}}} = N(Z \rightarrow \ell^+ \ell^-)_{\text{Inclusive}}^{H_T, H_T^{\text{miss}}} \cdot \mathcal{F}_{N_{\text{jet}}, N_{\text{b-jet}}} \cdot \mathcal{P} \cdot \mathcal{R} / (\mathcal{A} \cdot \epsilon), \quad (32)$$

1693 where  $\mathcal{P}$  is the purity of the  $Z$  sample,  $\mathcal{R} = 5.95$  [23] is the ratio of branching fractions,  $\mathcal{A}$  is the  
 1694 lepton acceptance, and  $\epsilon$  is the efficiency.

### 1695 H.1 Lepton acceptance

1696 The acceptance region is defined as  $Z$  decays where both muons have  $p_T \geq 10$  GeV and  $|\eta| <$   
 1697 2.4, or both electrons have  $p_T > 10$  and  $|\eta| < 2.5$ , as for the lepton vetoes for the main analysis,  
 1698 and where the  $Z$  invariant mass lies within 15 GeV of the nominal  $Z$  mass. The efficiency  $\mathcal{A}$   
 1699 for both leptons to lie within the acceptance is calculated from MC truth information from  $Z$   
 1700 decays in the DY MC sample.

### 1701 H.2 Lepton selection efficiency

1702 Our lepton selection efficiency is measured in each  $(H_T, H_T^{\text{miss}})$  bin using the full statistics of  
 1703 the Drell-Yan MC samples. To these efficiencies we apply a scale factor defined as the ratio  
 1704 of our Double Lepton (data) sample efficiency from Tag and Probe over the Drell-Yan MC  
 1705 efficiency. The measurements are taken from tables provided by the SUSY PAG Lepton Scale  
 1706 Factor Working Group [18, 19].

### 1707 H.3 Z sample purity

1708 The purity is obtained from the fits shown in Figure 107, as the area of the peak function divided  
 1709 by the total area within the  $Z$  mass window. Templates for the signal and background shapes  
 1710 are obtained from fitting the full  $Z \rightarrow e^+ e^-$  and  $Z \rightarrow \mu^+ \mu^-$  distributions in the Double Lepton  
 1711 sample with baseline selection applied. These template shapes are fixed when fitting for the  
 1712 fraction of signal events in the  $N_{\text{b-jet}}$  bin.

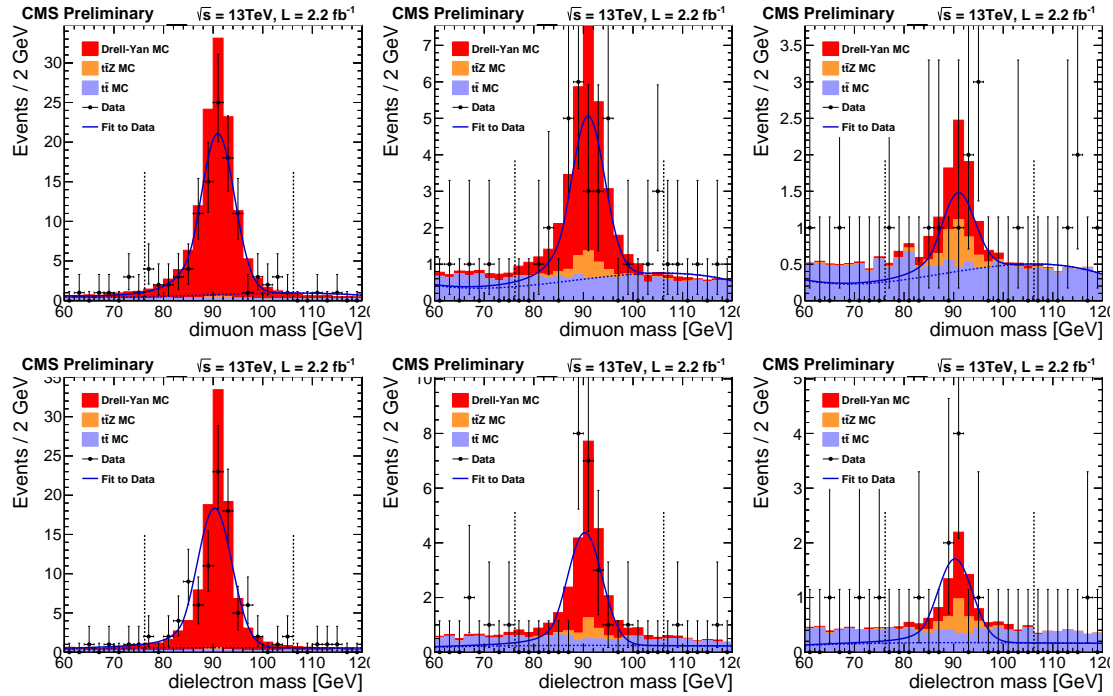


Figure 107: Fits to reconstructed  $Z$  candidates with  $0 N_{\text{b-jet}}$  (left),  $1 N_{\text{b-jet}}$  (middle), and  $\geq 2 N_{\text{b-jet}}$  (right), for the final states  $Z \rightarrow \mu^+\mu^-$  (above) and  $Z \rightarrow e^+e^-$  (below). The Fits are applied to data, Spring15 MC is overlaid for comparison.

#### 1713 H.4 Extrapolation factors

1714 The extrapolation factors  $\mathcal{F}_{N_{\text{jet}}, N_{\text{b-jet}}}$  appearing in Eq. 32 allow for extension of the kinematic  
 1715 distribution measured inclusively of  $N_{\text{jet}}$  and  $N_{\text{b-jet}}$  to be extended to the individual bins in  
 1716 these variables, under the assumption of factorization. The values for the extrapolation factors  
 1717 are given in Table 19. In Fig. 108 we test the factorization assumption in simulation for the three  
 1718  $N_{\text{jet}}$  bins, and for a limited range of  $N_{\text{b-jet}}$ , namely inclusive, one loose b-jet, and one CSV b-  
 1719 jet. The distributions are quite similar between (essentially) 0- and 1- $N_{\text{b-jet}}$ , and the trends in  
 1720  $H_{\text{T}}^{\text{miss}}$  appear quite similar, but there is evidence of a correlation of the  $H_{\text{T}}$  distribution with  
 1721  $N_{\text{jet}}$ . This breakdown of factorization motivates the choice of the hybrid approach, in which we  
 1722 depend on the  $\gamma + \text{jets}$  sample to determine the shape in  $(H_{\text{T}}, H_{\text{T}}^{\text{miss}}, N_{\text{jet}})$  for  $N_{\text{b-jet}} = 0$ . One of  
 1723 our models for extrapolation to  $N_{\text{b-jet}}$  utilizes binomial combinatorics, for which the  $\mathcal{F}$  factors  
 1724 are developed in Section H.5. As described in the main text, we use this model to determine  
 1725 the upper systematic uncertainty on  $\mathcal{F}$ .

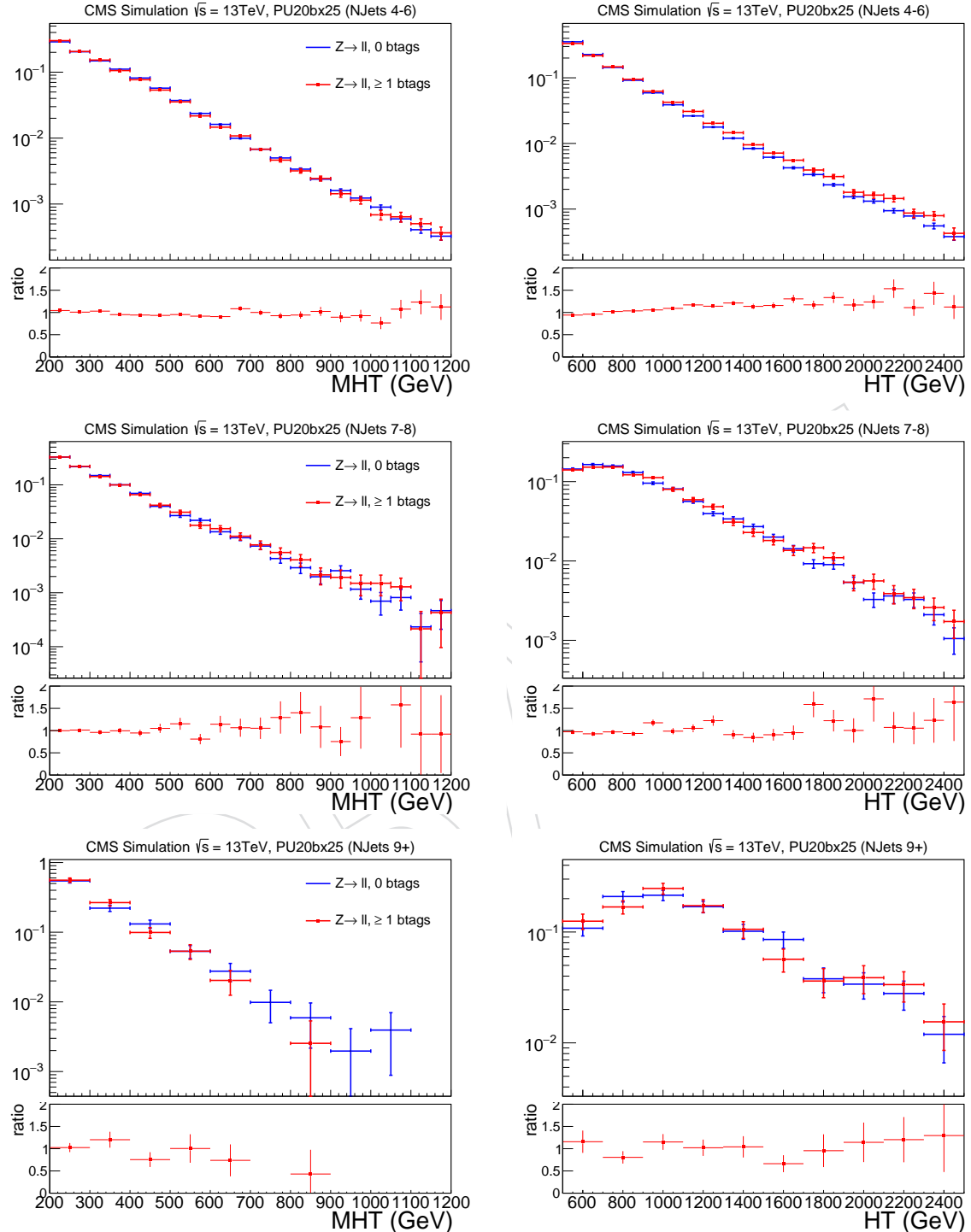


Figure 108:  $H_{\text{T}}^{\text{miss}}$  and  $H_{\text{T}}$  shapes of the PHYS14-MC  $Z \rightarrow \ell^+ \ell^-$  sample in the  $N_{\text{jet}}$  4-6 (top), 7-8 (middle), and 9+ (bottom) bins. The distributions plotted are with 0 b-tags (blue) and with at least 1 b-tag (red).

1726 **H.5 Combinatorial model for extrapolation from zero to  $n$  b-jets**

1727 As we impose stronger requirements on the number of b-jets the yields in the control samples  
 1728 used to determine the  $Z \rightarrow \nu\bar{\nu}$  background fall. As an aid to extrapolating to regions with  
 1729 too few events in data we seek an analytic function to describe the shape of the  $N_{\text{b-jet}}$  distribu-  
 1730 tions. We first note that although the physics constraint of flavor conservation implies that the  
 1731 b-jets are produced in pairs, this effect is thoroughly washed out in the distributions of recon-  
 1732 structed, tagged b-jets, as illustrated in Fig. 109. The upper-right plot shows that only about  
 1733 half the b-quarks in  $Z+\text{jets}$  events have  $p_T$  larger than the 30 GeV required in the baseline se-  
 1734 lection, and the lower-left plot shows that this alone removes much of the even-odd structure.  
 1735 The efficiency and fake rate of b tagging produce further feed-across among the bins in these  
 1736 distributions, so that little if any of the underlying pairing survives (Lower-right plot in Fig.  
 1737 109.) With this in mind we proceed to develop a model based on the assumption that these  
 1738 distributions are driven primarily by combinatorics.

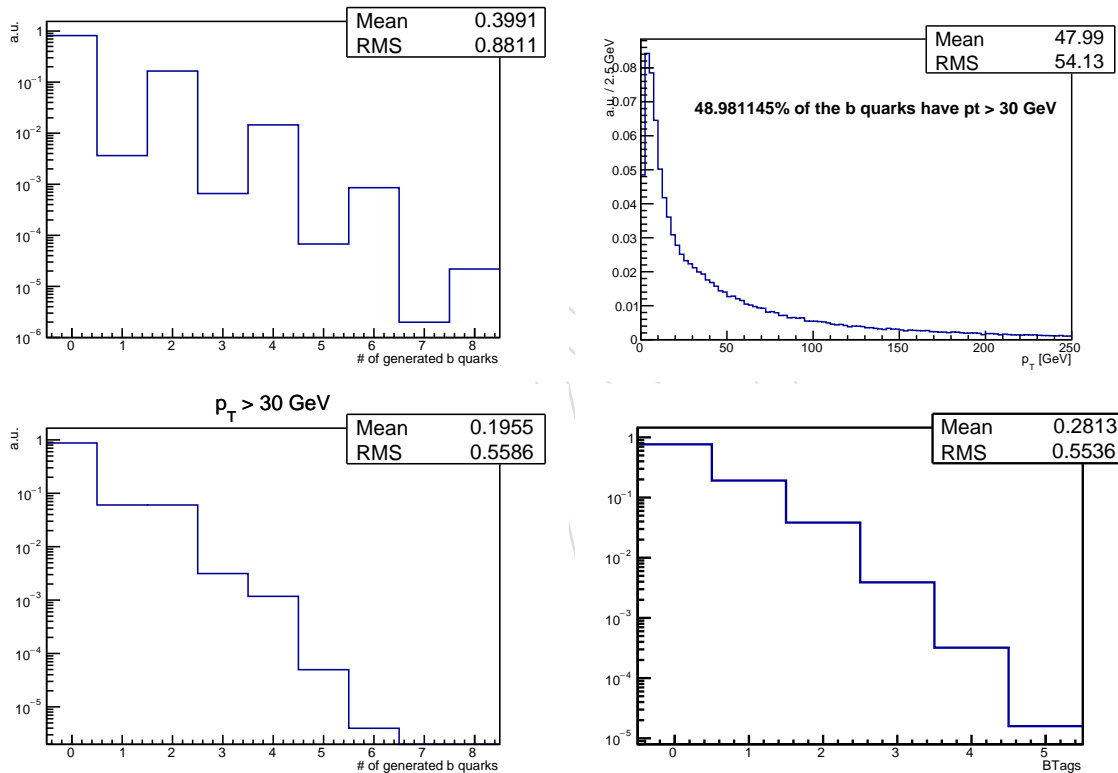


Figure 109: Distributions of b-quark yields for (upper left) generated b-quarks; (lower left) generated b-quarks with  $p_T > 30$  GeV; (lower right) reconstructed and tagged b-jets with  $p_T > 30$  GeV. The upper-right plot shows the  $p_T$ -distribution of the generated b-quarks. The data are from PHYS14 ( $Z \rightarrow \nu\bar{\nu}$ )+jets MC, and the distributions are normalized to total area within each plot.

1739 To extrapolate into the b-tag dimension, we compute the observed yield of the bins with  $N_{\text{b-jet}} =$   
 1740 0 and apply an extrapolation factor to each of the remaining 3 b-tag bins:  $N(Z \rightarrow \ell\ell)_{\text{JetBin}}^b =$   
 1741  $N(Z \rightarrow \ell\ell)_{\text{JetBin}}^{b=0} \cdot \mathcal{F}_{\text{JetBin}}^b$ . Since we get the normalization from the 0 b-tag bins,  $\mathcal{F}_{\text{JetBin}}^{b=0} = 1$  for all  
 1742  $N_{\text{jet}}$  bins.

For the  $N_{\text{jet}}$  4-6 bin, the b-tag scale factor is the simple ratio:

$$\mathcal{F}_{\text{Jets}4-6}^{\text{b}} = \frac{N(Z \rightarrow \ell\ell)_{\text{Jets}4-6}^{\text{b}}}{N(Z \rightarrow \ell\ell)_{\text{Jets}4-6}^{\text{b}=0}} \quad (33)$$

<sup>1743</sup> To correct for the b-tag dependence on the  $N_{\text{jet}}$  bin, we add a correction factor (Jet7-8 bin for  
<sup>1744</sup> example):

$$\mathcal{F}_{\text{Jets}7-8}^{\text{b}} = \mathcal{F}_{\text{Jets}4-6}^{\text{b}} \cdot \frac{C_{\text{Jets}7-8}^{\text{b}}}{C_{\text{Jets}7-8}^{\text{b}=0}} \quad (34)$$

<sup>1745</sup> The denominator in the correction factor is to enforce  $\mathcal{F}_{\text{Jets}7-8}^{\text{b}=0} = 1$ . By taking the yields from the  
<sup>1746</sup> 0 b-tag bins, we are already capturing the physics related to this term, so we must divide it out  
<sup>1747</sup> to avoid double counting.

The binomial correction terms are given in terms of the probability  $p$  for a jet to be a b-tagged jet by (Jet7-8 bin for example):

$$C_{\text{Jets}7-8}^{\text{b}} = \frac{\frac{N_{\text{jets}7}}{N_{\text{jets}7-8}} \binom{7}{b} \cdot p^b (1-p)^{7-b} + \frac{N_{\text{jets}8}}{N_{\text{jets}7-8}} \binom{8}{b} \cdot p^b (1-p)^{8-b}}{\frac{N_{\text{jets}4}}{N_{\text{jets}4-6}} \binom{4}{b} \cdot p^b (1-p)^{4-b} + \frac{N_{\text{jets}5}}{N_{\text{jets}4-6}} \binom{5}{b} \cdot p^b (1-p)^{5-b} + \frac{N_{\text{jets}6}}{N_{\text{jets}4-6}} \binom{6}{b} \cdot p^b (1-p)^{6-b}} \quad (35)$$

$$= \frac{\frac{N_{\text{jets}7}}{N_{\text{jets}7-8}} \binom{7}{b} (1-p)^3 + \frac{N_{\text{jets}8}}{N_{\text{jets}7-8}} \binom{8}{b} (1-p)^4}{\frac{N_{\text{jets}4}}{N_{\text{jets}4-6}} \binom{4}{b} + \frac{N_{\text{jets}5}}{N_{\text{jets}4-6}} \binom{5}{b} (1-p) + \frac{N_{\text{jets}6}}{N_{\text{jets}4-6}} \binom{6}{b} (1-p)^2} \quad (36)$$

The scale factor then becomes

$$\mathcal{F}_{\text{Jets}7-8}^{\text{b}} = \mathcal{F}_{\text{Jets}4-6}^{\text{b}} \cdot \frac{\frac{N_{\text{jets}7}}{N_{\text{jets}7-8}} \binom{7}{b} (1-p)^3 + \frac{N_{\text{jets}8}}{N_{\text{jets}7-8}} \binom{8}{b} (1-p)^4}{\frac{N_{\text{jets}4}}{N_{\text{jets}4-6}} \binom{4}{b} + \frac{N_{\text{jets}5}}{N_{\text{jets}4-6}} \binom{5}{b} (1-p) + \frac{N_{\text{jets}6}}{N_{\text{jets}4-6}} \binom{6}{b} (1-p)^2} \\ \cdot \frac{\frac{N_{\text{jets}4}}{N_{\text{jets}4-6}} \binom{4}{0} + \frac{N_{\text{jets}5}}{N_{\text{jets}4-6}} \binom{5}{0} (1-p) + \frac{N_{\text{jets}6}}{N_{\text{jets}4-6}} \binom{6}{0} (1-p)^2}{\frac{N_{\text{jets}7}}{N_{\text{jets}7-8}} \binom{7}{0} (1-p)^3 + \frac{N_{\text{jets}8}}{N_{\text{jets}7-8}} \binom{8}{0} (1-p)^4} \quad (37)$$

$$= \mathcal{F}_{\text{Jets}4-6}^{\text{b}} \cdot \frac{\frac{N_{\text{jets}7}}{N_{\text{jets}7-8}} \binom{7}{b} (1-p)^3 + \frac{N_{\text{jets}8}}{N_{\text{jets}7-8}} \binom{8}{b} (1-p)^4}{\frac{N_{\text{jets}7}}{N_{\text{jets}7-8}} (1-p)^3 + \frac{N_{\text{jets}8}}{N_{\text{jets}7-8}} (1-p)^4} \cdot \frac{\frac{N_{\text{jets}4}}{N_{\text{jets}4-6}} + \frac{N_{\text{jets}5}}{N_{\text{jets}4-6}} (1-p) + \frac{N_{\text{jets}6}}{N_{\text{jets}4-6}} (1-p)^2}{\frac{N_{\text{jets}4}}{N_{\text{jets}4-6}} \binom{4}{b} + \frac{N_{\text{jets}5}}{N_{\text{jets}4-6}} \binom{5}{b} (1-p) + \frac{N_{\text{jets}6}}{N_{\text{jets}4-6}} \binom{6}{b} (1-p)^2} \quad (38)$$

$$= \mathcal{F}_{\text{Jets}4-6}^{\text{b}} \cdot \frac{\binom{7}{b} + \frac{N_{\text{jets}8}}{N_{\text{jets}7}} \binom{8}{b} (1-p)}{1 + \frac{N_{\text{jets}8}}{N_{\text{jets}7}} (1-p)} \cdot \frac{1 + \frac{N_{\text{jets}5}}{N_{\text{jets}4}} (1-p) + \frac{N_{\text{jets}6}}{N_{\text{jets}4}} (1-p)^2}{\binom{4}{b} + \frac{N_{\text{jets}5}}{N_{\text{jets}4}} \binom{5}{b} (1-p) + \frac{N_{\text{jets}6}}{N_{\text{jets}4}} \binom{6}{b} (1-p)^2} \quad (39)$$

$$\simeq \mathcal{F}_{\text{Jets}4-6}^{\text{b}} \cdot \frac{\binom{7}{b} + \frac{N_{\text{jets}8}}{N_{\text{jets}7}} \binom{8}{b} (1-p)}{\binom{4}{b} + \frac{N_{\text{jets}5}}{N_{\text{jets}4}} \binom{5}{b} (1-p) + \frac{N_{\text{jets}6}}{N_{\text{jets}4}} \binom{6}{b} (1-p)^2}. \quad (40)$$

1748 The approximation at the last step assumes only that we have a fairly rapidly falling distribution  
 1749 in  $N_{\text{jet}}$  for  $N_{\text{jet}} > 4$ . The extrapolation factor depends only weakly on  $p$ .

1750 We measure the statistical uncertainty of the binomial extrapolation factors by evaluating Eq.  
 1751 39 for each of a set of toy MC experiments. The results are shown in Fig. 110.

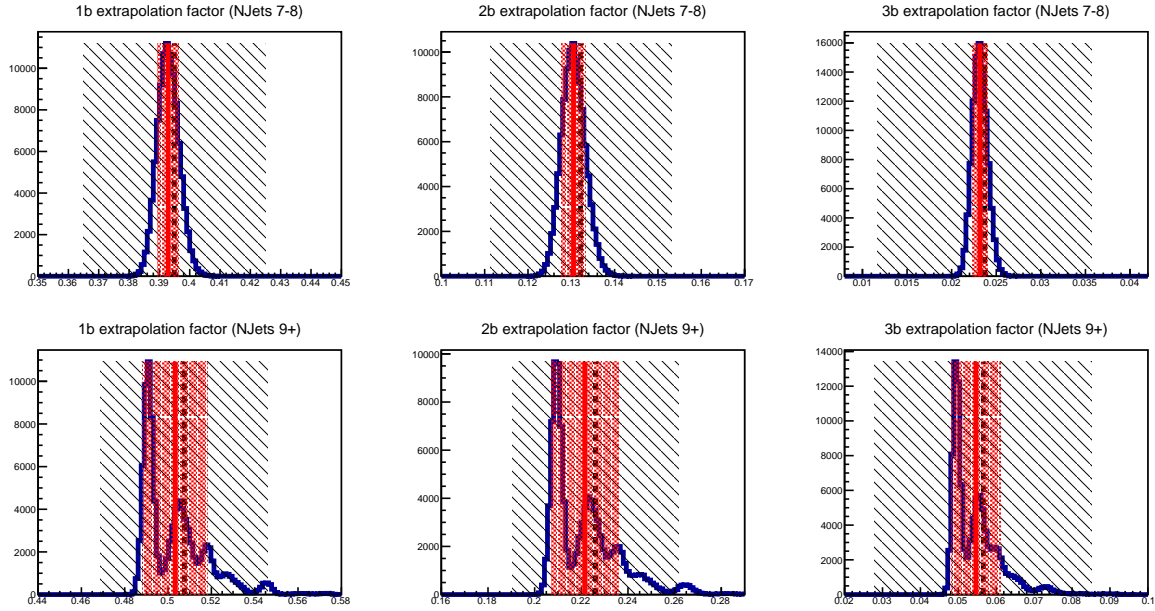


Figure 110: Comparison of binomial correction uncertainties in relation to the statistical uncertainty on  $\mathcal{F}_{\text{jets}4-6}^b$  for the  $N_{\text{jet}}$  7-8 (top) and  $N_{\text{jet}}$  9+ (bottom) bins of the 1b-tag (left), 2b-tag (middle), and  $\geq 3$ b-tag (right) extrapolation factors. The blue histograms are b-tag extrapolation factors resulting from 100,000 toy experiments assuming a Poisson distributed number of events in each  $N_{\text{jet}}$  term appearing in Eq. 39, with mean taken from  $Z \rightarrow \ell^+ \ell^-$  events in PHYS14 MC normalized to  $10 \text{ fb}^{-1}$ . The black shaded area is the statistical uncertainty on  $\mathcal{F}_{\text{jets}4-6}^b$  and the red shaded area is the  $\pm 1\sigma$  uncertainty from the distribution of the prediction from the toy experiments. When we observe 0 events with exactly 9 jets ( $\approx 3\%$  of toy experiments at  $10 \text{ fb}^{-1}$ ), the ratios with  $N_{\text{jets}9}$  in the denominator are taken from MC.

## 1752 I MC plots and expected yields with $3 \text{ fb}^{-1}$

1753 Here we reproduce the plots and tables from Chapter 4 with the MC scaled to  $3 \text{ fb}^{-1}$  to give an  
 1754 rough idea of how the analysis would look after the first round of 25 ns data-taking.

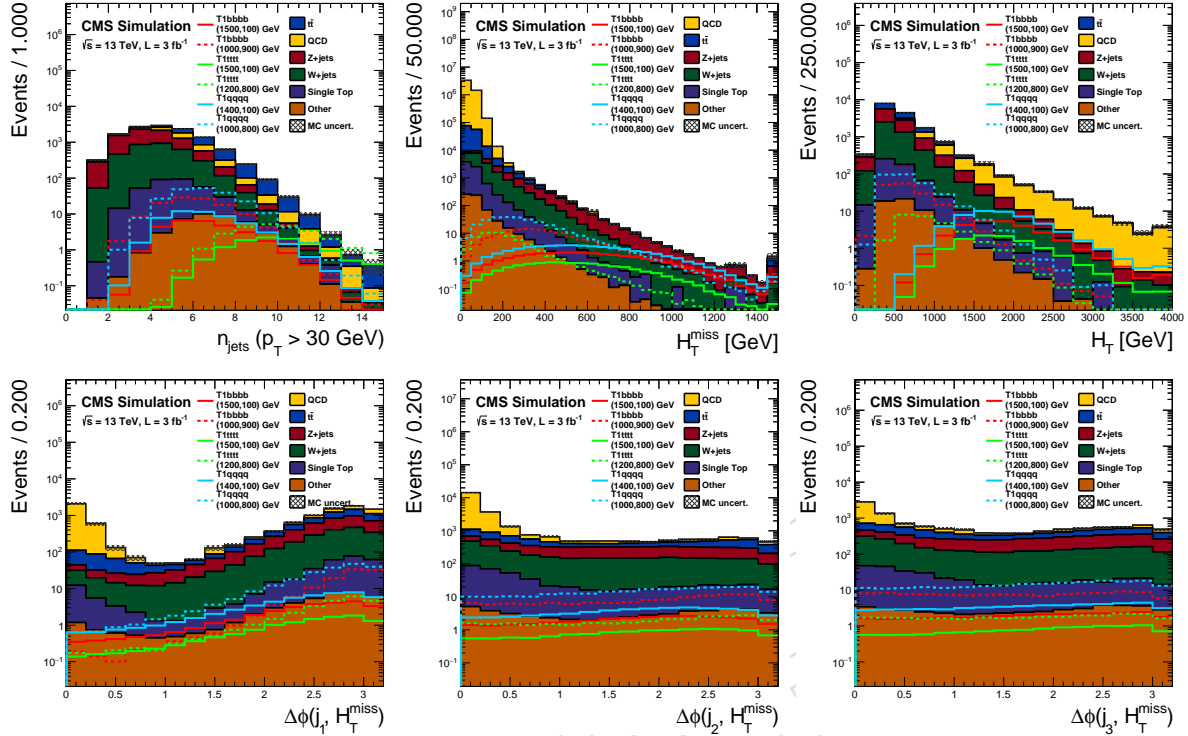


Figure 111:  $N - 1$  plots of  $N_{\text{jet}}$ ,  $H_T^{\text{miss}}$ , and  $H_T$ , as well as the  $\Delta\phi$  variables, described above. The SM and signal MC samples are scaled to  $3 \text{ fb}^{-1}$ .

## 1755 J Toy tests of statistical model

1756 An additional uncertainty is included in the statistical model for the fit to account for limited  
 1757 statistics in the control samples for the lost lepton and hadronic tau background predictions.  
 1758 We show here results from toy studies used to determine that the applied uncertainties give  
 1759 appropriate coverage of the uncertainties.

1760 For each of the hadronic tau and lost lepton backgrounds individually, we generate pseudo  
 1761 datasets based on the expected distribution of events from the weights of control sample events  
 1762 to predict the background in the signal region. We then fit these distributions with the statis-  
 1763 tical model in the fit to determine if the 1, 2, and  $3\sigma$  expected fluctuations are obtained an  
 1764 appropriate amount of the time based on pure background fluctuations. Sample results from  
 1765 the hadronic tau test are shown in Table 39. The tests are performed for a single bin and also  
 1766 for the combination of the 72 search bins. For the combination, a signal model must be used  
 1767 for the shape of the signal. We find some variation based on the model used, but overall the  
 1768 expected fraction of events is consistent with the expectations of 16%, 2.5%, and 0.15% of toys  
 1769 landing with  $\geq 1, 2, 3\sigma$ , respectively, which we take to indicate good coverage of the expected  
 1770 uncertainties for a variety of expected background yields.

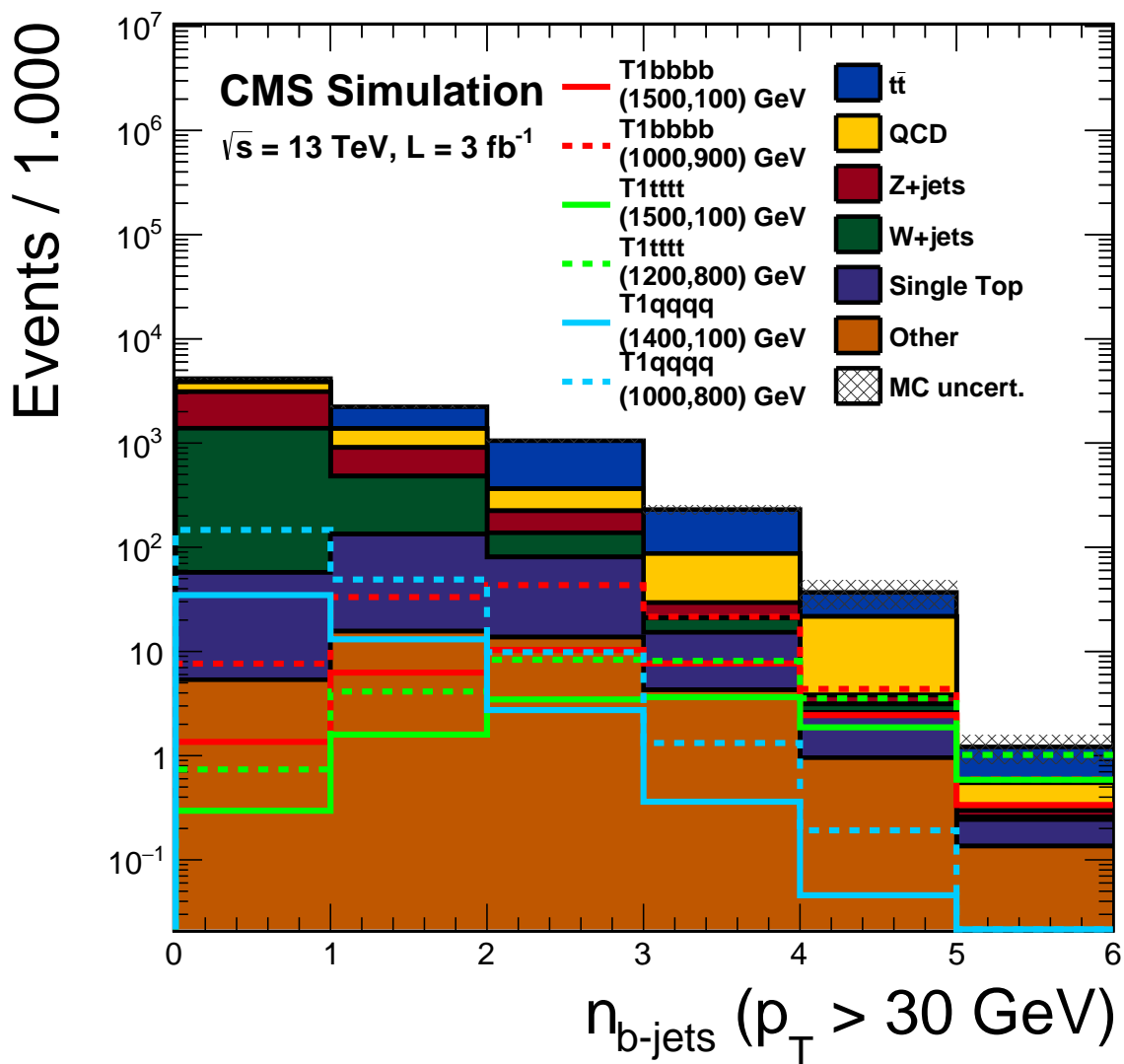


Figure 112: The number of b-tagged jets after the baseline selection. There is no minimum  $N_{\text{b-jet}}$  requirement in the baseline selection. The SM and signal MC samples are scaled to  $3 \text{ fb}^{-1}$ .

Table 37: Cutflow and expected yields at  $3 \text{ fb}^{-1}$  for SM backgrounds after baseline selection. The MC are scaled according to the cross sections listed in Section 3.1.

Cut	$t\bar{t}$	QCD	Z+jets	W+jets	Single top	Other	Sum
Start	$2 \times 10^6$	$> 10^7$	$10^6$	$8 \times 10^6$	$7 \times 10^5$	$4 \times 10^3$	$> 10^7$
$N_{\text{jet}} \geq 4$	$2 \times 10^6$	$> 10^7$	$7 \times 10^5$	$8 \times 10^5$	$10^5$	$4 \times 10^3$	$> 10^7$
$H_T > 500 \text{ GeV}$	$3 \times 10^5$	$> 10^7$	$10^5$	$10^5$	$2 \times 10^5$	$2 \times 10^3$	$> 10^7$
$H_T^{\text{miss}} > 200 \text{ GeV}$	13861	30216	3213	10563	2063	184	60099
$\mu$ veto	9363	30127	3208	7482	1411	123.8	51716
$e$ veto	5735	29789	3182	4572	858.8	81.09	44218
$\mu$ track veto	5309	29370	3162	4337	793.0	76.67	43017
$e$ track veto	4571	28189	3082	3886	690.0	68.85	40486
Had. track veto	3661	27489	3040	3166	548.5	60.46	37964
$\Delta\phi$ cuts	2084	2894	2263	1831	259.1	41.42	9372
Evt. cleaning	1995	1435	2243	1741	249.6	40.09	7706
$N_{\text{b-jet}}$ bins							
0 CSVM	294.6	748.4	1723	1330	51.98	5.36	4153
1 CSVM	852.0	472.6	425.0	347.4	118.0	15.64	2231
2 CSVM	689.7	140.1	86.10	57.15	66.84	13.73	1054
$\geq 3$ CSVM	159.1	75.81	9.16	6.21	12.75	5.37	268.4

## K Additional information on pre-fit vs post-fit results

The results given in Sec. 12 are those from our full fitting procedure described in Sec. 11. After the fit, we also study differences between the pre-fit and post-fit values for the background predictions and nuisance parameters to consider possible pathologies or unintended consequences of the fitting procedure. Figure 113 shows a comparison of the background estimates from the pre-fit and post-fit estimates compared to data. As expected, the post-fit results provide additional information to measure the backgrounds and generally move toward the data observations within allowed uncertainties.

We also compare the values of the nuisance parameters and their uncertainties before and after the fit. Figure 114 shows the change in the central value of the nuisance parameters in our fit. Figure 115 shows the change in the uncertainty of the nuisance parameters in our fit. The central values are found to move with the expected statistical scatter. The uncertainties are generally found to get smaller as expected from the additional information in the data available to the fit. No parameters are found to be pulled in an unphysical or overly constrained way by the fit.

Table 38: Cutflow and expected yields at  $3 \text{ fb}^{-1}$  for SMS model points after baseline selection. The MC are scaled according to the cross sections listed in Section 3.2. The efficiency of each cut, calculated with respect to the previous cut, is given in parentheses after the expected yield.

Cut	T1tttt (1500, 100)	T1tttt (1200, 800)	T1bbbb (1500, 100)	T1bbbb (1000, 900)	T1qqqq (1400, 100)	T1qqqq (1000, 800)
Start	42.57 (1.00)	256.93 (1.00)	42.57 (1.00)	976.16 (1.00)	75.89 (1.00)	976.16 (1.00)
$N_{\text{jet}} \geq 4$	42.55 (1.00)	256.45 (1.00)	41.21 (0.97)	487.45 (0.50)	73.48 (0.97)	764.93 (0.78)
$H_T > 500 \text{ GeV}$	42.52 (1.00)	211.85 (0.83)	41.20 (1.00)	196.45 (0.40)	73.46 (1.00)	417.04 (0.55)
$H_T^{\text{miss}} > 200 \text{ GeV}$	37.77 (0.89)	93.59 (0.44)	37.28 (0.91)	160.44 (0.82)	66.37 (0.90)	271.25 (0.65)
$\mu$ veto	24.15 (0.64)	60.74 (0.65)	36.93 (0.99)	156.41 (0.97)	66.25 (1.00)	270.78 (1.00)
$e$ veto	15.46 (0.64)	40.54 (0.67)	36.59 (0.99)	153.59 (0.98)	65.57 (0.99)	268.48 (0.99)
$\mu$ track veto	15.22 (0.98)	38.98 (0.96)	36.44 (1.00)	150.02 (0.98)	65.37 (1.00)	266.70 (0.99)
$e$ track veto	14.80 (0.97)	36.00 (0.92)	35.96 (0.99)	143.65 (0.96)	64.51 (0.99)	260.66 (0.98)
Had. track veto	14.48 (0.98)	33.59 (0.93)	35.81 (1.00)	141.61 (0.99)	64.19 (1.00)	255.68 (0.98)
$\Delta\phi$ cuts	11.72 (0.81)	26.33 (0.78)	28.78 (0.80)	111.93 (0.79)	51.91 (0.81)	209.89 (0.82)
Evt. cleaning	11.45 (0.98)	25.88 (0.98)	28.43 (0.99)	110.70 (0.99)	51.00 (0.98)	207.21 (0.99)
$N_{\text{b-jet bins}}$						
0 CSVM	0.30 (0.03)	0.74 (0.03)	1.36 (0.05)	7.64 (0.07)	34.77 (0.68)	146.79 (0.71)
1 CSVM	1.59 (0.14)	4.13 (0.16)	6.27 (0.22)	33.23 (0.30)	13.08 (0.26)	49.04 (0.24)
2 CSVM	3.46 (0.30)	8.33 (0.32)	10.35 (0.36)	43.32 (0.39)	2.74 (0.05)	9.84 (0.05)
$\geq 3$ CSVM	6.10 (0.53)	12.69 (0.49)	10.45 (0.37)	26.50 (0.24)	0.41 (0.01)	1.53 (0.01)

test case	frac. toy $> 1\sigma$	frac. toy $> 2\sigma$	frac. toy $> 3\sigma$
single bin nBkg = 0.3 events	0.167	0.0025	0.0011
single bin nBkg = 0.1 events	0.080	0.0029	0.0001
all bins T1bbbb(1500,100)	0.055	0.0051	0.0009
all bins T1bbbb(1000,800)	0.092	0.0131	0.0006
all bins T1qqqq(1000,900)	0.183	0.0320	0.0027

Table 39: Results from toy tests for hadronic tau background prediction.

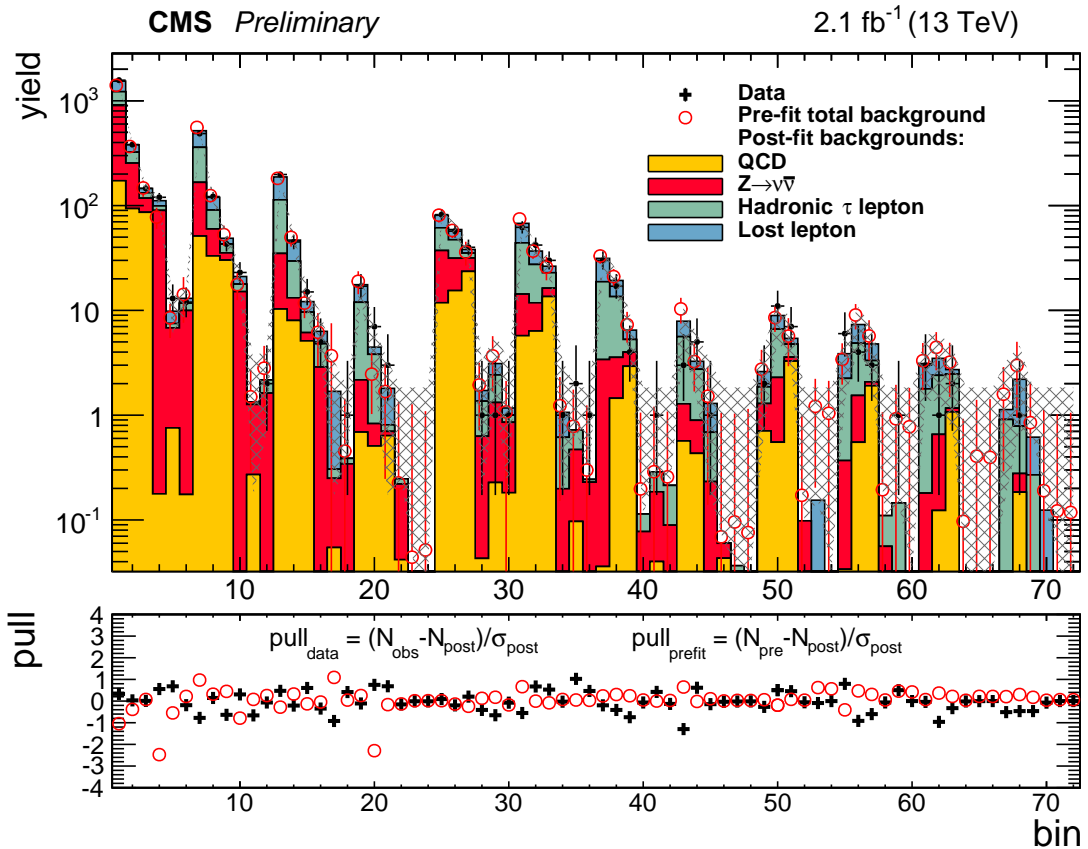


Figure 113: Background predictions for the 72 signal search bins from the pre-fit and post-fit results compared to the data observations. The pull quantities (bottom panel) are defined as:  $(N_{\text{pre}} - N_{\text{post}})/\sigma_{\text{post}}$  [red] and  $(N_{\text{obs}} - N_{\text{post}})/\sigma_{\text{post}}$  [black]

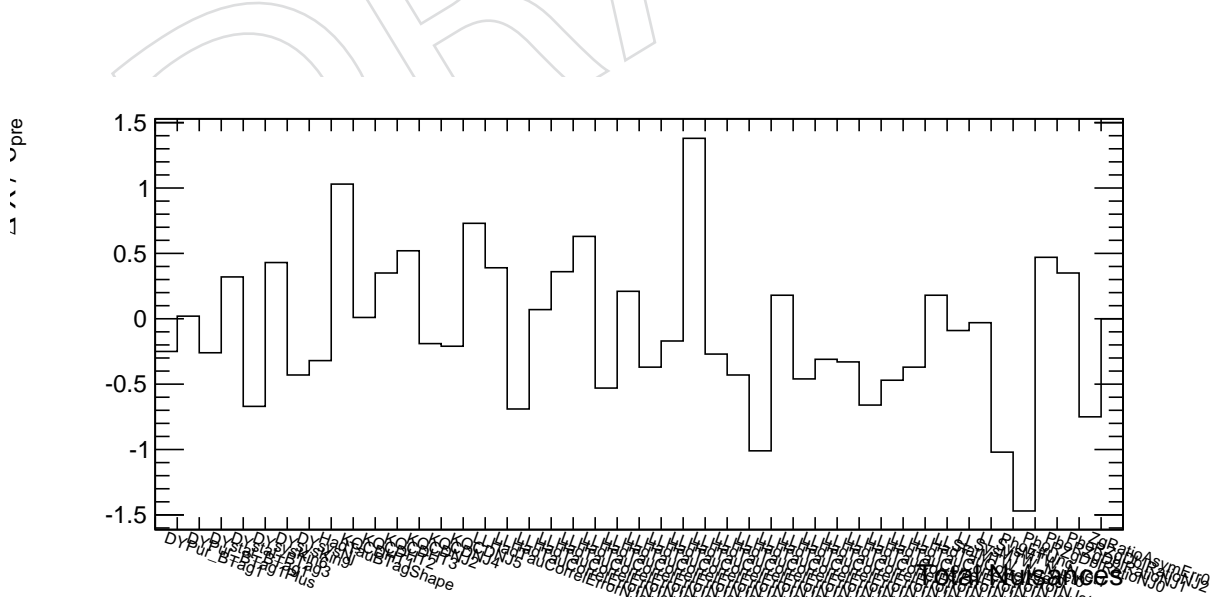


Figure 114: Post-fit minus pre-fit central values divided by pre-fit uncertainties for nuisance parameters in the fit.

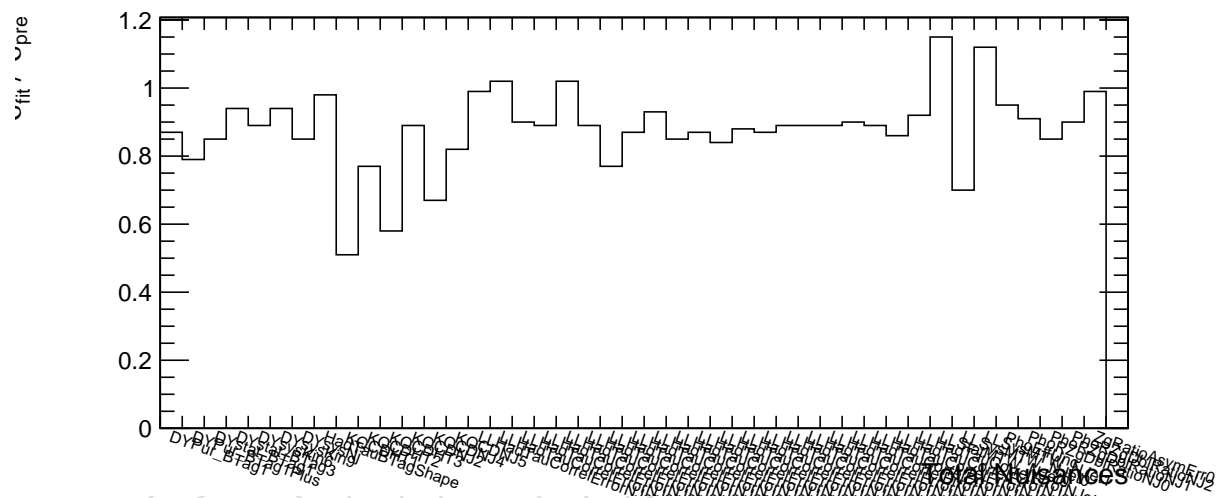


Figure 115: Ratio of post-fit uncertainty over pre-fit uncertainty for nuisance parameters in the fit.

## 1786 L Additional Background Techniques

1787 Two additional techniques have been studied for background prediction methods. Neither is  
 1788 included in the baseline search for the first results with 13 TeV. Progress is shown here toward  
 1789 their deployment for future iterations of this search.

### 1790 L.1 QCD background from Rebalance-and-Smear

1791 The Rebalance-and-Smear (R+S) method is aiming for a prediction of the multi-jet background  
 1792 with “fake” missing transverse energy because of jet mis-measurements, which is dominated  
 1793 by QCD, with negligible contributions from fully hadronic  $t\bar{t}$  and  $W/Z+jets$  events. The main  
 1794 idea is, to take a fully inclusive jet sample (triggered by HT triggers, for which the lower thresh-  
 1795 olds have high prescales) and adjust the jet momenta within their uncertainties in such a way,  
 1796 that no missing transverse energy is present. The jets of the resulting events are corresponding  
 1797 to “genJet” like jets, but the data event topology defined by jet multiplicity,  $b$ -tag multiplicity,  
 1798  $H_T, \dots$  is preserved. The rebalanced jets are smeared with jet response templates, which  
 1799 are obtained from simulation but which is corrected for data-MC differences. This results in a  
 1800 toy-QCD sample to which the event selection is applied.

1801 To increase the statistical accuracy, a “boot-strapping” method is implemented, which repeats  
 1802 the smearing  $N$  times to get  $N$  toy data sets. For each of this sets a prediction can be calculated  
 1803 for any arbitrary selection, resulting in a distribution of predictions. From this distribution  
 1804 the mean is the central prediction, and the square root of the variance is an estimator of the  
 1805 statistical uncertainty. Furthermore each event is potentially sampled multiple times, either  
 1806 because the corresponding prescale (for data) or because the MC event weight is large.

1807 *Remark:* Although, all relevant steps of the method are documented here, additional details can  
 1808 be found in the documentation of the 8 TeV multi-jet+MHT search [12].

#### 1809 L.1.1 Jet Response Templates from Simulated Events

1810 The complete shape of the jet energy response are only experimentally accessible in a very  
 1811 limited way, e.g. from  $\gamma+jet$  events. So, they are obtained on simulated events in a fine  $p_T$  (20,  
 1812 30, 50, 80, 120, 170, 230, 300, 380, 470, 570, 680, 800, 1000, 1300, 1700, 2200, 2800, 3500, 4300,  
 1813 5200, 6500 GeV) and  $\eta$  (0.0, 0.3, 0.5, 0.8, 1.1, 1.4, 1.7, 2.0, 2.3, 2.8, 3.2, 4.1, 5.0) binning.

1814 A delicate detail is the definition of the genJet-recoJet matching. Obviously, a pure closest  $\Delta R$   
 1815 matching will lead to a problem, as one genJet could be reconstructed as two recoJets or vice  
 1816 versa. In this case the response will have tail contributions which lead to a bad performance  
 1817 of the method. The main reason for this is, that the rebalanced jets are smeared, as if they  
 1818 are genJets, to exactly one smeared jet. This requires also a 1-1 matching for the response  
 1819 template definition. However it has been shown, that a very tight 1-1 matching leads to a bad  
 1820 performance: the main reason is, that further jet activity is present around the reco jet which  
 1821 cannot be associated with a further genJet. If this activity is neglected in the response template  
 1822 definition the response has an artificially reduced tail at high response values. Therefore the  
 1823 following matching is performed: For each genJet no further significant ( $p_T > 20$  GeV or rel.  
 1824  $p_T > 0.01$ ) genJet is found within  $\Delta R$  cone of 0.7. The four-vectors of all recoJets within  $\Delta R$   
 1825 cone of 0.35 are summed up and used for the response calculation:  $r = p_T^{\sum \text{reco:} \Delta R < 0.35} / p_T^{\text{gen}}$ .

1826 Furthermore the response templates are separated for  $b$ -tagged jets and non- $b$ -tagged jets, since  
 1827 later the  $b$ -tag information is inherited from the seed jets and smeared accordingly after re-  
 1828 balancing. To account for possible data-MC differences of the jet energy response, correction  
 1829 factors are obtained for the Gaussian resolution and the non-Gaussian tails from di-jet events.

1830 **L.1.2 Jet Energy Resolution and Response Tail Measurements**

Di-jet events are selected with both leading jet being back-to-back ( $\Delta\phi > 2.7$ ) and furthermore it is required that both jets are located in the same  $\eta$  bin. By this it is guaranteed that the response of both jets should follow the the same response distribution. The events are triggered with prescaled  $p_{T,\text{ave}} = (p_T^{1\text{st}} + p_T^{2\text{nd}})/2$  triggers. The di-jet asymmetry  $\mathcal{A}$  is defined as

$$\mathcal{A} = \frac{p_T^{1\text{st}} - p_T^{2\text{nd}}}{p_T^{1\text{st}} + p_T^{2\text{nd}}}, \quad (41)$$

and in the case of perfect di-jet events the width of the asymmetry is related to the with of the relative jet energy resolution

$$\frac{\sigma_{\text{jet}}(p_T)}{\langle p_T \rangle} = \sqrt{2}\sigma_{\mathcal{A}}(\bar{p}_T). \quad (42)$$

However, there are never pure di-jet events and further jet activity is breaking the momentum balance of the di-jet system in the transverse plane. To account for this,  $\mathcal{A}$  is binned in an estimator for the additional jet activity:  $\alpha$ . The measured width of  $\mathcal{A}$  is then extrapolated to  $\alpha = 0$ . Previously, inclusive bins ( $\alpha < \alpha_{\text{max}}$ ) have been used for the definition  $\alpha = \bar{p}_T^{3\text{rd}} / p_{T,\text{ave}}$ . This makes the treatment of statistical correlations among the different bins more challenging, but shows a nice linear dependence of  $\sigma_{\mathcal{A}}$  on  $\alpha$ . However, this linearity is only empirically found and hard to justify. Therefore, we investigate the usage of a more sophisticated definition of alpha:

$$\alpha_{||} = \bar{p}_T^{3\text{rd}} \cdot \hat{i} \quad \text{with} \quad \hat{i} = \frac{\bar{p}_T^{1\text{st}} - \bar{p}_T^{2\text{nd}}}{|\bar{p}_T^{1\text{st}} - \bar{p}_T^{2\text{nd}}|}. \quad (43)$$

1831 If we bin  $\mathcal{A}$  exclusively in  $\alpha_{||}$  we do expect that the most probable value of the distribution is  
 1832 shifted by an amount which is directly proportional to  $\alpha_{||}$ . The width of the core is then less  
 1833 dependent on the additional jet activity and we expect to obtain small extrapolation uncertainties.  
 1834 The correction factor for the Gaussian resolution is obtained as the ratio of the extrapolated  
 1835 value for data and simulation.

1836 The non-Gaussian tail correction factors are also obtained from the di-jet asymmetry, but in  
 1837 this case looking not the distribution around the maximum but at large asymmetry values, e.g.  
 1838  $\mathcal{A} > \mu(\mathcal{A}) + 2.5\sigma_{\mathcal{A}}$ . The ratio of the extrapolated fraction of events in data and simulation is  
 1839 then defined as a tail scaling factor to be applied on the MC jet energy response templates.

1840 **L.1.3 Generator Jet Smearing**

1841 One of the first fundamental test of the method is the genJet smearing closure test, where in-  
 1842 stead of rebalancing the genJets are smeared directly with the jet energy response templates.  
 1843 For this we used the  $\hat{p}_T$  binned pythia samples, except for the sample with  $1800 < \hat{p}_T < 2400$   
 1844 which was temporarily not available. Figure 116 shows the performance for several relevant  
 1845 variables. Overall we can state that the performance is very good. The largest deviations are  
 1846 observed at very low and very high MHT with approximately 25%.

1847 **L.1.4 Rebalancing**

1848 Events are rebalanced using a kinematic fit (TKinFitter implementation of CMSSW). The mo-  
 1849 mentum of the jets are adjusted within the jet energy resolutions to fulfill the constraint of no  
 1850 missing transverse energy. There could be possibly multiple solutions to the minimization  
 1851 problem, but we take the one solution to which the kinematic fit has converged. It is not ex-  
 1852 pected that a different solution will have significant differences in variables like jet  $p_T$ ,  $H_T$ , or

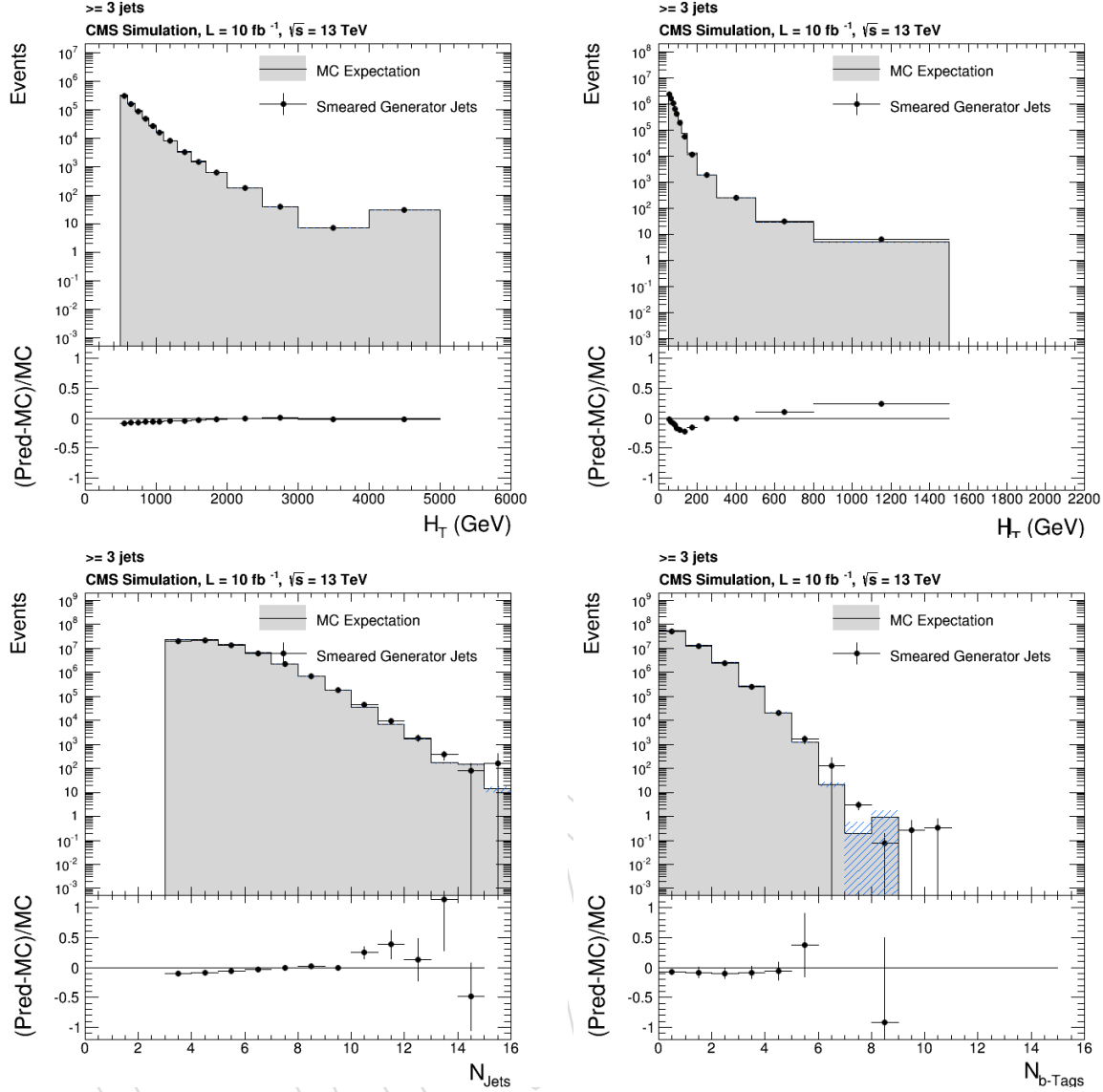


Figure 116: Comparison of MC expectation and prediction from genJet smearing for several important variables.

1853  $N_{\text{jet}}$ . Any possible bias which is introduced by this, will be covered by the non-closure systematics.  
 1854 The input jet energy resolutions are obtained directly from the MC jet energy response  
 1855 templates, with possible modification for data-MC differences. Obviously, it would be a bad  
 1856 idea to use as  $p_T$  threshold for the jets going into the rebalancing 0 GeV: First of all these objects  
 1857 are hard to calibrate and understand in detail. On the other hand, low thresholds would lead  
 1858 to a large fraction of PU jets which do not belong to the hard interaction and therefore should  
 1859 not take part in the rebalancing step. Figure 117 shows the closure for the MHT distribution for  
 1860 three different settings of the  $p_T$  threshold. The cut at 10 GeV, which is the lowest acceptable  
 1861 value in terms of jet quality understanding, seems to perform best and is therefore used in the  
 1862 following studies.

1863 The presence of a jet  $p_T$  threshold leads to a bias of the jet  $p_T$  in the rebalancing step. To demon-  
 1864 strate this, figure 118 shows the ratio of the transverse momentum of the rebalanced jet and the  
 1865 closest matched genJet as a function of  $p_T$ . This bias is leading to a possible change of the jet  
 1866 multiplicity, which can be seen on the left hand side of figure 119. If the transverse momentum

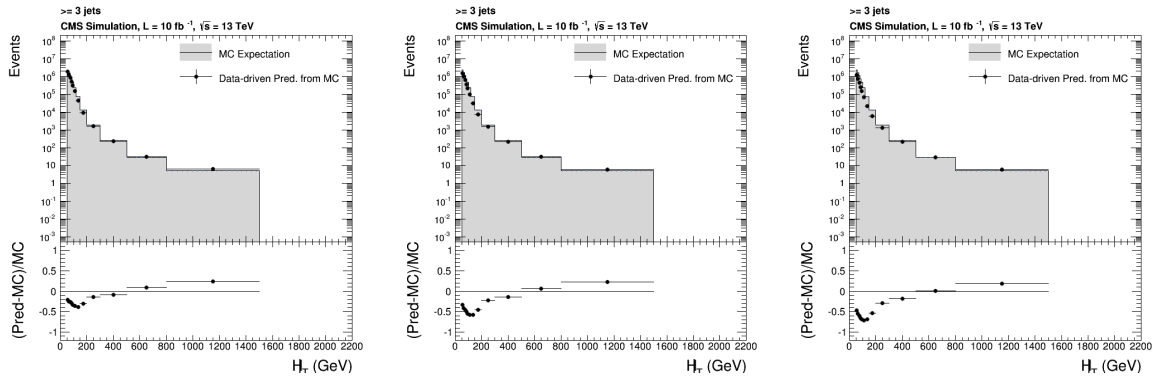


Figure 117: Comparison of MHT distribution from R+S and simulation for three different jet  $p_T$  threshold values. Lower thresholds, e.g. 10 GeV, perform better than larger values.

of the recoJets are first corrected with the inverse of the aforementioned ratio, before passed to the rebalancing step, on observes a much better closure of the jet multiplicity, as can be seen on the right hand side of figure 119.

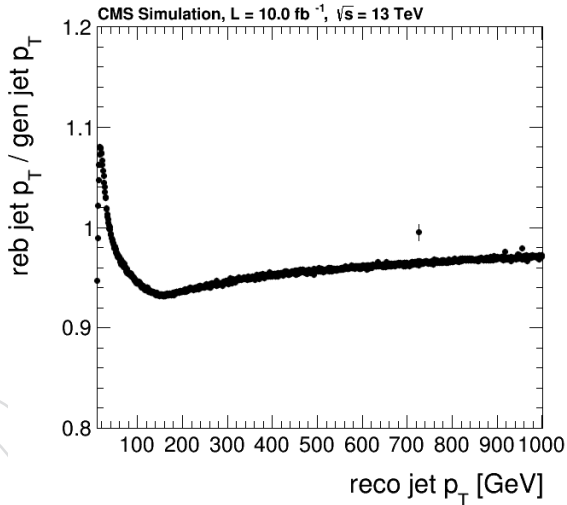


Figure 118: Ratio of  $p_T$  from rebalanced jet and matched genJet.

### L.1.5 Full R+S Closure

The final performance test is the application of the full method to simulated events and compare is to expectation from simulation. Again, we first have a look at the closure for the relevant search variables for very inclusive selections (see. figure 120) Overall a good performance can be seen, with maximal syst. biases of  $\sim 30\%$ .

Much more interesting is of course the closure in each of the 72 search regions, which is presented in figure 121. The statistical precision of the prediction is here increased by smearing highly weighted events multiple times (up to 100) with a correspondingly reduced event weight. Although for a lot of bins the statistical precision of the expectation from simulation is insufficient to make a conclusive statement, there are some deviations which require more detailed studies with more inclusive selections.

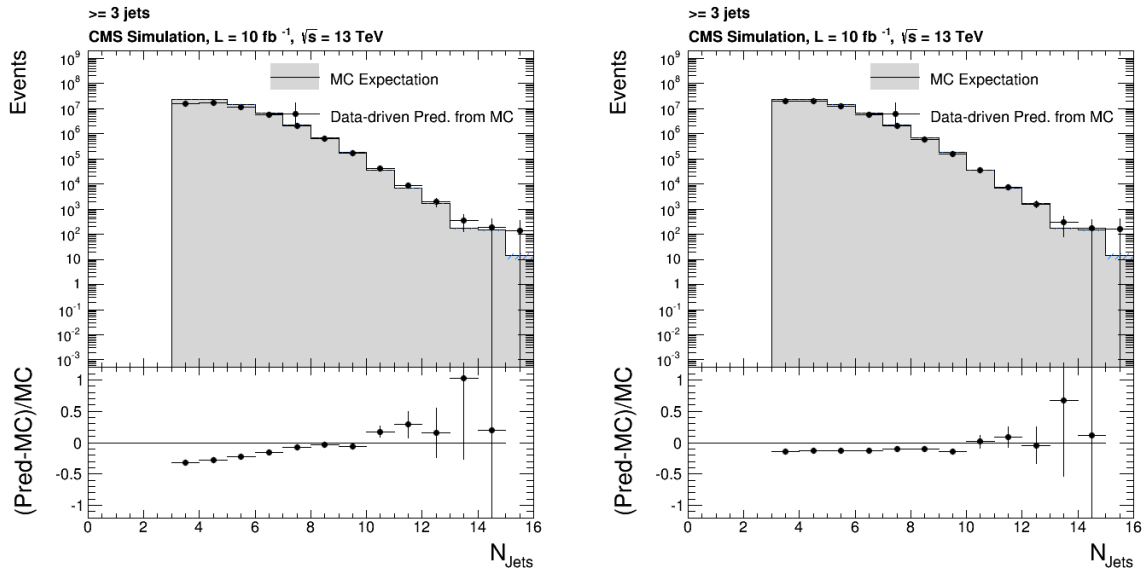


Figure 119: Comparison of predicted and expected jet multiplicity without (left) and with (right) rebalance correction.

### L.1.6 Systematic Uncertainties

The following systematic uncertainties are considered.

Tail and core of jet response: As discussed in section L.1.2 the jet response can be different for data and simulation, and dedicated analyses are measuring these differences from di-Jet events. So far, the best estimate for the expected differences of the non-Gaussian tails and the core resolution are from 7 and 8 TeV measurements. To estimate the approximate uncertainty from this source, we varied the jet resolution by 10% and the non-Gaussian tails by 20%. The variation of the resolution results in a shift of the R+S prediction from  $\sim 10\%$  to  $\sim 20\%$  for low to high jet multiplicities. The variation of the non-Gaussian tails results in a shift of up to  $\sim 30\%$ . The previously mentioned numbers are only valid for bins which have a significant contribution from QCD. In other bins, the statistical uncertainties are often much larger, so no precise value can be determined, but the stat. uncertainties give a conservative upper bound on the corresponding effect.

Non-Closure: The bin-by-bin closure is for many bins clearly limited by the statistics of the simulated QCD samples. On the other hand inclusive tests for different search variables are maybe not representative for tight selections. To overcome this problem a similar strategy as at 8 TeV will be carried out (the exact procedure is still to be defined, but a possible strategy could look like the following): For every jet and b-jet multiplicity four selections are defined of low and high MHT and HT (cut values to be optimized). Furthermore, for each of these wider bins a QCD-enriched control region of inverted  $\min\Delta\phi$  is defined, and finally control regions at even lower MHT than the baseline cut (e.g. 100 to 200 GeV) are defined. The first step of the procedure is the check in the wider search bins: if a non-closure is statistically significant or if the statistical uncertainties of the method are small enough (threshold to be defined) we take the result from this region. Else, in the second step the  $\min\Delta\phi$  inverted control region is used. If also in this bin the result is not statistically significant, the lower MHT regions are used or b-jet multiplicity bins are combined.

Pile up: This uncertainty is obtained from a data and simulation comparison: the trend of

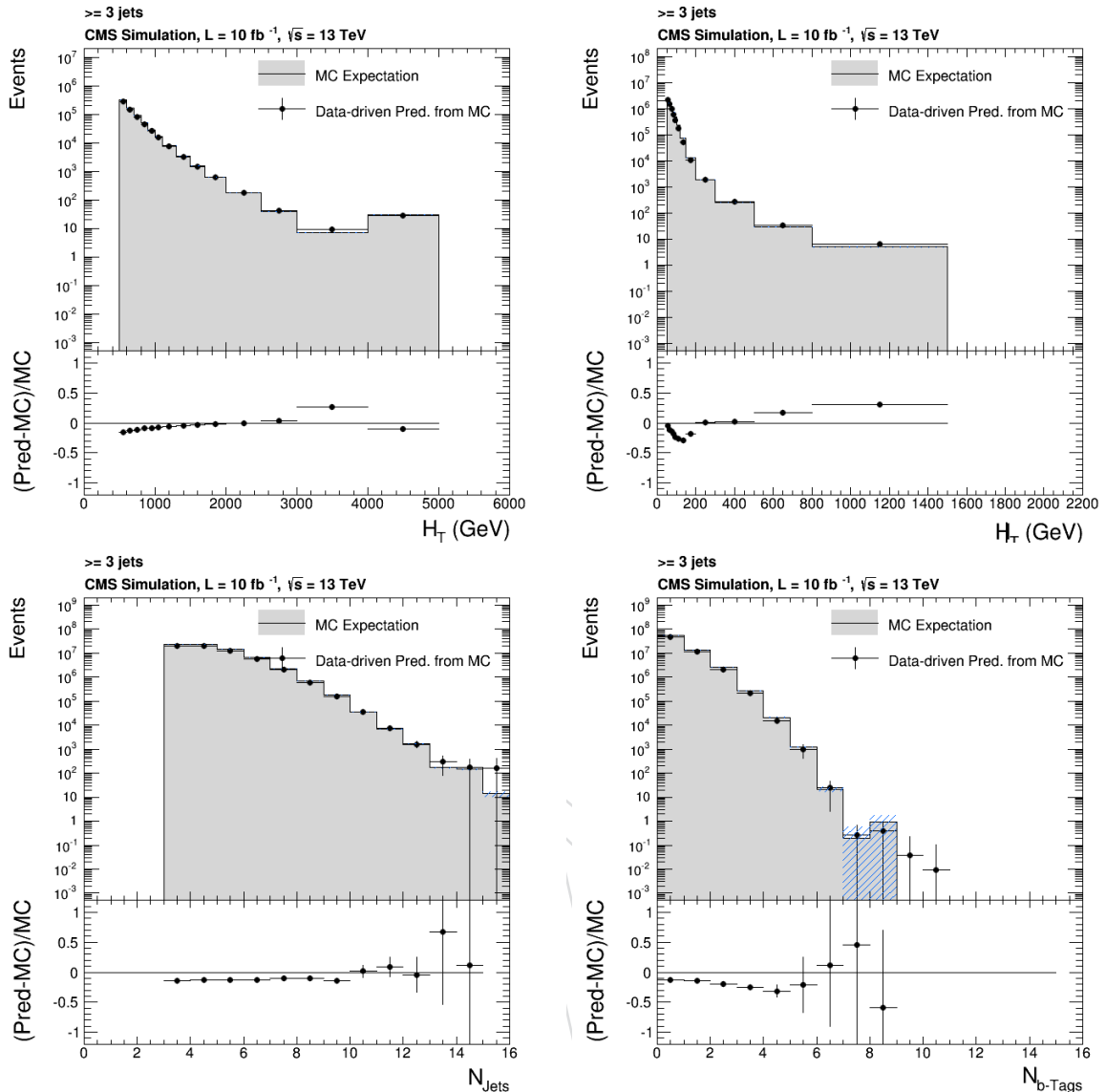


Figure 120: Comparison of MC expectation and prediction from full R+S smearing for several important variables.

the QCD prediction (normalized to the number of used seed events) is determined for various bins of primary vertices. The resulting distributions for data and simulation are normalized to the same low PU prediction. This is justified, since for low number of primary vertices no PU difference is expected. The difference at larger number of primary vertices is then used to estimate the PU uncertainty. As for the non-Closure uncertainty this uncertainty has to be determined in combined search bins. In previous interations of this analysis, the PU uncertainty was statistically limited and of minor importance!

Stat. uncertainties from sampling: These uncertainties are obtained from the variance of the distributions of predictions. They are limited by sampling events with large weights multiple times. For search bins with a significant QCD contribution, the uncertainties are relatively small, compared to other systematic uncertainties. However, for bins with very low QCD expectations these (relative) uncertainties can be quite large, since the event weight is still much larger than the average prediction.

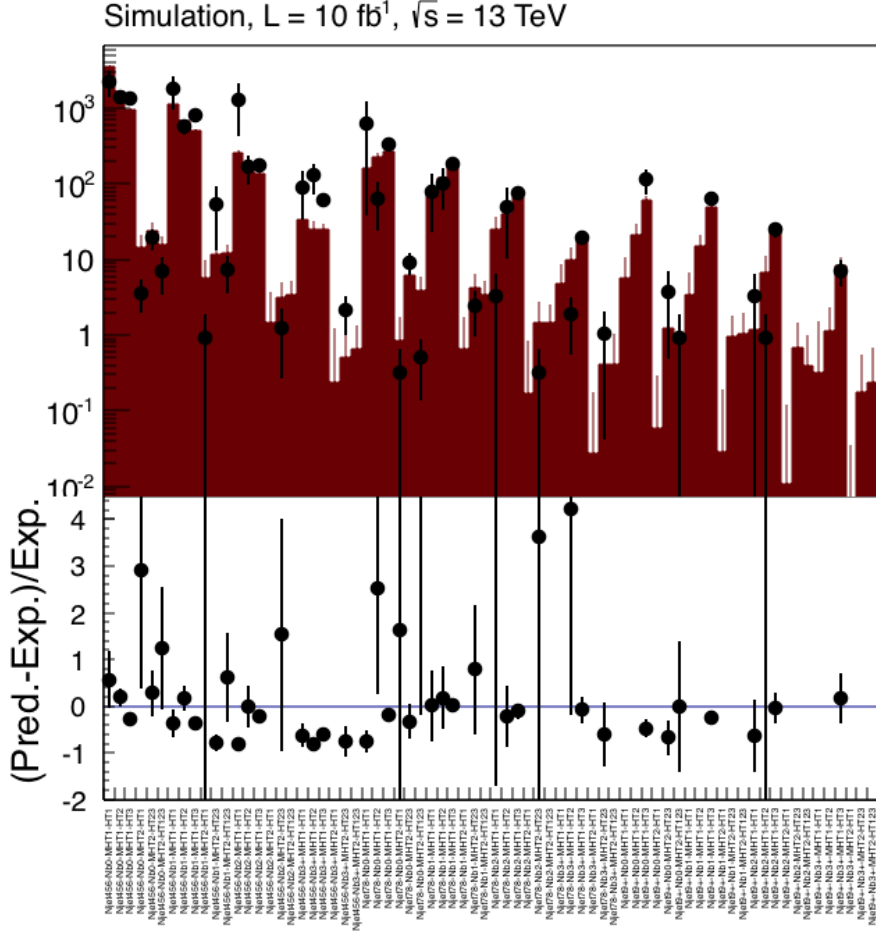


Figure 121: Comparison of full R+S prediction (red bars) and MC expectation (points). Statistical uncertainties on the expectation are very large.

But because of the small QCD contribution in such bins, the overall sensitivity is not negatively influenced by these large uncertainties.

## L.2 Extrapolating background estimates from medium to high $H_T^{\text{miss}}$

The lost-lepton method described in Sec.6.1 relies on a control sample to search sample ratio of about 2 to 1. For our most sensitive search bins, with background below a few events, and relatively good signal efficiency, the statistical uncertainty on the lost-lepton background estimate can be substantial and sometimes the dominant background uncertainty. The expected exclusion sensitivity (i.e. the expected upper limit on the signal cross section if the signal does not exist) does not strongly depend on the statistical uncertainty on the background in these very low background bins. However, reducing the statistical uncertainty on the lost-lepton background estimate can substantially improve the discovery sensitivity (i.e. the significance of an excess due to a real signal), since a smaller background uncertainty reduces the likelihood of the null hypothesis if an excess is observed. This is the motivation for the method described in this subsection.

The lost-lepton  $H_T^{\text{miss}}$  spectrum depends on the underlying  $p_T$  spectrum of the leptonically decaying  $W$  and the angular distribution of the  $W$  decay. The  $W$   $p_T$  spectrum depends on the

1940 top quark  $p_T$  spectrum, for which the Monte Carlo is less reliable than the angular distribution  
 1941 of the  $W$  decay, which is well understood (see Sec. 7 of [34] and [35]). The shape of the  
 1942  $H_T^{\text{miss}} / p_T(W)$  distribution is closely related to the angular distribution of the  $W$  decay and thus  
 1943 expected to be well modeled by the Monte Carlo.

1944 We use Monte Carlo distributions of  $H_T^{\text{miss}} / p_T(W)$  for lost leptons to translate the observed  $W$   
 1945  $p_T$  spectrum into a lost lepton  $H_T^{\text{miss}}$  spectrum. This lost lepton  $H_T^{\text{miss}}$  spectrum is then used  
 1946 to estimate a high-to-medium  $H_T^{\text{miss}}$  ratio  $R^{\text{MHT}}$ , which can be used to extrapolate a lost-lepton  
 1947 background estimate at medium  $H_T^{\text{miss}}$ , from the method described in Sec. 6.1, to high  $H_T^{\text{miss}}$ ,  
 1948 thus reducing the statistical uncertainty of the lost-lepton background estimate in the most  
 1949 sensitive search bins.

1950 Figure 122 shows an example single lepton control sample  $H_T^{\text{miss}}$  vs  $p_T^W$  distribution. The statisti-  
 1951 cal uncertainty on the  $H_T^{\text{miss}}$  extrapolation ratio  $R^{\text{MHT}}$  is mostly determined by the number of  
 1952 single lepton control sample events with  $p_T^W > H_T^{\text{miss}}_{\text{low}}$ , where  $H_T^{\text{miss}}_{\text{low}}$  is the low edge of the  
 1953 high- $H_T^{\text{miss}}$  search bin (see Sec. L.3 for details). For example, the extrapolation ratio  $R^{\text{MHT}}$  going  
 1954 from  $H_T^{\text{miss}}$  bin 1 to  $H_T^{\text{miss}}$  bin 2, which is from 500 to 750 GeV, uses all single lepton control sam-  
 1955 ple events with  $p_T^W > 500$  GeV, while the standard lost-lepton method only uses single-lepton  
 1956 events with  $H_T^{\text{miss}}$  between 500 to 750 GeV to predict the background for  $H_T^{\text{miss}}$  bin 2. Figure 122  
 1957 illustrates the source of the improvement in control sample statistics, which is typically more  
 1958 than a factor of four.

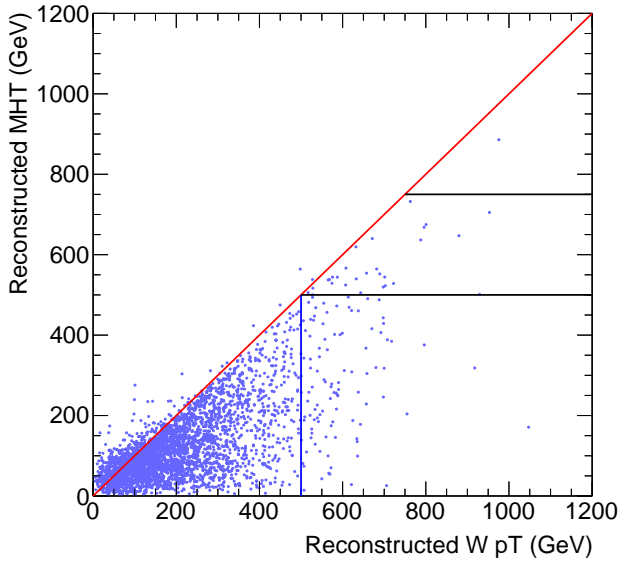


Figure 122: Example  $H_T^{\text{miss}}$  vs  $W p_T$  distribution for single-lepton control sample events from the  $t\bar{t}$  Monte Carlo with  $H_T > 1200$  GeV,  $N_{\text{jet}} \geq 7$ , and  $N_{\text{b-jet}} \geq 3$ . The horizontal lines define  $H_T^{\text{miss}}$  bin 2 (500 to 750). The  $H_T^{\text{miss}}$  extrapolation method uses all events above the vertical line with  $p_T^W > 500$  GeV in the estimation of the  $H_T^{\text{miss}}$  spectrum above 500 GeV.

1959 Figure 123 shows the  $H_T^{\text{miss}} / p_T(W)$  distribution of lost lepton events, including the separate  
 1960 contributions from  $W \rightarrow e, \mu$ , and  $W \rightarrow \tau \rightarrow e, \mu$ . The distribution for  $W \rightarrow \tau \rightarrow$  hadrons  
 1961 events is also included. Figure 123 also shows the ratio of lost lepton events to single lepton  
 1962 control sample events  $R^{LC}$  as a function of the reconstructed  $W p_T$ . This isn't flat, indicating  
 1963 that lost lepton and control sample events have different  $W p_T$  spectra, so this must be taken  
 1964 into account. Both the  $H_T^{\text{miss}} / p_T(W)$  and  $R^{LC}$  distributions have some additional dependence

1965 on  $N_{\text{jet}}$  and  $H_T$ . This is taken into account by using separate distributions for each  $N_{\text{jet}}$  and  $H_T$   
 1966 bin combination, as shown in Section L.3.

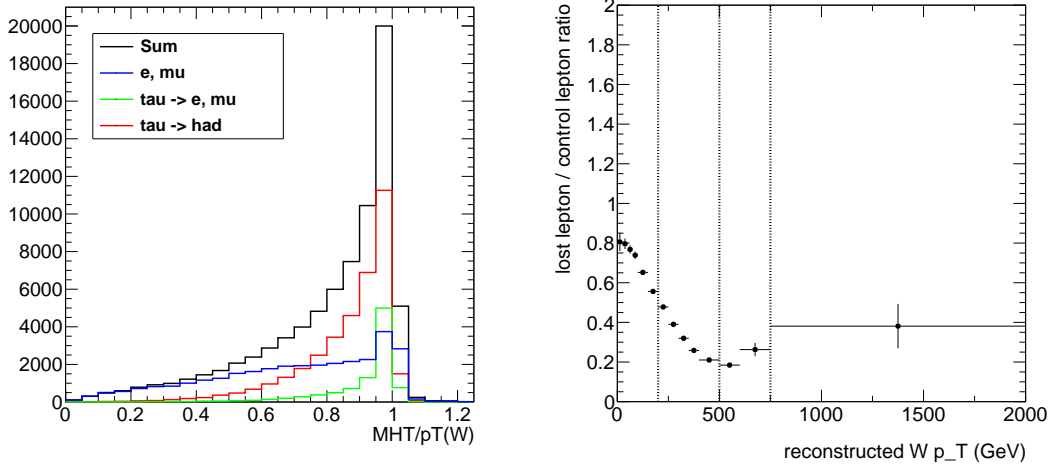


Figure 123: Distribution of  $H_T^{\text{miss}} / p_T(W)$  (left) for lost leptons and the ratio of lost lepton events / control lepton events as a function of  $p_T^W$  from the  $t\bar{t}$  Monte Carlo. The left figure is summed over all search bins and shows the contributions from  $W \rightarrow e\nu$  and  $W \rightarrow \mu\nu$  (blue),  $W \rightarrow \tau\nu$  with  $\tau \rightarrow e$  or  $\mu$  (green), and  $W \rightarrow \tau\nu$  with  $\tau \rightarrow \text{hadrons}$  (red) and includes a  $p_T(W) > 200$  GeV requirement, in addition to the baseline  $H_T$  and  $N_{\text{jet}}$  requirements. Note that we are not yet applying this method to the  $\tau \rightarrow \text{hadrons}$  estimation. The right plot is an example distribution corresponding to events in  $N_{\text{jet}}$  bin 1,  $H_T$  bin 2. The vertical dashed lines in the right plot show the location of the  $H_T^{\text{miss}}$  bin boundaries. The points below 200 GeV are not used in the analysis.

1967 The high / medium  $H_T^{\text{miss}}$  ratios for each  $N_{\text{jet}}$ ,  $H_T$  bin combination are derived from  $H_T^{\text{miss}}$   
 1968 distributions constructed from the single lepton control sample, where each event makes a  
 1969 contribution from the corresponding  $H_T^{\text{miss}} / p_T(W)$  distribution weighted by the lost / control  
 1970 ratio  $R^{LC}$ . The resulting  $H_T^{\text{miss}}$  distributions are compared with the Monte Carlo lost lepton  
 1971  $H_T^{\text{miss}}$  distributions in Fig.124. The agreement is reasonable.

1972 Figure 125 compares the predicted number of  $t\bar{t}$  lost lepton background events with the ob-  
 1973 served number for all of the search bins for  $H_T^{\text{miss}}$  bins 2 and 3, where the extrapolation was  
 1974 done from  $H_T^{\text{miss}}$  bin 1. The agreement is reasonable. The difference in error bars is an indica-  
 1975 tion of the improvement in the statistical uncertainty of the lost lepton background estimate.  
 1976 More details on the  $H_T^{\text{miss}}$  extrapolation method, including how the statistical errors from the  
 1977 single lepton control sample are propagated to the BG predictions, are given in Section L.3.

1978 The extrapolation method described here does not currently include events with a hadronic tau  
 1979 decay, though they could be incorporated. The hadronic tau events would contribute to both  
 1980 the lost lepton  $H_T^{\text{miss}} / p_T(W)$  distribution (Fig.123, left) and the numerator of the lost / control  
 1981 ratio  $R^{LC}$  (Fig.123, right) but would be absent from the single lepton control sample.

1982 For the purpose of this preliminary study, the lost / control ratio  $R^{LC}$  as a function of  $p_T^W$  are  
 1983 taken from Monte Carlo and will depend on the lepton acceptance, identification, and isolation  
 1984 efficiency. This dependence is also captured by the translation factors calculated in the classical  
 1985 method to model the lost-lepton search region from the single-lepton control sample (equations  
 1986 11-16). Thus, the  $R^{LC}$  ratios needed to translate the  $W$   $p_T$  spectrum measured in the control  
 1987 region to the  $W$   $p_T$  spectrum in the search region will be taken from the classical method and  
 1988 validated via a tag-and-probe method in data. We do not anticipate the systematic uncertainties

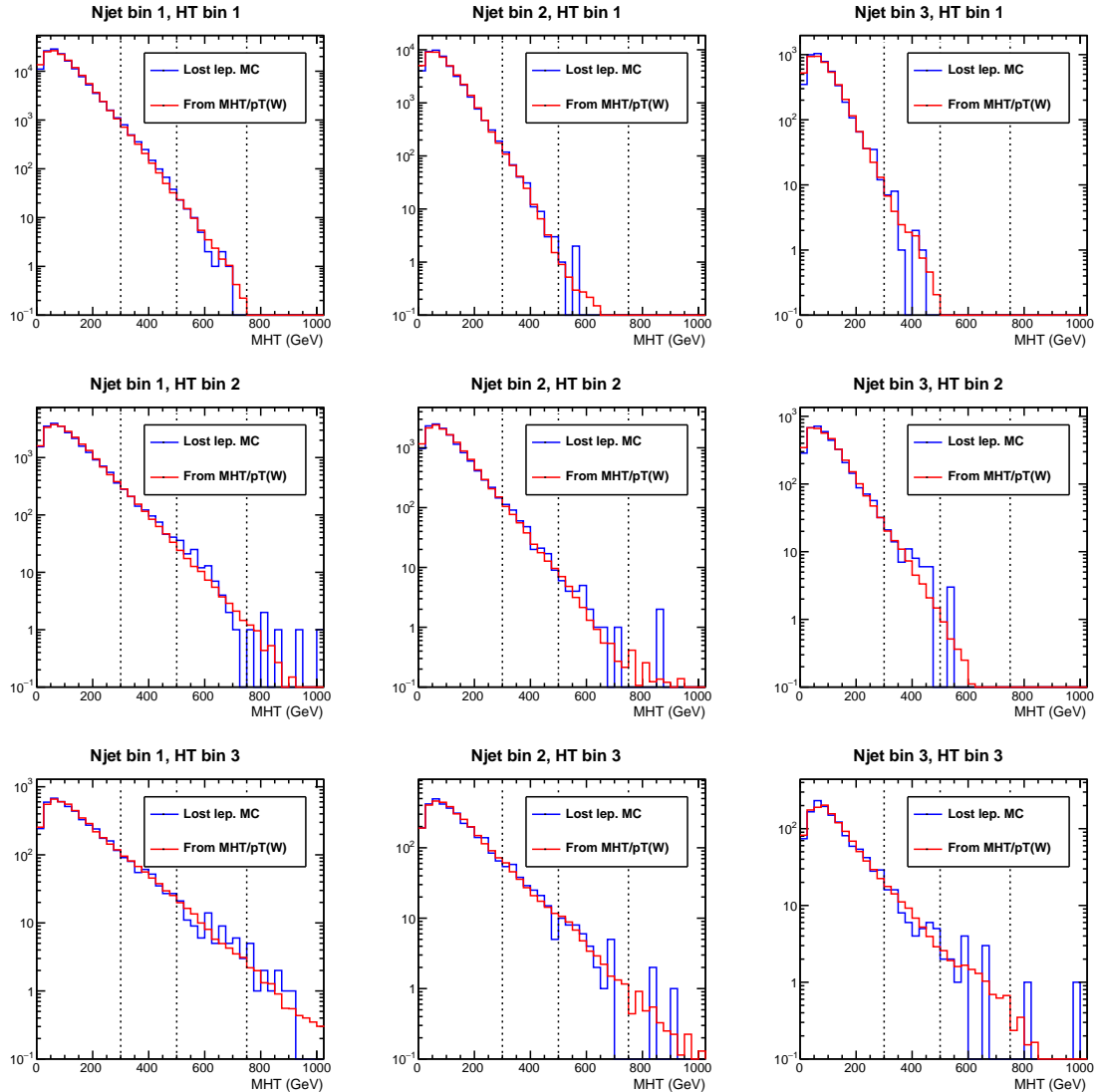


Figure 124: Distributions of  $H_T^{\text{miss}}$  for the 9  $N_{\text{jet}}$ ,  $H_T$  analysis bin combinations for the  $t\bar{t}$  Monte Carlo sample. The blue distributions are from the lost lepton Monte Carlo, while the red distributions are built from the single lepton control sample, applying the method described in this section.

associated with these efficiencies and ratios to be larger than the statistical uncertainties in the most sensitive search bins. The material shown in this section is based on the  $t\bar{t}$  Monte Carlo, though it will be extended to include the other lost lepton sources:  $W+jets$  and single top. No trigger requirement was imposed for the material shown in this section. We expect to use the single lepton plus hadronic activity cross triggers, which have an online  $H_T$  requirement of 400 GeV and an online  $E_T^{\text{miss}}$  requirement of 70 GeV, to measure the  $W$   $p_T$  spectrum. This trigger will allow us to capture more of the  $W$   $p_T$  spectrum than is accessible with the main hadronic analysis trigger, namely events with  $W$   $p_T > 200$  GeV and  $H_T^{\text{miss}} < 200$  GeV. This is illustrated in Figure 126, which shows the reconstructed  $W$   $p_T$  spectrum for offline  $H_T^{\text{miss}}$ ,  $H_T$ , and lepton  $p_T$  thresholds.

To gauge the statistical power of this method in a direct analysis context, we compare the lost- $e/\mu$  background in the  $N_{\text{b-jet}} \geq 2$  bins from  $10 \text{ fb}^{-1}$  of  $t\bar{t}$  MC with the estimations from the

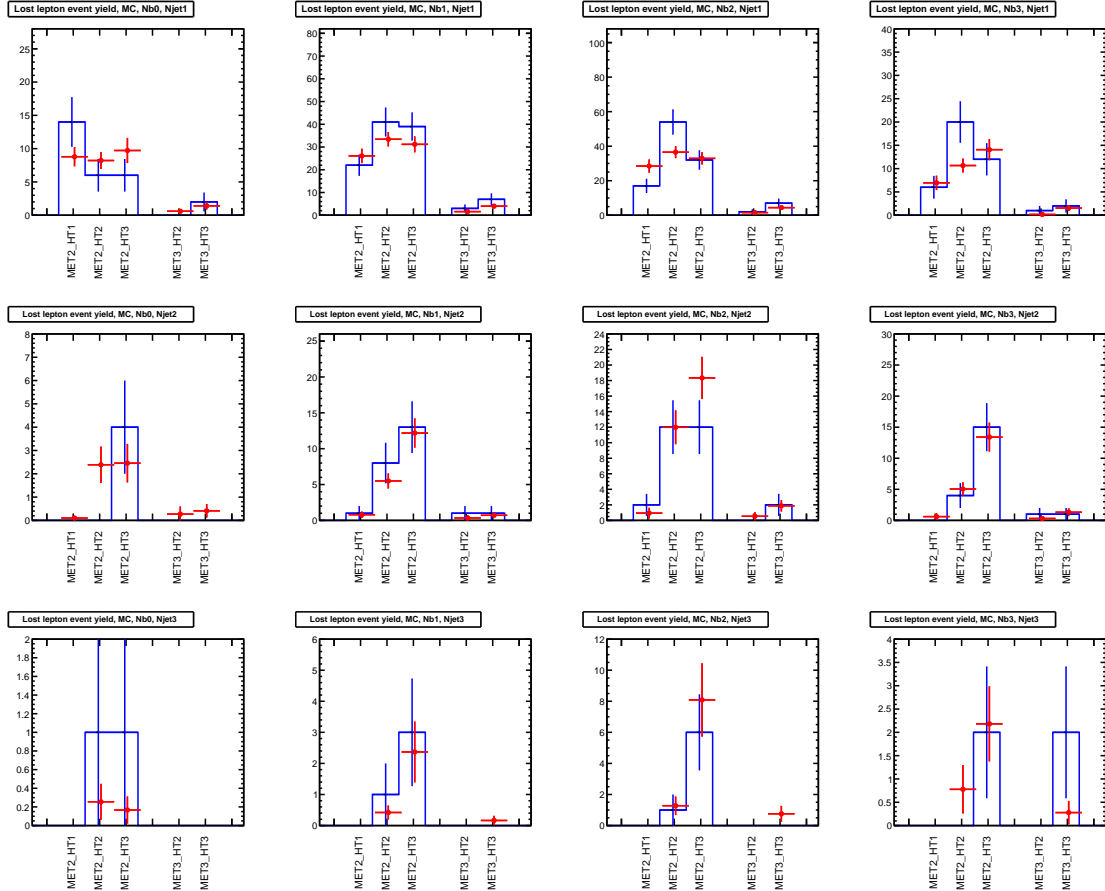


Figure 125: Number of  $t\bar{t}$  lost lepton background events in the analysis search bins from the Monte Carlo (blue) and the  $H_T^{\text{miss}}$  extrapolation method (red). The equivalent integrated luminosity of the  $t\bar{t}$  Monte Carlo sample is about  $31 \text{ fb}^{-1}$ .

2001 classical method and the extrapolation method in Tables 40-45 and Figures 127-132. The most  
 2002 noticeable result of this comparison is the fact that all of the bins that had no control sample  
 2003 statistics under the classical method have an effective control sample under the extrapolation  
 2004 method. The closure of the two methods is comparable within the statistics of the MC. We plan  
 2005 to evaluate this method with a higher statistics sample to test for any biases introduced by the  
 2006 extrapolation.

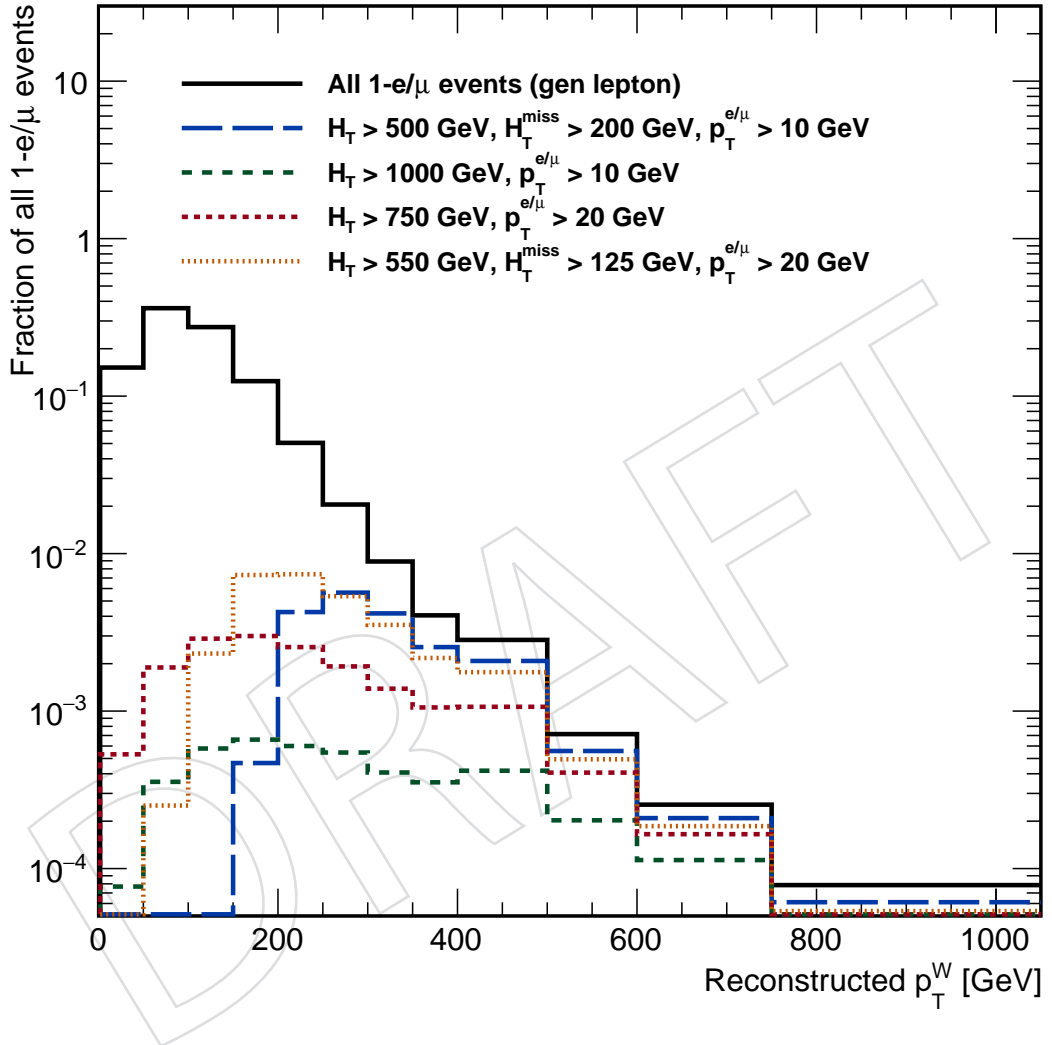


Figure 126: Comparison of the true  $W$   $p_T$  spectrum (black) in all single-muon  $t\bar{t}$  events with the  $W$   $p_T$  spectrum reconstructed from an isolated muon and the  $H_T^{\text{miss}}$ . The orange histogram most likely corresponds to the selection required by the trigger we will use to measure the  $W$   $p_T$  spectrum in single-lepton events.

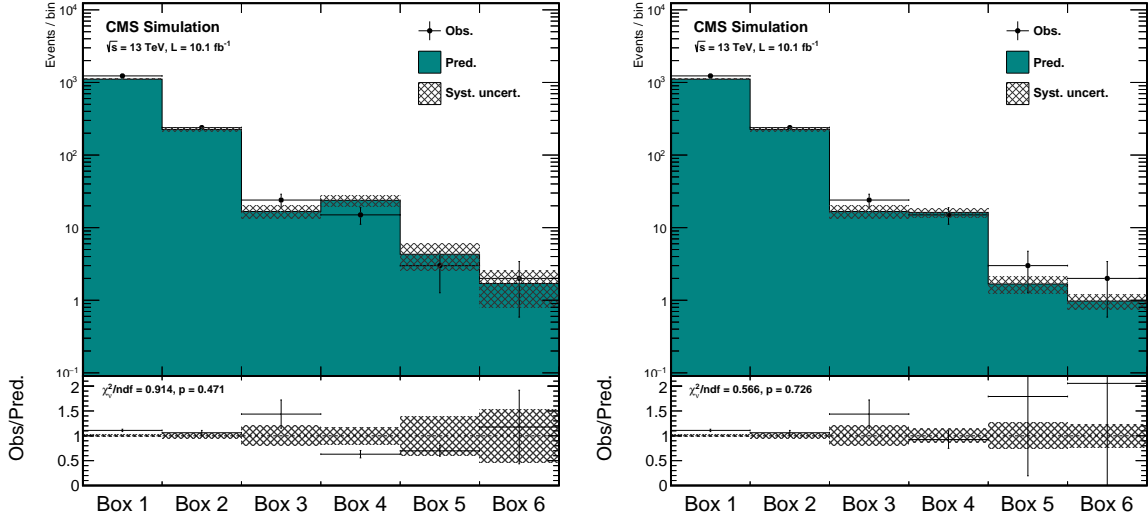


Figure 127: Lost-lepton estimation closure tests in search bins with  $N_{\text{b-jet}} = 2$  and  $4 \leq N_{\text{jet}} \leq 6$ . The black markers are the true expected backgrounds taken directly from  $10 \text{ fb}^{-1}$  of  $t\bar{t}$  MC. The teal histogram corresponds to the background predicted by either the classical (left) or extrapolation method (right). The systematic uncertainties, which are dominated by control sample statistics in the most sensitive bins, correspond to  $10 \text{ fb}^{-1}$  of data. Note that the background in MHT-HT boxes 1-3 is always predicted by the classical method.

Table 40: Closure test for search bins with  $N_{\text{b-jet}} = 2$  and  $4 \leq N_{\text{jet}} \leq 6$ , plotted in Figure 127

MHT-HT Bin	Classical Pred.	Extrapolated Pred.	Obs.
Box 1		$1110.0 \pm 25.8$	1231
Box 2		$225.1 \pm 11.8$	239
Box 3		$16.7 \pm 3.3$	24
Box 4	$23.8 \pm 4.2$	$29.2 \pm 5.1$	15
Box 5	$4.30 \pm 1.70$	$2.92 \pm 1.37$	3
Box 6	$1.70 \pm 0.90$	$1.09 \pm 0.36$	2

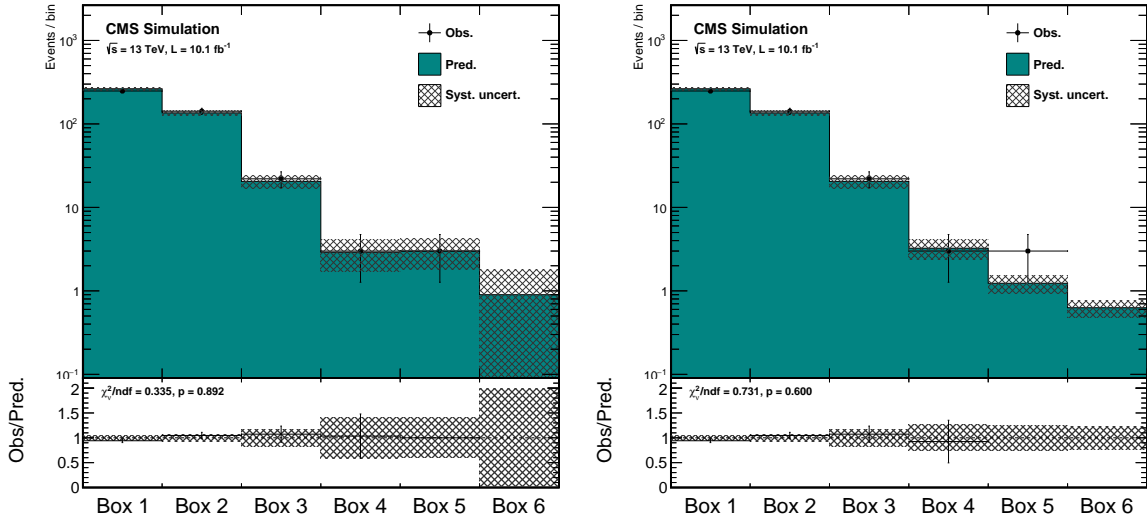


Figure 128: Lost-lepton estimation closure tests in search bins with  $N_{b\text{-jet}} = 2$  and  $7 \leq N_{\text{jet}} \leq 8$ . The black markers are the true expected backgrounds taken directly from  $10 \text{ fb}^{-1}$  of  $t\bar{t}$  MC. The teal histogram corresponds to the background predicted by either the classical (left) or extrapolation method (right). The systematic uncertainties, which are dominated by control sample statistics in the most sensitive bins, correspond to  $10 \text{ fb}^{-1}$  of data. Note that the background in MHT-HT boxes 1-3 is always predicted by the classical method.

Table 41: Closure test for search bins with  $N_{b\text{-jet}} = 2$  and  $7 \leq N_{\text{jet}} \leq 8$ , plotted in Figure 128

MHT-HT Bin	Classical Pred.	Extrapolated Pred.	Obs.
Box 1		$263.6 \pm 11.8$	248
Box 2		$135.6 \pm 8.7$	142
Box 3		$20.5 \pm 3.5$	22
Box 4	$2.90 \pm 1.20$	$4.75 \pm 1.82$	3
Box 5	$3.00 \pm 1.20$	$2.89 \pm 1.17$	3
Box 6	$0.90 \pm 0.90$	$0.71 \pm 0.23$	0

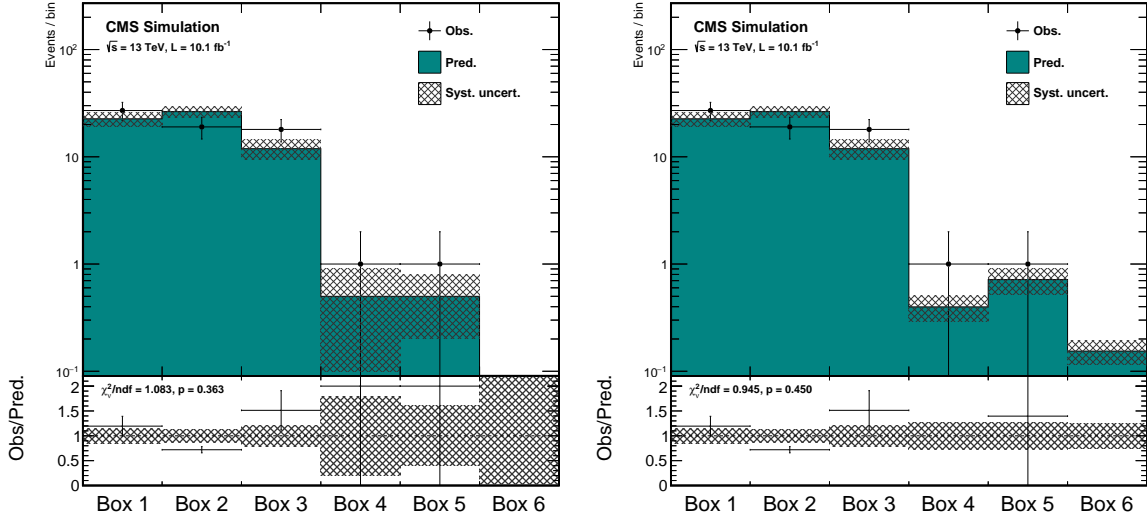


Figure 129: Lost-lepton estimation closure tests in search bins with  $N_{\text{b-jet}} = 2$  and  $N_{\text{jet}} \geq 9$ . The black markers are the true expected backgrounds taken directly from  $10 \text{ fb}^{-1}$  of  $t\bar{t}$  MC. The teal histogram corresponds to the background predicted by either the classical (left) or extrapolation method (right). The systematic uncertainties, which are dominated by control sample statistics in the most sensitive bins, correspond to  $10 \text{ fb}^{-1}$  of data. Note that the background in MHT-HT boxes 1-3 is always predicted by the classical method.

Table 42: Closure test for search bins with  $N_{\text{b-jet}} = 2$  and  $N_{\text{jet}} \geq 9$ , plotted in Figure 129

MHT-HT Bin	Classical Pred.	Extrapolated Pred.	Obs.
Box 1		$22.6 \pm 3.5$	27
Box 2		$26.4 \pm 3.3$	19
Box 3		$11.9 \pm 2.5$	18
Box 4	$0.50 \pm 0.40$	$0.58 \pm 0.23$	1
Box 5	$0.50 \pm 0.30$	$1.68 \pm 0.71$	1
Box 6	0	$0.17 \pm 0.06$	0

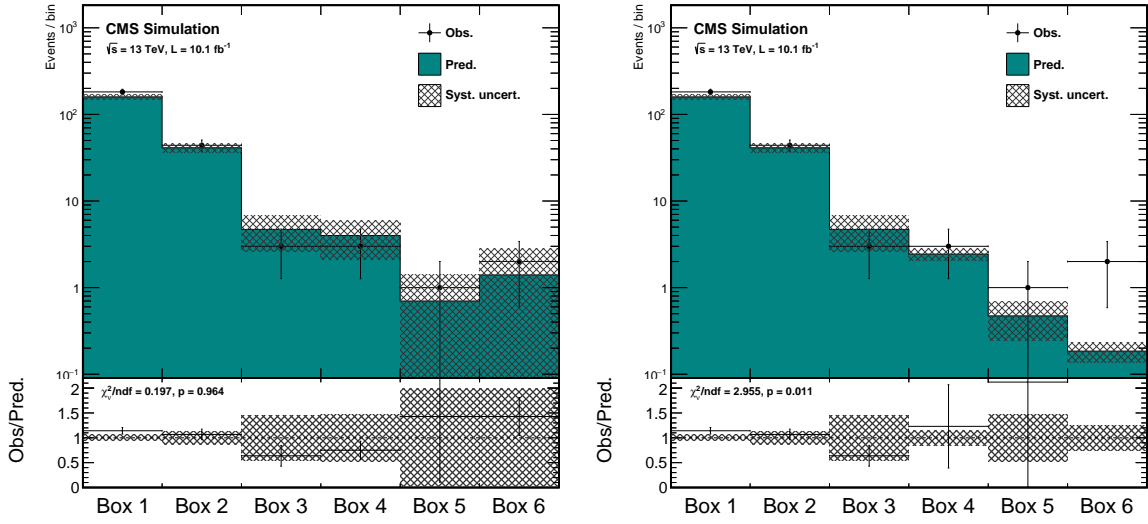


Figure 130: Lost-lepton estimation closure tests in search bins with  $N_{\text{b-jet}} \geq 3$  and  $4 \leq N_{\text{jet}} \leq 6$ . The black markers are the true expected backgrounds taken directly from  $10 \text{ fb}^{-1}$  of  $t\bar{t}$  MC. The teal histogram corresponds to the background predicted by either the classical (left) or extrapolation method (right). The systematic uncertainties, which are dominated by control sample statistics in the most sensitive bins, correspond to  $10 \text{ fb}^{-1}$  of data. Note that the background in MHT-HT boxes 1-3 is always predicted by the classical method.

Table 43: Closure test for search bins with  $N_{\text{b-jet}} \geq 3$  and  $4 \leq N_{\text{jet}} \leq 6$ , plotted in Figure 130

MHT-HT Bin	Classical Pred.	Extrapolated Pred.	Obs.
Box 1		$159.4 \pm 9.7$	182
Box 2		$41.2 \pm 5.2$	44
Box 3		$4.7 \pm 2.1$	3
Box 4	$4.00 \pm 1.90$	$4.39 \pm 0.80$	3
Box 5	$0.70 \pm 0.70$	$0.82 \pm 0.51$	1
Box 6	$1.40 \pm 1.40$	$0.21 \pm 0.07$	2

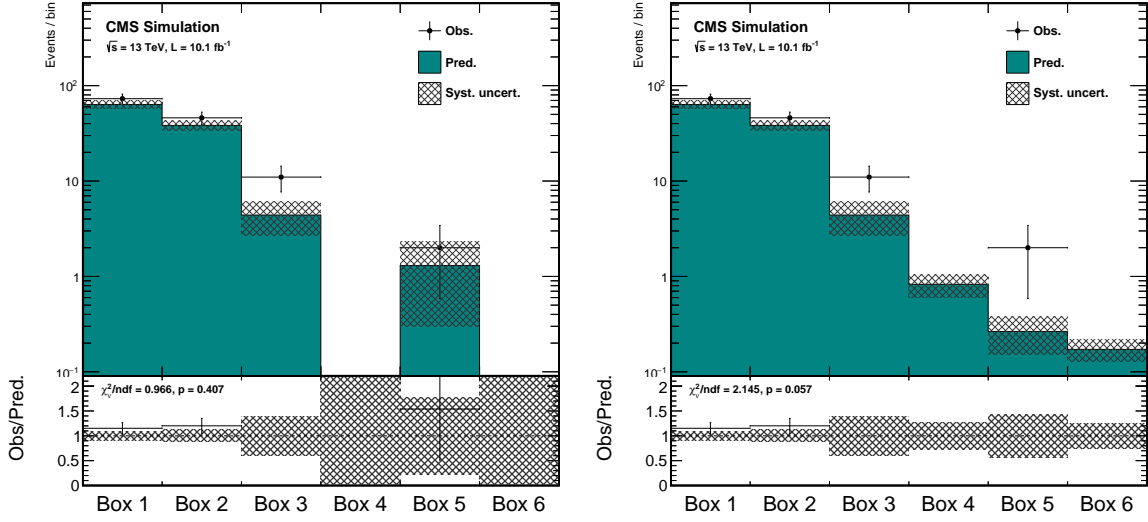


Figure 131: Lost-lepton estimation closure tests in search bins with  $N_{\text{b-jet}} \geq 3$  and  $7 \leq N_{\text{jet}} \leq 8$ . The black markers are the true expected backgrounds taken directly from  $10 \text{ fb}^{-1}$  of  $t\bar{t}$  MC. The teal histogram corresponds to the background predicted by either the classical (left) or extrapolation method (right). The systematic uncertainties, which are dominated by control sample statistics in the most sensitive bins, correspond to  $10 \text{ fb}^{-1}$  of data. Note that the background in MHT-HT boxes 1-3 is always predicted by the classical method.

Table 44: Closure test for search bins with  $N_{\text{b-jet}} \geq 3$  and  $7 \leq N_{\text{jet}} \leq 8$ , plotted in Figure 131

MHT-HT Bin	Classical Pred.	Extrapolated Pred.	Obs.
Box 1		$63.4 \pm 5.7$	73
Box 2		$38.3 \pm 4.7$	46
Box 3		$4.4 \pm 1.7$	11
Box 4	0	$1.21 \pm 0.47$	0
Box 5	$1.30 \pm 1.00$	$0.62 \pm 0.33$	2
Box 6	0	$0.19 \pm 0.07$	0

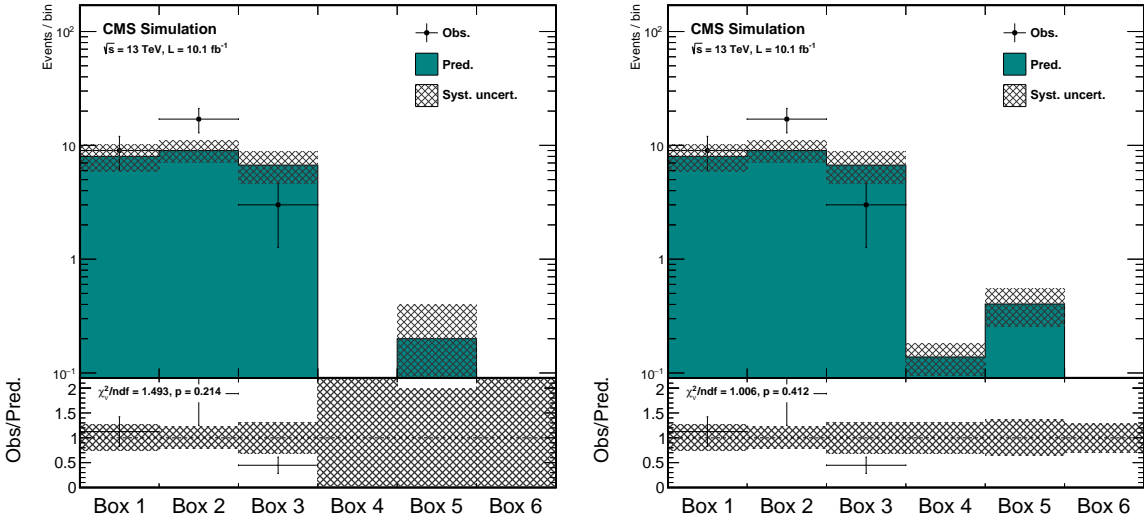


Figure 132: Lost-lepton estimation closure tests in search bins with  $N_{\text{b-jet}} \geq 3$  and  $N_{\text{jet}} \geq 9$ . The black markers are the true expected backgrounds taken directly from  $10 \text{ fb}^{-1}$  of  $t\bar{t}$  MC. The teal histogram corresponds to the background predicted by either the classical (left) or extrapolation method (right). The systematic uncertainties, which are dominated by control sample statistics in the most sensitive bins, correspond to  $10 \text{ fb}^{-1}$  of data. Note that the background in MHT-HT boxes 1-3 is always predicted by the classical method.

Table 45: Closure test for search bins with  $N_{\text{b-jet}} \geq 3$  and  $N_{\text{jet}} \geq 9$ , plotted in Figure 132

MHT-HT Bin	Classical Pred.	Extrapolated Pred.	Obs.
Box 1		$8.0 \pm 2.1$	9
Box 2		$9.0 \pm 2.0$	17
Box 3		$6.7 \pm 2.1$	3
Box 4	0	$0.20 \pm 0.08$	0
Box 5	$0.20 \pm 0.20$	$0.95 \pm 0.46$	0
Box 6	0	$0.07 \pm 0.03$	0

### 2007 L.3 Details of the $H_T^{\text{miss}}$ extrapolation method

2008 Note: for this preliminary study, the lost lepton / control sample lepton ratios are taken from  
2009 MC as a function of  $H_T$ ,  $N_{\text{jet}}$ , and the  $W p_T$ . We are planning, however, to take these ratios  
2010 from the classical lost-lepton method, as described in Section L.2.

2011 The distributions of  $H_T^{\text{miss}} / p_T(W)$  and the lost lepton / control sample lepton ratio as a function  
2012 of  $p_T^W$  in the analysis bins of  $N_{\text{jet}}$  and  $H_T$  are shown in Figures 133 and 134.

The details of how the lost lepton  $H_T^{\text{miss}}$  distribution is constructed from the single lepton control sample are as follows. For each single lepton control sample event, the  $H_T^{\text{miss}} / p_T(W)$  PDF is translated into a  $H_T^{\text{miss}}$  PDF using the reconstructed  $p_T(W)$ . The integral of the  $H_T^{\text{miss}}$  pdf for the high (medium)  $H_T^{\text{miss}}$  bin for event  $i$  is  $I_{ijk}^H$  ( $I_{ijk}^M$ ), where event  $i$  falls in  $N_{\text{jet}}$ ,  $H_T$  bin combination  $j$  and  $p_T^W$  bin  $k$ . The contribution of the event is weighted by the lost / control ratio  $R_{jk}^{LC}$ . Summing over all single lepton control sample events gives

$$S_j^H = \sum_{i,k} R_{jk}^{LC} I_{ijk}^H \quad \text{and} \quad S_j^M = \sum_{i,k} R_{jk}^{LC} I_{ijk}^M \quad (44)$$

2013 and the  $H_T^{\text{miss}}$  ratio  $R_j^{\text{MHT}} = S_j^H / S_j^M$ .

The uncertainty on  $R_j^{\text{MHT}}$  due to the single lepton control sample statistics and the uncertainty on the  $R_{jk}^{\text{LC}}$  is given by

$$\sigma_{R_j^{\text{MHT}}}^2 = \sum_{i,k} \left( \frac{R_{jk}^{\text{LC}} I_{ijk}^H}{S_j^M} - \frac{S_j^H}{(S_j^M)^2} R_{jk}^{\text{LC}} I_{ijk}^M \right)^2 + \sum_k \left( \frac{\sum_i I_{ijk}^H}{S_j^M} - \frac{S_j^H}{(S_j^M)^2} \sum_i I_{ijk}^M \right)^2 \sigma_{R_{jk}^{\text{LC}}}^2 \quad (45)$$

which is approximately

$$\sigma_{R_j^{\text{MHT}}}^2 \approx (R_j^{\text{MHT}})^2 \frac{1}{N_j^H} + \sum_k \left( \frac{\sum_i I_{ijk}^H}{S_j^M} - \frac{S_j^H}{(S_j^M)^2} \sum_i I_{ijk}^M \right)^2 \sigma_{R_{jk}^{\text{LC}}}^2, \quad (46)$$

2014 where  $N_j^H$  is the number of single lepton control sample events with a non-zero contribution to  
2015 the high  $H_T^{\text{miss}}$  bin sum  $S_j^H$ , which is the number of events with  $p_T^W > H_T^{\text{miss}}_{\text{low}}$ , where  $H_T^{\text{miss}}_{\text{low}}$

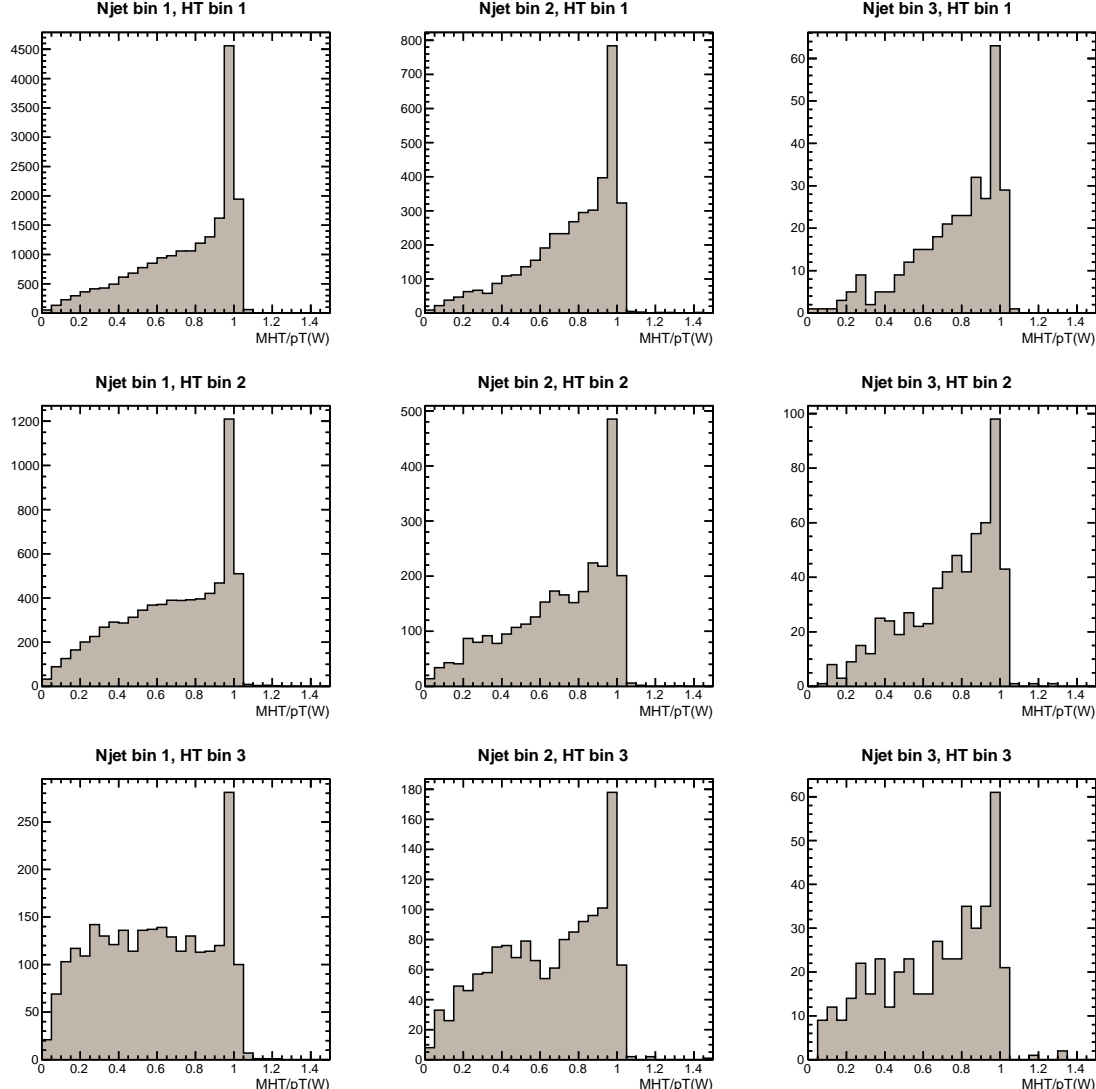


Figure 133: Distribution of  $H_T^{\text{miss}} / p_T(W)$  for lost leptons in the analysis bins of  $N_{\text{jet}}$  and  $H_T$  for the  $t\bar{t}$  Monte Carlo sample.

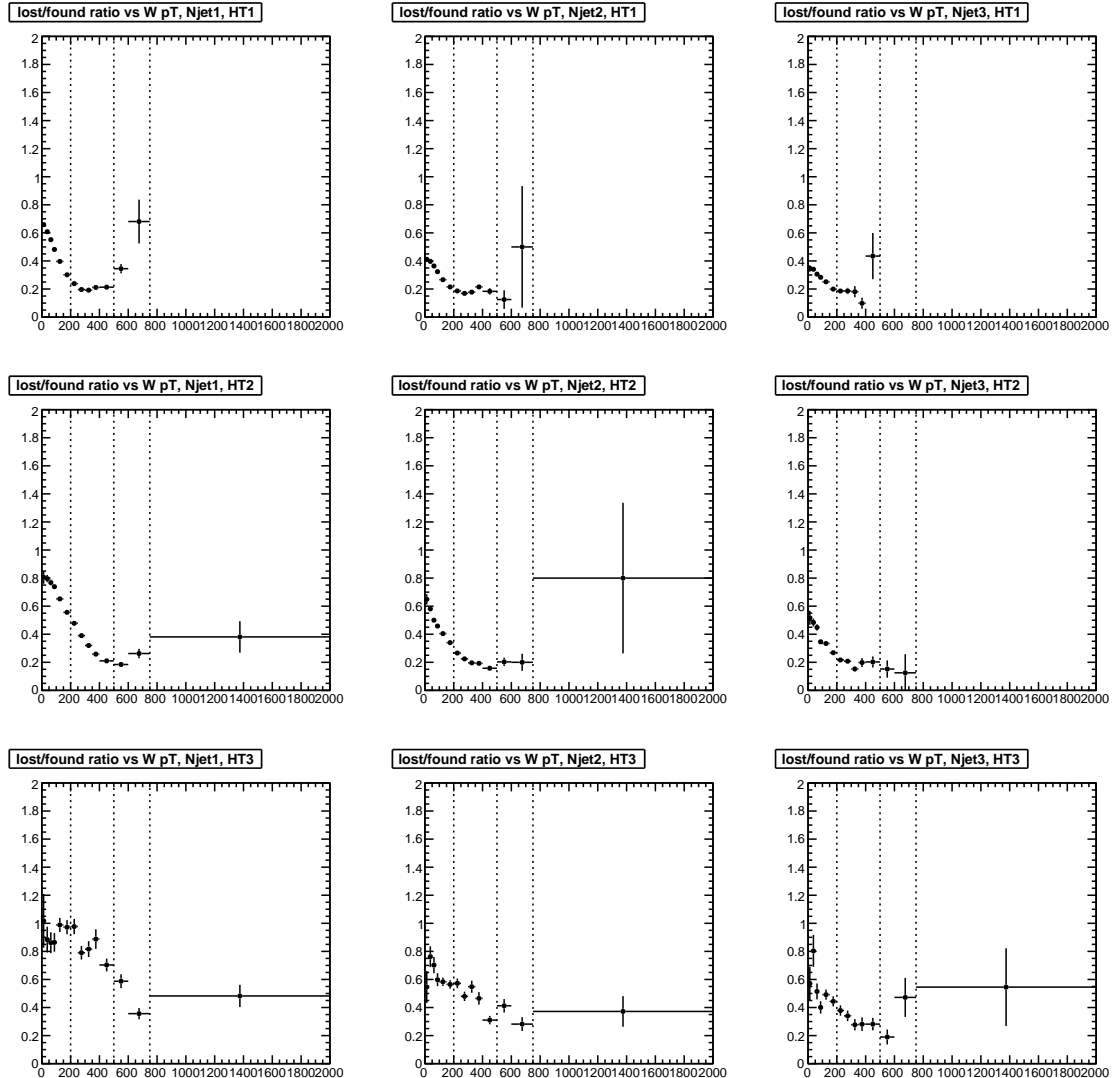


Figure 134: The lost lepton / control sample lepton ratio as a function of  $p_T^W$  in the analysis bins of  $N_{\text{jet}}$  and  $H_T$  for the  $t\bar{t}$  Monte Carlo sample. The vertical dashed lines are at the boundaries of the analysis  $H_T^{\text{miss}}$  bins. The points below 200 GeV are not used in the analysis.

2016 is the low edge of the high  $H_T^{\text{miss}}$  bin. The first term dominates for bins with relatively small  
2017  $N_j^H$ , giving the somewhat expected result of  $\sigma_{R_j^{\text{MHT}}} / R_j^{\text{MHT}} \approx 1 / \sqrt{N_j^H}$ . In the analysis, the full  
2018 expression given in Eqn.45 will be used.

DRAFT

## 2019 M Study of QCD bad jet categorization and $H_T^{\text{miss}}$ dependence

2020 With our current  $\Delta\phi$  requirements and integrated luminosity, the QCD background for  $H_T^{\text{miss}} >$   
 2021 300 GeV is too small to be able to directly constrain with data using our method of fitting for  
 2022 the high/low  $\Delta\phi$  QCD ratio. We take the  $H_T^{\text{miss}}$  dependence of the QCD high/low  $\Delta\phi$  ratio  
 2023 from the QCD Monte Carlo, based on the study described in this Appendix.

2024 We use gen-jet reco-jet matching to identify the jet in each event with the most poorly recon-  
 2025 structed  $p_T$ , which we define to be the one with the largest absolute gen - reco  $p_T$  difference.  
 2026 Events are separated into cases where the worst jet is or is not included in the four jets that are  
 2027 used in the  $\Delta\phi$  selection requirements. Distributions of  $\Delta\phi_{\min}$  are shown in Fig. 135. We find  
 2028 that the worst jet is not included in the  $\Delta\phi_{\min}$  jets in only about 2% of the QCD events that pass  
 2029 the baseline selection ( $H_T > 500$ ,  $H_T^{\text{miss}} > 200$ ,  $N_{\text{jet}} \geq 4$ ) and that there's no apparent  $H_T^{\text{miss}}$   
 2030 dependence in this fraction. Of this 2% of events, where the worst jet is not included in the  
 2031  $\Delta\phi_{\min}$  jets, half of the time is because the reconstructed jet  $p_T$  is not in the top 4, though it is  
 2032 central ( $|\eta| < 2.4$ ). In the remaining cases (about 1%), the worst jet is not included in the  $\Delta\phi_{\min}$   
 2033 jets because it is in the forward region ( $|\eta| > 2.4$ ).

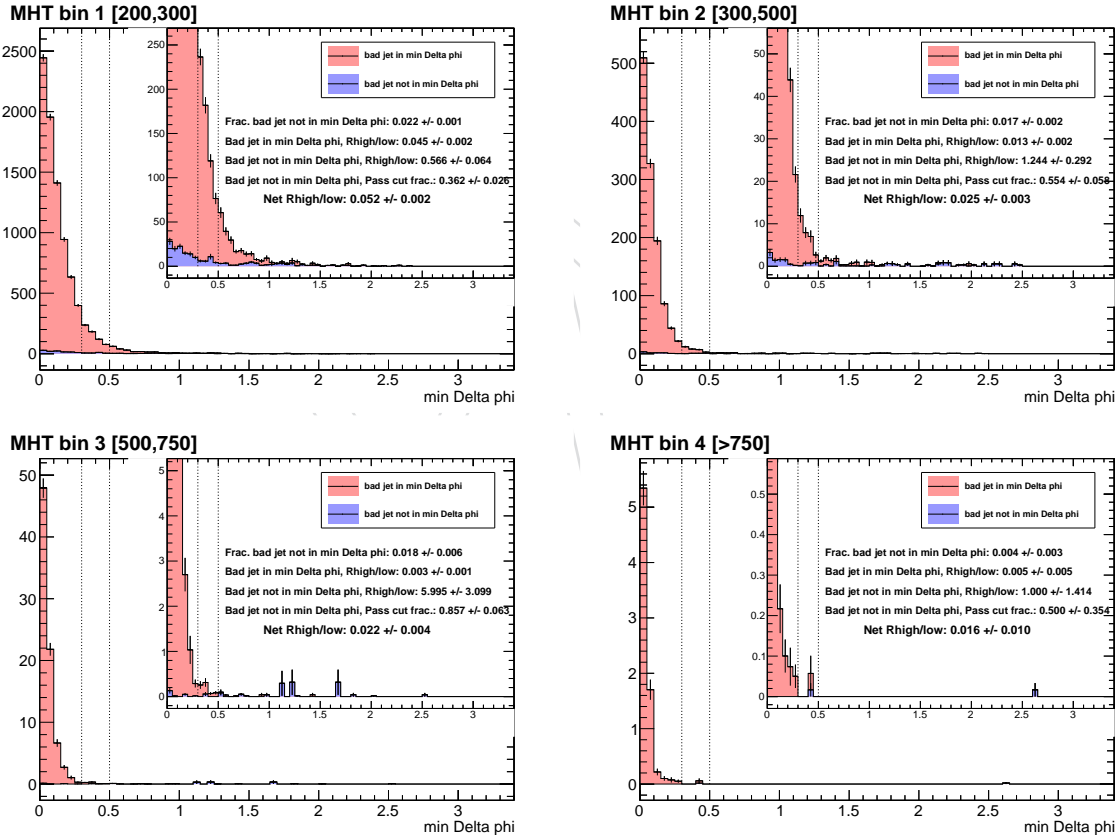


Figure 135: Distributions of  $\Delta\phi_{\min}$  in bins of  $H_T^{\text{miss}}$ . The blue distribution shows the events were the jet with the worst  $p_T$  reconstruction (largest absolute gen - reco  $p_T$  difference) is not one of the four jets included in  $\Delta\phi_{\min}$ . The red distribution is the remaining events where the worst jet is one of the four jets included in  $\Delta\phi_{\min}$ .

2034 The  $\Delta\phi_{\min}$  distributions shown in Fig. 135 display expected features. When the worst jet is  
 2035 included in  $\Delta\phi_{\min}$ , the width of the peak at zero falls strongly with increasing  $H_T^{\text{miss}}$ , which  
 2036 is a long-known property of QCD events, and the high/low ratio, which is about the same  
 2037 as the fraction of events passing the  $\Delta\phi$  requirements, falls from about 5% to below 1%. The

2038  $\Delta\phi_{\min}$  distribution for events where the worst jet is not included in  $\Delta\phi_{\min}$ , is much flatter,  
 2039 where the fraction of these events passing the  $\Delta\phi$  requirements ranges from 36% to 85%. The  
 2040 contribution to the QCD high/low ratio from these two classes of events as a function of  $H_T^{\text{miss}}$   
 2041 is shown in Fig. 136. The dominant contribution to the QCD background for  $H_T^{\text{miss}}$  bins 3 and  
 2042 4 ( $H_T^{\text{miss}} > 500$ ) is from events where the worst jet is not in the four  $\Delta\phi$  jets, giving a QCD  
 2043 high/low ratio or search/control ratio of about 2%.

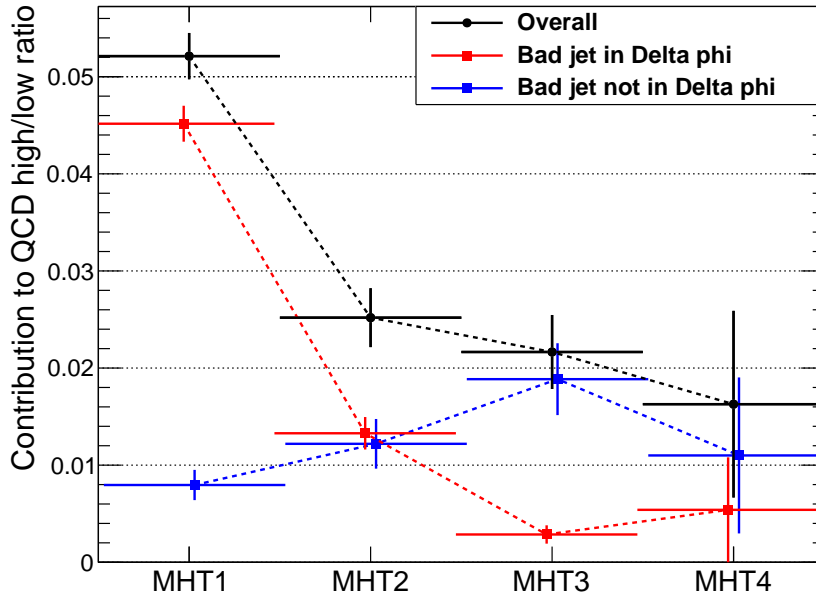


Figure 136: Contribution to QCD high/low  $\Delta\phi_{\min}$  ratio as a function of  $H_T^{\text{miss}}$  bin. The contributions are split by whether the jet with the worst  $p_T$  reconstruction (largest absolute gen - reco  $p_T$  difference) is (red) or is not (blue) included in the four  $\Delta\phi_{\min}$  jets.

2044 The  $H_T^{\text{miss}}$  dependence of the QCD model, described in Sec. 7.1, is included with the multiplica-  
 2045 tive factor  $S_{MHT,j}^{QCD}$  in Eqn. 22, which is the correction for  $H_T^{\text{miss}}$  bin  $j$  with respect to the first  $H_T^{\text{miss}}$   
 2046 bin. If we assume a 100% uncertainty on the component where the worst jet is not in the four  
 2047  $\Delta\phi$  jets, this gives

- 2048 •  $S_{MHT,2}^{QCD} = 1$  (fixed) by definition of the parameter,  $H_T^{\text{miss}}$  in the range 200 to 300.
- 2049 •  $S_{MHT,2}^{QCD} = 0.50 \pm 0.25$  for  $H_T^{\text{miss}}$  in the range 300 to 500,
- 2050 •  $S_{MHT,3}^{QCD} = 0.50 \pm 0.50$  for  $H_T^{\text{miss}}$  in the range 500 to 750,
- 2051 •  $S_{MHT,4}^{QCD} = 0.50 \pm 0.50$  for  $H_T^{\text{miss}}$  above 750.

2052 These are included as nuisance parameters of the QCD BG model.

Table 46: Expected number of QCD and signal events for events passing the  $\Delta\phi$  requirements with  $H_T^{\text{miss}}$  between 200 and 300 GeV. The “H” and “C” in the signal model label refer to “Heavy gluino” (with light LSP) and “Compressed” points.

Signal model	Sum over bins			Bin name	Bin with highest Sig/QCD		
	QCD	Sig	Sig/QCD		QCD	Sig	Sig/QCD
T1bbbbH	442.9	1.21	0.003	Njets=7,8; HT3	28.9	0.33	0.012
T1bbbbC	442.9	9.15	0.022	Njets=7,8; HT1	14.0	1.82	0.130
T1qqqqH	442.9	2.15	0.005	Njets=6; HT3	33.9	0.53	0.016
T1qqqqC	442.9	29.58	0.070	Njets=7,8; HT1	14.0	4.84	0.346
T1ttttH	442.9	0.20	0.000	Njets=7,8; HT3	28.9	0.13	0.005
T1ttttC	442.9	2.68	0.006	Njets=7,8; HT1	14.0	1.74	0.125

## 2053 N Signal contamination in the QCD background evaluation

2054 The QCD analysis determines the  $H_T$  and  $N_{\text{jet}}$  dependence of the  $\Delta\phi$  high/low ratio in a binned  
 2055 likelihood analysis of the data, as described in Section 7.1. This analysis only uses events in the  
 2056  $H_T^{\text{miss}}$  range of 200 to 300 GeV, which is background dominated for signal models close to the  
 2057 current exclusion boundary, as we will show in this section. We will show that for these signal  
 2058 models, we can safely neglect the effects of signal contamination, both at low and high  $\Delta\phi$ ,  
 2059 because the events with  $H_T^{\text{miss}}$  between 200 and 300 are background dominated.

2060 Table 46 gives the expected number of QCD and signal events in the likelihood fit for the QCD  
 2061 BG high/low ratio model parameters for the six benchmark signal models. With the exception  
 2062 of the compressed T1qqqq point (gluino mass of 1000, LSP mass of 800), the signal contamina-  
 2063 tion is at most 2%.

2064 To test the expected effect of unaccounted for signal contamination in the data determination  
 2065 of the QCD model parameters, we performed the  $\chi^2$  fit of the high/low ratios, described in  
 2066 Sec. 7.1, twice; once where the ratios include signal contamination and once for the pure QCD  
 2067 MC ratios. The results are shown in Fig. 137. Again, with the exception of the compressed  
 2068 T1qqqq point, the shift in the QCD model parameters is less than 4%. The fit uncertainties on  
 2069 the QCD model parameters (see Tab 16), are substantially larger and range from 35% to 300%.  
 2070 We therefore feel justified in currently neglecting signal contamination in the determination of  
 2071 the QCD model parameters.

2072 Please note that signal contamination in the low  $\Delta\phi$  control sample is included in the evaluation  
 2073 of the QCD BG in the search region. Please also note that signal contamination for a given signal  
 2074 model can be included in the determination of the QCD model parameters.

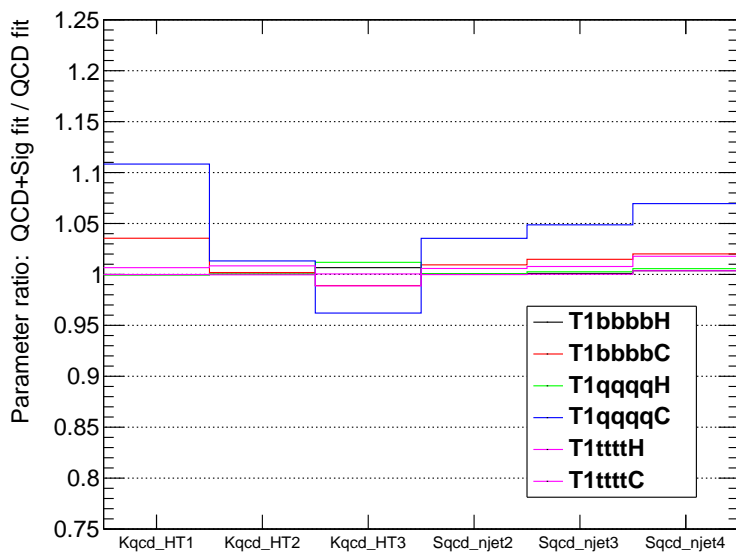


Figure 137: QCD model parameter ratios comparing  $\chi^2$  fit results of high/low ratios that include signal contamination (unaccounted for) divided by the pure QCD MC ratios.

## 2075 O Study of $N_{\text{b-jet}}$ dependence in the QCD background model

2076 To test for  $N_{\text{b-jet}}$  dependence, we split the 55 bins shown in Fig. 60 into the 4  $N_{\text{b-jet}}$  bins, for a total  
 2077 of 220 bins and repeated the fit including three  $S_{nb,l}^{QCD}$  parameters, which allow for corrections  
 2078 for the top 3  $N_{\text{b-jet}}$  bins relative to the first  $N_{\text{b-jet}}$  bins, where the  $N_{\text{b-jet}}$  dependence is assumed  
 2079 to factorize, relative to  $H_T$ ,  $N_{\text{jet}}$ , and  $H_T^{\text{miss}}$ . The  $S_{nb,l}^{QCD}$  parameters are  $0.83 \pm 0.06$ ,  $0.91 \pm 0.11$ ,  
 2080 and  $0.73 \pm 0.11$  for  $N_{\text{b-jet}} = 1, 2, 3+$ , respectively. The event weights for the  $H_T$ -binned QCD  
 2081 Monte Carlo samples span 4 orders of magnitude, which can cause a large change in value and  
 2082 statistical uncertainty if the number of high-weight events in a given ratio point is small. We  
 2083 do not feel there's evidence of any true  $N_{\text{b-jet}}$  dependence, so we do not make any corrections  
 2084 as a function of  $N_{\text{b-jet}}$ . However, we include systematic uncertainties of 20%, 20%, and 30% for  
 2085 the  $N_{\text{b-jet}} = 1, 2, 3+$  predictions, respectively, based on the results given above.

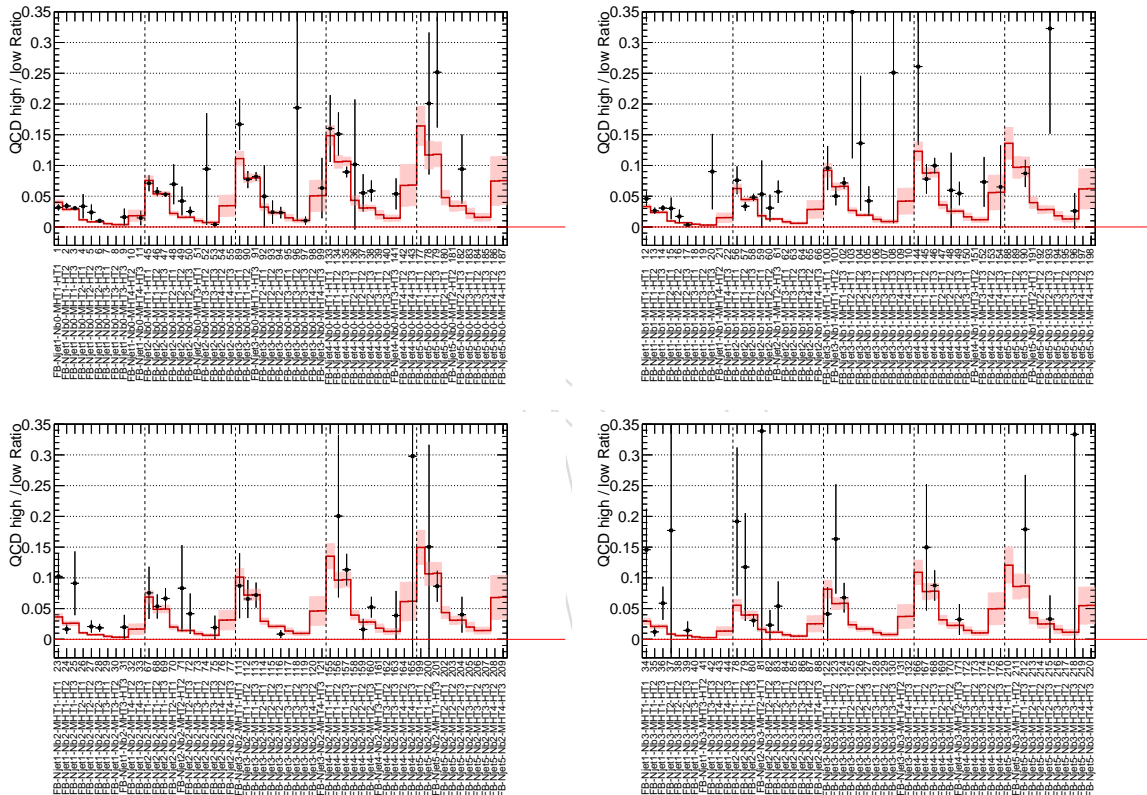


Figure 138: QCD MC high/low ratio for the search  $\Delta\phi_{\min}$  requirement split by the number of b tags, with  $N_{\text{b-jet}} = 0$  (upper left),  $N_{\text{b-jet}} = 1$  (upper right),  $N_{\text{b-jet}} = 2$  (lower left), and  $N_{\text{b-jet}} \geq 3$  (lower right). The black points with error bars are the QCD Monte Carlo. The red histogram with shaded errors is the  $\chi^2$  fit result, where the floating parameters in the fit were the  $K^{QCD}$  and  $S^{QCD}$  model parameters.

---

**P Detailed results of QCD BG estimation from min  $\Delta\phi_{\min}$** 

2086 These are the results of the QCD BG estimation from min  $\Delta\phi_{\min}$  for the 2.1  $\text{fb}^{-1}$  data sample.

DRAFT

Bin	$N_{obs}^{LDP}$	Non-QCD	$N_{obs}$ - Non-QCD	$R_{QCD}$	QCD BG	MC
SB-Njet1-Nb0-MHTHT1 1	4250	$814.3 \pm 59.6$	$3435.7 \pm 88.3$	$0.064 \pm 0.032$	$219.9 \pm 110.0$	$182.8 \pm 18.9$
SB-Njet1-Nb0-MHTHT2 2	3501	$306.7 \pm 23.4$	$3194.3 \pm 63.6$	$0.031 \pm 0.010$	$99.8 \pm 33.5$	$161.4 \pm 13.7$
SB-Njet1-Nb0-MHTHT3 3	2376	$99.8 \pm 10.2$	$2276.2 \pm 49.8$	$0.040 \pm 0.011$	$90.4 \pm 24.2$	$137.4 \pm 6.1$
SB-Njet1-Nb0-MHTHT4 4	45	$28.3 \pm 3.8$	$16.7 \pm 7.7$	$0.023 \pm 0.024$	$0.4 \pm 0.4$	$1.1 \pm 0.7$
SB-Njet1-Nb0-MHTHT5 5	54	$10.9 \pm 2.4$	$43.1 \pm 7.7$	$0.023 \pm 0.023$	$1.0 \pm 1.0$	$0.8 \pm 0.5$
SB-Njet1-Nb0-MHTHT6 6	17	$6.2 \pm 2.0$	$10.8 \pm 4.6$	$0.020 \pm 0.021$	$0.2 \pm 0.3$	$0.2 \pm 0.1$
SB-Njet1-Nb1-MHTHT1 7	1383	$339.1 \pm 27.5$	$1043.9 \pm 46.3$	$0.066 \pm 0.036$	$69.2 \pm 37.4$	$70.4 \pm 11.3$
SB-Njet1-Nb1-MHTHT2 8	1277	$152.1 \pm 12.8$	$1124.9 \pm 38.0$	$0.032 \pm 0.013$	$36.4 \pm 14.3$	$48.2 \pm 6.5$
SB-Njet1-Nb1-MHTHT3 9	830	$44.1 \pm 5.4$	$785.9 \pm 29.3$	$0.041 \pm 0.014$	$32.5 \pm 11.0$	$52.9 \pm 4.0$
SB-Njet1-Nb1-MHTHT4 10	12	$8.8 \pm 2.1$	$3.2 \pm 4.0$	$0.012 \pm 0.013$	$0.1 \pm 0.1$	$0.0 \pm 0.0$
SB-Njet1-Nb1-MHTHT5 11	21	$5.2 \pm 1.7$	$15.8 \pm 4.9$	$0.024 \pm 0.025$	$0.4 \pm 0.4$	$2.0 \pm 1.2$
SB-Njet1-Nb1-MHTHT6 12	2	$3.2 \pm 1.6$	$-1.2 \pm 2.2$	$0.033 \pm 0.036$	$0.0 \pm 0.1$	$0.0 \pm 0.0$
SB-Njet1-Nb2-MHTHT1 13	333	$116.5 \pm 12.2$	$216.5 \pm 21.9$	$0.072 \pm 0.039$	$15.9 \pm 8.8$	$28.3 \pm 7.7$
SB-Njet1-Nb2-MHTHT2 14	328	$59.2 \pm 6.6$	$268.8 \pm 19.3$	$0.035 \pm 0.014$	$9.5 \pm 3.8$	$12.2 \pm 2.8$
SB-Njet1-Nb2-MHTHT3 15	144	$15.4 \pm 2.7$	$128.6 \pm 12.3$	$0.043 \pm 0.015$	$5.6 \pm 2.0$	$15.8 \pm 3.9$
SB-Njet1-Nb2-MHTHT4 16	3	$2.3 \pm 1.3$	$0.7 \pm 2.2$	$0.011 \pm 0.012$	$0.0 \pm 0.0$	$0.1 \pm 0.1$
SB-Njet1-Nb2-MHTHT5 17	3	$0.5 \pm 0.8$	$2.5 \pm 1.9$	$0.027 \pm 0.029$	$0.1 \pm 0.1$	$0.1 \pm 0.0$
SB-Njet1-Nb2-MHTHT6 18	1	$0.3 \pm 1.1$	$0.7 \pm 1.5$	$0.027 \pm 0.029$	$0.0 \pm 0.0$	$0.0 \pm 0.0$
SB-Njet1-Nb3-MHTHT1 19	28	$12.3 \pm 3.4$	$15.7 \pm 6.3$	$0.073 \pm 0.044$	$1.2 \pm 0.8$	$9.1 \pm 2.7$
SB-Njet1-Nb3-MHTHT2 20	28	$9.0 \pm 2.7$	$19.0 \pm 6.0$	$0.037 \pm 0.017$	$0.7 \pm 0.4$	$3.3 \pm 1.3$
SB-Njet1-Nb3-MHTHT3 21	17	$1.4 \pm 1.3$	$15.6 \pm 4.3$	$0.046 \pm 0.019$	$0.7 \pm 0.4$	$1.3 \pm 0.3$
SB-Njet1-Nb3-MHTHT4 22	1	$0.0 \pm 1.1$	$1.0 \pm 1.5$	$0.046 \pm 0.054$	$0.0 \pm 0.1$	$0.0 \pm 0.0$
SB-Njet1-Nb3-MHTHT5 23	0	$0.0 \pm 0.8$	$0.0 \pm 0.8$	$0.025 \pm 0.027$	$0.0 \pm 0.0$	$0.0 \pm 0.0$
SB-Njet1-Nb3-MHTHT6 24	0	$0.0 \pm 1.1$	$0.0 \pm 1.1$	$0.022 \pm 0.024$	$0.0 \pm 0.0$	$0.0 \pm 0.0$
SB-Njet2-Nb0-MHTHT1 25	106	$26.9 \pm 3.2$	$79.1 \pm 10.8$	$0.173 \pm 0.099$	$14.1 \pm 8.2$	$16.0 \pm 4.8$
SB-Njet2-Nb0-MHTHT2 26	242	$30.1 \pm 3.4$	$211.9 \pm 15.9$	$0.077 \pm 0.033$	$16.3 \pm 7.1$	$29.7 \pm 6.4$
SB-Njet2-Nb0-MHTHT3 27	265	$17.4 \pm 2.8$	$247.6 \pm 16.5$	$0.093 \pm 0.035$	$23.0 \pm 8.8$	$32.0 \pm 2.9$
SB-Njet2-Nb0-MHTHT4 28	2	$0.7 \pm 0.8$	$1.3 \pm 1.6$	$0.041 \pm 0.045$	$0.1 \pm 0.1$	$0.0 \pm 0.0$
SB-Njet2-Nb0-MHTHT5 29	6	$1.0 \pm 0.8$	$5.0 \pm 2.6$	$0.051 \pm 0.055$	$0.3 \pm 0.3$	$0.3 \pm 0.1$
SB-Njet2-Nb0-MHTHT6 30	4	$0.4 \pm 0.8$	$3.6 \pm 2.1$	$0.051 \pm 0.055$	$0.2 \pm 0.2$	$0.0 \pm 0.0$
SB-Njet2-Nb1-MHTHT1 31	73	$26.2 \pm 3.0$	$46.8 \pm 9.0$	$0.173 \pm 0.104$	$8.1 \pm 5.1$	$9.5 \pm 4.1$
SB-Njet2-Nb1-MHTHT2 32	132	$35.5 \pm 4.0$	$96.5 \pm 12.2$	$0.078 \pm 0.037$	$7.6 \pm 3.7$	$8.9 \pm 2.5$
SB-Njet2-Nb1-MHTHT3 33	165	$17.7 \pm 2.8$	$147.3 \pm 13.1$	$0.093 \pm 0.040$	$13.7 \pm 5.9$	$17.7 \pm 2.0$
SB-Njet2-Nb1-MHTHT4 34	0	$0.7 \pm 0.7$	$-0.7 \pm 0.7$	$0.064 \pm 0.071$	$0.0 \pm 0.1$	$0.0 \pm 0.0$
SB-Njet2-Nb1-MHTHT5 35	4	$1.6 \pm 0.8$	$2.4 \pm 2.2$	$0.051 \pm 0.056$	$0.1 \pm 0.2$	$0.2 \pm 0.1$
SB-Njet2-Nb1-MHTHT6 36	0	$0.2 \pm 0.7$	$-0.2 \pm 0.7$	$0.046 \pm 0.050$	$0.0 \pm 0.1$	$0.0 \pm 0.0$
SB-Njet2-Nb2-MHTHT1 37	20	$20.0 \pm 3.1$	$0.0 \pm 5.5$	$0.173 \pm 0.105$	$0.2 \pm 0.6$	$0.0 \pm 0.0$
SB-Njet2-Nb2-MHTHT2 38	50	$20.9 \pm 2.6$	$29.1 \pm 7.5$	$0.074 \pm 0.035$	$2.1 \pm 1.1$	$5.6 \pm 3.5$
SB-Njet2-Nb2-MHTHT3 39	52	$10.5 \pm 2.0$	$41.5 \pm 7.5$	$0.086 \pm 0.037$	$3.5 \pm 1.6$	$6.0 \pm 1.2$
SB-Njet2-Nb2-MHTHT4 40	0	$0.8 \pm 0.8$	$-0.8 \pm 0.8$	$0.064 \pm 0.071$	$0.0 \pm 0.1$	$0.0 \pm 0.0$
SB-Njet2-Nb2-MHTHT5 41	1	$0.5 \pm 0.5$	$0.5 \pm 1.1$	$0.051 \pm 0.056$	$0.0 \pm 0.1$	$0.0 \pm 0.0$
SB-Njet2-Nb2-MHTHT6 42	0	$0.1 \pm 0.7$	$-0.1 \pm 0.7$	$0.046 \pm 0.050$	$0.0 \pm 0.1$	$0.0 \pm 0.0$
SB-Njet2-Nb3-MHTHT1 43	10	$4.1 \pm 1.4$	$5.9 \pm 3.4$	$0.173 \pm 0.112$	$1.1 \pm 0.9$	$0.0 \pm 0.0$
SB-Njet2-Nb3-MHTHT2 44	12	$4.4 \pm 1.2$	$7.6 \pm 3.7$	$0.078 \pm 0.041$	$0.6 \pm 0.4$	$1.2 \pm 0.7$
SB-Njet2-Nb3-MHTHT3 45	2	$2.0 \pm 0.9$	$0.0 \pm 1.7$	$0.102 \pm 0.049$	$0.0 \pm 0.1$	$0.9 \pm 0.2$
SB-Njet2-Nb3-MHTHT4 46	1	$0.0 \pm 0.7$	$1.0 \pm 1.2$	$0.041 \pm 0.046$	$0.0 \pm 0.1$	$0.0 \pm 0.0$
SB-Njet2-Nb3-MHTHT5 47	0	$0.0 \pm 0.5$	$0.0 \pm 0.5$	$0.051 \pm 0.057$	$0.0 \pm 0.1$	$0.0 \pm 0.0$
SB-Njet2-Nb3-MHTHT6 48	0	$0.0 \pm 0.7$	$0.0 \pm 0.7$	$0.046 \pm 0.051$	$0.0 \pm 0.1$	$0.0 \pm 0.0$
SB-Njet3-Nb0-MHTHT1 49	6	$0.9 \pm 0.9$	$5.1 \pm 2.6$	$0.159 \pm 0.118$	$0.9 \pm 0.8$	$1.9 \pm 1.3$
SB-Njet3-Nb0-MHTHT2 50	14	$3.0 \pm 0.9$	$11.0 \pm 3.9$	$0.071 \pm 0.045$	$0.8 \pm 0.6$	$3.5 \pm 1.6$
SB-Njet3-Nb0-MHTHT3 51	49	$2.9 \pm 1.1$	$46.1 \pm 7.1$	$0.085 \pm 0.051$	$3.9 \pm 2.4$	$11.2 \pm 3.6$
SB-Njet3-Nb0-MHTHT4 52	0	$0.2 \pm 0.7$	$-0.2 \pm 0.7$	$0.059 \pm 0.070$	$0.0 \pm 0.1$	$0.0 \pm 0.0$
SB-Njet3-Nb0-MHTHT5 53	1	$1.7 \pm 1.0$	$-0.7 \pm 1.4$	$0.047 \pm 0.055$	$0.0 \pm 0.0$	$0.0 \pm 0.0$
SB-Njet3-Nb0-MHTHT6 54	0	$0.2 \pm 0.7$	$-0.2 \pm 0.7$	$0.042 \pm 0.049$	$0.0 \pm 0.1$	$0.0 \pm 0.0$
SB-Njet3-Nb1-MHTHT1 55	3	$2.1 \pm 1.0$	$0.9 \pm 2.0$	$0.097 \pm 0.081$	$0.1 \pm 0.2$	$0.9 \pm 0.9$
SB-Njet3-Nb1-MHTHT2 56	16	$4.1 \pm 1.1$	$11.9 \pm 4.1$	$0.074 \pm 0.050$	$0.9 \pm 0.6$	$0.0 \pm 0.0$
SB-Njet3-Nb1-MHTHT3 57	32	$3.2 \pm 1.1$	$28.8 \pm 5.8$	$0.084 \pm 0.053$	$2.4 \pm 1.6$	$4.0 \pm 0.9$
SB-Njet3-Nb1-MHTHT4 58	0	$0.1 \pm 0.7$	$-0.1 \pm 0.7$	$0.059 \pm 0.071$	$0.0 \pm 0.1$	$0.0 \pm 0.0$
SB-Njet3-Nb1-MHTHT5 59	0	$0.5 \pm 0.6$	$-0.5 \pm 0.6$	$0.047 \pm 0.056$	$0.0 \pm 0.1$	$0.0 \pm 0.0$
SB-Njet3-Nb1-MHTHT6 60	0	$0.1 \pm 0.7$	$-0.1 \pm 0.7$	$0.042 \pm 0.050$	$0.0 \pm 0.1$	$0.1 \pm 0.1$
SB-Njet3-Nb2-MHTHT1 61	1	$1.8 \pm 0.9$	$-0.8 \pm 1.3$	$0.119 \pm 0.094$	$0.0 \pm 0.1$	$0.0 \pm 0.0$
SB-Njet3-Nb2-MHTHT2 62	7	$3.2 \pm 1.4$	$3.8 \pm 3.0$	$0.069 \pm 0.046$	$0.3 \pm 0.2$	$0.5 \pm 0.5$
SB-Njet3-Nb2-MHTHT3 63	18	$2.8 \pm 1.0$	$15.2 \pm 4.4$	$0.090 \pm 0.057$	$1.4 \pm 0.9$	$0.9 \pm 0.2$
SB-Njet3-Nb2-MHTHT4 64	0	$0.4 \pm 0.7$	$-0.4 \pm 0.7$	$0.059 \pm 0.071$	$0.0 \pm 0.1$	$0.0 \pm 0.0$
SB-Njet3-Nb2-MHTHT5 65	0	$0.2 \pm 0.5$	$-0.2 \pm 0.5$	$0.047 \pm 0.056$	$0.0 \pm 0.1$	$0.0 \pm 0.0$
SB-Njet3-Nb2-MHTHT6 66	0	$0.0 \pm 0.7$	$0.0 \pm 0.7$	$0.042 \pm 0.050$	$0.0 \pm 0.1$	$0.0 \pm 0.0$
SB-Njet3-Nb3-MHTHT1 67	0	$0.4 \pm 0.7$	$-0.4 \pm 0.7$	$0.119 \pm 0.098$	$0.0 \pm 0.2$	$0.0 \pm 0.0$
SB-Njet3-Nb3-MHTHT2 68	4	$0.9 \pm 0.7$	$3.1 \pm 2.1$	$0.076 \pm 0.053$	$0.3 \pm 0.2$	$0.0 \pm 0.0$
SB-Njet3-Nb3-MHTHT3 69	2	$1.2 \pm 0.9$	$0.8 \pm 1.7$	$0.047 \pm 0.039$	$0.0 \pm 0.1$	$0.4 \pm 0.2$
SB-Njet3-Nb3-MHTHT4 70	0	$0.0 \pm 0.7$	$0.0 \pm 0.7$	$0.059 \pm 0.072$	$0.0 \pm 0.1$	$0.0 \pm 0.0$
SB-Njet3-Nb3-MHTHT5 71	0	$0.1 \pm 0.5$	$-0.1 \pm 0.5$	$0.047 \pm 0.057$	$0.0 \pm 0.1$	$0.0 \pm 0.0$
SB-Njet3-Nb3-MHTHT6 72	0	$0.0 \pm 0.7$	$0.0 \pm 0.7$	$0.042 \pm 0.051$	$0.0 \pm 0.1$	$0.0 \pm 0.0$

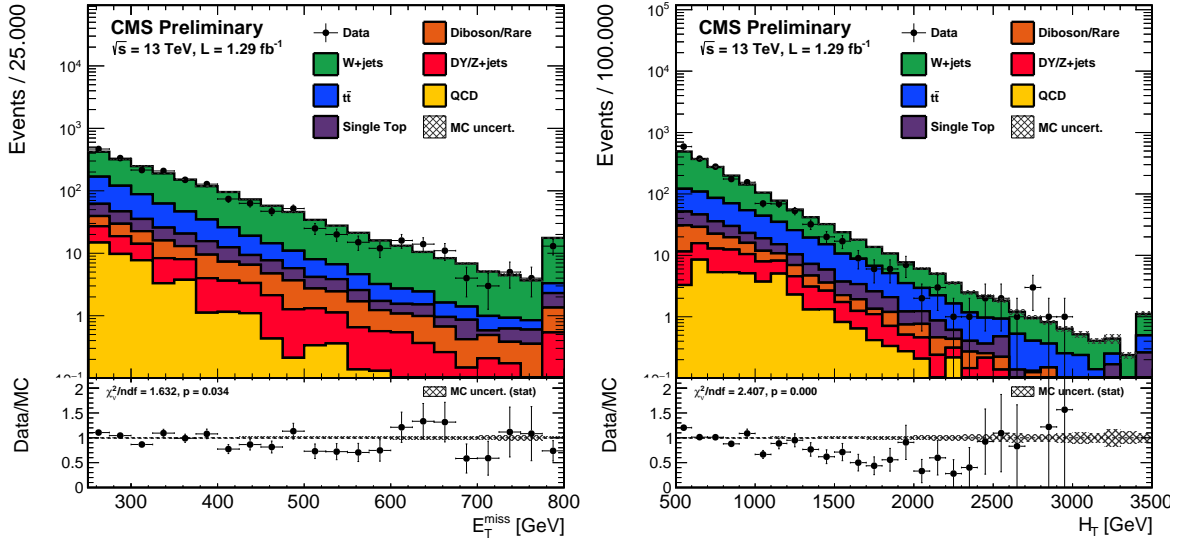


Figure 139: Data-MC comparisions of the  $E_T^{\text{miss}}$  and  $H_T$  distributions with a single-muon selection.

## Q Additional data-MC comparisons

The data used in this appendix, unless otherwise noted, are from the HTMHT primary datasets and required to pass the HLT\_PFT350\_PFMET100\_JetIDCleaned\_v\* triggers. The MC samples included are listed in Chapter 3.1. No simulated triggers are applied to the MC. The MC samples are normalized to the integrated luminosity of the data. No other normalization correction factors are applied.

### Q.1 Single-muon control region plots requested by the inclusive searches group

The cuts applied in this section are:

- $E_T^{\text{miss}} > 250 \text{ GeV}$
- $H_T > 500 \text{ GeV}$
- $N_{\text{jet}} \geq 2$  ( $p_T > 40 \text{ GeV}$ ,  $|\eta| < 2.4$ ), passing POG loose ID
- Exactly one muon and zero electrons
- $p_T^\mu > 25 \text{ GeV}$ , passing POG medium ID
- $m_T < 120 \text{ GeV}$
- All  $E_T^{\text{miss}}$ -related filters listed in Chapter 4

In this sample, we observe 1880 events in data and expect 1892 from simulation (data/MC=0.994).

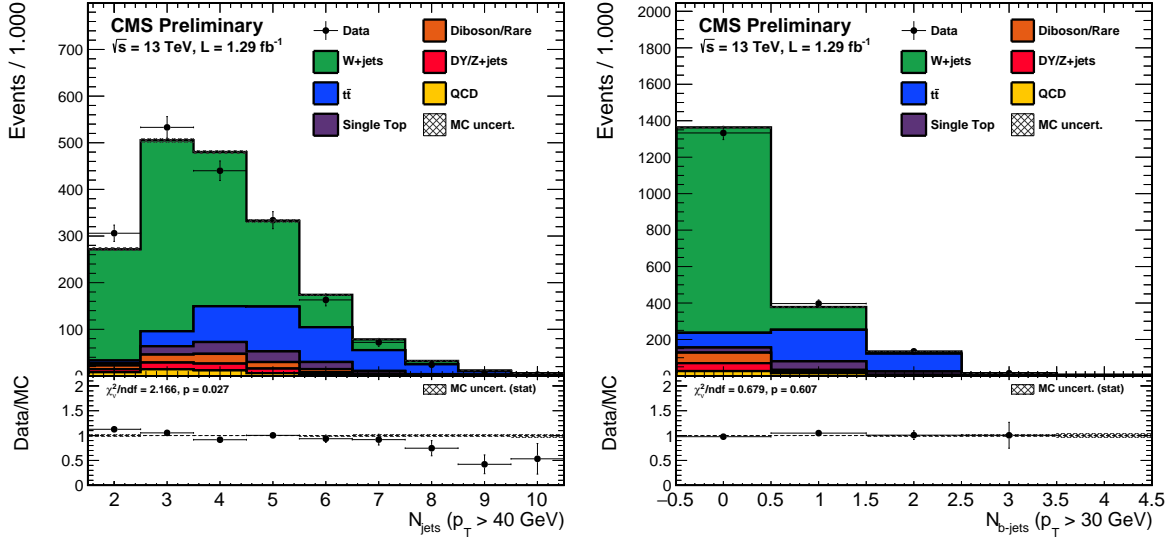


Figure 140: Data-MC comparisions of the  $N_{\text{jet}}$  and  $N_{\text{b-jet}}$  distributions with a single-muon selection.

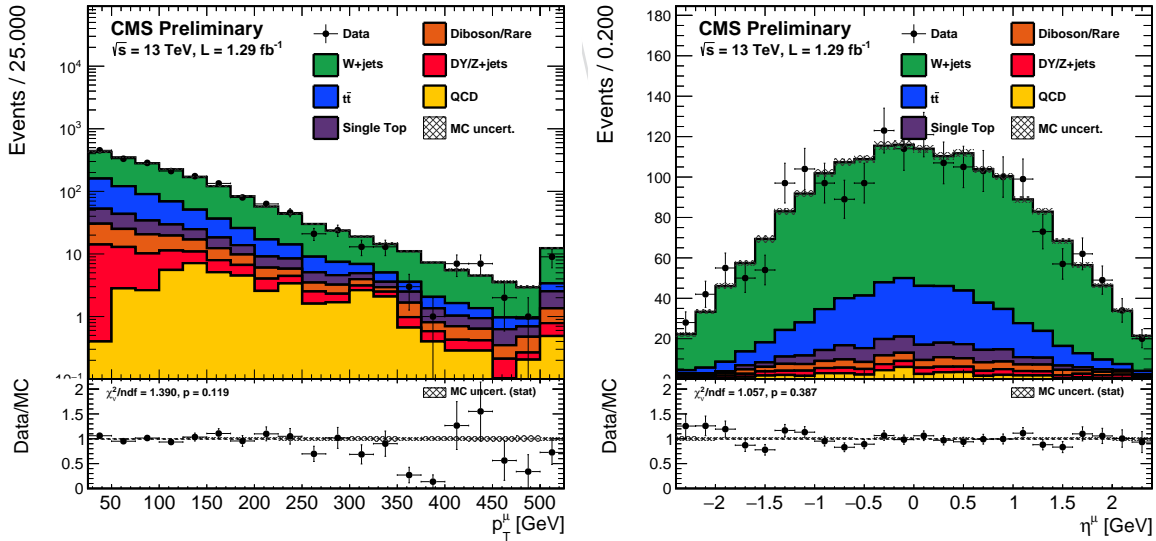


Figure 141: Data-MC comparisions of the muon  $p_T$  and  $\eta$  distributions with a single-muon selection.